



Swansea University  
Prifysgol Abertawe



## Swansea University E-Theses

---

# Development of a Raman system for in-line monitoring of tritium at the Karlsruhe Tritium Neutrino (KATRIN) experiment.

Lewis, Richard James

### How to cite:

---

Lewis, Richard James (2007) *Development of a Raman system for in-line monitoring of tritium at the Karlsruhe Tritium Neutrino (KATRIN) experiment.*. thesis, Swansea University.  
<http://cronfa.swan.ac.uk/Record/cronfa42885>

### Use policy:

---

This item is brought to you by Swansea University. Any person downloading material is agreeing to abide by the terms of the repository licence: copies of full text items may be used or reproduced in any format or medium, without prior permission for personal research or study, educational or non-commercial purposes only. The copyright for any work remains with the original author unless otherwise specified. The full-text must not be sold in any format or medium without the formal permission of the copyright holder. Permission for multiple reproductions should be obtained from the original author.

Authors are personally responsible for adhering to copyright and publisher restrictions when uploading content to the repository.

Please link to the metadata record in the Swansea University repository, Cronfa (link given in the citation reference above.)

<http://www.swansea.ac.uk/library/researchsupport/ris-support/>

**DEVELOPMENT OF A RAMAN SYSTEM FOR IN-LINE  
MONITORING OF TRITIUM AT THE KARLSRUHE  
TRITIUM NEUTRINO (KATRIN) EXPERIMENT**

**Richard James Lewis MPhys AMInstP**

**Department of Physics**

**Swansea University**

**Submitted to the University of Wales in fulfilment of the requirements for the**

**Degree of Doctor of Philosophy**

**February 2007**

ProQuest Number: 10821275

All rights reserved

INFORMATION TO ALL USERS

The quality of this reproduction is dependent upon the quality of the copy submitted.

In the unlikely event that the author did not send a complete manuscript and there are missing pages, these will be noted. Also, if material had to be removed, a note will indicate the deletion.



ProQuest 10821275

Published by ProQuest LLC (2018). Copyright of the Dissertation is held by the Author.

All rights reserved.

This work is protected against unauthorized copying under Title 17, United States Code  
Microform Edition © ProQuest LLC.

ProQuest LLC.  
789 East Eisenhower Parkway  
P.O. Box 1346  
Ann Arbor, MI 48106 – 1346



*To Mam and Dad, who taught me to read and write.*

## SUMMARY

The overall objective of this thesis was the development of a laser Raman spectroscopic system to monitor the purity of tritium injected into the Windowless Gaseous Tritium Source (WGTS) tube of the Karlsruhe Tritium Neutrino (KATRIN) experiment.

KATRIN is a next-generation direct (beta decay endpoint) neutrino mass measurement experiment currently under construction at Forschungszentrum Karlsruhe (FZK) that is designed to improve the sensitivity in the measurement of the electron neutrino mass by an order of magnitude over the recent Mainz and Troitsk experiments, i.e. to reach a mass sensitivity of  $0.2\text{eV}/c^2$  (90% C.L.). A definite measurement of the electron neutrino mass by KATRIN would be a discovery of profound importance for particle physics, astrophysics and cosmology. In order to minimise systematic errors in the determination of the electron neutrino mass, the purity of the tritium gas used as the beta decay source must be monitored continuously and to a minimum precision of about  $\pm 0.2\%$ , with  $\pm 0.1\%$  being an ideal-case 'gold standard'.

A fibre-coupled laser Raman monitoring system (including complimentary Raman spectrum simulation and post-acquisition data processing software) has been developed and tested both off-line at Swansea University under low-laser power, high-pressure conditions, and in-line at the Test of Inner Loop (TILO) mock-up WGTS system at FZK. Both sets of measurements demonstrate that the minimum purity precision of  $\pm 0.2\%$  can be met easily, and that it is probable that even the 'gold standard' of  $\pm 0.1\%$  will be surpassed in near-future repeats of the in-line experimental runs.

## ACKNOWLEDGEMENTS

I would firstly like to thank my supervisor, Professor Helmut Telle, for his guidance, patience, and good humour throughout my PhD studentship.

I would also like to thank my colleagues in the Department of Physics for their time and support, with special thanks to Julian Kivell, David Payne, Hugh Thomas, Mike Charlton, Simon Hands, Dirk van der Werf, Ray Squires, and Linda Andrews, who have always made time to help and / or have a chat. Thanks also to my friends and fellow students at Swansea University, who have been of immeasurable help – in particular I would like to thank Chris Baker, Peter Watkeys, and Mark Holton.

Many thanks are due to the staff of the Tritiumlabor Karlsruhe (TLK), who have supported me immensely during my time in Germany. I would like to acknowledge in particular Beate Bornschein and Norbert Kernet for their time and welcome whenever I have been at TLK. I would also like to thank Dieter Stern and Siegfried Horn for their saint-like patience with my poor grasp of the German language, and for doing such a sterling job with construction and modification of the Raman bench assembly.

Most importantly, I would like to thank Mam, Dad, Peter, Kathryn and Sarah for their belief in me and their unreserved love and support.

# CONTENTS

## CHAPTER ONE: NEUTRINO MASSES AND THE KATRIN EXPERIMENT ....1-15

1.1	Direct Neutrino Mass Experiments.....	2
1.1.1	Beta decay spectrum endpoint analysis .....	2
1.1.2	The Mainz and Troitsk experiments .....	5
1.1.3	Measurements of $m_{\bar{\nu}_e}$ at Mainz and Troitsk .....	8
1.1.4	The KATRIN experiment .....	8
1.2	The KATRIN Design Requirements for Raman Spectroscopy .....	10
1.2.1	Laser Raman monitoring of hydrogen isotopomers .....	11
1.3	Summary .....	13
1.4	References for Chapter One.....	13

## CHAPTER TWO: THE THEORY OF THE RAMAN EFFECT.....16-38

2.1	Classical Treatment.....	18
2.2	Quantum Mechanical Treatment .....	26
2.3	Summary .....	36
2.4	References for Chapter Two .....	37
2.4.1	Cited references .....	37
2.4.2	Further reading.....	37

## CHAPTER THREE: COMPUTER MODELLING OF NORMAL RAMAN SPECTRA OF HYDROGEN ISOTOPOMERS.....39-91

3.1	Raman Bands and Selection Rules .....	40
3.2	Stokes Raman Line Positions .....	42
3.2.1	Calculating line positions for pure rotational transitions.....	44
3.2.2	Line positions for pure rotational transitions.....	46
3.2.3	Line positions for vibration-rotation transitions .....	50
3.2.4	Modelling line positions for vibration-rotation transitions.....	55
3.2.5	The effect of the refractive index of air on Raman line positions .....	60
3.3	Stokes Raman Line Intensities.....	63
3.3.1	The constant $k_{\nu}$ .....	64



3.3.2	The fourth power of the absolute wavenumber $(\tilde{\nu}_s)^4$ .....	64
3.3.3	The population factor $N_i$ .....	65
3.3.4	The line strength function $\Phi(a^2, \gamma^2, \theta)$ .....	71
3.3.5	The irradiance $\mathcal{I}$ .....	77
3.4	SpecGen .....	79
3.4.1	Approximations currently employed in the SpecGen code .....	79
3.4.2	SpecGen structure .....	81
3.4.3	Simulated Raman spectra and comparison with measured spectra .....	85
3.5	Summary and Outlook .....	89
3.6	References for Chapter Three .....	90
3.6.1	Cited references .....	90
3.6.2	Further reading .....	90

**CHAPTER FOUR: INSTRUMENTATION AND SOFTWARE REQUIRED FOR LASER RAMAN SPECTROSCOPY OF GASEOUS SAMPLES.....92-152**

4.1	Excitation Sources .....	94
4.1.1	The Nd:YAG laser .....	95
4.1.2	The Nd:YVO <sub>4</sub> laser.....	99
4.2	Interaction (Scattering) Region.....	101
4.2.1	The LARA cell.....	102
4.2.2	Geometry of the interaction region.....	104
4.3	Transportation of scattered light.....	107
4.3.1	Direct imaging .....	107
4.3.2	Translational imaging .....	110
4.3.3	Fibre-coupled imaging.....	112
4.4	Spectrometers.....	118
4.4.1	Czerny-Turner spectrometers .....	121
4.4.2	Transmitting optics-type spectrometers.....	122
4.5	Detectors .....	124
4.5.1	CCD background noise.....	124
4.5.2	CCD chip cooling .....	125
4.5.3	CCD detector quantum efficiency .....	126

4.6	Other apparatus .....	126
4.6.1	Safety equipment: enclosures, shutters, interlocks, and beam dumps .....	127
4.6.2	Edge filters .....	127
4.6.3	Faraday isolators .....	129
4.7	Post-Acquisition Spectra Processing Software .....	130
4.7.1	Correction of image astigmatism in the HTS lens spectrograph .....	131
4.7.2	Cosmic ray event removal: TrigCRR .....	139
4.7.3	Cosmic ray event removal: RCRR.....	141
4.7.4	Cosmic ray event removal: DCRR .....	144
4.7.5	Background subtraction and baseline scaling .....	147
4.7.6	Grating efficiency and detector quantum efficiency correction .....	148
4.8	Summary.....	150
4.9	References for Chapter Four.....	151
4.9.1	Cited references (books and papers).....	151
4.9.2	Cited references (manuals and datasheets) .....	151
4.9.3	Further reading.....	152

**CHAPTER FIVE: DIRECT IMAGING SYSTEM CHARACTERISATION ...153-206**

5.1	The TLK Raman System .....	156
5.1.1	The TLK system: overview and general remarks .....	157
5.1.2	Raman spectra measured at TLK.....	160
5.2	The UWS Raman System .....	168
5.2.1	The UWS system: overview and general remarks.....	168
5.2.2	Cosmic ray removal .....	172
5.2.3	Correction of HTS-system image distortion.....	175
5.2.4	Raman spectra measured at UWS.....	177
5.3	Comparison of the TLK and UWS Raman Systems.....	184
5.3.1	Signal-to-noise ratio calculations.....	184
5.3.2	Interface and software issues .....	188
5.3.3	Modifications to the ASER design .....	190
5.3.4	System footprint issues .....	191
5.4	Concluding Remarks to the Comparative Survey.....	192
5.5	Post-Review Direct Imaging Experiments (UWS System) .....	192

5.5.1	1200gr·mm <sup>-1</sup> HTS Grating Test.....	193
5.5.2	Direct Imaging Survey (50mW and 100mW Excitation).....	196
5.5.3	Translational Imaging Survey.....	200
5.6	Summary.....	204
5.7	References for Chapter Five.....	205
5.7.1	Papers.....	205
5.7.2	Datasheets.....	206

**CHAPTER SIX: IN-LINE FIBRE-COUPLED RAMAN MEASUREMENTS AT THE TILO EXPERIMENT.....207-245**

6.1	Preliminary Fibre-Coupled Raman Measurements at UWS.....	207
6.1.1	Spectrometer-end fibre alignment issues.....	210
6.1.2	General fibre-related issues.....	212
6.1.3	Detector noise issues.....	214
6.1.4	Raman spectra measured with the fibre-coupled HTS/SPEC-10 system ..	216
6.2	Fibre-Coupled Raman Measurements at TILO.....	218
6.2.1	Laser Raman system mounting bench design.....	218
6.2.2	TILO system setup and alignment.....	221
6.2.3	Detector noise issues.....	222
6.2.4	Raman spectra measured in-line at TILO.....	226
6.2.5	Invariance of system performance under high / low flow conditions.....	229
6.2.6	Missing contributions from the HD isotopomer.....	230
6.2.7	'Anomalously' low Q <sub>1</sub> -branch intensities.....	234
6.3	Summary.....	242
6.4	References for Chapter Six.....	244
6.4.1	Cited references (books and papers).....	244
6.4.2	Cited internet resources.....	245

**CHAPTER SEVEN: SUMMARY AND OUTLOOK.....246-249**

7.1	Summary.....	246
7.1.1	Summary of hardware development.....	246
7.1.2	Summary of software development.....	247
7.2	Outlook.....	248

**APPENDIX A1: SPECGEN – A HYDROGEN ISOTOPOMER STOKES RAMAN SPECTRUM MODELLER (LABVIEW CODE).....250-284**

A1.1	SpecGen Architecture .....	250
A1.2	Tier 1: SpecGen User Interface .....	252
A1.3	Tier 2: High-Level SubVI Handling & Lineshape Convolution .....	258
A1.4	Tier 3a: Calculation of Raman Line Positions.....	261
A1.4.1	SpecGen_SubVI_S0(J).vi .....	261
A1.4.2	SpecGen_SubVI_O1(J).vi .....	263
A1.4.3	SpecGen_SubVI_Q1(J).vi .....	265
A1.4.4	SpecGen_SubVI_S1(J).vi .....	267
A1.4.5	SpecGen_SubVI_Spectroscopic_Constants.vi .....	269
A1.5	Tier 3b: Calculation of Raman Line Relative Intensities .....	271
A1.5.1	SpecGen_SubVI_vs^4.vi .....	271
A1.5.2	SpecGen_SubVI_giNi.vi .....	273
A1.5.3	SpecGen_SubVI_F(J) .vi .....	275
A1.5.4	SpecGen_SubVI_Phi(a^2_g^2_q) .vi .....	276
A1.5.5	SpecGen_SubVI_b(2)J-2,J.vi .....	278
A1.5.6	SpecGen_SubVI_b(2)J,J.vi.....	279
A1.5.7	SpecGen_SubVI_b(2)J+2,J.vi .....	280
A1.5.8	SpecGen_SubVI_Tensor_Invariants.vi .....	281
A1.6	Tier 3c: Spectral Lineshape Convolution .....	283
A1.6.1	SpecGen_SubVI_Convolute_Gaussian.vi .....	283

**APPENDIX A2: POST-ACQUISITION PROCESSING AND CORRECTION OF RAMAN SPECTRA (LABVIEW CODE).....285-315**

A2.1	Astigmatism Correction.....	288
A2.1.1	AstCalc.vi.....	288
A2.1.2	AstCorr.vi.....	293
A2.2	Cosmic Ray Event Removal .....	297
A2.2.1	TrigCRR.vi.....	297
A2.2.2	RCRR_SubVI.vi .....	299
A2.2.3	DCRR_SubVI.vi .....	301
A2.2.4	DCRR_SubVI.vi (Segment A).....	304

A2.2.5 DCRR_SubVI.vi (Segment B).....	304
A2.2.6 DCRR_SubVI.vi (Segment C).....	305
A2.2.7 DCRR_SubVI.vi (Segment D).....	306
A2.2.8 DCRR_SubVI.vi (Segment E).....	307
A2.2.9 DCRR_SubVI.vi (Segment F) .....	308
A2.2.10 DCRR_SubVI.vi (Segment G).....	309
A2.3 High-Level Handling of Spectrum Correction SubVIs .....	311
A2.3.1 DCRR_High_Example.vi .....	311
A2.3.2 Average_2D_Array_SubVI.vi .....	314
A2.4 Outlook .....	315

## DECLARATION

This work has not previously been accepted in substance for any degree and is not being concurrently submitted in candidature for any degree.

Signed . ..... (candidate)

Date ... 25/04/07 .....

## STATEMENT 1

This thesis is the result of my own investigations, except where otherwise stated. Other sources are acknowledged by giving explicit references.

Signed . ..... (candidate)

Date ... 25/04/07 .....

## STATEMENT 2

I hereby give consent for my thesis, if accepted, to be available for photocopying and for inter-library loan, and for the title and summary to be made available to outside organisations.

Signed . ..... (candidate)

Date ... 25/04/07 .....

## CHAPTER ONE

### NEUTRINO MASSES AND THE KATRIN EXPERIMENT

Determination of the rest masses of the neutrinos remains one of the most challenging tasks facing modern particle physics. The Standard Model of particle physics has, until recently, assumed these particles to be massless. However, investigations into solar and atmospheric neutrinos, most notably those performed at Super-Kamiokande and the Sudbury Neutrino Observatory (SNO) have provided strong evidence for weak flavour eigenstate oscillations between the electron, muon, and tau neutrinos. The existence of neutrino oscillations requires a non-trivial mixing between the weak interaction eigenstates ( $\nu_e$ ,  $\nu_\mu$ ,  $\nu_\tau$ ) and the corresponding mass eigenstates ( $\nu_1$ ,  $\nu_2$ ,  $\nu_3$ ), and that the mass eigenstates differ from each other. Neutrinos, therefore, are required to have non-zero masses.

The implications of non-zero neutrino masses are profound and far-reaching. Neutrinos and their properties play important roles in astrophysics and cosmology. The relative contributions of neutrino hot dark matter and cold dark matter are important parameters in many cosmological models, for example – neutrinos with masses of the order of an eV would play an important role as neutrino hot dark matter in the formation of large scale structures in the universe. Furthermore, a definite measurement of neutrino mass would aid determination of the correct hierarchy between the mass eigenstates, as the squares of the mass differences between eigenstates are fairly well determined from neutrino oscillation experiments.

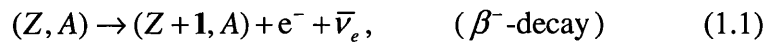
The Neutrino Oscillation Industry website (<http://www.hep.anl.gov/ndk/hypertext/>) is an excellent place to gain an impression of the scale of the investigations into neutrino masses and oscillations. Theoretical approaches aside, the experimental avenues of approach include: solar neutrino experiments, double beta decay experiments, reactor neutrino experiments, atmospheric neutrino experiments, short- and long-baseline accelerator experiments, neutrino telescopes, horizontal air showers, and direct neutrino mass experiments. The combined effort and expertise being applied in this field is considerable, as befits a subject area of such fundamental importance.

## 1.1 Direct Neutrino Mass Experiments

Direct neutrino mass experiments look for a distortion in the shape of the beta spectrum in the endpoint energy region, and therefore attempt to measure the endpoint of the spectrum as accurately as possible. Since the measurement is direct, the results of such investigation are independent of assumptions regarding the neutrino mass type (i.e. whether the neutrino is a Majorana or a Dirac particle). This is in contrast with neutrinoless double beta decay ( $0\nu\beta\beta$ ) experiments, for example, which assume the neutrino mass to be of the Majorana type.

### 1.1.1 Beta decay spectrum endpoint analysis

Beta decay is a nuclear transition in which the atomic number of a nucleus changes by one unit, while the atomic mass remains unchanged. There are three possible decay modes, namely  $\beta^-$ -decay,  $\beta^+$ -decay, and electron capture. The decay mode relevant to the investigation of the neutrino mass is  $\beta^-$ -decay:



where  $Z$  and  $A$  are the atomic number and atomic mass of the decaying nucleus, respectively. On the quark level the underlying mechanism is



The decay energy,  $Q_{\beta^-}$ , of the  $\beta^-$ -decay mode is given by

$$\begin{aligned} Q_{\beta^-} &= [m(Z, A) - Zm_e]c^2 - [m(Z+1, A) - (Z+1)m_e]c^2 \\ &= [m(Z, A) - m(Z+1, A)]c^2, \end{aligned} \quad (1.3)$$



where  $m(Z, A)$  is the mass of neutral atom (not the nucleus). The energy spectrum of the decay electrons is commonly formulated as a Kurie plot, which is given by the expression

$$\sqrt{\frac{N(p_e)}{p_e^2 F(Z+1, E)}} = A(Q_{\beta^-} - E_e) \left[ 1 - \left( \frac{m_{\nu_e} c^2}{Q_{\beta^-} - E_e} \right)^2 \right]^{1/4}, \quad (1.4)$$

where  $N(p_e)$  is the number of decay electrons of momentum  $p_e$ ,  $E_e$  is the energy of the decay electrons, and  $F(Z+1, E)$  is the Fermi function, a correction factor which in the non-relativistic limit can be approximated as

$$F(Z+1, E) = \frac{x}{1 - e^{-x}}, \quad (1.5)$$

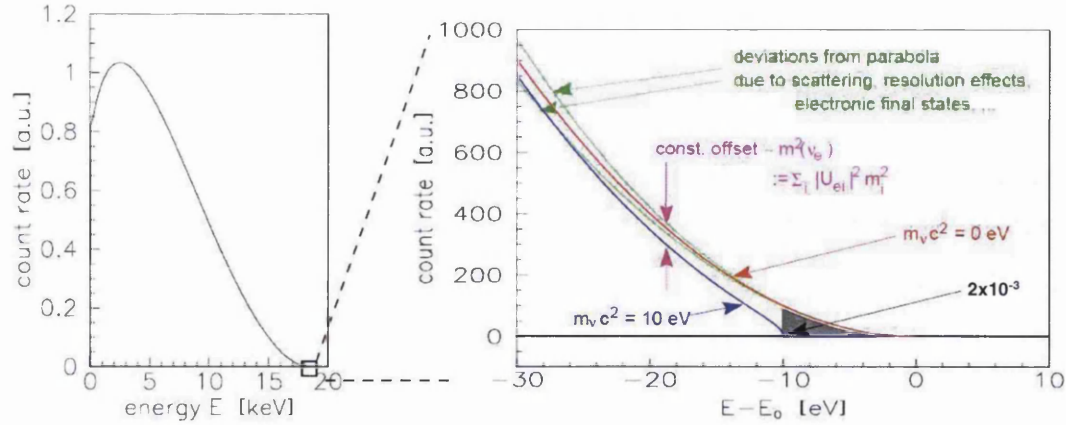
where  $x$  is given by the following expression for the case of  $\beta^-$ -decay:

$$x = -\frac{2\pi(Z+1)\alpha}{\beta}. \quad (1.6)$$

In this expression,  $\alpha$  is the fine structure constant and  $\beta = v/c$  (Zuber (2004)). In the case of massless neutrinos, we can set  $m_{\nu_e} = 0$ , and equation (1.4) therefore reduces to

$$\sqrt{\frac{N(p_e)}{p_e^2 F(Z+1, E)}} = A(Q_{\beta^-} - E_e), \quad (1.7)$$

which is simply a straight line intersecting the x-axis at  $Q_{\beta^-}$ . For small neutrino masses, the Kurie plot is distorted in the region close to  $Q_{\beta^-}$ ; the endpoint of the beta decay spectrum in this case is slightly lower at  $Q_{\beta^-} - m_{\nu_e} c^2$ , as shown in Figure 1.1.



**Figure 1.1** Distortion of the endpoint of the beta decay spectrum of tritium, showing the undistorted (zero mass) case (red) and the effect of an arbitrary value of  $10\text{eV}/c^2$  for  $m_{\bar{\nu}_e}$  (blue). Note that  $E - E_0 \equiv E - Q_{\beta^-}$ . (From Osipowicz et al. (2001)).

In order for a firm measurement to be made (as opposed to setting an upper limit), the energy resolution of the system must be better than  $m_{\bar{\nu}_e}$ , assuming that  $m_{\nu_e} \equiv m_{\bar{\nu}_e}$ . The most sensitive direct measurements of  $m_{\bar{\nu}_e}$  to date have been performed in the Mainz and Troitsk experiments (see Section 1.1.2). Both of these experiments have used tritium ( ${}^3\text{H}$ ) as a source. The  $\beta^-$ -decay of tritium is

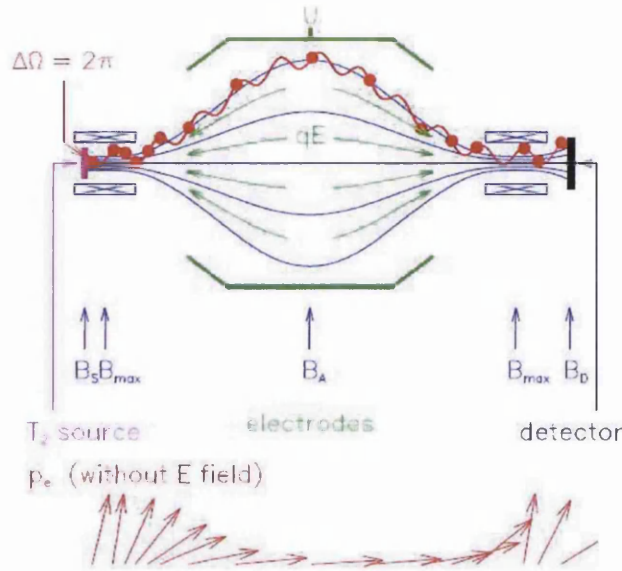


Tritium is an almost ideal source for direct neutrino mass investigations. Tritium has the second lowest endpoint energy ( $Q_{\beta^-} = 18.6\text{keV}$ ) of all elements, and a short half-life of 12.3 years. The  $\beta^-$ -decay is a superallowed transition, which simplifies the theoretical considerations as no corrections from the nuclear transition matrix elements have to be taken into account. Further, the low nuclear charge,  $Z$ , ensures that the inelastic scattering of outgoing decay electrons with the source is a relatively small contribution to the energy spectrum, and the simple electronic structure of both tritium and the daughter helium ion means that atomic corrections for the decaying atom (or molecule) and the corrections for the interaction of outgoing decay electrons with the source are relatively straightforward (see Drexlin, Weinheimer et al. (2005)).

### 1.1.2 *The Mainz and Troitsk experiments*

Prior to 1990, direct measurements of  $m_{\bar{\nu}_e}$  were most commonly performed utilising magnetic spectrometers. The currently running Mainz and Troitsk experiments use a type of electrostatic retarding spectrometer known as a MAC-E-Filter (Magnetic Adiabatic Collimation combined with an Electrostatic Filter), which was first proposed by Beamson et al. in 1980, and developed specifically for direct  $m_{\bar{\nu}_e}$  searches independently by Lobashev et al. (1985) and Picard et al. (1992), for the Troitsk and Mainz experiments respectively. The main advantages of the MAC-E-Filter over older magnetic spectrometer designs are high luminosity and (crucially) high energy resolution, both of which are vital prerequisites for measuring  $m_{\bar{\nu}_e}$ .

The principle of a MAC-E-Filter is shown diagrammatically in Figure 1.2. Two superconducting solenoids at either end of the spectrometer vessel produce a guiding magnetic field. The decay electrons enter the vessel from the left solenoid into the forward hemisphere and are guided in a cyclotron motion around the magnetic field lines into the spectrometer, resulting in a maximum accepted solid angle of  $2\pi$  sr. The magnetic field drops by several orders of magnitude between the entrance solenoid and the centre of the spectrometer, and therefore the force on the electrons due to the magnetic gradient transforms the majority of the cyclotron energy into longitudinal motion. The momentum transformation is adiabatic since the magnetic field varies slowly, and the magnetic moment therefore remains constant. The decay electrons (isotropically emitted at the source) have therefore been transformed into a broad beam of electrons moving almost parallel to the magnetic field lines (Drexlin, Weinheimer et al. (2005)).



**Figure 1.2** Principle of the Magnetic Adiabatic Collimation combined with an Electrostatic Filter (MAC-E-Filter) design, showing the two superconducting solenoids (blue) and the retarding / reaccelerating electrostatic potential (green). The adiabatic momentum transformation is represented by the red arrows. The acceptance solid angle of the system is  $2\pi$  sr. (From Drexlin, Weinheimer et al. (2005))

The electron beam runs against a retarding electrostatic potential formed by cylindrical electrodes. All electrons with sufficient energy to pass the electrostatic barrier are reaccelerated and collimated onto the detector, while all the others are reflected. In essence, the spectrometer acts as an integrating high-energy pass filter. Varying the retarding potential allows the (integration mode) measurement of the beta spectrum. The normalised transmission function,  $T(E, qU)$ , of a MAC-E-Filter is given by the expression (Drexlin, Weinheimer, et al. (2005))

$$T(E, qU) = \begin{cases} 0 & E - qU < 0 \\ 1 - \sqrt{1 - \frac{E - qU}{E} \cdot \frac{B_S}{B_A}} & 0 \leq E - qU \leq \Delta E, \\ 1 - \sqrt{1 - \frac{\Delta E}{E} \cdot \frac{B_S}{B_A}} & \\ 0 & E - qU > \Delta E \end{cases} \quad (1.9)$$

where  $E$  is the energy of the isotropic electron source,  $q$  is the electronic charge,  $U$  is the retarding electrostatic potential,  $B_s$  is the magnetic field at the location of the electron source,  $B_A$  is the magnetic field at the centre of the spectrometer, and  $\frac{\Delta E}{E}$  is the relative sharpness of the filter, which is given by

$$\frac{\Delta E}{E} = \frac{B_A}{B_{\max}}, \quad (1.10)$$

where  $B_{\max}$  is the magnetic field at the location of the superconducting solenoids.

In order to discriminate electrons of energy close to the retarding potential from the background of higher-energy electrons the spectrometer can be run in a non-integrating time-of-flight mode – electrons of energy close to the retarding potential are very slow when passing the analysing plane and can therefore be distinguished from higher-energy electrons which will have attained a significant fraction of the speed of light. In this mode the MAC-E-Filter is essentially acting as an energy band pass filter of the same energy resolution and nearly the same luminosity as for the integrating high energy pass filter mode (Drexlin, Weinheimer, et al. (2005)).

In order to achieve high resolution, a MAC-E-Filter has to be made rather large. The Mainz and Troitsk MAC-E-Filters differ somewhat in size, but both are sizeable vessels; the Mainz spectrometer is of 1m diameter and 4m in length, while the Troitsk spectrometer is larger at 1.5m diameter and 7m length. Despite the difference in size, the energy resolution of both systems is comparable.

The principal difference between the two experiments is the nature of their tritium sources. In the Mainz experiment, a thin film of tritium is frozen onto a substrate, while the Troitsk experiment uses a Windowless Gaseous Tritium Source (WGTS). The WGTS approach was first pioneered by Robertson et al. in 1991 for the Los Alamos experiment and works on the principle of adiabatic transport of electrons in a strong longitudinal magnetic field and the circulation of low-pressure (0.01mbar) tritium gas through the 3m long, 50mm diameter source tube by means of a differential pumping system. The use of a strong

magnetic field for electron transport permits the use of multiple bends in the transport channel, which in turn allows for better differential pumping and a smooth coupling to the MAC-E-Filter vessel. The WGTS approach is superior to the tritium film configuration due to the guaranteed homogeneity over the cross section of the source and the near total elimination of backscattering (Drexlin, Weinheimer et al. (2005)). In addition, a WGTS provides very high luminosities combined with small systematic uncertainties. The reader is referred to Weinheimer et al. (1999) and Lobashev et al. (1999) for further technical details regarding the Mainz and Troitsk experiments.

### *1.1.3 Measurements of $m_{\bar{\nu}_e}$ at Mainz and Troitsk*

The results of the Mainz and Troitsk experiments amount to the following upper limits for the value of  $m_{\bar{\nu}_e}$  :

Mainz (data from 1998, 1999, and 2001):  $m_{\bar{\nu}_e} < 2.30\text{eV}/c^2$  (95% C.L.)

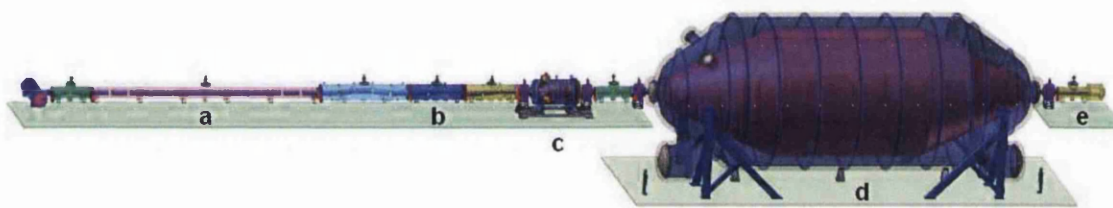
Troitsk (data from 1994 to 1999, and 2001):  $m_{\bar{\nu}_e} < 2.05\text{eV}/c^2$  (95% C.L.)

Due to the design limitations of the Mainz and Troitsk experiments with regard to source luminosity and MAC-E-Filter energy resolution, further data from these experiments are unlikely to significantly improve the sensitivity of the upper limit values of  $m_{\bar{\nu}_e}$  .

### *1.1.4 The KATRIN experiment*

The Karlsruhe Tritium Neutrino (KATRIN) experiment is a next-generation direct neutrino mass measurement experiment currently under construction at Forschungszentrum Karlsruhe (FZK) that is designed to improve the sensitivity in the measurement of  $m_{\bar{\nu}_e}$  by an order of magnitude over the recent Mainz and Troitsk experiments, i.e. to reach a mass sensitivity of  $0.2\text{eV}/c^2$  (90% C.L.). The KATRIN experiment design combines the best features of the Mainz and Troitsk experiments, namely the MAC-E-Filter and WGTS concepts, but on a necessarily much increased scale.

The electrostatic filter system of KATRIN consists of two MAC-E-Filter spectrometers – a (relatively) small pre-spectrometer and a very larger main spectrometer. The KATRIN main spectrometer is far larger than either the Mainz or Troitsk vessels, with an inner diameter of 9.8m and an overall length of 23.28m. The size of the KATRIN WGTS source tube is also much larger than the Troitsk design, being 5m long and 90mm in diameter. Since the total luminosity of the WGTS is proportional to the cross sectional area of the source tube, the KATRIN WGTS has a more than a factor of three greater luminosity than the Troitsk WGTS. The overall design of the KATRIN experiment is shown in Figure 1.3.



**Figure 1.3** KATRIN experiment design, showing the five major sections of the design: (a) source (WGTS), (b) transport system, (c) pre-spectrometer, (d) main spectrometer, and (e) final plane detector (FPD). The KATRIN main spectrometer is the world's largest XHV vessel (operating in the  $10^{-12}$  mbar regime), with an internal volume of  $1400\text{m}^3$ . (From Drexlin, Weinheimer et al. (2005)).

As shown in the figure, the KATRIN experiment can be divided into five main sections, namely (a) the tritium source, (b) transport system, (c) the pre-spectrometer, (d) the main spectrometer, and (e) the final plane detector (FPD). The principles underlying the operation of the source (WGTS) and transport system (differential pumping), and the main spectrometer (MAC-E-Filter) have already been mentioned in Section 1.1.2 and will not be repeated here.

The pre-spectrometer operates at a fixed retarding energy of approximately 300eV below the endpoint of the beta spectrum, and therefore only allows electrons with the highest energies to pass into the main spectrometer vessel. The main task of the pre-spectrometer is to limit the number of electrons that might scatter on residual gas molecules in the main spectrometer, which would increase the rate of background events. The two spectrometers are connected by two 1m long superconducting transport magnets. The FPD is located in a separate superconducting solenoid, which post-accelerates the incident electrons to coincide with the optimised energy range of the FPD (between 5 and 50keV). The energy

resolution of the detector is approximately 230eV (FWHM), which overall corresponds to the  $0.2\text{eV}/c^2$  (90% C.L.) sensitivity in the value of  $m_{\bar{\nu}_e}$ . The reader is referred to the KATRIN Design Report (Drexlin, Weinheimer et al. (2005)) for further technical details regarding the KATRIN experiment design.

## ***1.2 The KATRIN Design Requirements for Raman Spectroscopy***

In order to minimise systematic uncertainties in the determination of the neutrino mass, a continuous and precise knowledge of the beta activity and stability of the WGTS is required. These parameters are indispensable in order to correctly apply energy loss corrections to data taken at different MAC-E-Filter retarding voltage settings. There are three WGTS parameters which require particularly close attention, namely: (i) the tritium inlet pressure, (ii) the column density, and (iii) the isotopic purity. The tritium inlet pressure is stabilised and monitored by means of a pressure-controlled tritium buffer vessel, while the column density is stabilised by stabilising the temperature of the WGTS to  $\pm 0.03\text{K}$  by circulating liquid neon thermally coupled to the tritium tube. By stabilising the temperature in this way, the column density can be controlled and stabilised by means of the pressure of the buffer vessel alone (Drexlin, Weinheimer et al. (2005)).

The isotopic purity, characterised by the tritium concentration,  $\epsilon\text{T}$ , is stabilised by means of circulating a fraction of the gas from the inner loop (buffer vessels and source tube) into an outer loop where it undergoes detritiation and isotope separation, and is replaced by tritium gas of the highest purity possible (nominally  $>95\%$ ). Since 100% purity is not achievable, it is essential to quantitatively monitor the composition of the gas mixture in-line and as close to real-time as practicable. The quantification of the contribution of the hydrogen isotopomers HT and DT is of particular importance since the beta decay recoil dynamics (and hence decay electron energies) of the HT and DT molecules are quite different to those for  $\text{T}_2$ . High-precision of the isotopomeric composition of the gas injected into the WGTS source tube is therefore essential.

Two methods will be combined in order to monitor the isotopic purity: (i) high-resolution mass spectrometry at one of the differential pumping ports, and (ii) laser Raman



spectroscopy at a location close to the pressure-controlled tritium buffer vessels. The target sensitivity for the detection of isotopic impurities in both cases is  $\pm 0.2\%$ , with  $\pm 0.1\%$  being a 'gold standard' to be reached if possible.

Laser Raman spectroscopy has several advantages which are of particular importance to the specific case of tritium purity monitoring at KATRIN. The technique is non-contact, non-destructive, has excellent separation between hydrogen isotopomer species (due to their rather different reduced masses), and allows the location of monitoring equipment outside of the enclosures necessary to guard against the leakage of tritium gas, access being provided by means of windows in a specially-designed gas bypass cell – see section 4.2.1. The theory of the Raman Effect is discussed in Chapter 2, and the specific theoretical case of the hydrogen isotopomers in Chapter 3, but a brief introductory overview of the technique and its application to hydrogen isotopomer monitoring is given below.

### *1.2.1 Laser Raman monitoring of hydrogen isotopomers*

Laser Raman spectroscopy is an ideal tool for non-contact monitoring of hydrogen isotopomers. The Raman Effect is an inelastic scattering process whereby the wavelength of the incident laser light is altered by a quantifiable change in the rotational and / or vibrational state of the scattering molecules, which in turn leads to a characteristic set of peaks at wavelengths either longer (Stokes Raman) or shorter (anti-Stokes Raman) than the exciting radiation. For complicated molecules present in a sample of unknown composition, Raman spectroscopy can usually only be used to give a qualitative description of the molecules present, relying on distinctive intensity patterns in the spectrum. In the case of the hydrogen isotopomers, however, the Raman lines are excellently separated (especially between species) and the quantum mechanical theory that allows predictions of line positions (and to a lesser extent, intensities) is relatively tractable. It is therefore possible to extract quantitative information regarding sample composition in this case, limited essentially by the spectral resolution and sensitivity of the spectroscopic monitoring system.

The principal technical difficulty with the technique is the low intensity of the Raman scattered light – typically a factor of  $10^{-3}$  of the Rayleigh (elastically) scattered light. This problem is exacerbated if the target sample is of low density (as is the case of the <100mbar tritium gas circulating in the inner loop feeding the WGTS) or if the irradiance of the excitation laser is low, as the scattering intensity is directly proportional to both these parameters. Therefore, although the hydrogen isotopomers are excellently separated in the spectra (particularly in vibration-rotation Raman spectra – see Chapter 3), the low intensity of the scattering necessitates the use of very high-quality excitation sources, scattered light transport techniques and detector systems.

Examples of tritium purity monitoring in the literature are rather scarce, but of note is the fibre-coupled tritium accounting system developed by O'hira et al. in 2000 to improve the safe handling and control of tritium for the fuel cycle of the ITER tokomak fusion reaction concept. This system demonstrated that the isotomeric composition of a tritium gas flow under high flow (up to  $200 \text{ Pa}\cdot\text{m}^3\cdot\text{s}^{-1}$ ), and fairly low pressure ( $\sim 100$  to  $1000\text{mbar}$ ) can be measured to an accuracy of  $\sim 0.3\%$  - comparable with the minimum KATRIN design requirement of 0.2 – with acquisition times of 120s.

Laser Raman spectroscopy of the hydrogen isotopomers has also been performed previously at FZK by Taylor et al. (2001). In that case, the Raman spectra of the isotopomers  $\text{H}_2$ , HD, and  $\text{D}_2$  were measured using an actively stabilised external resonator (ASER) cavity to enhance the Raman signal strength by a factor of 250 or more. The excitation laser and the gas bypass cell design from these earlier experiments were retained for use in this work, although the ASER cavity is currently not planned for incorporation into the KATRIN monitoring system design (see Section 5.3.3).

### ***1.3 Summary***

A definite measurement of the electron neutrino mass by KATRIN would be of profound importance for particle physics, astrophysics and cosmology. Although a relatively small component of the KATRIN experiment, the laser Raman monitoring system is of vital importance in minimising systematic errors in such a sensitive high-resolution experiment. It is therefore crucial that the monitoring system performs at least to the 0.2% level of isotopomeric composition sensitivity specified in the KATRIN design report (Drexlin, Weinheimer et al. (2005)). The goal of the work described in this thesis was to develop a spectroscopic system and supporting software that can provide the 0.1% ‘gold standard’ sensitivity level at as close to a real-time monitoring situation as possible. The ITER system developed by O’hira et al. has demonstrated that such a system should indeed be feasible.

In Chapter 2, the classical and quantum mechanical theoretical treatments of the Raman Effect will be discussed in general. The quantum mechanical treatment is applied to the specific case of the hydrogen isotopomers in Chapter 3. In Chapter 4, the instrumentation, techniques, and software employed throughout this work for the measurement of Raman spectra of gas mixtures will be discussed. Chapter 5 describes with off-line (no gas flow), low laser power, atmospheric pressure Raman measurements, while Chapter 6 summarises the in-line, high laser power, low pressure Raman measurements made at the Test of Inner Loop (TILO) WGTS mock-up at FZK. Chapter 7 summarises the results of the thesis as a whole and provides an outlook for future work.

### ***1.4 References for Chapter One***

Beamson G., Porter H. Q., Turner D. W. (1980) “The collimating and magnifying properties of a superconducting field photoelectron spectrometer.” J. Phys. E: Sci. Instrum. **13**: 64-66

Caldwell, D. O., Ed. (2001). Current Aspects of Neutrino Physics. Heidelberg (Germany), Springer-Verlag.

Drexlin G., Weinheimer C., et al. (2005). KATRIN Design Report 2004. Wissenschaftliche Berichte FZKA 7090, ISSN 0947-8620

Lobashev V. M. and Spivak P. E (1985) "A method for measuring the electron antineutrino rest mass." Nuclear Instruments and Methods in Physics Research Section A: Accelerators, Spectrometers, Detectors and Associated Equipment **240**(2): 305-310

Lobashev V. M., Aseev V. N., Belesev A. I, Berlev A. I., Geraskin E. V., Golubev A. A. A. A., Kazachenko, Kuznetsov Y. E., Ostroumov R. P., Rivkis L. A., et al. (1999). "Direct search for mass of neutrino and anomaly in the tritium beta-spectrum." Physics Letters B **460**: 227-235

O'hira S., Hayashi T., Nakamura H., Kobayashi K., Tadokoro T., Nakamura H., Itoh T., Yamanishi T., Kawamura Y., Iwai Y., Arita T., Maruyama T., Kakuta T., Konishi S., Enoeda M., Yamada M., Suzuki T., Nishi M., Nagashima T., Ohta M. (2000). "Improvement of tritium accountancy technology for ITER fuel cycle safety enhancement." Nuclear Fusion **40**(3Y)

Osipowicz, A., et al. (2001). "A next Generation Tritium Beta Decay Experiment with sub-eV Sensitivity for the Electron Neutrino Mass" Wissenschaftliche Berichte FZKA 6691

Picard A., Backe H., Barth H., Bonn J., Degen B., Edling T., Haid R., Hermann A., Leiderer P., Loeken Th., et al. (1992) Nuclear Instruments and Methods in Physics Research Section B: Beam Interactions with Materials and Atoms **63**(3): 345-358

Robertson R. G. H., Bowles T. J., Stephenson, Jr. G. J., Wark D. L., Wilkerson J. F., and Knapp D. A. (1991). "Limit on  $\bar{\nu}_e$  mass from observation of the  $\beta$  decay of molecular tritium." Phys. Rev. Lett. **67**: 957 – 960

Taylor D. J., Glugla M., Penzhorn R.-D. (2001). "Enhanced Raman sensitivity using an actively stabilized external resonator." Review of Scientific Instruments **72**(4): 1970-1976.

Weinheimer C., Degenddag B., Bleile A., Bonn J., Bornschein L., Kazachenko O., Kovalik A., Otten E. W. (1999) "High precision measurement of the tritium  $\beta$  spectrum near its endpoint and upper limit on the neutrino mass." Physics Letters B **460**: 219-226

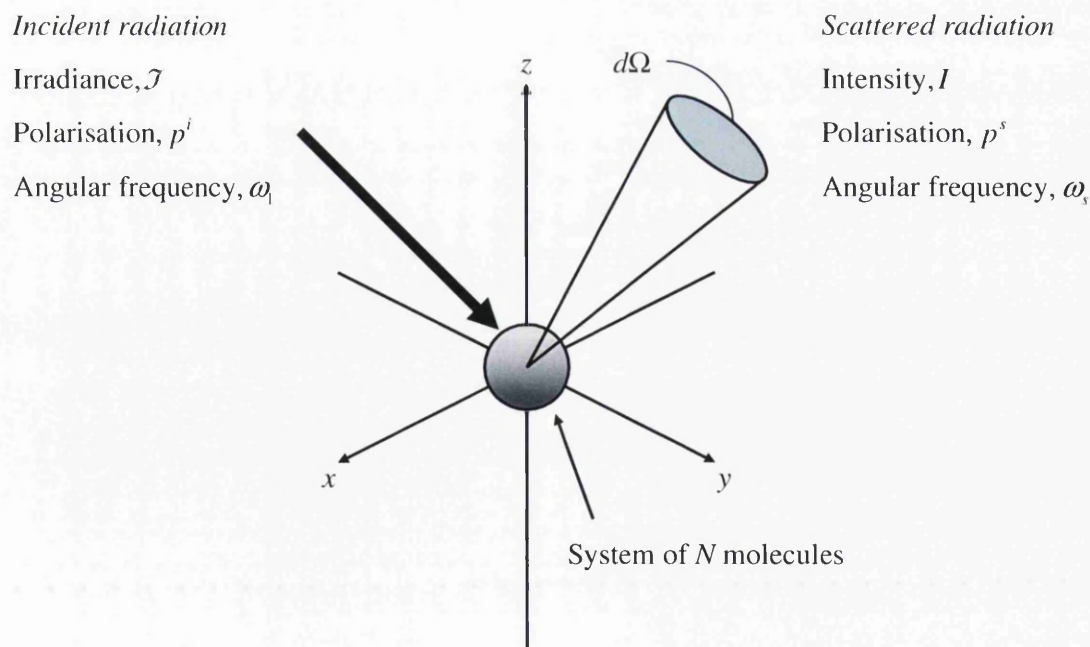
Zuber, K. (2004). Neutrino Physics. Bristol (U.K.), Institute of Physics Publishing.

## CHAPTER TWO

### THE THEORY OF THE RAMAN EFFECT

In this chapter an overview of both classical and quantum mechanical treatments of the theory of the Raman Effect are presented. Many fine textbooks have been written on this subject, notably Herzberg (1950) and Long (2002). There is, however, the inevitability of a lack of standardisation with respect to notation. In the interests of clarity, all equations used in this chapter and later on in this thesis have been standardised to the notation found in Long (2002).

Figure 2.1 shows a generalised incoherent light scattering experiment. In most practical (i.e. spectroscopic) situations, one would like to know how the properties of the material system and the illumination-observation geometry determine the relation between the incident and scattered radiation properties.



**Figure 2.1** Generalised incoherent light scattering experiment.  
Adapted from Long (2002)

In both the classical and quantum mechanical treatments of Raman scattering, the scattered radiation is considered to be produced by the oscillating electric (or magnetic) multipole moments of the incident electromagnetic radiation. The time-averaged power per unit solid angle radiated by an oscillating electric dipole,  $p_0$ , induced in a molecule due to incident electromagnetic radiation of frequency,  $\omega_i$ , is known as the intensity,  $I$ , and is given by

$$I = k'_\omega \omega_s^4 p_0^2 \sin^2 \theta, \quad (2.1)$$

where  $\omega_s$  is the angular frequency of the scattered radiation and  $\theta$  is the angle between the observation direction and the axis of the induced dipole. The term  $k'_\omega$  is given by

$$k'_\omega = \frac{1}{32\pi^2 \epsilon_0 c_0^3}.$$

It is often convenient to reformulate equation (2.1) in terms of wavenumber  $\tilde{\nu}$  instead of angular frequency  $\omega$  when dealing with real-world spectra, as in most analytical applications the emphasis is on the position of bands in a spectrum rather than their intensities. It is also common practice to present measured Raman spectra in terms of wavenumber shift instead of wavelength or frequency. The two formulations are related by the well-known expression

$$\omega_s = 2\pi c_0 \tilde{\nu}_s.$$

Equation (2.1) can thus be rewritten as

$$I = k'_\tilde{\nu} \tilde{\nu}_s^4 p_0^2 \sin^2 \theta, \quad (2.2)$$

with

$$k'_\tilde{\nu} = \frac{\pi^2 c_0}{2\epsilon_0}.$$

In this chapter, the emphasis is on deriving the frequency dependence of induced electric dipole moment vectors, which in turn gives the intensities of the scattered light at those frequencies. For this purpose, the angular frequency formulation is the most tractable. Note that in Chapter 3, Raman spectra for specific molecules are modelled, for which the wavenumber formulation is somewhat more convenient.

## 2.1 *Classical Treatment*

A classical treatment of a molecular scattering process will inevitably be incomplete compared to a full quantum mechanical treatment, but such an approach to the Raman effect still yields useful results. The classical approach is particularly useful for Raman spectroscopists who are mostly interested in qualitative analysis. The classical theory correctly predicts the frequency dependence for Rayleigh and vibrational Raman scattering, and therefore is adequate to provide the characteristic molecular vibrational frequencies to identify substances in a given sample. In addition, one can obtain the correct dependence of the Rayleigh scattering tensor on the equilibrium polarisability tensor and (under certain conditions) the dependence of the vibrational Raman scattering tensor on the derived polarisability tensor.

The principal limitation of a classical treatment is the lack of discrete assignment of rotational frequencies to molecular rotational energy levels, although for a qualitative analysis this is not too critical, and one can even extract useful first-order approximations associated some of the selection rules.

The total time-dependent induced electric dipole moment vector,  $\mathbf{p}$ , can be written as a sum of time-dependent induced electric dipole moment vectors:

$$\mathbf{p} = \mathbf{p}^{(1)} + \mathbf{p}^{(2)} + \mathbf{p}^{(3)} + \dots \quad (2.3)$$



This is a rapidly converging series since

$$\mathbf{p}^{(1)} \gg \mathbf{p}^{(2)} \gg \mathbf{p}^{(3)}.$$

The relationships between  $\mathbf{p}^{(1)}, \mathbf{p}^{(2)}, \mathbf{p}^{(3)}$  and  $\mathbf{E}$  involves tensors and are given by

$$\mathbf{p}^{(1)} = \boldsymbol{\alpha} \cdot \mathbf{E}; \quad \mathbf{p}^{(2)} = \frac{1}{2} \boldsymbol{\beta} \cdot \mathbf{E}\mathbf{E}; \quad \mathbf{p}^{(3)} = \frac{1}{6} \boldsymbol{\gamma} \cdot \mathbf{E}\mathbf{E}\mathbf{E}, \quad (2.4)$$

where  $\boldsymbol{\alpha}$  is the polarisability tensor,  $\boldsymbol{\beta}$  is the (first) hyperpolarisability tensor, and  $\boldsymbol{\gamma}$  is the second hyperpolarisability tensor. These tensors are generally time-dependent, associated with molecular vibrations. The time-dependencies of  $\mathbf{p}^{(1)}, \mathbf{p}^{(2)}, \mathbf{p}^{(3)}$  are therefore determined by the time dependencies of both the tensors involved and the appropriate term in  $\mathbf{E}$ ,  $\mathbf{E}\mathbf{E}$  or  $\mathbf{E}\mathbf{E}\mathbf{E}$ .

As higher-order electric dipole moment vectors are considered, both the rank of the relating tensor and the appropriate term in  $\mathbf{E}$  increase;  $\mathbf{p}^{(1)}$  is linear in  $\mathbf{E}$ , with  $\boldsymbol{\alpha}$  of second rank;  $\mathbf{p}^{(2)}$  is quadratic, with  $\boldsymbol{\beta}$  of third rank,  $\mathbf{p}^{(3)}$  cubic, with  $\boldsymbol{\gamma}$  of fourth rank; and so on. In addition, expressions for the dipole moment vectors will in general contain several frequency components, the number of which increases with the order of the term concerned.

In most textbooks, only the first three terms ( $\mathbf{p}^{(1)}, \mathbf{p}^{(2)}, \mathbf{p}^{(3)}$ ) are considered as these are sufficient to characterise the most useful Rayleigh and (non-resonance) Raman scattering types from the point of view of practical spectroscopy, *viz.* normal, hyper-, and second-hyper Raman scattering. Note that, since the classical theory does not include discrete electronic energy levels, resonance Raman scattering cannot be described.

Equations (2.4) can be expressed in component form as

$$p_{\rho}^{(1)} = \alpha_{\rho\sigma} E_{\sigma}; \quad p_{\rho}^{(2)} = \frac{1}{2} \beta_{\rho\sigma\tau} E_{\sigma} E_{\tau}; \quad p_{\rho}^{(3)} = \frac{1}{6} \gamma_{\rho\sigma\tau\nu} E_{\sigma} E_{\tau} E_{\nu}, \quad (2.5)$$

where the Greek subscripts  $\rho, \sigma, \tau, \nu$  can denote  $x, y, z$ , with implied summation over repeated indices. This formulation is particularly useful when deriving explicit expressions for dipole polarisability vectors in terms of their frequency components.

In the case of the first-order dipole moment vector,  $\mathbf{p}^{(1)}$ , three frequency components are encountered, one associated with Rayleigh scattering at the incident frequency  $\omega_1$ , and two associated with Stokes and anti-Stokes Raman scattering at frequencies  $\omega_1 - \omega_M$  and  $\omega_1 + \omega_M$  respectively, where  $\omega_M$  is a molecular vibrational frequency that modulates the oscillation of the induced electric dipole. The first-order term in equations (2.4) can therefore be re-written as

$$\mathbf{p}_0(\omega_1) = \boldsymbol{\alpha}^{Ray} \cdot \mathbf{E}_0(\omega_1) \quad \text{and} \quad \mathbf{p}_0(\omega_1 \pm \omega_M) = \boldsymbol{\alpha}^{Ram} \cdot \mathbf{E}_0(\omega_1), \quad (2.6)$$

where  $\mathbf{p}_0(\omega_1)$  and  $\mathbf{p}_0(\omega_1 \pm \omega_M)$  are time-independent amplitudes related to the induced electric dipole moments oscillating with frequencies  $\omega_1$  and  $\omega_1 \pm \omega_M$ , respectively, and are related to the scattered intensity at those frequencies. The equilibrium polarisability tensor,  $\boldsymbol{\alpha}^{Ray}$ , is associated with Rayleigh scattering, and  $\boldsymbol{\alpha}^{Ram}$  is a polarisability tensor associated with Raman scattering. Equations (2.6) can be written in component form as

$$p_{\rho_0}(\omega_1) = \alpha_{\rho\sigma}^{Ray} E_{\sigma_0}(\omega_1) \quad \text{and} \quad p_{\rho_0}(\omega_1 \pm \omega_M) = \alpha_{\rho\sigma}^{Ram} E_{\sigma_0}(\omega_1). \quad (2.7)$$

The same procedure can be carried out for the higher order terms. For example,  $\mathbf{p}^{(2)}$  has one frequency component associated with hyper-Rayleigh scattering with frequency  $2\omega_1$  (twice the frequency of the incident radiation), and two associated with hyper-Raman scattering with frequencies  $2\omega_1 \pm \omega_M$ .

The practical application of the Raman effect in this thesis is confined to first-order normal Raman scattering. The higher-order classical terms are therefore neglected in the following discussion – the reader is referred to Long (2002) for a thorough treatment.

Here the first-order frequency-dependent linear induced electric dipole moment vectors  $\mathbf{p}^{(1)}$  are calculated for a single molecule. The extension to a bulk material is straight forward, as the intensity of the scattering is linear with the number density of scattering molecules. Starting from the expression for the first-order dipole moment vector;

$$\mathbf{p}^{(1)} = \boldsymbol{\alpha} \cdot \mathbf{E}, \quad (2.8)$$

one can obtain the correct frequency dependence of  $\mathbf{p}^{(1)}$  by substituting the correct frequency dependence of the polarisability tensor  $\boldsymbol{\alpha}$  (generally a function of the nuclear coordinates and therefore the molecular vibrational frequencies) and the incident radiation  $\mathbf{E}$ .

The scattering system under consideration is taken to be a single molecule undergoing pure vibration. In other words the nuclei can vibrate about their equilibrium positions, but the space-fixed molecule does not rotate. As previously mentioned, the lack of discrete rotational energy levels precludes a treatment of vibrational and rotation vibrational scattering. One can expand the components  $\alpha_{\rho\sigma}$  of the polarisability tensor  $\boldsymbol{\alpha}$  as a Taylor series about the equilibrium configuration (denoted by '0' on the derivative subscripts) with respect to the normal coordinates of vibration  $Q_k, Q_l, \dots$  as follows:

$$\alpha_{\rho\sigma} = (\alpha_{\rho\sigma})_0 + \sum_k \left( \frac{\partial \alpha_{\rho\sigma}}{\partial Q_k} \right)_0 Q_k + \frac{1}{2} \sum_{k,l} \left( \frac{\partial^2 \alpha_{\rho\sigma}}{\partial Q_k \partial Q_l} \right)_0 Q_k Q_l + \dots, \quad (2.9)$$

where  $(\alpha_{\rho\sigma})_0$  is the equilibrium value of  $\alpha_{\rho\sigma}$ . This expansion expresses the variation of the polarisability with vibrations of the molecule at frequencies  $\omega_k, \omega_l, \dots$ , with summation over all normal coordinates. Commonly, one makes use of the electric harmonic approximation at this point: the variation of the polarisability in a vibration is treated as proportional to the first power of a displacement  $Q_k$ , allowing one to neglect terms in  $Q$  of higher than first-order.

Concentrating on one normal mode of vibration  $Q_k$ , we can re-write equation (2.9) as

$$(\alpha_{\rho\sigma})_k = (\alpha_{\rho\sigma})_0 + (\alpha'_{\rho\sigma})_k Q_k, \quad (2.10)$$

where  $(\alpha'_{\rho\sigma})_k$  are the components of the derived polarisability tensor  $\alpha'_k$ , so-called since its components are entirely composed of polarisability derivatives with respect to the normal coordinate  $Q_k$ :

$$(\alpha'_{\rho\sigma})_k = \left( \frac{\partial \alpha_{\rho\sigma}}{\partial Q_k} \right)_0.$$

Equation (2.10) is valid for all tensor components and so can be re-written, once more in tensor notation as follows:

$$\alpha_k = \alpha_0 + \alpha'_k Q_k. \quad (2.11)$$

A further approximation is required here. The molecular restoring force is considered to be proportional to the first power of the displacement  $Q_k$ . This is known as the mechanical harmonic approximation: the nuclei vibrate with simple harmonic motion. Therefore, the frequency dependence of  $Q_k$  is given by

$$Q_k = Q_{k_0} \cos(\omega_k t + \delta_k), \quad (2.12)$$

where  $Q_{k_0}$  is the amplitude of the normal coordinate and  $\delta_k$  is the phase of the normal vibration  $Q_k$  relative to the electric field and will be different for different molecules. Substituting this frequency dependence into equation (2.11) yields

$$\alpha_k = \alpha_0 + \alpha'_k Q_{k_0} \cos(\omega_k t + \delta_k). \quad (2.13)$$

The frequency dependence of  $E$  can now be introduced:

$$\mathbf{E} = E_0 \cos \omega_1 t. \quad (2.14)$$

Substituting the frequency dependence for  $\alpha_k$  and  $E$  from equations (2.13) and (2.14) into equation (2.8) gives

$$\mathbf{p}^{(1)} = \alpha_0 E_0 \cos \omega_1 t + \alpha'_k E_0 Q_{k_0} \cos(\omega_k t + \delta_k) \cos \omega_1 t. \quad (2.15)$$

The second term in equation (2.15) can be reformulated using the trigonometric identity

$$\cos A \cos B = \frac{1}{2} \{ \cos(A+B) + \cos(A-B) \},$$

giving an explicit expression for the frequency dependence of  $\mathbf{p}^{(1)}$ :

$$\mathbf{p}^{(1)} = \alpha_0 E_0 \cos \omega_1 t + \frac{1}{2} \alpha'_k E_0 Q_{k_0} \{ \cos(\omega_1 + \omega_k + \delta_k)t + \cos(\omega_1 t - \omega_k t - \delta_k)t \} \quad (2.16)$$

This can be re-written to more clearly show the frequency dependence as

$$\mathbf{p}^{(1)} = \mathbf{p}^{(1)}(\omega_1) + \mathbf{p}^{(1)}(\omega_1 - \omega_k) + \mathbf{p}^{(1)}(\omega_1 + \omega_k), \quad (2.17)$$

where

$$\mathbf{p}^{(1)}(\omega_1) = \mathbf{p}_0^{\text{Ray}} \cos \omega_1 t. \quad (2.18)$$

Here the 'Ray' superscript denotes the association of this dipole moment vector term with Rayleigh scattering. The vector  $\mathbf{p}_0^{\text{Ray}}$  is given by

$$\mathbf{p}_0^{\text{Ray}} = \alpha^{\text{Ray}} \cdot E_0, \quad (2.19)$$

where  $\alpha^{\text{Ray}}$  is the polarisability tensor introduced in equation (2.6):

$$\alpha^{\text{Ray}} = \alpha_0.$$

The terms associated with Raman scattering ('Ram' superscripts) are

$$p^{(1)}(\omega_1 \pm \omega_k) = p_{k_0}^{\text{Ram}} \cos(\omega_1 \pm \omega_k \pm \delta_k)t. \quad (2.20)$$

Here  $p_{k_0}^{\text{Ram}}$  is given by

$$p_{k_0}^{\text{Ram}} = \alpha_k^{\text{Ram}} \cdot E_0, \quad (2.21)$$

where  $\alpha_k^{\text{Ram}}$  is the polarisability tensor introduced by equation (2.6), here expressed with respect to the  $Q_k$  normal coordinate:

$$\alpha_k^{\text{Ram}} = \frac{1}{2} \alpha'_k Q_k. \quad (2.22)$$

The cosine terms in equations (2.18) and (2.20) define the frequencies of the induced dipoles, and complete the frequency dependence specification.

This classical treatment provides a useful qualitative picture of the Raman and Rayleigh scattering mechanisms. Rayleigh scattering is due to the electric dipole oscillating at the same frequency  $\omega_1$  as the incident radiation, with the necessary condition that  $\alpha^{\text{Ray}}$  is non-zero. Since all molecules are polarisable to some extent, the polarisability tensor  $\alpha_0$  will always be non-zero (although often only for certain components), and since  $\alpha^{\text{Ray}}$  and  $\alpha_0$  are the same term, all molecules will exhibit Rayleigh scattering.

In order to observe Raman scattering, there is the corresponding condition that  $\alpha^{\text{Ram}}$  has to be non-zero. Since  $\alpha^{\text{Ram}}$  is a scalar multiple of the derived polarisability tensor  $\alpha'_k$ , the condition is that at least one of the components of  $\alpha'_k$  be non-zero. Since the components

of  $\alpha'_k$  are the derivatives of the corresponding coordinates of the polarisability tensor, taken at the equilibrium position, the necessary condition for Raman scattering is that at least one component of the polarisability tensor should have a non-zero derivative at the equilibrium position.

In the quantum mechanical treatment, the exponential formulation is used throughout. For purposes of comparison, the trigonometric expressions derived above can be reformulated as follows:

Equation (2.12) becomes:

$$Q_k = \frac{1}{2} Q_{k_0} \{ \exp(-i(\omega_k t + \delta_k)) + \exp(i(\omega_k t + \delta_k)) \}. \quad (2.23)$$

Equation (2.14) becomes:

$$E = \frac{1}{2} E_0 \{ \exp(-i\omega_1 t) + \exp(i\omega_1 t) \}. \quad (2.24)$$

Equation (2.18) becomes:

$$P^{(1)}(\omega_1) = \frac{1}{2} P_0^{\text{Ray}} \{ \exp(-i\omega_1 t) + \exp(i\omega_1 t) \}. \quad (2.25)$$

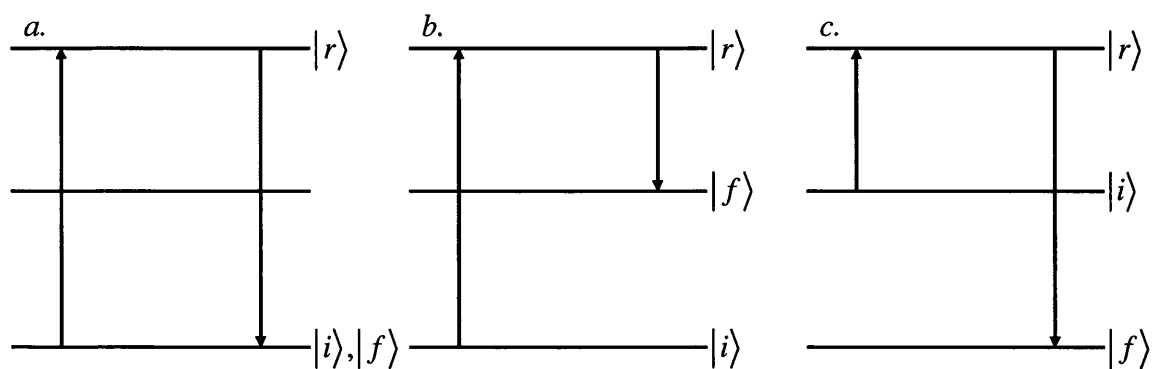
Equation (2.20) becomes:

$$P^{(1)}(\omega_1 \pm \omega_k) = \frac{1}{2} P_0^{\text{Ram}} \{ \exp[-i((\omega_1 \pm \omega_k)t \pm \delta_k)] + \exp[i((\omega_1 \pm \omega_k)t \pm \delta_k)] \}. \quad (2.26)$$

## 2.2 Quantum Mechanical Treatment

The quantum mechanical treatment of the Raman Effect is formally quite similar to the classical treatment, as both treat the electromagnetic radiation as classical fields. However, the quantum mechanical treatment of the scattering molecule allows a full quantitative analysis of the scattering process. The classical electric and magnetic fields are considered to produce perturbations in the state vectors of the molecular system, and the properties of the perturbed system are investigated quantum mechanically via time-independent perturbation theory. For example, the classical dipole polarisability tensor and induced electric dipole moment vector are replaced with the quantum mechanical transition polarisability tensor and electric transition dipole moment.

The emphasis in the quantum mechanical treatment is on the allowed transitions between states of the molecule under the perturbing influence of the classical electric and magnetic fields. Figure 2.2 shows the energy level diagrams for normal non-resonance Raman and Rayleigh scattering via a short-lived intermediate state  $|r\rangle$ . Note that  $|r\rangle$  is not a real state but a so-called 'dressed-state', an entity combining an initial molecular quantum state with a photon in close proximity. The transition moments are linked since their products each contribute to the amplitude of the transition polarisability tensor.



**Figure 2.2** Energy level diagrams for non-resonant photon excitation:  
a. Rayleigh, b. Stokes Raman, and c. anti-Stokes Raman scattering

Note also that the replacement of the classical dipole polarisability tensor and induced electric dipole moment vector with the quantum mechanical transition polarisability tensor and transition electric dipole moment is a change of profound significance. Whereas



classically these quantities could only be qualitatively linked to molecular properties, in the quantum mechanical treatment the transition tensors and moments can be in principle linked quantitatively to molecular properties.

The aim, therefore, of a quantum mechanical treatment is to derive explicit expressions for the transition dipole moment vector and the transition polarisability tensor. The classical total induced electric dipole moment vector  $\mathbf{p}$  is replaced by the quantum mechanical total induced transition electric dipole vector  $(\mathbf{p})_{fi}$ , which is given by

$$(\mathbf{p})_{fi} = \langle \Psi_f' | \hat{\mathbf{p}} | \Psi_i' \rangle, \quad (2.27)$$

where  $\hat{\mathbf{p}}$  is the electric dipole moment operator and the wave functions  $\Psi_i'$  and  $\Psi_f'$  are the perturbed time-dependent initial and final states of the molecule, respectively.

These perturbed wave functions can be written as series expansions, i.e.

$$\Psi_i' = \Psi_i^{(0)} + \Psi_i^{(1)} + \Psi_i^{(2)} + \dots + \Psi_i^{(n)}, \quad (2.28)$$

where  $\Psi_i^{(0)}$  is the unperturbed initial state of the molecule,  $\Psi_i^{(1)}$  is the first-order modification to  $\Psi_i^{(0)}$ ,  $\Psi_i^{(2)}$  the second-order modification and so on. Similarly, for the final state one has

$$\Psi_f' = \Psi_f^{(0)} + \Psi_f^{(1)} + \Psi_f^{(2)} + \dots + \Psi_f^{(n)}. \quad (2.29)$$

Restricting the consideration to the case where the interaction Hamiltonian  $\hat{H}$  only contains an electric dipole term,  $\hat{H}_p$ , time-independent perturbation theory allows one to write these modifications to the unperturbed initial state wave function as linear combinations of the unperturbed wave function  $\Psi_i^{(0)}$  as follows:

$$\Psi_i^{(1)} = \sum_r a_{p_{ir}}^{(1)} \Psi_r^{(0)}; \quad \Psi_i^{(2)} = \sum_r a_{p_{ir}}^{(2)} \Psi_r^{(0)}; \quad \dots; \quad \Psi_i^{(n)} = \sum_r a_{p_{ir}}^{(n)} \Psi_r^{(0)}, \quad (2.30)$$

where the  $a_{p_{ir}}$  are scalar coefficients, and the term in  $(n)$  may be seen to represent the general case for the initial state. Similarly for the final state one obtains

$$\Psi_f^{(n)} = \sum_r a_{p_{fr}}^{(n)} \Psi_r^{(0)}, \quad (2.31)$$

where the  $a_{p_{fr}}$  are again scalar coefficients.

Analogous to equation (2.3), one can write the total induced transition electric dipole vector  $(\mathbf{p})_{fi}$  as a series expansion:

$$(\mathbf{p})_{fi} = (\mathbf{p}^{(1)})_{fi} + (\mathbf{p}^{(2)})_{fi} + (\mathbf{p}^{(3)})_{fi} + \dots, \quad (2.32)$$

where ascending order terms increase their order dependence on  $\mathbf{E}$ :  $(\mathbf{p}^{(1)})_{fi}$  is linear in  $\mathbf{E}$ ,  $(\mathbf{p}^{(2)})_{fi}$  is quadratic in  $\mathbf{E}$ ,  $(\mathbf{p}^{(3)})_{fi}$  cubic, and so on. This series expansion, along with the series expansions for the initial and final perturbed wave functions given in equations (2.28) and (2.29) are now substituted into equation (2.27).

Collecting terms according to their dependence on the electric field  $\mathbf{E}$  yields the following expressions for the terms in equation (2.32):

$$(\mathbf{p}^{(0)})_{fi} = \langle \Psi_f^{(0)} | \hat{\mathbf{p}} | \Psi_i^{(0)} \rangle \quad (2.33.a)$$

$$(\mathbf{p}^{(1)})_{fi} = \langle \Psi_f^{(1)} | \hat{\mathbf{p}} | \Psi_i^{(0)} \rangle + \langle \Psi_f^{(0)} | \hat{\mathbf{p}} | \Psi_i^{(1)} \rangle \quad (2.33.b)$$

$$(\mathbf{p}^{(2)})_{fi} = \langle \Psi_f^{(2)} | \hat{\mathbf{p}} | \Psi_i^{(0)} \rangle + \langle \Psi_f^{(0)} | \hat{\mathbf{p}} | \Psi_i^{(2)} \rangle + \langle \Psi_f^{(1)} | \hat{\mathbf{p}} | \Psi_i^{(1)} \rangle \quad (2.33.c)$$

$$(\mathbf{p}^{(3)})_{fi} = \langle \Psi_f^{(3)} | \hat{\mathbf{p}} | \Psi_i^{(0)} \rangle + \langle \Psi_f^{(0)} | \hat{\mathbf{p}} | \Psi_i^{(3)} \rangle + \langle \Psi_f^{(1)} | \hat{\mathbf{p}} | \Psi_i^{(2)} \rangle + \langle \Psi_f^{(2)} | \hat{\mathbf{p}} | \Psi_i^{(1)} \rangle \quad (2.33.d)$$

Note that  $(\mathbf{p}^{(0)})_{fi}$  is independent of  $\mathbf{E}$  as it only involved unperturbed wave functions. It is not considered further since it relates to a direct transition between unperturbed initial and final states, respectively, and not to light scattering – Rayleigh and Raman scattering require a ‘dressed’ intermediate state. The dependence of the transition electric dipole moment vectors on  $\mathbf{E}$  can be shown quite simply by considering the coefficients involved in the relevant expression. For example,  $(\mathbf{p}^{(3)})_{fi}$  is clearly cubic in  $\mathbf{E}$  since it only involves the coefficients  $a_{p_{ir}}^{(3)}$ ,  $a_{p_{fr}}^{(3)}$ ,  $a_{p_{fr}}^{(2)}a_{p_{ir}}^{(1)}$  and  $a_{p_{fr}}^{(1)}a_{p_{ir}}^{(2)}$ .

As for the classical treatment, the transition dipole moment vectors will in general have several frequency components. The amplitudes of the first-order electric dipole vectors will in general contain three frequency components: one related to Rayleigh scattering, and two associated with Raman scattering, i.e.

$$\left(\mathbf{p}_0^{(1)}(\omega_1)\right)_{ii} = (\boldsymbol{\alpha})_{ii} \cdot \mathbf{E}_0(\omega_1) \quad \text{and} \quad \left(\mathbf{p}_0^{(1)}(\omega_1 \pm \omega_M)\right)_{fi} = (\boldsymbol{\alpha})_{fi} \cdot \mathbf{E}_0(\omega_1), \quad (2.34)$$

where the transition polarisability tensors  $(\boldsymbol{\alpha})_{ii}$  and  $(\boldsymbol{\alpha})_{fi}$  are associated with Rayleigh and Raman scattering, respectively, and are the quantum mechanical analogues of the classical polarisability tensors  $\boldsymbol{\alpha}^{\text{Ray}}$  and  $\boldsymbol{\alpha}^{\text{Ram}}$ .

The procedure can be extended to the amplitudes of the higher-order terms, with  $(\mathbf{p}_0^{(2)})_{fi}$  associated with hyper-Rayleigh and hyper-Raman scattering, and  $(\mathbf{p}_0^{(3)})_{fi}$  with second hyper-Rayleigh and second hyper-Raman scattering. However, as previously mentioned, only the first-order terms are of relevance to this work.

A brief mention should be made here regarding the neglect of terms other than electric dipole term  $\hat{H}_p$  in the interaction Hamiltonian  $\hat{H}$ . A finer level of approximation to the system could be obtained by including the scattering due to the magnetic dipole  $\hat{H}_m$  and the electric quadrupole term  $\hat{H}_q$ . The interaction Hamiltonian would then be written as

$$\hat{H} = \hat{H}_p + \hat{H}_m + \hat{H}_\theta. \quad (2.35)$$

The magnetic dipole and electric quadrupole terms are associated with the total transition multipole vectors  $(\mathbf{m})_{fi}$  and  $(\Theta)_{fi}$ , respectively:

$$(\mathbf{m})_{fi} = \langle \Psi'_f | \hat{\mathbf{m}} | \Psi'_i \rangle \quad \text{and} \quad (\Theta)_{fi} = \langle \Psi'_f | \hat{\Theta} | \Psi'_i \rangle, \quad (2.36)$$

where  $\hat{\mathbf{m}}$  is the magnetic dipole operator and  $\hat{\Theta}$  the electric quadrupole operator.

The series expansions for the  $\Psi_i^{(n)}$  terms would then be as follows. Note that one can replace the  $i$  subscripts with  $f$  to arrive at the expressions for the final state terms

$$\begin{aligned} \Psi_i^{(1)} &= \sum_r (a_{p_{ir}}^{(1)} + a_{m_{ir}}^{(1)} + a_{\theta_{ir}}^{(1)}) \Psi_r^{(0)} \\ \Psi_i^{(2)} &= \sum_r (a_{p_{ir}}^{(2)} + a_{m_{ir}}^{(2)} + a_{\theta_{ir}}^{(2)}) \Psi_r^{(0)} \\ &\quad \vdots \\ \Psi_i^{(n)} &= \sum_r (a_{p_{ir}}^{(n)} + a_{m_{ir}}^{(n)} + a_{\theta_{ir}}^{(n)}) \Psi_r^{(0)} \end{aligned} \quad (2.37)$$

The addition of magnetic dipole and electric quadrupole terms is only justified if the Hamiltonian operators  $\hat{H}_m$  and  $\hat{H}_\theta$  are non-zero. For this to occur, the electric field gradient must be non-zero over the molecule<sup>1</sup>. For visible light, the wavelength of the radiation is about  $10^3$  greater than the dimensions of a molecule. Therefore it is an excellent approximation to include only the electric dipole term  $\hat{H}_p$  in the interaction Hamiltonian.

Since this thesis is concerned with the normal Raman scattering of visible light from hydrogen isotopomers, any higher terms, along with the transition dipole moment vector terms involving hyper- and second-hyper polarisability tensors are not discussed further.

---

<sup>1</sup> Although the terms themselves are actually all linearly proportional to the electric field  $E$ .

Let us now return to the first-order term in the series expansion for the total induced transition electric dipole moment vector introduced in equation (2.33.b), which is in general a complex quantity:

$$\left(\tilde{\mathbf{p}}^{(1)}\right)_{fi} = \left\langle \Psi_f^{(1)} \left| \hat{\mathbf{p}} \right| \Psi_i^{(0)} \right\rangle + \left\langle \Psi_f^{(0)} \left| \hat{\mathbf{p}} \right| \Psi_i^{(1)} \right\rangle, \quad (2.38)$$

where the relationship of  $\left(\tilde{\mathbf{p}}^{(1)}\right)_{fi}$  to the real quantity  $\left(\mathbf{p}^{(1)}\right)_{fi}$  is

$$\left(\mathbf{p}^{(1)}\right)_{fi} = \left(\tilde{\mathbf{p}}^{(1)}\right)_{fi} + \left(\tilde{\mathbf{p}}^{(1)}\right)_{fi}^*.$$

In order to evaluate equation (2.38), the relationships between the unperturbed wave functions  $\Psi_i^{(0)}$  and  $\Psi_f^{(0)}$ , and the perturbed wave functions  $\Psi_i^{(1)}$  and  $\Psi_f^{(1)}$  have to be derived. The wave functions are considered to be complex to maintain generality.

It will prove useful to separate the time-dependent wave functions into their time-dependent and time-independent parts. For the initial state  $i$ , with similar expressions for intermediate ( $r$ ) and final ( $f$ ) states, one finds

$$\Psi_i = \psi_i \exp -i(\omega_i - i\Gamma_i)t, \quad (2.39)$$

where the wave function  $\psi_i$  is the time independent part of  $\Psi_i$ , and  $\Gamma_i$  is the half width of the level  $i$ . The full width  $2\Gamma_i$  is related to the lifetime of the level  $i$  through the uncertainty principle. The frequency term  $\omega_i$  is related to the energy of the state  $i$  through the expression

$$\omega_i = \frac{E_i}{\hbar}.$$

Making the relevant substitutions into equation (2.38), and assuming an perturbation of first order, gives the following expression for the  $\rho$ -component of  $\left(\mathbf{p}^{(1)}\right)_{fi}$  for real wave functions (collecting terms according to their frequency dependence):

$$\begin{aligned}
(p_\rho^{(1)})_{fi} = & \frac{1}{2\hbar} \sum_{r \neq i} \left\{ \frac{\langle \psi_f | \hat{p}_\rho | \psi_r \rangle \langle \psi_r | \hat{p}_\sigma | \psi_i \rangle}{\omega_{ri} - \omega_1 - i\Gamma_r} \tilde{E}_{\sigma_0} \exp -i(\omega_1 - \omega_{fi})t \right. \\
& \left. + \frac{\langle \psi_f | \hat{p}_\rho | \psi_r \rangle \langle \psi_r | \hat{p}_\sigma | \psi_i \rangle}{\omega_{ri} + \omega_1 + i\Gamma_r} \tilde{E}_{\sigma_0}^* \exp i(\omega_1 + \omega_{fi})t \right\} \\
& + \frac{1}{2\hbar} \sum_{r \neq f} \left\{ \frac{\langle \psi_f | \hat{p}_\sigma | \psi_r \rangle \langle \psi_r | \hat{p}_\rho | \psi_i \rangle}{\omega_{rf} - \omega_1 - i\Gamma_r} \tilde{E}_{\sigma_0}^* \exp i(\omega_1 + \omega_{fi})t \right. \\
& \left. + \frac{\langle \psi_f | \hat{p}_\sigma | \psi_r \rangle \langle \psi_r | \hat{p}_\rho | \psi_i \rangle}{\omega_{rf} + \omega_1 + i\Gamma_r} \tilde{E}_{\sigma_0} \exp -i(\omega_1 - \omega_{fi})t \right\} \\
& + \text{complex conjugate}
\end{aligned} \tag{2.40}$$

where  $\hat{p}_\rho$  and  $\hat{p}_\sigma$  are the  $\rho$ - and  $\sigma$ -components of the electric dipole moment operator and where double subscripts on the frequency terms denote a difference:

$$\omega_{ri} \equiv \omega_r - \omega_i \quad \text{or} \quad \omega_{rf} \equiv \omega_r - \omega_f .$$

A number of assumptions can be made in order to make equation (2.40) more tractable. Firstly, one can make the approximation that the lifetimes of the initial and final states are 'infinite'. This is a reasonable assumption given that the lifetime of the intermediate 'dressed' state is virtually zero. Thus the widths of the states  $i$  and  $f$  are set to zero:

$$\Gamma_i = \Gamma_f \cong 0 .$$

We can re-write equation (2.39) as

$$\Psi_i = \psi_i \exp -i\omega_i t , \tag{2.41}$$

and similarly for the final state,  $f$ . Further, it is possible to omit terms whose exponents contain  $(\omega_1 + \omega_{fi})$ , as these describe the induced emission of two quanta from an initial excited state unrelated to Rayleigh or Raman scattering. The terms in  $(\omega_1 - \omega_{fi})$  are sufficient to describe Rayleigh and Raman scattering, provided  $(\omega_1 - \omega_{fi}) > 0$ .

Since  $\omega_l$  is a constant, it is the value of  $\omega_{fi}$  that determines which scattering mechanism is being described and which may be summarised as follows:

<i>Sign of <math>\omega_{fi}</math></i>	<i>Energy level relationship</i>	<i>Scattering mechanism</i>
$\omega_{fi} > 0$	$E_i < E_f$	Stokes Raman
$\omega_{fi} = 0$	$E_i = E_f$	Rayleigh
$\omega_{fi} < 0$	$E_i > E_f$	Anti-Stokes Raman

These assumptions greatly simplify equation (2.40), leading to the following expression for the Stokes and anti-Stokes part of  $(p_\rho^{(1)})_{fi}$ :

$$(p_\rho^{(1)})_{fi} = \frac{1}{2\hbar} \sum_{r \neq i, f} \left\{ \frac{\langle f | \hat{p}_\rho | r \rangle \langle r | \hat{p}_\sigma | i \rangle}{\omega_{ri} - \omega_l - i\Gamma_r} + \frac{\langle f | \hat{p}_\sigma | r \rangle \langle r | \hat{p}_\rho | i \rangle}{\omega_{rf} + \omega_l + i\Gamma_r} \right\} \tilde{E}_{\sigma_0} \exp -i\omega_s t \quad (2.42)$$

+ complex conjugate

Note that the notation has been simplified, following the treatment given in Long (2002), with  $|i\rangle$  written for  $|\psi_i\rangle$ ,  $|f\rangle$  for  $|\psi_f\rangle$  and  $|r\rangle$  for  $|\psi_r\rangle$ . The absolute frequency of the scattered radiation  $\omega_s$  is defined as

$$\omega_s = \omega_l - \omega_{fi}.$$

It follows that one can define the  $\rho\sigma$ -component of the general transition polarisability tensor  $(\alpha)_{fi}$ , already seen in equation (2.34), as

$$(\alpha_{\rho\sigma})_{fi} = \frac{1}{\hbar} \sum_{r \neq i, f} \left\{ \frac{\langle f | \hat{p}_\rho | r \rangle \langle r | \hat{p}_\sigma | i \rangle}{\omega_{ri} - \omega_l - i\Gamma_r} + \frac{\langle f | \hat{p}_\sigma | r \rangle \langle r | \hat{p}_\rho | i \rangle}{\omega_{rf} + \omega_l + i\Gamma_r} \right\}. \quad (2.43)$$

Note that although real wave functions are used, the components of the general transition polarisability tensor are generally complex due to the presence of the phenomenological damping term  $i\Gamma_r$  in the denominators. However, for normal (non-resonance) Raman

scattering,  $i\Gamma_r$  is small compared with the frequency terms  $(\omega_f \pm \omega_l)$  in the denominators and can normally be neglected. This leads to the Kramer-Heisenberg-Dirac (KHD) expression for the now unambiguously real components of the general transition polarisability tensor (Smith and Dent (2005)):

$$(\alpha_{\rho\sigma})_{fi} = \frac{1}{\hbar} \sum_{r \neq i, f} \left\{ \frac{\langle f | \hat{p}_\rho | r \rangle \langle r | \hat{p}_\sigma | i \rangle}{\omega_i - \omega_l} + \frac{\langle f | \hat{p}_\sigma | r \rangle \langle r | \hat{p}_\rho | i \rangle}{\omega_f + \omega_l} \right\}. \quad (2.44)$$

Let us return briefly to the more general complex formulation. Using the definition of the general transition polarisability tensor in equation (2.43) allows one to re-write equation (2.42) in the more readable form

$$(p_\rho^{(1)})_{fi} = \frac{1}{2} (\alpha_{\rho\sigma})_{fi} \left\{ \tilde{E}_{\sigma_0}(\omega_l) \exp -i\omega_s t + \tilde{E}_{\sigma_0}^*(\omega_l) \exp i\omega_s t \right\}. \quad (2.45)$$

This general form can be split into real and imaginary parts as follows:

$$(p_\rho^{(1)})_{fi} = \frac{1}{2} \left\{ (\tilde{p}_{\rho_0}^{(1)})_{fi} \exp -i\omega_s t + (\tilde{p}_{\rho_0}^{(1)})_{fi}^* \exp i\omega_s t \right\}, \quad (2.46)$$

where

$$(\tilde{p}_{\rho_0}^{(1)})_{fi} = (\alpha_{\rho\sigma})_{fi} \tilde{E}_{\sigma_0}(\omega_l) \quad \text{and} \quad (\tilde{p}_{\rho_0}^{(1)})_{fi}^* = (\alpha_{\rho\sigma})_{fi} \tilde{E}_{\sigma_0}^*(\omega_l).$$

In the case of real electric field amplitudes, the time-dependent transition dipole moment amplitude becomes real as well, yielding

$$\tilde{E}_{\sigma_0}(\omega_l) = \tilde{E}_{\sigma_0}^*(\omega_l) = E_{\sigma_0}(\omega_l) \Rightarrow (\tilde{p}_{\rho_0}^{(1)})_{fi} = (\tilde{p}_{\rho_0}^{(1)})_{fi}^* = (p_{\rho_0}^{(1)})_{fi}. \quad (2.47)$$



Equation (2.46) can now be re-written as

$$\left(p_{\rho}^{(1)}\right)_{fi} = \frac{1}{2} \left(p_{\rho_0}^{(1)}\right)_{fi} \{\exp -i\omega_s t + \exp i\omega_s t\}, \quad (2.48)$$

with

$$\left(p_{\rho_0}^{(1)}\right)_{fi} = \left(\alpha_{\rho\sigma}\right)_{fi} E_{\sigma_0}(\omega_1). \quad (2.49)$$

For purposes of comparison with the classical results, the exponential equations (2.48) and (2.49) can be recast in trigonometric form:

$$\left(p_{\rho}^{(1)}\right)_{fi} = \left(p_{\rho_0}^{(1)}\right)_{fi} \cos \omega_s t, \quad (2.50)$$

with

$$\left(p_{\rho}^{(1)}\right)_{fi} = \left(\alpha_{\rho\sigma}\right)_{fi} E_{\sigma_0}(\omega_1) \cos \omega_s t. \quad (2.51)$$

### 2.3 Summary

While useful in qualitative analysis and although exhibiting similarity to the quantum mechanical treatment, it is not possible to use the classical model of Rayleigh and Raman scattering for any detailed quantitative analysis of real-world molecular systems. For the latter, the quantum mechanical treatment is required, which allows one – at least in principle – to derive a correlation between the properties of the transition polarisability tensor and measurable molecular properties. The following table summarises the most important quantities and the form of the polarisability tensor for both treatments:

<i>Classical treatment</i>		<i>Quantum mechanical treatment</i>	
Parameter, symbol	Equation	Parameter, symbol	Equation
Total time-dependent induced electric dipole moment vector, $\mathbf{p}$	(2.3)	Total time-dependent induced transition electric dipole moment vector, $(\mathbf{p})_{fi}$	(2.32)
First-order frequency-dependent linear induced electric dipole moment vector, $\mathbf{p}^{(1)}$	(2.8)	First-order frequency-dependent linear induced transition electric dipole moment vector, $(\mathbf{p}^{(1)})_{fi}$	(2.38)
Rayleigh-associated time-independent electric dipole moment vector amplitude, $\mathbf{p}_0(\omega_1)$	(2.6)	Rayleigh-associated time-independent transition electric dipole moment vector amplitude, $(\mathbf{p}_0^{(1)}(\omega_1))_{ii}$	(2.34)
Raman-associated time-independent electric dipole moment vector amplitude, $\mathbf{p}_0(\omega_1 \pm \omega_M)$	(2.6)	Raman-associated time-independent transition electric dipole moment vector amplitude, $(\mathbf{p}_0^{(1)}(\omega_1 \pm \omega_M))_{fi}$	(2.34)
Polarisability tensor ( $\rho\sigma$ -component), $\alpha_{\rho\sigma}$	(2.9)	Transition polarisability tensor ( $\rho\sigma$ -component), $(\alpha_{\rho\sigma})_{fi}$	(2.43)
$\alpha_{\rho\sigma} = (\alpha_{\rho\sigma})_0 + \sum_k \left( \frac{\partial \alpha_{\rho\sigma}}{\partial Q_k} \right)_0 Q_k$ $+ \frac{1}{2} \sum_{k,l} \left( \frac{\partial^2 \alpha_{\rho\sigma}}{\partial Q_k \partial Q_l} \right)_0 Q_k Q_l + \dots$		$(\alpha_{\rho\sigma})_{fi} = \frac{1}{\hbar} \sum_{r \neq i, f} \left\{ \frac{\langle f   \hat{p}_\rho   r \rangle \langle r   \hat{p}_\sigma   i \rangle}{\omega_{ri} - \omega_1} \right.$ $\left. + \frac{\langle f   \hat{p}_\sigma   r \rangle \langle r   \hat{p}_\rho   i \rangle}{\omega_{rf} + \omega_1} \right\}$	

When modelling is the objective (as in Chapter 3), it will prove essential to use the quantum mechanical approach, since the application of quantum statistics is the only way to correctly calculate the vibrational and rotational state populations which are essential for estimating the relative intensities of the scatterings related to allowed transitions. It is also the only way in which the complete set of selection rules can be derived for vibrational, rotation-vibrational and rotational Raman scattering.

## ***2.4 References for Chapter Two***

### *2.4.1 Cited references*

Herzberg, G. (1950). Molecular Spectra and Molecular Structure I. Spectra of Diatomic Molecules. New York (U.S.A.), Van Nostrand Reinhold Company.

Long, D. A. (2002). The Raman Effect - A Unified Treatment of the Theory of Raman Scattering by Molecules. Chichester (U.K.), John Wiley & Sons, Ltd.

Smith, E. and Dent, G. (2005). Modern Raman Spectroscopy - A Practical Approach. Chichester (U.K.), John Wiley & Sons, Ltd.

### *2.4.2 Further reading*

Allen, H. C. and Cross, P. C. (1963). Molecular Vib-Rotors - The Theory and Interpretation of High Resolution Infrared Spectra. New York (U.S.A.), John Wiley & Sons, Inc.

Anderson, A. (1971). The Raman Effect. New York (U.S.A.), Marcel Dekker, Inc.

Koningstein, J. A. (1972). Introduction to the Theory of the Raman Effect. Dordrecht (The Netherlands), D. Reidel Publishing Company.

Lefebvre-Brion, H. and Field, R. W. (2004). The Spectra and Dynamics of Diatomic Molecules. Amsterdam (The Netherlands), Elsevier Academic Press.

McCreery, R. L. (2000). Raman Spectroscopy for Chemical Analysis. New York (U.S.A.), John Wiley & Sons, Inc.

Person, W. B. and Zerbi, G. (1982). Vibrational Intensities in Infrared and Raman Spectroscopy. Amsterdam (The Netherlands), Elsevier Scientific Publishing Company.

## CHAPTER THREE

### COMPUTER MODELLING OF NORMAL RAMAN SPECTRA OF HYDROGEN ISOTOPOMERS

In this chapter we summarise the important principles, derivations and calculations necessary for computer modelling of the Raman spectra of hydrogen isotopomers. The aim is to calculate the line positions and relative intensities of each of the branches of interest for each of the six hydrogen isotopomers. A *LabVIEW* program called *SpecGen* has been written to perform these calculations and to optionally convolute the data points with a lineshape function such as a Gaussian or Voigt profile.

*LabVIEW* is particularly useful for the calculation and presentation of spectra since it is designed for data acquisition and manipulation – its excellent file handling capability allows for spectra to be outputted for use in *Origin* or other data analysis packages. Calculation parameters such as temperature, number density or the wavelength of the excitation source can be assigned to front panel controls to allow for real-time manipulation of these parameters. Real-world considerations such as background noise and finite linewidth are simple to simulate and can also be varied in real-time via front panel controls. Further, writing the program in *LabVIEW* allows for easy integration with other *LabVIEW* programs. It is possible, for example, to simulate ‘dirty’ spectra to test the efficacy of cleaning routines without having to first save a spectrum and then load it again into the cleaning routine.

Line position calculations were especially important in determining which of the two principal parts (pure rotation or vibration-rotation) of the Raman spectrum would be most suitable for use in the KATRIN monitoring system – the choice to concentrate on the vibration-rotation branches was made on the fact that at the proposed operating temperatures of the inner loop, the first (and strongest) few tritium pure rotational lines would be suppressed by the laser filter. Intensity calculations are also highly valuable as they show the strong dependence of Raman scattering with respect to polarisation.

The line positions and relative intensities for pure rotational and vibration-rotation transitions are considered separately. The case for rigid molecules is considered first since the more general case of a non-rigid molecule involves just small corrections to this first-order approximation.

### 3.1 Raman Bands and Selection Rules

The theoretical treatment presented in this chapter is based on that given by Long (2002), but note that a few minor departures have been made from Long's notation regarding the symbols used for the wavenumber shifts and labelling of the various branches of the Raman spectrum.

For example, in Long's work the term 'S-branch' could refer either to a pure rotational transition ( $\Delta v = 0$ ,  $v' = v'' = 0$ ;  $\Delta J = +2$ ) or a vibration-rotation transition ( $\Delta v = +1$ ,  $v' = 1$ ,  $v'' = 0$ ;  $\Delta J = +2$ ). In order to avoid such ambiguity, I have added ' $\Delta v$ ' subscripts to the branch labels – i.e. a '0' subscript indicates pure rotational transition (thus, the pure rotational S-branch is referred to as the 'S<sub>0</sub>-branch'), and a '1' subscript indicates a vibration-rotation transition (hence 'O<sub>1</sub>-branch', 'Q<sub>1</sub>-branch' and 'S<sub>1</sub>-branch').

Secondly, since Long's work deals with quite general cases with regard to vibration-rotation transitions, so the symbols used for the wavenumber\* shifts of the various branches, i.e.  $O(J);|\Delta\tilde{\nu}|$ ,  $Q(J);|\Delta\tilde{\nu}|$ , and  $S(J);|\Delta\tilde{\nu}|$  (with  $J = J''$ , see below) necessarily represent general cases for which the sign of the  $\Delta\tilde{\nu}$  is clarified by context. Since we are considering very specific cases in this thesis, these symbols are replaced by explicit labels following the convention outlined in the previous paragraph. This labelling convention is summarised in Table 3.1

---

\* Note that the terms 'wavenumber shift' and 'Raman shift' can be used interchangeably.

**Table 3.1** The notation convention for the branches of the Raman spectrum under consideration in this thesis.

Type of scattering	Selection rules		Branch name (this work)	Wavenumber shift symbol (this work)	Wavenumber shift symbol Long (2002)
	$\Delta\nu$	$\Delta J$			
Rayleigh	0	0	$Q_0$	N/A	N/A
Raman (pure rotation)	0	+2	$S_0$	$S_0(J)$	$S(J);  \Delta\tilde{\nu} $
Raman (rotation-vibration)	+1	-2	$O_1$	$O_1(J)$	$O(J);  \Delta\tilde{\nu} $
	+1	0	$Q_1$	$Q_1(J)$	$Q(J);  \Delta\tilde{\nu} $
	+1	+2	$S_1$	$S_1(J)$	$S(J);  \Delta\tilde{\nu} $

Note that here we only consider the Stokes Raman lines since the high pass filter used in the later experiments cuts out all anti-Stokes lines. Furthermore, we would like to make some remarks here regarding the definition of  $\Delta J$ :  $\Delta J = J' - J''$ .

The single prime refers to the upper energy level in a given transition, and a double prime refers to the lower energy level, regardless of whether  $J'$  belongs to the same rotational manifold as  $J''$ , or is a member of the manifold of a different vibrational or electronic state. Nevertheless, the  $J$ -parameter in the wavenumber shift symbols and in the rotational energy function  $\tilde{F}(J)$  (q.v.) is always associated with  $J''$  for all Stokes transitions considered here, whether pure rotational or rotation-vibration Raman transitions.

Finally, although not a factor in this work since only the Stokes Raman lines are considered, it should be noted that following the naming convention for Raman branches based on the value of  $\Delta J$ , both the Stokes and anti-Stokes pure rotational branches would be referred to as 'S<sub>0</sub>-branches', since  $\Delta J = +2$  regardless of whether the upper energy level was the initial or final rotational level. In vibration-rotation transitions, however, the separation of initial and final rotational levels by adjacent vibrational states means that this notation is unambiguous.

A rigorous derivation of the selection rules for Raman spectra is beyond the scope of this chapter and the reader is referred to Long (2002) for a rigorous treatment. No further consideration of selection rules is made here other than those summarised in Table 3.1.

### 3.2 Stokes Raman Line Positions

The position of a Raman line is generally quoted in the literature as a wavenumber shift from the exciting radiation, in units of reciprocal centimetres. Therefore, as mentioned in Chapter 2, it is somewhat more convenient to adopt the wavenumber representation for this theoretical treatment. In the following treatment, all energy terms are in wavenumbers, and in equations they are written with a tilde above the symbol to emphasise the fact.

The transition wavenumber for a molecule,  $\tilde{\nu}_M$ , is conventionally defined in terms of the total upper and lower energy state terms:

$$\tilde{\nu}_M = \tilde{T}' - \tilde{T}'' \quad (3.1)$$

where  $\tilde{T}'$  and  $\tilde{T}''$  are the total upper and lower state energies, respectively. Again, note that no reference is being made to initial and final states in this definition. The total energy terms can be reasonably expressed as a sum of electronic, vibrational, and rotational terms

$$\tilde{T} = \tilde{T}_e + \tilde{G} + \tilde{F} = \tilde{T}_e(n) + \tilde{G}(v) + \tilde{F}(J), \quad (3.2)$$

where  $\tilde{T}_e$ ,  $\tilde{G}$ , and  $\tilde{F}$  are the electronic, vibrational, and rotational terms parameterised by the quantum numbers  $n$ ,  $v$ , and  $J$ , respectively. In this thesis, we are concerned with hydrogen isotopomers at low temperatures, therefore it is reasonable to consider only transitions within the ground electronic state, so that

$$\tilde{T}'_e = \tilde{T}''_e = 0. \quad (3.3)$$



For a pure rotational transition, the transition wavenumber is simply the difference between the rotational terms

$$\tilde{\nu}_M = \tilde{F}' - \tilde{F}'', \quad (3.4)$$

where, following the convention of using primes to indicate upper and lower energy levels,  $\tilde{F}'$  is the rotational term for the upper energy level, and  $\tilde{F}''$  the term related to the lower level. For a vibration-rotation transition, the transition wavenumber is given by the sum of the vibrational and rotational shifts

$$\tilde{\nu}_M = (\tilde{G}' - \tilde{G}'') + (\tilde{F}' - \tilde{F}''), \quad (3.5)$$

where  $\tilde{G}'$  and  $\tilde{G}''$  are the upper and lower vibrational terms, respectively.

Note that although to a reasonable approximation the total energy term can be written as a sum of the electronic, vibrational and rotational terms, it does not in any way imply that these terms are independent of each other. In reality, the rotational term has a small dependence on the vibrational quantum number  $\nu$  associated with the change of moment of inertia for vibrational states in an anharmonic molecular potential. Thus, one has to take the vibration-rotation interaction into account, which is denoted by adding a ' $\nu$ '-subscript to the rotational terms. For a rotation-vibration Raman transition, equation (3.5) must be written as

$$\tilde{\nu}_M = (\tilde{G}' - \tilde{G}'') + (\tilde{F}'_{\nu} - \tilde{F}''_{\nu}). \quad (3.6)$$

In the specific case of hydrogen isotopomers at 300K, the population ratio between the ground ( $\nu'' = 0$ ) and first excited ( $\nu' = 1$ ) vibrational level is between  $\sim 10^{-9}$  ( $\text{H}_2$ ) to  $\sim 10^{-6}$  ( $\text{T}_2$ ). It is therefore reasonable to consider pure rotational transitions from the ground state, and vibration-rotation transitions from the ground vibrational state to the first excited vibrational state.

The quantity  $(\tilde{G}' - \tilde{G}'')$  can therefore be written as a constant

$$(\tilde{G}' - \tilde{G}'') = \tilde{G}(1) - \tilde{G}(0) = \tilde{\nu}_{\text{vib}}, \quad (3.7)$$

where  $\tilde{\nu}_{\text{vib}}$  is known as the vibrational band offset.

### 3.2.1 Calculating line positions for pure rotational transitions

We consider first the case of a rigid-rotor diatomic molecule – the selection rules permit only an  $S_0$ -branch ( $\Delta J = +2$ ). The wavenumber shift of a transition from an initial (lower) rotational level  $J'' = J$  to a final (upper) level  $J' = (J + 2)$  is then given by the difference between the  $J^{\text{th}}$  and  $(J + 2)^{\text{th}}$  rotational terms  $\tilde{F}(J)$  and  $\tilde{F}(J + 2)$

$$S_0(J) = \tilde{F}(J + 2) - \tilde{F}(J), \quad (3.8)$$

where  $J = J'' = 0, 1, 2, \dots$ . The case where the upper level is the initial state corresponds to anti-Stokes pure rotational Raman transitions and is not considered further here.

The rotational term for a rigid diatomic molecule is given by the expression

$$\tilde{F}(J) = B_0 J(J + 1), \quad (3.9)$$

where the constant of proportionality is given by

$$B_0 = \frac{h}{8\pi^2 c_0 I_b}, \quad (3.10)$$

and  $I_b$  is the moment of inertia of the molecule about the axis perpendicular to the internuclear axis and passing through the molecule's centre of gravity. The '0' subscript refers to the ground vibrational state.

Substituting for  $\tilde{F}(J)$  and  $\tilde{F}(J+2)$  from equation (3.9) gives

$$S_0(J) = 4B_0(J + \frac{3}{2}). \quad (3.11)$$

In the rigid molecule (first-order) approximation the first rotational line has a wavenumber shift of  $6B$  from the exciting line, and successive rotational lines are equally spaced by increments of  $4B$ . In the case of a non-rigid rotor molecule, centrifugal stretching must be considered. To a second-order approximation, the rotational term is modified with a centrifugal stretching correction proportional to  $J^2(J+1)^2$

$$\tilde{F}(J) = B_0J(J+1) - D_0J^2(J+1)^2 + \dots, \quad (3.12)$$

where  $D_0$  is a small (positive) centrifugal stretching constant. The centrifugal stretching effects are small, but not insignificant – the ratio  $\frac{D_0}{B_0}$  varies between  $\sim 4 \times 10^{-4}$  ( $T_2$ ) and  $\sim 8 \times 10^{-4}$  ( $H_2$ ) for the hydrogen isotopomers. Equation (3.8) can then be re-written by substituting for  $\tilde{F}$  from equation (3.12) to give the wavenumber shift for pure rotational lines taking into account centrifugal stretching

$$S_0(J) = (4B_0 - 6D_0)(J + \frac{3}{2}) - 8D_0(J + \frac{3}{2})^3, \quad (3.13)$$

where  $J = 0, 1, 2, \dots$  as per the selection rule. The net effect of this correction is that the rotational lines no longer have equal interline spacing – the interline spacing decreases with increasing  $J$ .

The series expansion for the rotational term can be carried out in the same manner for higher-order corrections. In this thesis, the positions of the rotational lines were modelled based on a third-order approximation for the rotational term

$$\tilde{F}(J) = B_0J(J+1) - D_0J^2(J+1)^2 + H_0J^3(J+1)^3 - \dots, \quad (3.14)$$

where  $H_0$  is a very small positive correction to the line position – the ratio  $H_0/B_0$  for hydrogen isotopomers varies between  $\sim 6 \times 10^{-8}$  ( $T_2$ ) and  $\sim 9 \times 10^{-7}$  ( $H_2$ ). The expression for the wavenumber shift of the  $S_0$ -branch is then given by

$$S_0(J) = (4B_0 - 6D_0 + \frac{27}{4}H_0)(J + \frac{3}{2}) - (8D_0 - 34H_0)(J + \frac{3}{2})^3 + 12H_0(J + \frac{3}{2})^5. \quad (3.15)$$

### 3.2.2 Line positions for pure rotational transitions

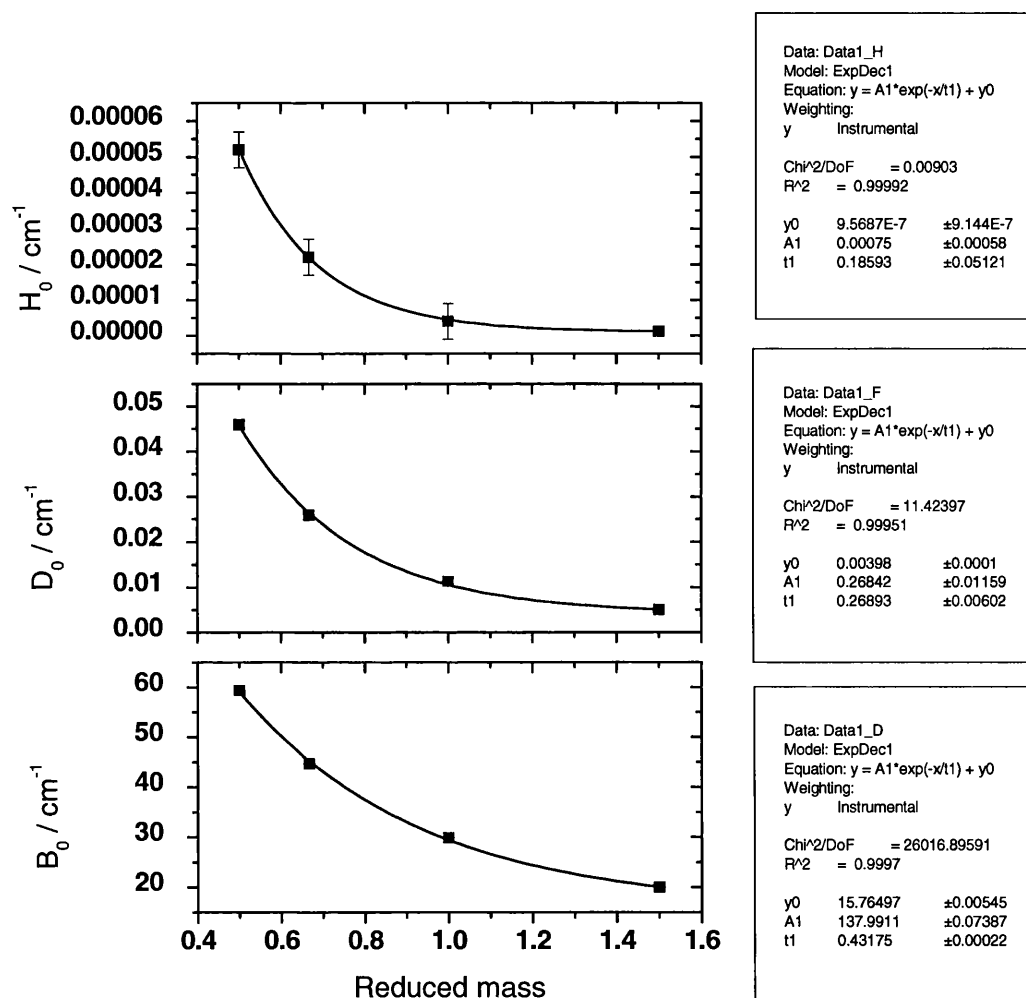
In order to model the line positions for the  $S_0$ -branch lines as wavenumber shifts, the appropriate values for the constants  $B_0$ ,  $D_0$ , and  $H_0$  must be substituted into equation (3.15). The primary reference for these values in this thesis is the article by Edwards et al. (1978). In this paper, the constants for the isotopomers  $H_2$ , HD,  $D_2$ , and  $T_2$  are provided to high accuracy, particularly for  $T_2$ . A summary of the values for the rotational constants for all six hydrogen isotopomers is given in Table 3.2.

**Table 3.2** Values of the rotational constants  $B_0$ ,  $D_0$ , and  $H_0$  used for modelling purposes in this thesis. The values for HT and DT were obtained by interpolation of known values (for  $H_2$ , HD,  $D_2$  and  $T_2$ ) with respect to isotopomer reduced mass.

Isotopomer	$B_0 / \text{cm}^{-1}$	$D_0 / 10^2 \text{cm}^{-1}$	$H_0 / 10^6 \text{cm}^{-1}$	Source
$H_2$	59.339±0.005	4.60±0.03	52±5	Edwards et al. (1978)
HD	44.668±0.005	2.59±0.03	22±5	Edwards et al. (1978)
HT	40.055	2.05	14	Interpolation
$D_2$	29.911±0.005	1.13±0.03	4±5	Edwards et al. (1978)
DT	24.331	0.71	2	Interpolation
$T_2$	20.0386±0.0005	0.499±0.004	1.2±0.8	Edwards et al. (1978)

In order to complete the set of constants, the values for the isotopomers HT and DT were estimated using an interpolation method based on fitting a function to the variation of the rotational constants with respect to the isotopomer reduced mass. The functional dependence was found to resemble a first-order exponential decay by applying a non-linear

curve fit algorithm to the data in the data analysis package *Origin*. The values for HT and DT were then estimated by substituting the reduced masses of these two isotopomers into the fitted equation for the exponential decay. The graphs used to obtain the interpolated estimates are shown in Figure 3.1.



**Figure 3.1** Interpolated estimates of the rotational constants  $B_0$ ,  $D_0$ , and  $H_0$  for the isotopomers HT and DT. The functional dependence of the values from Edwards et al. (1978) on the reduced mass of the isotopomers is a first-order exponential decay.

Although in principle the line positions of an arbitrary range of  $J''$  values could be derived, Raman spectra as measured by the apparatus employed in this thesis are satisfactorily simulated by considering less than the first ten lines of each branch. The *LabVIEW* code is flexible, and it is merely a matter of changing the value of the number of

iterations of the for-loop  $J''$  containing the expressions for the wavenumber shifts (and intensities, q.v.) to extend the simulation over a greater range (note that this would only be important for very high temperatures,  $T \gg 300\text{K}$ ). In the case of the  $S_0$ -branch, we have calculated the range of  $J = J'' = 0 \rightarrow 9$ . The calculated values for the wavenumber shifts for the six isotopomers is summarised in Table 3.3.

**Table 3.3** Raman (wavenumber) shifts for the first ten lines of the Stokes  $S_0$ -branch for the six hydrogen isotopomers.

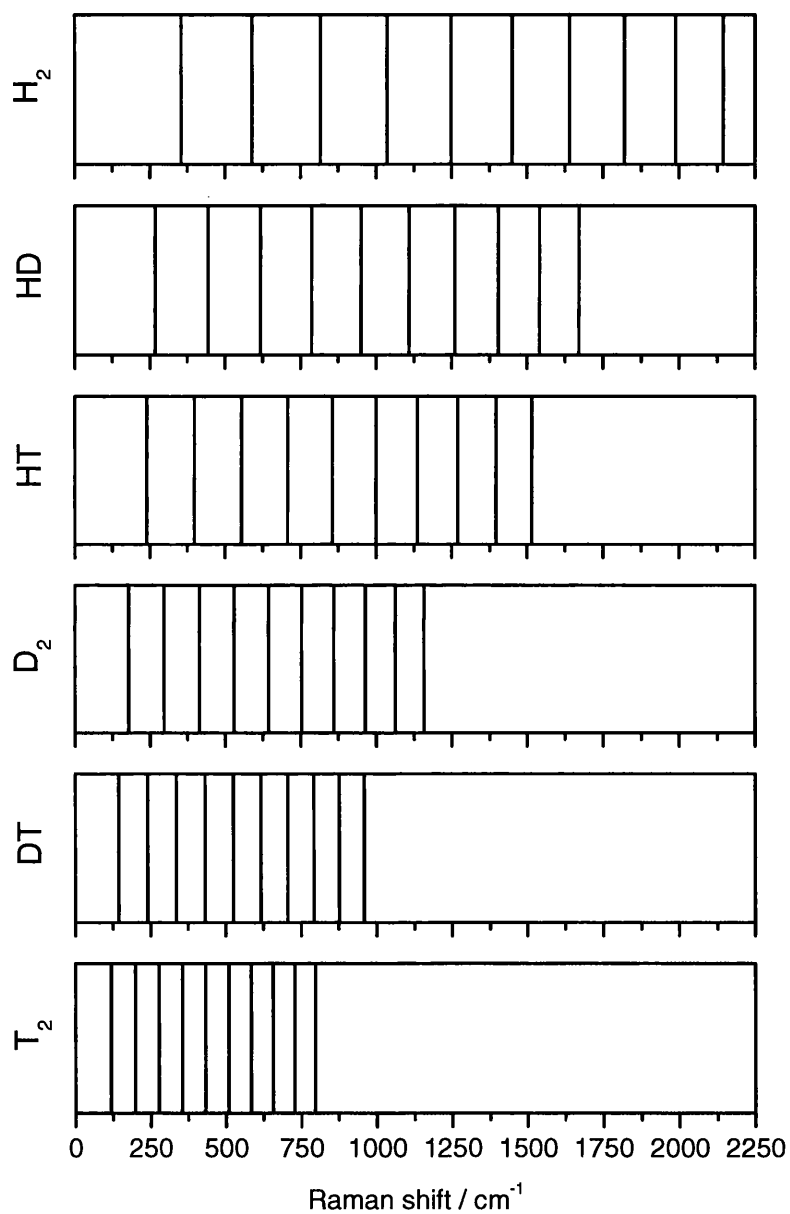
$J''$	Raman shift $S_0(J) / \text{cm}^{-1}$					
	$\text{H}_2$	HD	HT	$\text{D}_2$	DT	$\text{T}_2$
0	354.389	267.080	239.597	179.060	145.732	120.052
1	587.039	443.092	397.708	297.535	242.323	199.689
2	814.407	616.096	553.426	414.672	338.074	278.733
3	1034.640	785.000	705.865	529.956	432.662	356.953
4	1246.151	948.822	854.212	642.893	525.770	434.122
5	1447.686	1106.725	997.744	753.014	617.099	510.024
6	1638.406	1258.044	1135.852	859.881	706.366	584.451
7	1817.958	1402.319	1268.062	963.094	793.306	657.206
8	1986.549	1539.330	1394.051	1062.298	877.680	728.105
9	2145.024	1669.126	1513.672	1157.185	959.274	796.980

Note that although the wavenumber (Raman) shifts relative to the exciting line are quoted here as positive quantities for convenience, it should be borne in mind that these shifts are in fact subtracted from the absolute wavenumber value for the exciting radiation – the Stokes Raman lines are of longer wavelength (lower energy) than the exciting radiation and hence the absolute wavenumber value of the scattered radiation will be lower than that of the incident radiation. The expression for the absolute wavenumber  $\tilde{\nu}_s$  (here the ‘s’-subscript refers to ‘scattered’) of an  $S_0$ -branch line is given by

$$\tilde{\nu}_s = \tilde{\nu}_i - S_0(J), \quad (3.16)$$

where  $\tilde{\nu}_i$  is the absolute wavenumber value of the incident radiation. Figure 3.2 shows graphically the positions of the  $S_0$ -branches for the six isotopomers. Note that the spacing

of the lines is smaller for the heavier isotopomers and that the line spacing decreases with increasing  $J''$ .



**Figure 3.2** Raman line positions for the Stokes  $S_0$ -branches of the six hydrogen isotopomers. Top to bottom:  $H_2$ , HD, HT,  $D_2$ , DT,  $T_2$ . Note the marked narrowing of the line spacing with increasing isotopic mass. The first ten lines of each branch are shown. The values of  $J''$  run from 0 to 9 from left to right.

### 3.2.3 Line positions for vibration-rotation transitions

In the case of vibration-rotation transitions, the additional complication of vibration-rotation interactions arises. To a fair approximation these interactions can be neglected. In the case of a rigid diatomic molecule undergoing the vibrational transition  $(v'' = 0) \rightarrow (v' = 1)$ , the position of S<sub>1</sub>-branch lines ( $\Delta J = +2$ ) is given by

$$S_1(J) = \tilde{G}(v') + \tilde{F}(J+2) - \tilde{G}(v'') - \tilde{F}(J), \quad (3.17)$$

where  $J = J'' = 0, 1, 2, \dots$ . Since we are neglecting vibration-rotation interactions at this stage, we can use equation (3.9) (as this expression for the rotational term is independent of the vibrational state) to substitute for the rotational terms  $\tilde{F}(J)$  and  $\tilde{F}(J+2)$  in equation (3.17). Together with the expression for  $\tilde{G}$  from equation (3.7) this yields

$$S_1(J) = \tilde{\nu}_{\text{vib}} + 4B_0(J + \frac{3}{2}), \quad (3.18)$$

where  $\tilde{\nu}_{\text{vib}}$  is the vibrational band offset. We can repeat the procedure for calculating the positions of the O<sub>1</sub>-branch lines

$$O_1(J) = \tilde{G}(v') + \tilde{F}(J-2) - \tilde{G}(v'') - \tilde{F}(J), \quad (3.19)$$

where  $J = J'' = 2, 3, 4, \dots$ . Substituting from equations (3.7) and (3.9) one obtains

$$O_1(J) = \tilde{\nu}_{\text{vib}} - 4B_0(J - \frac{1}{2}). \quad (3.20)$$

At this level of approximation, the Q<sub>1</sub>-branch is a single line located at the vibrational band offset:

$$Q(J); |\Delta \tilde{\nu}| = \tilde{\nu}_{\text{vib}}. \quad (3.21)$$



Accordingly, for a rigid rotor, the  $O_1$ - and  $S_1$ -branches are a series of equally spaced lines at  $(\pm 0, \pm 4B_0, \pm 10B_0, \pm 14B_0, \dots)$ , commencing at  $\tilde{\nu}_{\text{vib}} \pm 6B_0$ , and the  $Q_1$ -branch has collapsed to be represented by a single line at the position of the vibrational band offset  $\tilde{\nu}_{\text{vib}}$ .

Following the procedure carried out for the pure rotational lines, a better order of approximation can be obtained by considering the effect of centrifugal stretching, i.e. a non-rigid rotor. As for the pure rotational case, the net effect is that the interline spacing decreases for increasing  $J$ . At this higher level of approximation, equations (3.18) and (3.20) become

$$S_1(J) = \tilde{\nu}_{\text{vib}} + (4B_0 - 6D_0)(J + \frac{3}{2}) - 8D_0(J + \frac{3}{2})^3, \quad (3.22)$$

where  $J = J'' = 0, 1, 2, \dots$ , and

$$O_1(J) = \tilde{\nu}_{\text{vib}} - (4B_0 - 6D_0)(J - \frac{1}{2}) + 8D_0(J - \frac{1}{2})^3, \quad (3.23)$$

where  $J = J'' = 2, 3, 4, \dots$ . The  $Q_1$ -branch is still a single line at the vibrational band offset even when centrifugal stretching is taken into account:

$$Q_1(J) = \tilde{\nu}_{\text{vib}}. \quad (3.24)$$

To further improve on this level of approximation, the vibration-rotation interaction has to be taken into account. For this, the vibrational state-independent expression (3.10) has to be modified to take this interaction into account. The relevant term in equation (3.10) is the moment of inertia

$$I_b = \mu r^2, \quad (3.25)$$

where  $\mu$  is the reduced mass of the molecule and  $r$  is the internuclear spacing. In order to correctly account for the vibration-rotation interaction the square of the internuclear spacing  $r^2$  has to be replaced with the mean square value for the vibrational state under

consideration. It is valid to use a mean value for the internuclear spacing since the period of a molecular vibration is small in comparison with that of a rotation. Equation (3.25) becomes

$$I_b = \mu \overline{r^2}_v, \quad (3.26)$$

where  $\overline{r^2}_v$  is the mean value of  $r^2$  for the vibrational state  $v$ . Substituting for  $I_b$  from equation (3.26) into equation (3.10) yields the following expression for the rotational term for the vibrational level  $v$

$$B_v = \frac{h}{8\pi^2 c_0 \mu} \overline{\frac{1}{r^2}}_v. \quad (3.27)$$

A quantum mechanical treatment (not included here) shows that the rotational term  $B_v$  can be expanded around an equilibrium position as

$$B_v = B_e - \alpha_e(v + 1/2) + \dots, \quad (3.28)$$

where  $B_e$  is the equilibrium value. The series can in principle be extended to higher-order terms, but this is rarely necessary. The coefficient  $\alpha_e$  is small in comparison to  $B_e$  and is given by

$$\alpha_e = 24 \frac{B_e^3 r_e^3 g}{\tilde{\nu}_e^3} - 6 \frac{B_e^2}{\tilde{\nu}_e}, \quad (3.29)$$

where  $r_e$  is the equilibrium internuclear spacing,  $\tilde{\nu}_e$  is the harmonic vibration wavenumber and  $g$  a parameter that determines the asymmetry of the molecular potential energy curve.

Taking into account the vibration-rotation interaction we arrive at the following expression for the rotational term for a rigid diatomic molecule;

$$\tilde{F}_v(J) = B_v J(J+1). \quad (3.30)$$

The expressions for the positions of the vibration-rotation branches are then as follows:

$$S_1(J) = \tilde{\nu}_{\text{vib}} + 6B_1 + (5B_1 - B_0)J + (B_1 - B_0)J^2 \quad \text{with } J = J'' = 0, 1, 2, \dots, \quad (3.31)$$

$$O_1(J) = \tilde{\nu}_{\text{vib}} + 2B_1 - (3B_1 + B_0)J + (B_1 - B_0)J^2 \quad \text{with } J = J'' = 2, 3, 4, \dots, \quad (3.32)$$

$$Q_1(J) = \tilde{\nu}_{\text{vib}} + (B_1 - B_0)J + (B_1 - B_0)J^2 \quad \text{with } J = J'' = 0, 1, 2, \dots \quad (3.33)$$

Note that by including the vibration-rotation interaction the  $Q_1$ -branch now consists of a series of lines.

Taking centrifugal distortion into account we can write the rotational term as

$$\tilde{F}_v(J) = B_v J(J+1) - D_v J^2(J+1)^2 + H_v J^3(J+1)^3 + \dots, \quad (3.34)$$

where  $D_v$  and  $H_v$  are the values of the centrifugal stretching constants  $D$  and  $H$  for the vibrational state  $v$ , taking vibration-rotation interaction into account. As for  $B_v$ , expressions for  $D_v$  and  $H_v$  can be derived in terms of their value around an equilibrium internuclear separation, but their form need not concern us here. In most cases, the difference between  $H_v$  and its equilibrium value  $H_e$  is so small that it is reasonable to set  $H_v \approx H_e$ . Furthermore, in the absence of available literature values of  $H_v$  for the hydrogen isotopomers, the value of  $H_v$  has been set to zero, but since  $H_v \ll D_v$ , this is not such an unreasonable approximation – in fact, this third-order correction is well below the resolution of the  $600 \text{ grmm}^{-1}$  grating installed in the HTS spectrometer used for the majority of data acquisition in this thesis.

Setting  $H_v = 0$ , the rotational term for an anharmonic, non-rigid diatomic molecule taking vibration-rotation interaction into account is given by

$$\tilde{F}_v(J) = B_v J(J+1) - D_v J^2(J+1)^2, \quad (3.35)$$

This is the level of approximation employed in the simulations described in this thesis. The positions of the  $S_1$ -branch lines are given by the following expression

$$\begin{aligned} S_1(J) = & \tilde{\nu}_{\text{vib}} + 6B_1 + (5B_1 - B_0)J + (B_1 - B_0)J^2 \\ & - \frac{9}{16}(D_1 - D_0) - \frac{3}{2}(D_1 + D_0)(2J + 3) - \frac{11}{8}(D_1 - D_0)(2J + 3)^2, \\ & - \frac{1}{2}(D_1 + D_0)(2J + 3)^3 - \frac{1}{16}(D_1 - D_0)(2J + 3)^4 \end{aligned} \quad (3.36)$$

where  $J = J'' = 0, 1, 2, \dots$

Similarly for the  $O_1$ -branch:

$$\begin{aligned} O_1(J) = & \tilde{\nu}_{\text{vib}} + 2B_1 - (3B_1 + B_0)J + (B_1 - B_0)J^2 \\ & - \frac{9}{16}(D_1 - D_0) + \frac{3}{2}(D_1 + D_0)(2J - 1) - \frac{11}{2}(D_1 - D_0)(2J - 1)^2, \\ & + \frac{1}{2}(D_1 + D_0)(2J - 1)^3 - \frac{1}{16}(D_1 - D_0)(2J - 1)^4 \end{aligned} \quad (3.37)$$

where  $J = J'' = 2, 3, 4, \dots$

For the  $Q_1$ -branch the line positions are given by

$$Q_1(J) = \tilde{\nu}_{\text{vib}} + (B_1 - B_0)J(J+1) - (D_1 - D_0)J^2(J+1)^2, \quad (3.38)$$

where  $J = J'' = 0, 1, 2, \dots$

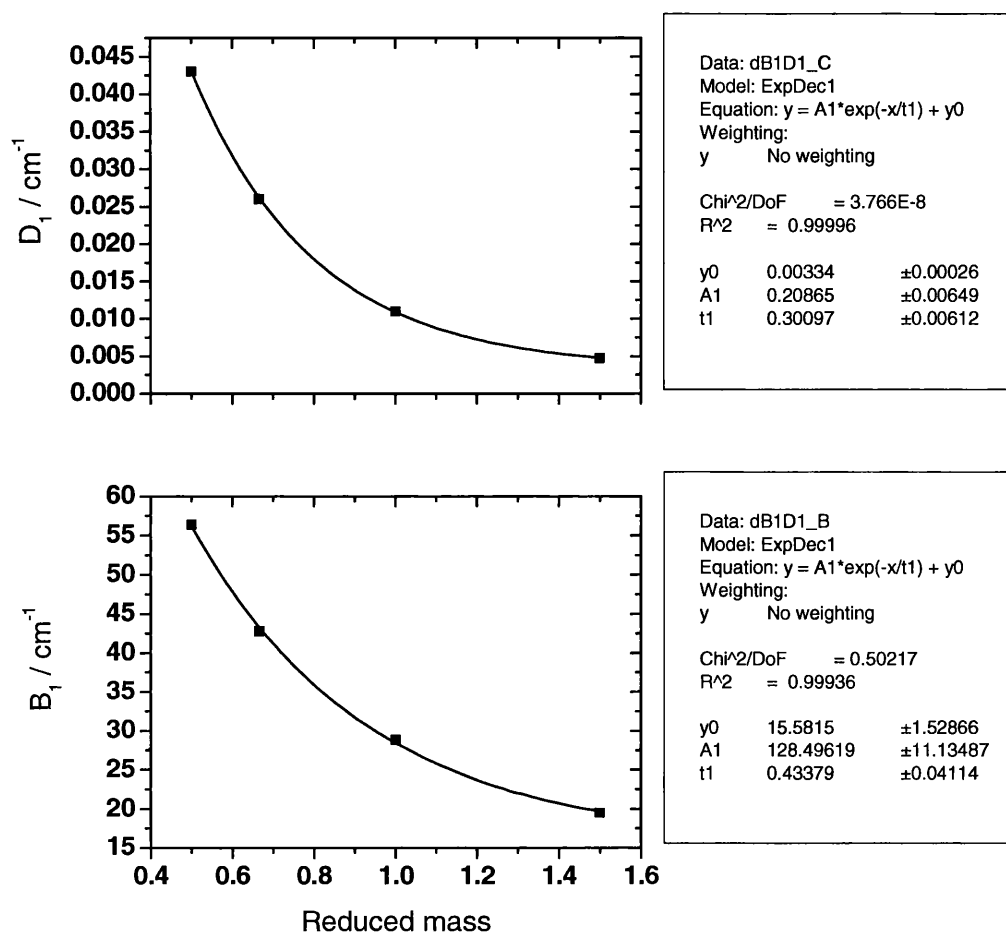
### 3.2.4 Modelling line positions for vibration-rotation transitions

Modelling the positions of the vibration-rotation transition line positions requires the values of the constants  $B_1$  and  $D_1$  in addition to the values of  $B_0$  and  $D_0$  already stated in Table 3.2, together with values for the vibrational band offset  $\tilde{\nu}_{\text{vib}}$ . The source of these constants is again the paper by Edwards et al. (1978). A summary of the values for these constants for all six hydrogen isotopomers is given in Table 3.4.

**Table 3.4** Values of the constants  $\tilde{\nu}_{\text{vib}}$ ,  $B_1$  and  $D_1$ . The values for HT and DT were obtained by interpolation of known values (for H<sub>2</sub>, HD, D<sub>2</sub> and T<sub>2</sub>) with respect to isotopomer reduced mass. No errors were quoted for  $\tilde{\nu}_{\text{vib}}$  except in the case of T<sub>2</sub>.

Isotopomer	$\tilde{\nu}_{\text{vib}} / \text{cm}^{-1}$	$B_1 / \text{cm}^{-1}$	$D_1 / 10^2 \text{cm}^{-1}$	Source
H <sub>2</sub>	4161.14	56.36±0.01	4.3±0.1	Edwards et al. (1978)
HD	3632.05	42.74±0.01	2.6±0.1	Edwards et al. (1978)
HT	3445.68	38.39	2.1	Interpolation
D <sub>2</sub>	2993.56	28.85±0.01	1.1±0.1	Edwards et al. (1978)
DT	2723.46	23.66	0.7	Interpolation
T <sub>2</sub>	2464.324±0.001	19.4530±0.0007	0.470±0.005	Edwards et al. (1978)

As in the case for the ground vibrational state constants, the values of  $B_1$  and  $D_1$  have to be estimated for the isotopomers HT and DT. The same interpolation procedure as used in Section 3.2.2 for the ground vibrational state constants  $B_0$  and  $D_0$  was applied to  $\tilde{\nu}_{\text{vib}}$ ,  $B_1$ , and  $D_1$  as shown in Figure 3.3.



**Figure 3.3** Interpolated estimates of the constants  $\tilde{\nu}_{\text{vib}}$ ,  $B_1$ , and  $D_1$  for the isotopomers HT and DT. The functional dependence of the values from Edwards et al. (1978) with respect to the reduced mass of the isotopomers is a first-order exponential decay.

As previously mentioned, the first ten lines of each branch are used in the *SpecGen* simulation. This corresponds to a range of  $J = J'' = 0 \rightarrow 9$  for the  $S_1$ - and  $Q_1$ -branches, and  $J = J'' = 2 \rightarrow 11$  for the  $O_1$ -branch. Tables 3.5, 3.6, and 3.7 list the first ten wavenumber shifts for the six isotopomers for the  $S_1$ -,  $Q_1$ , and  $O_1$ -branches, respectively.

**Table 3.5** Raman (wavenumber) shifts for the first ten lines of the Stokes  $S_1$ -branch for the six hydrogen isotopomers.

	Raman shift $S_1(J) / \text{cm}^{-1}$					
$J''$	H <sub>2</sub>	HD	HT	D <sub>2</sub>	DT	T <sub>2</sub>
0	4497.752	3887.554	3675.264	3166.264	2865.168	2580.873
1	4712.774	4051.954	3823.308	3278.399	2957.738	2657.026
2	4916.762	4209.374	3965.486	3387.101	3048.129	2731.452
3	5107.796	4358.564	4100.768	3491.855	3136.007	2803.939
4	5284.028	4498.266	4228.106	3592.156	3221.043	2874.283
5	5443.682	4627.224	4346.445	3687.504	3302.907	2942.286
6	5585.054	4744.178	4454.715	3777.407	3381.274	3007.756
7	5706.512	4847.864	4551.833	3861.381	3455.817	3070.511
8	5806.496	4937.020	4636.705	3938.947	3526.215	3130.373
9	5883.518	5010.376	4708.225	4009.636	3592.145	3187.172

**Table 3.6** Raman (wavenumber) shifts for the first ten lines of the Stokes  $Q_1$ -branch for the six hydrogen isotopomers.

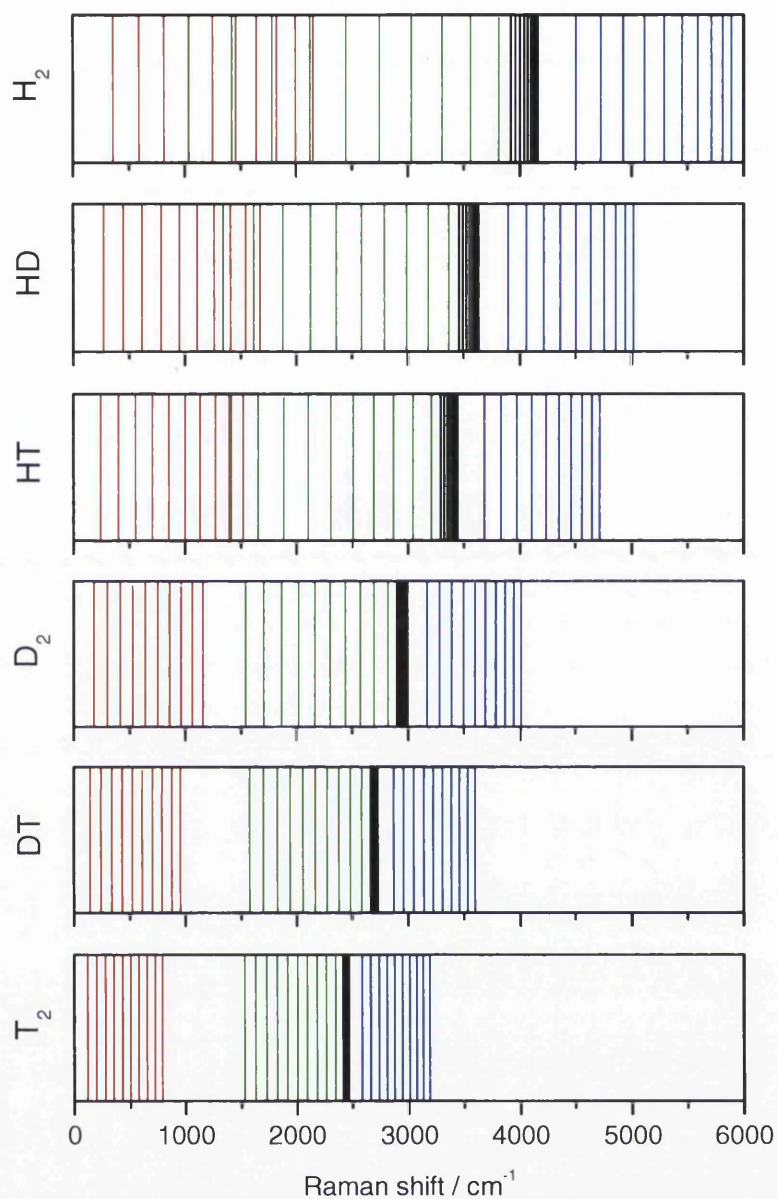
	Raman shift $Q_1(J) / \text{cm}^{-1}$					
$J''$	H <sub>2</sub>	HD	HT	D <sub>2</sub>	DT	T <sub>2</sub>
0	4161.140	3632.050	3445.680	2993.560	2723.460	2464.324
1	4155.194	3628.194	3442.348	2991.439	2722.118	2463.154
2	4143.374	3620.478	3435.670	2987.205	2719.437	2460.821
3	4125.824	3608.900	3425.624	2980.871	2715.419	2457.339
4	4102.760	3593.450	3412.170	2972.46	2710.071	2452.728
5	4074.470	3574.120	3395.261	2962.000	2703.399	2447.017
6	4041.314	3550.898	3374.835	2949.527	2695.414	2440.240
7	4003.724	3523.768	3350.817	2935.085	2686.125	2432.440
8	3962.204	3492.716	3323.121	2918.723	2675.547	2423.664
9	3917.330	3457.720	3291.649	2900.500	2663.693	2413.969

**Table 3.7** Raman (wavenumber) shifts for the first ten lines of the Stokes  $O_1$ -branch for the six hydrogen isotopomers.

$J''$	Raman shift $O_1(J) / \text{cm}^{-1}$					
	$\text{H}_2$	HD	HT	$\text{D}_2$	DT	$\text{T}_2$
2	3803.669	3363.102	3204.574	2813.709	2577.225	2343.934
3	3556.093	3177.863	3038.803	2690.820	2477.836	2262.140
4	3297.582	2985.642	2867.150	2564.507	2376.270	2178.628
5	3026.216	2785.186	2688.582	2434.257	2272.195	2093.187
6	2740.147	2575.240	2502.055	2299.564	2165.279	2005.613
7	2437.599	2354.546	2306.512	2159.927	2055.195	1915.706
8	2116.868	2121.845	2100.882	2014.856	1941.615	1823.278
9	1776.322	1875.873	1884.083	1863.864	1824.215	1728.142
10	1414.401	1615.367	1655.022	1706.476	1702.672	1630.124
11	1029.617	1339.058	1412.591	1542.220	1576.663	1529.053

Together with the wavenumber shifts for the  $S_0$ -branch, we now have a complete set of the first ten Stokes Raman lines for the region of interest for this thesis. The complete spectra for the six isotopomers are shown below in Figure 3.4.





**Figure 3.4** Raman line positions for the Stokes  $S_0$ -,  $S_1$ -,  $Q_1$ -, and  $S_1$ -branches of the six hydrogen isotopomers. Top to bottom:  $H_2$ ,  $HD$ ,  $HT$ ,  $D_2$ ,  $DT$ ,  $T_2$ . Note the marked narrowing of the line spacing with increasing isotopic mass. The first ten lines of each branch are shown. The value of  $J''$  runs from 0 to 9 from left to right for the  $S_0$ - (red) and  $S_1$ -branches (blue), and from right to left for the  $Q_1$ -branches (black). In the case of the  $O_1$ -branches (green), the value of  $J''$  runs from 2 to 11 from right to left.

### 3.2.5 *The effect of the refractive index of air on Raman line positions*

When using Raman shift values to determine the absolute wavenumber (or wavelength) of a specified Raman transition, given the absolute wavenumber (or wavelength) of the excitation radiation, one has to take into account the medium in which the scattered light is observed. The Raman shifts calculated in the preceding sections are valid for an isolated molecule in vacuum, but when the observation apparatus are in a different medium (usually air), the effect of the refractive index of the medium on the value of the wavenumber / wavelength of the scattered light must be taken into account.

Since all measurements in this thesis were performed with the measurement apparatus in air, we can focus our attention on conversion between values measured in vacuum and those in air. The two sets of values are related to each other by the expression

$$\lambda_{\text{vac}} = \eta_{\text{air}} \lambda_{\text{meas}} = \frac{1}{\tilde{\nu}_{\text{vac}}} = \frac{\eta_{\text{air}}}{\tilde{\nu}_{\text{meas}}}, \quad (3.39)$$

where  $\lambda_{\text{vac}}$  and  $\tilde{\nu}_{\text{vac}}$  are the wavelength and absolute wavenumber measured in vacuum,  $\lambda_{\text{meas}}$  and  $\tilde{\nu}_{\text{meas}}$  are the wavelength and absolute wavenumber measured in air, and  $\eta_{\text{air}}$  is the refractive index of air. Note that it is only the refractive index of the medium in which the observing apparatus (i.e. detector) are located that is of importance. Intervening media (such as the glass windows of a gas cell) are of no importance to this calculation.

In order to determine the refractive index of air, it is necessary to use Edlén's formula. This has been developed significantly since Edlén's original formulation and has been heavily modified over the years. A 1998 paper in *Metrologia* by Bönsch and Potulski provides a useful form of Edlén's formula that can be used to calculate the value of the refractive index of standard dry air<sup>†</sup> for a given wavelength:

---

<sup>†</sup> Standard dry air is defined in Bönsch and Potulski (1998) as: temperature = 20°C, pressure = 1000mbar, CO<sub>2</sub> content = 400ppm, and zero humidity.

$$(\eta_N - 1) \cdot 10^8 = 8091.37 + \frac{2\,333\,983}{\left\{130 - \left(10^{-3}/\lambda_{\text{meas}}\right)^2\right\}} + \frac{15\,518}{\left\{38.9 - \left(10^{-3}/\lambda_{\text{meas}}\right)^2\right\}}, \quad (3.40.a)$$

where  $\eta_N$  is the refractive index of standard dry air, and  $\lambda_{\text{meas}}$  is the wavelength of the radiation measured in air in units of nanometres. The equivalent wavenumber form of equation (3.40.a) is given by

$$(\eta_N - 1) \cdot 10^8 = 8091.37 + \frac{2\,333\,983}{\{130 - (10^4 \tilde{\nu}_{\text{meas}})^2\}} + \frac{15\,518}{\{38.9 - (10^4 \tilde{\nu}_{\text{meas}})^2\}}, \quad (3.40.b)$$

where  $\tilde{\nu}_{\text{meas}}$  is the absolute wavenumber (not wavenumber shift) of the radiation measured in air in units of reciprocal centimetres. Once  $\eta_{\text{air}}$  has been calculated, one can use equation (3.39) to convert between vacuum and air values for a given Raman transition. Note that if the value of the wavelength / wavenumber of the exciting radiation is measured in air, then equation (3.39) should be used to convert the measured (air) value to its vacuum value in order to correctly calculate the (vacuum) wavelength of the Raman scattered light. These values then need to be converted back to air values in order to correctly correlate the transitions with lines in measured spectra.

If high precision is required, then a modified form of equation (3.40) should be used to apply a correction to the standard values, in order to take into account variations in the value of the refractive index of the air, caused by variations in temperature, pressure, humidity, and / or CO<sub>2</sub> content. This modified equation is given by Bönsch and Potulski (1998) as:

$$\eta_{tpf} - \eta_p = -(f) \cdot \left\{ 3.8020 - 0.0384 \left( 10^{-3} / \lambda_{\text{meas}} \right)^2 \right\} \cdot 10^{-10}, \quad (3.41)$$

where  $\eta_{tpf}$  is the refractive index of air with temperature, pressure, humidity, and CO<sub>2</sub> content parameters  $t$ ,  $p$ ,  $f$ , and  $x$ , respectively. The parameter  $t$  is the deviation (in °C) from the standard dry air temperature of 20°C,  $p$  is the deviation in pressure (in mbar) from the

standard pressure of 1000mbar, and  $f$  is the partial pressure of the water vapour (in mbar). The  $x$  parameter is contained in the expression for  $\eta_p$ .

The refractive index  $\eta_p$  is for dry ( $f=0$ ) air with temperature, pressure and CO<sub>2</sub> content parameters ( $t$ ,  $p$ , and  $x$ ), is given by

$$\eta_p - 1 = \frac{(\eta_x - 1) \cdot p}{93214.60} \cdot \frac{\{1 + 10^{-8} \cdot (0.5953 - 0.009876tp)\}}{(1 + 0.0036610)t}, \quad (3.42)$$

where  $\eta_x$  is the refractive index of dry air at standard pressure and temperature, but with a deviation  $x$  (in ppm) from the standard CO<sub>2</sub> content of 400ppm and is given by

$$(\eta_x - 1) = (\eta_N - 1) \cdot \{1 + 0.5327 \cdot (x - 0.0004)\}. \quad (3.43)$$

Equations (3.40) to (3.43) can be used to calculate the effect on the refractive index of air with respect to changes in the parameters  $t$ ,  $p$ ,  $f$ , and  $x$ . A summary of all effects is provided in Table 3.8.

**Table 3.8** Effect of changes in temperature, pressure, humidity and CO<sub>2</sub> content on the value of the refractive index of air,  $\eta_{air}$ , with respect to the refractive index of standard dry air,  $\eta_N$ .

Parameter	Change in parameter with respect to standard dry air	Change in refractive index, $\eta_{air}$ , with respect to $\eta_N$
Temperature, $t$	$\pm 1$ °C	$\mp 9.26 \times 10^{-7}$
Pressure, $p$	$\pm 1$ mbar	$\pm 2.68 \times 10^{-7}$
Water vapour partial pressure, $f$	$\pm 1$ mbar	$\mp 2.73 \times 10^{-8}$
CO <sub>2</sub> content, $x$	$\pm 100$ ppm	$\pm 1.47 \times 10^{-8}$

Most Raman spectra in this thesis were measured using the PIActon HTS / Spec-10 spectrometer / CCD detector system. A reasonable estimate of the system accuracy is half a pixel of the CCD array, which corresponds to an uncertainty of about  $\pm 1 \text{cm}^{-1}$  at 632nm ( $\sim 15823 \text{cm}^{-1}$ ). Within the region of interest (i.e. between 532nm and 800nm), this

corresponds to an error of the order  $10^{-5}$  in the measurement of absolute wavenumber or wavelength positions. Recalling equation (3.39), one can show that in order for changes in  $t$ ,  $p$ ,  $f$ , or  $x$  to be comparable to system accuracy, the values of  $t$ ,  $p$ ,  $f$ , and  $x$ , would have to be of the order of  $10^\circ\text{C}$ ,  $1000\text{mbar}$ ,  $1000\text{mbar}$ , and  $100,000\text{ppm}$ , respectively. Since deviations of this order were not realised in practice during the course of this thesis, the variations in the value of  $\eta_{air}$  due to deviations from standard dry air parameters can be safely neglected – it is sufficient to perform conversion between vacuum and air values for line positions using the standard dry air parameters.

### 3.3 Stokes Raman Line Intensities

The intensity,  $I(\theta; p^s, p^i)$ , (units:  $\text{Wsr}^{-1}$ ) of scattered radiation, due to a rotational or vibration-rotation transition from a population of diatomic molecules in thermal equilibrium subject to an exciting irradiance,  $\mathcal{J}$ , (units:  $\text{Wm}^{-2}$ ) is given by the following expression (see Long (2002))<sup>‡</sup>:

$$I(\theta; p^s, p^i) = k_{\tilde{\nu}}(\tilde{\nu}_s)^4 N_i \Phi(a^2, \gamma^2, \theta) \mathcal{J}, \quad (3.44)$$

where the parameters  $\theta$ ,  $p^s$ , and  $p^i$  refer to the observation angle relative to the incident radiation, the polarisation of the scattered light and the polarisation of the incident light, respectively,  $k_{\tilde{\nu}}$  is a constant defined by equation (3.45),  $\tilde{\nu}_s$  is the wavenumber of the scattered radiation,  $N_i$  is the number of molecules populating the initial state (thus the form of  $N_i$  depends on the transition involved),  $\Phi(a^2, \gamma^2, \theta)$  is a line strength function parameterised by the squares of transition polarisability tensor components and the collection geometry, and  $\mathcal{J}$  is the irradiance.

Note that although this expression can give the absolute intensity of a Raman line, the immediate practical application in this thesis is rather to obtain correct *relative* intensities between branches and between lines in the same branch. Therefore, although the treatment

---

<sup>‡</sup> This expression is only valid provided the transition polarisability tensor is symmetric.

given below could be used to calculate absolute intensities, a series of simplifications at the end of the treatment allow the calculation of relative intensities in the absence of literature values for the transition polarisability tensor components. Each of the terms in equation (3.44) is now considered separately.

### 3.3.1 *The constant $k_{\nu}$*

The constant  $k_{\nu}$  is related to the permittivity of vacuum,  $\epsilon_0$ , by the expression:

$$k_{\nu} = \frac{\pi^2}{\epsilon_0^2} \approx 1.259 \times 10^{23} \text{ F}^{-2} \text{ m}^2. \quad (3.45)$$

### 3.3.2 *The fourth power of the absolute wavenumber $(\tilde{\nu}_s)^4$*

The term  $(\tilde{\nu}_s)^4$  is the fourth power of the absolute wavenumber of the scattered radiation, where  $\tilde{\nu}_s$  is expressed in reciprocal meters as opposed to the more usual reciprocal centimetres. This is merely the familiar reciprocal fourth power dependence of light scattering on wavelength expressed in wavenumbers.

Since this term is a function of an absolute wavenumber value, it is therefore a function of the incident radiation wavenumber value. In practice, the wavelength (hence absolute wavenumber) of the incident radiation is measured in air with a wavemeter. It is therefore necessary to use equation (3.39) to convert this value into a vacuum value. Once this has been done one can subtract the relevant Raman shift and correctly evaluate  $(\tilde{\nu}_s)^4$ .

### 3.3.3 The population factor $N_i$

The number of molecules in the initial state,  $N_i$ , is given by the expression:

$$N_i = \frac{Ng_i \exp\{-E_i/kT\}}{Q}, \quad (3.46)$$

where  $N$  is the total number of molecules irradiated,  $g_i$  is the statistical weight of the initial state,  $E_i$  is the energy of the initial state,  $k$  is the Boltzmann constant,  $T$  is the temperature of the molecules, and  $Q$  is the molecular partition function defined as:

$$Q = \sum_j g_j \exp\{-E_j/kT\}. \quad (3.47)$$

To a very good approximation, the partition function can be regarded as a product of independent electronic ( $Q_e$ ), vibrational ( $Q_v$ ), and rotational ( $Q_R$ ) partition functions, i.e.

$$Q = Q_e Q_v Q_R. \quad (3.48)$$

The form of the electronic partition function is given in terms of the electronic energy term  $\tilde{T}_e$  as:

$$Q_e = \sum_j g_{e_j} \exp\{-\tilde{T}_{e_j} hc_0/kT\}, \quad (3.49)$$

where the product of the Planck constant,  $h$ , and the speed of light in vacuum,  $c_0$ , have been introduced to maintain dimensionality – note that the term  $\tilde{T}_{e_j}$  has to be converted into reciprocal meters. The summation is over all electronic energy levels ( $j = n$ ), but as mentioned in Section 3.2, the Raman transitions under consideration are within the same energy level. Therefore, as in equation (3.3), we can set  $\tilde{T}_{e_j} = \tilde{T}'_e = \tilde{T}''_e = 0$ , and so  $Q_e = 1$ .

The form of the vibrational partition function is given in terms of the vibrational energy term  $\tilde{G}$  (remembering to convert  $\tilde{G}$  into reciprocal metres) as

$$Q_v = \sum_j g_{v_j} \exp\{-\tilde{G}_j hc_0 / kT\}. \quad (3.50)$$

According to Long (2002), it is usually satisfactory to assume that the simple (mechanical) harmonic approximation applies. For a diatomic molecule with vibrational wavenumber,  $\tilde{\nu}$ <sup>§</sup>, we can then write

$$\tilde{G}(v) = (v + \frac{1}{2})\tilde{\nu}, \quad (3.51)$$

where  $v = 0, 1, 2, \dots$ . If we elect to measure energies from the zero-point energy level then this can be simplified to

$$\tilde{G}_0(v) = \tilde{G}(v) - \tilde{G}(0) = (v + \frac{1}{2})\tilde{\nu} - \frac{1}{2}\tilde{\nu} = v\tilde{\nu}. \quad (3.52)$$

Assuming non-degenerate vibrational energy levels (i.e. setting  $g_{v_j} = 1$ ) and substituting  $\tilde{G}_0(v)$  for  $\tilde{G}(v)$  from equation (3.52) into equation (3.51) yields

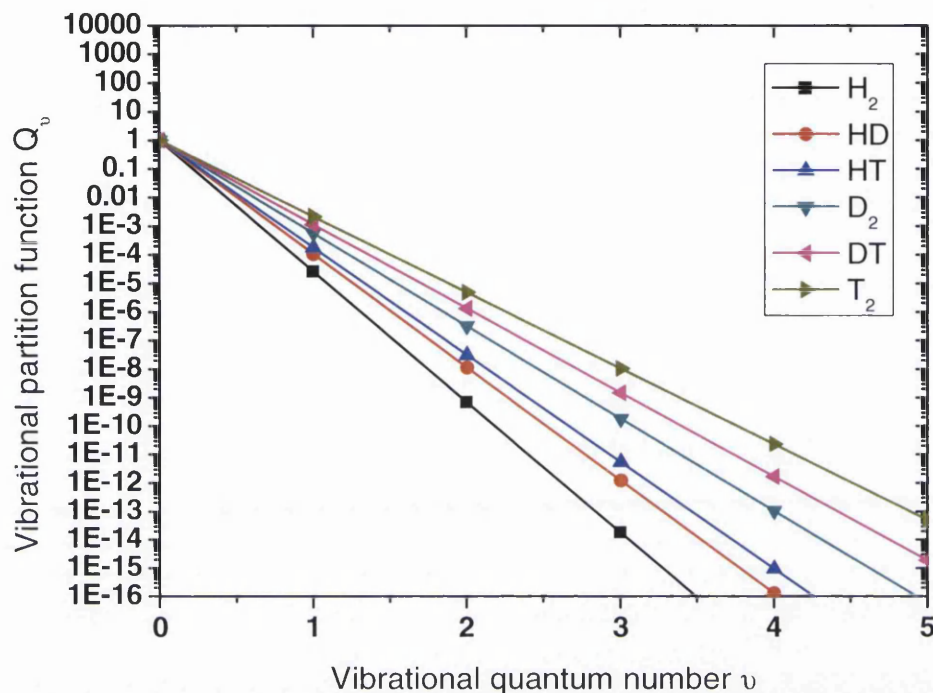
$$Q_v = \sum_v \exp\left\{\frac{-hc_0}{kT}(v\tilde{\nu})\right\}. \quad (3.53)$$

Provided that  $\tilde{\nu}$  is large enough, the terms in this summation with  $v > 0$  can be neglected and so we can set  $Q_v = 1$ . This is generally a good approximation, which greatly simplifies intensity calculations. In the specific case of the hydrogen isotopomers, the ratio  $\frac{Q_0}{Q_1}$  varies from  $\sim 10^{-3}$  ( $T_2$ ) to  $\sim 10^{-5}$  ( $H_2$ ), so this is a valid approximation to make in our specific case, as Figure 3.5 demonstrates (for  $T = 300K$ ).

---

<sup>§</sup> In older references, the vibrational wavenumber is often written ' $\omega_e$ ', with the second-order term written ' $\omega_e x_e$ '. The expansion of the vibrational energy term is given by:  $G(v) = \omega_e(v + \frac{1}{2}) - \omega_e x_e(v + \frac{1}{2})^2 + \dots$





**Figure 3.5** The dependence of the vibrational partition function  $Q_\nu$  on the vibrational quantum number  $\nu$  for the hydrogen isotopomers in the simple harmonic approximation, with  $T = 300\text{K}$ . One can clearly see the strong exponential suppression with increasing  $\nu$ . The values of  $\tilde{\nu}$  were obtained from Herzberg (1950).

The important (i.e. not equal to 1) term in the partition function is then the rotational term, parameterised by the rotational energy term  $\tilde{F}$  (in reciprocal metres)

$$Q_R = \sum_j g_{R_j} \exp\{-\tilde{F}_j hc_0 / kT\}. \quad (3.54)$$

In the specific case of a diatomic molecule (treated as a rigid rotor) this is given by

$$Q_R = \sum_J g_J (2J + 1) \exp\{-\tilde{F}(J) hc_0 / kT\}, \quad (3.55)$$

where the product  $g_J (2J + 1)$  is the statistical weight of the  $J^{\text{th}}$  rotational energy level, and  $g_J$  specifically is the statistical weight due to the effects of nuclear spin statistics on the

relative populations of even and odd rotational levels in the case of homonuclear molecules (q.v.)

Having set  $Q_v = Q_e = 1$ , and assuming all transitions are from the ground electronic and vibrational states, we can substitute from equation (3.55) into equation (3.46) to obtain the formula for the population of the  $J^{\text{th}}$  rotational energy level of a diatomic molecule

$$N_i = \frac{Ng_J(2J+1)\exp\{-\tilde{F}(J)hc_0/kT\}}{\sum_J g_J(2J+1)\exp\{-\tilde{F}(J)hc_0/kT\}}. \quad (3.56)$$

The simplest case of equation (3.56) is that of a heteronuclear diatomic molecule (which is the case for HD, HT, and DT) for which  $g_N = 1$  for all levels

$$N_i = \frac{N(2J+1)\exp\{-\tilde{F}(J)hc_0/kT\}}{\sum_J (2J+1)\exp\{-\tilde{F}(J)hc_0/kT\}}. \quad (3.57)$$

In the *SpecGen* code, the temperature of the gas is a user-definable parameter, and  $\tilde{F}$  is calculated (in reciprocal centimetres) in a dedicated subVI<sup>\*\*</sup>. It is therefore convenient to re-write equation (3.57) in a way that  $\tilde{F}$  can be substituted without unit conversion, thus leaving  $T$  as a free parameter. Equation (3.57) then simplifies to

$$N_i = \frac{N(2J+1)\exp\{-\tilde{F}(J)/\eta T\}}{\sum_J (2J+1)\exp\{-\tilde{F}(J)/\eta T\}}, \quad (3.58)$$

where  $\eta = 0.695\,038\,862$ , and the units of  $\tilde{F}$  and  $T$  are  $\text{cm}^{-1}$  and K, respectively.

In the case of the homonuclear isotopomers  $\text{H}_2$ ,  $\text{D}_2$ , and  $\text{T}_2$ , the statistical weight due to the nuclear spin degeneracy takes different values for odd and even values of  $J$ . The theory

---

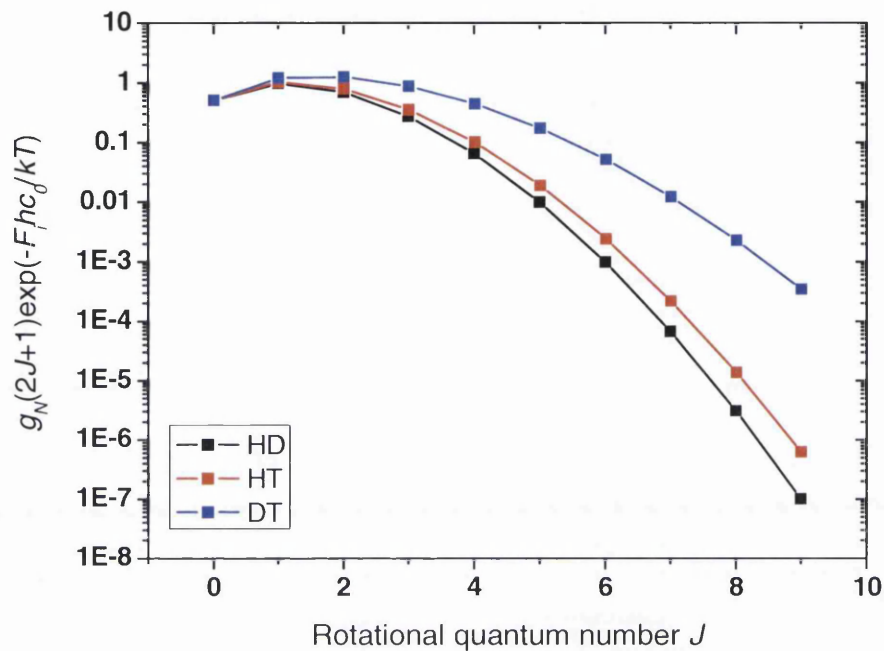
<sup>\*\*</sup> A 'VI' or 'Virtual Instrument' is a section of code in the *LabVIEW* graphical programming environment. A 'subVI' is the equivalent of a subroutine in a line-based programming language, but whose definition is a VI that is used in another VI. A subVI appears on the block diagram (code) as an icon with user specified connectors for inputs and outputs.

of the nuclear spin statistics is beyond the scope of this chapter – the reader is referred to Herzberg (1950). Here it is sufficient to know the values that  $g_N$  takes for each isotopomer, which are summarised in Table 3.9.

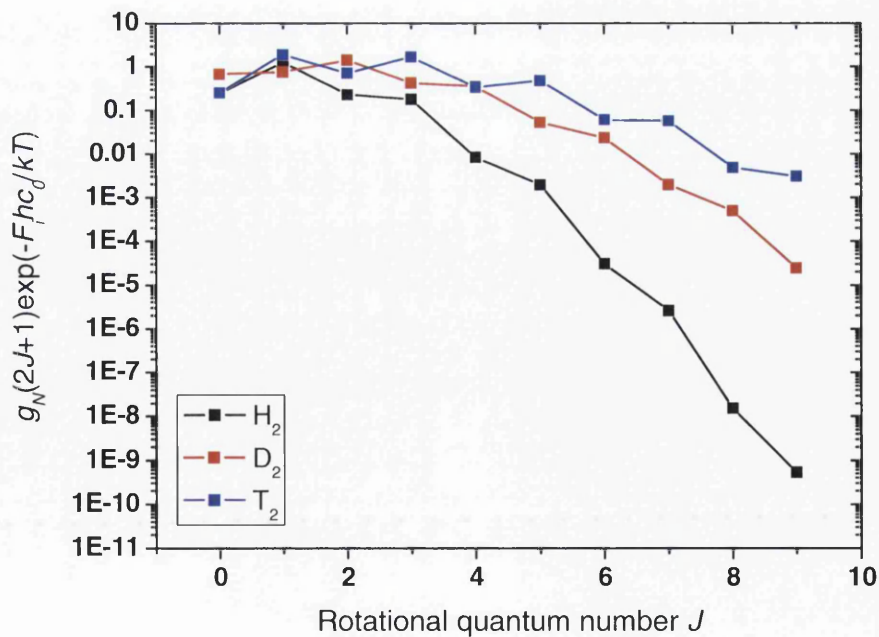
**Table 3.9** Nuclear spin statistics and relative intensities of rotational Raman lines for the homonuclear hydrogen isotopomers H<sub>2</sub>, D<sub>2</sub>, and T<sub>2</sub>. Adapted from Long (2002).

Species		H <sub>2</sub> , T <sub>2</sub>	D <sub>2</sub>
Total nuclear spin, $I$		$\frac{1}{2}$	1
Nuclear spin degeneracy, $T = 2I + 1$		2	3
Statistics		Fermi	Bose
Ground electronic state		$\Sigma_g^+$	$\Sigma_g^+$
Nuclear spin statistical weight, $g_N$	$J$ odd	3	3
	$J$ even	1	6
Relative intensities of Raman lines	$J$ odd	3	1
	$J$ even	1	2

The parameter  $g_N(2J+1)\exp\{-\tilde{F}_i hc_0/kT\}$  has the greatest influence on the shape of the intensity distribution over a Raman branch since it has the strongest dependence on  $J$ . As will be seen in the next section, the Placzek-Teller  $b$ -factors included in the line strength function  $\Phi(a^2, \gamma^2, \theta)$  are relatively insensitive to the value of  $J$ . Figures 3.6 and 3.7 shows the variation of the parameter  $g_N(2J+1)\exp\{-\tilde{F}_i hc_0/kT\}$  for the six hydrogen isotopomers at  $T = 300\text{K}$ . Note the initial increase of this function with respect to  $J$ , the strong suppression due to the exponential term, and the 3/1 (H<sub>2</sub>, T<sub>2</sub>) or 1/2 (D<sub>2</sub>) alternation of the homonuclear isotopomer odd / even line populations.



**Figure 3.6** Variation of the parameter  $g_N(2J+1)\exp\{-\tilde{F}_i hc_0/kT\}$  with respect to the rotational quantum number  $J$  for the heteronuclear hydrogen isotopomers, with  $T = 300\text{K}$ .



**Figure 3.7** Variation of the parameter  $g_N(2J+1)\exp\{-\tilde{F}_i hc_0/kT\}$  with respect to the rotational quantum number  $J$  for the homonuclear hydrogen isotopomers, with  $T = 300\text{K}$ .

It is worth re-iterating that we are only considering transitions from the ground vibrational state within the same electronic state. At  $T = 300\text{K}$  (the temperature at which most experiments in this thesis were performed), the ratio of the population of the first to zeroth vibrational level is of the order  $10^{-9}$ . The contributions from higher vibrational states can therefore be safely neglected.

### 3.3.4 The line strength function $\Phi(a^2, \gamma^2, \theta)$

The line strength function  $\Phi(a^2, \gamma^2, \theta)$  is given by the appropriate isotropic averages of squares of the transition polarisability tensor components with  $\Lambda = 0$  and  $S = 0$  for both rotational and vibration-rotation transitions. Although the dependence of  $\Phi(a^2, \gamma^2, \theta)$  on  $J$  is less sensitive to the value of  $J$  than the population parameter  $g_N(2J+1)\exp\{-\tilde{F}_i hc_0 / kT\}$ , the line strength function dictates the relative intensities of the Raman branches with respect to each other.

In order to correctly evaluate  $\Phi(a^2, \gamma^2, \theta)$ , the appropriate component(s) of the transition polarisability tensor must be selected, given a particular polarisation regime and collection geometry. The experiments performed during the course of this work have exclusively utilised a  $90^\circ$  collection geometry. In the case of incident radiation linearly polarised along the y-axis (recall Figure 2.1 from Chapter 2), there are two important regimes, which for brevity we shall label using the intensity symbol introduced in equation (3.44). These are:

$$I(\pi/2; \perp^s, \perp^i) \quad \Phi(a^2, \gamma^2, \theta) = \langle (\alpha_{yy})_{fi}^2 \rangle, \quad (3.59)$$

and

$$I(\pi/2; \parallel^s, \perp^i) \quad \Phi(a^2, \gamma^2, \theta) = \langle (\alpha_{xy})_{fi}^2 \rangle. \quad (3.60)$$

The reader is referred to Long (2002) for the derivation of the following formulae that relate the values of the isotropic averages  $\langle (\alpha_{yy})_{fi}^2 \rangle$  and  $\langle (\alpha_{xy})_{fi}^2 \rangle$  to the Placzek invariants  $(\mathcal{G}^{(0)})_{fi}$  and  $(\mathcal{G}^{(2)})_{fi}$ :

$$\langle (\alpha_{yy})_{fi}^2 \rangle = \frac{1}{(2J^i + 1)} \left\{ \frac{1}{3} (\mathcal{G}^{(0)})_{fi} + \frac{2}{15} (\mathcal{G}^{(2)})_{fi} \right\}, \quad (3.61)$$

and

$$\langle (\alpha_{xy})_{fi}^2 \rangle = \frac{1}{(2J^i + 1)} \left\{ \frac{1}{10} (\mathcal{G}^{(2)})_{fi} \right\}, \quad (3.62)$$

where  $J^i$  is the initial rotational level. Note the use of the labels  $i$  and  $f$ , since equations (3.61) and (3.62) are general cases between initial and final states. The values of the invariants are given by

$$(\mathcal{G}^{(0)})_{v^f J^f : v^i J^i} = (2J^i + 1) \left| \langle v^f | \alpha_0^{(0)} | v^i \rangle \right|^2, \quad (3.63)$$

and

$$(\mathcal{G}^{(2)})_{v^f J^f : v^i J^i} = (2J^i + 1) b_{J^f, J^i}^{(2)} \left| \langle v^f | \alpha_0^{(2)} | v^i \rangle \right|^2, \quad (3.64)$$

where  $|v^i\rangle$  and  $\langle v^f|$  are the initial and final state wave functions, respectively. They have been written with the vibrational quantum number to show that the transition in question may or may not include a change of vibrational state. Placzek-Teller  $b$ -factors,  $b_{J^f, J^i}^{(2)}$ , are functions of  $J$  and vary in form between branches ( $J^f = J^i \pm 0, 2$ ). For the  $Q_1$ -branch  $b_{J^f, J^i}^{(2)}$  is given by

$$b_{J, J}^{(2)} = \frac{J(J+1)}{(2J-1)(2J+3)}, \quad (3.65)$$

and similarly for the  $S_0$ - and  $S_1$ -branches:

$$b_{J+2, J}^{(2)} = \frac{3(J+1)(J+2)}{2(2J+1)(2J+3)}, \quad (3.66)$$

and finally for the  $O_1$ -branch:

$$b_{J-2,J}^{(2)} = \frac{3J(J-1)}{2(2J-1)(2J+1)}, \quad (3.67)$$

where, as standardised throughout this work,  $J = J^i = J''$ . Note that although these are given in relation to specific cases, these factors hold in general – which is why the  $S_0$ - and  $S_1$ -branches share the same factor.

It is more usual to express equations (3.63) and (3.64) in terms of the tensor invariants  $a$  and  $\gamma$ , where  $|\alpha_0^{(0)}| = 3a$  and  $|\alpha_0^{(2)}| = \sqrt{2}/\sqrt{3} \gamma$ . Equations (3.63) and (3.64) then become

$$(\mathcal{G}^{(0)})_{v^f J^f, v^i J^i} = 3(2J^i + 1) \left| \langle v^f | a | v^i \rangle \right|^2, \quad (3.68)$$

and

$$(\mathcal{G}^{(2)})_{v^f J^f, v^i J^i} = \frac{2}{3} (2J^i + 1) b_{J^f, J^i}^{(2)} \left| \langle v^f | \gamma | v^i \rangle \right|^2. \quad (3.69)$$

Substituting equations (3.68) and (3.69) into equations (3.61) and (3.62) yields the required formulae for the two linear polarisation regimes. In the  $I(\pi/2; \perp^s, \perp^i)$  regime the formula is

$$\Phi(a^2, \gamma^2, \theta) = \left| \langle v^f | a | v^i \rangle \right|^2 + \frac{4}{45} b_{J^f, J^i}^{(2)} \left| \langle v^f | \gamma | v^i \rangle \right|^2, \quad (3.70)$$

and similarly for the  $I(\pi/2; \parallel^s, \perp^i)$  regime:

$$\Phi(a^2, \gamma^2, \theta) = \langle (\alpha_{xy})_{\bar{f}\bar{i}}^2 \rangle = \frac{1}{15} b_{J^f, J^i}^{(2)} \left| \langle v^f | \gamma | v^i \rangle \right|^2. \quad (3.71)$$

Once  $\left| \langle v^f | a | v^i \rangle \right|^2$  and  $\left| \langle v^f | \gamma | v^i \rangle \right|^2$  are known, equations (3.70) and (3.71) can be evaluated to obtain the value of  $\Phi(a^2, \gamma^2, \theta)$  for any given branch. Table 3.10 summarises

the values of  $\Phi(a^2, \gamma^2, \theta)$  for Rayleigh scattering and the Raman branches of interest in this thesis for these two linear polarisation regimes.

**Table 3.10** The values of the line strength function  $\Phi(a^2, \gamma^2, \theta)$  for the linear polarisation regimes  $I(\pi/2; \perp^s, \perp^i)$ ,  $I(\pi/2; \parallel^s, \perp^i)$ , together with the depolarisation ratio  $\rho(\pi/2; \perp^i)$  for diatomic molecules, based on isotropic averages of squares of transition polarisability tensor components with  $\Lambda=0$  and  $S=0$  for rotational and vibration-rotation transitions. Normal Stokes Raman branches are shown. Adapted from Long (2002).

Type of scattering	Branch	Selection rules		$\Phi(a^2, \gamma^2, \theta)$		$\rho(\pi/2; \perp^i)$
		$\Delta\nu$	$\Delta J$	$I(\pi/2; \perp^s, \perp^i)$	$I(\pi/2; \parallel^s, \perp^i)$	
Rayleigh	Q <sub>0</sub>	0	0	$(a)_0^2 + \frac{4}{45} b_{J,J}^{(2)}(\gamma)_0^2$	$\frac{1}{15} b_{J,J}^{(2)}(\gamma)_0^2$	$\frac{3b_{J,J}^{(2)}(\gamma)_0^2}{45(a)_0^2 + 4b_{J,J}^{(2)}(\gamma)_0^2}$
Raman (pure rotation)	S <sub>0</sub>	0	+2	$\frac{4}{45} b_{J+2,J}^{(2)}(\gamma)_0^2$	$\frac{1}{15} b_{J+2,J}^{(2)}(\gamma)_0^2$	$\frac{3}{4}$
Raman (vibration-rotation)	O <sub>1</sub>	+1	-2	$\frac{4}{45} b_{J-2,J}^{(2)}(\gamma)^2$	$\frac{1}{15} b_{J-2,J}^{(2)}(\gamma)^2$	$\frac{3}{4}$
	Q <sub>1</sub>	+1	0	$(a')^2 + \frac{4}{45} b_{J,J}^{(2)}(\gamma)^2$	$\frac{1}{15} b_{J,J}^{(2)}(\gamma)^2$	$\frac{3b_{J,J}^{(2)}(\gamma)^2}{45(a')^2 + 4b_{J,J}^{(2)}(\gamma)^2}$
	S <sub>1</sub>	+1	+2	$\frac{4}{45} b_{J+2,J}^{(2)}(\gamma)^2$	$\frac{1}{15} b_{J+2,J}^{(2)}(\gamma)^2$	$\frac{3}{4}$

Note:  $(a)_0^2 = |\langle 0|a|0 \rangle|^2$ ,  $(a')^2 = |\langle 1|a|0 \rangle|^2$ ,  $(\gamma)_0^2 = |\langle 0|\gamma|0 \rangle|^2$ , and  $(\gamma)^2 = |\langle 1|\gamma|0 \rangle|^2$ .

A similar argument can be made for circularly polarised light with a 180° collection geometry. Although not obviously applicable to this work, since all experiments were performed with a 90° geometry, calculations in these regimes proved tangentially useful in explaining the unexpectedly low Q<sub>1</sub>-branch intensities during initial fibre-coupled collection experiments at the TILO facility (see Chapter 6) and are summarised here for completeness.

There are two  $\theta=0$  circularly polarised regimes, namely  $I(0; R^s, R^i) = I(0; L^s, L^i)$  and  $I(0; L^s, R^i) = I(0; R^s, L^i)$ , where “L” and “R” represent left- and right-handed circular polarisations, respectively. The function  $\Phi(a^2, \gamma^2, \theta)$  for the  $I(0; R^s, R^i) = I(0; L^s, L^i)$  regime is given by



$$\Phi(a^2, \gamma^2, \theta) = \left| \langle v^f | a | v^i \rangle \right|^2 + \frac{1}{45} b_{J^f, J^i}^{(2)} \left| \langle v^f | \gamma | v^i \rangle \right|^2, \quad (3.72)$$

and similarly for the  $I(0; L^s, R^i) = I(0; R^s, L^i)$  regime:

$$\Phi(a^2, \gamma^2, \theta) = \langle (\alpha_{xy})_{fi}^2 \rangle = \frac{2}{15} b_{J^f, J^i}^{(2)} \left| \langle v^f | \gamma | v^i \rangle \right|^2. \quad (3.73)$$

Table 3.11 summarises the values of  $\Phi(a^2, \gamma^2, \theta)$  for Rayleigh scattering and the Raman branches of interest in this thesis in these two circular polarisation regimes.

**Table 3.11** The values of the line strength function  $\Phi(a^2, \gamma^2, \theta)$  for the circular polarisation regime  $I(0; R^s, R^i) = I(0; L^s, L^i)$ , and  $I(0; L^s, R^i) = I(0; R^s, L^i)$ , together with the depolarisation ratio  $P(0) = P^{-1}(\pi)$  for diatomic molecules, based on isotropic averages of squares of transition polarisability tensor components with  $\Lambda = 0$  and  $S = 0$  for rotational and vibration-rotation transitions. Normal Stokes Raman branches are shown. Adapted from Long (2002).

Type of scattering	Branch	Selection rules		$\Phi(a^2, \gamma^2, \theta)$		$P(0) = P^{-1}(\pi)$
		$\Delta v$	$\Delta J$	$I(0; R^s, R^i)$ $= I(0; L^s, L^i)$	$I(0; L^s, R^i)$ $= I(0; R^s, L^i)$	
Rayleigh	Q <sub>0</sub>	0	0	$(a)_0^2 + \frac{1}{45} b_{J, J}^{(2)} (\gamma)_0^2$	$\frac{2}{15} b_{J, J}^{(2)} (\gamma)_0^2$	$\frac{6b_{J, J}^{(2)} (\gamma)_0^2}{45(a)_0^2 + 4b_{J, J}^{(2)} (\gamma)_0^2}$
Raman (pure rotation)	S <sub>0</sub>	0	+2	$\frac{1}{45} b_{J+2, J}^{(2)} (\gamma)_0^2$	$\frac{2}{15} b_{J+2, J}^{(2)} (\gamma)_0^2$	6
Raman (vibration-rotation)	O <sub>1</sub>	+1	-2	$\frac{1}{45} b_{J-2, J}^{(2)} (\gamma')^2$	$\frac{2}{15} b_{J-2, J}^{(2)} (\gamma')^2$	6
	Q <sub>1</sub>	+1	0	$(a')^2 + \frac{1}{45} b_{J, J}^{(2)} (\gamma')^2$	$\frac{2}{15} b_{J, J}^{(2)} (\gamma')^2$	$\frac{6b_{J, J}^{(2)} (\gamma')^2}{45(a')^2 + 4b_{J, J}^{(2)} (\gamma')^2}$
	S <sub>1</sub>	+1	+2	$\frac{1}{45} b_{J+2, J}^{(2)} (\gamma')^2$	$\frac{2}{15} b_{J+2, J}^{(2)} (\gamma')^2$	6

Note:  $(a)_0^2 = |\langle 0 | a | 0 \rangle|^2$ ,  $(a')^2 = |\langle 1 | a | 0 \rangle|^2$ ,  $(\gamma)_0^2 = |\langle 0 | \gamma | 0 \rangle|^2$ , and  $(\gamma')^2 = |\langle 1 | \gamma | 0 \rangle|^2$ .

The relative values of the derived invariants  $(a')^2$  and  $(\gamma')^2$  determine the relative intensity between the Q<sub>1</sub>-branch and the O<sub>1</sub>- and S<sub>1</sub>-branch lines in the  $I(\pi/2; \perp^s, \perp^i)$  and

$I(0;R^s, R^i) = I(0;L^s, L^i)$  polarisation regimes<sup>††</sup>. The relative intensities of the  $S_0$ -branch lines with respect to the  $O_1$ -,  $Q_1$ -, and  $S_1$ -branch lines is determined by the relative values of the invariants  $(\gamma)_0^2$  and  $(\gamma')^2$ .

Regardless of the polarisation regime under consideration, in order to correctly model the absolute intensities of Raman scattering, one needs to know the values of the squares of the tensor invariants  $(a')^2$ ,  $(\gamma)_0^2$ , and  $(\gamma')^2$ . The tensor invariant  $(a)_0^2$  is associated with Rayleigh scattering and is not considered further here since the Rayleigh line is usually suppressed by an edge or notch filter in practical spectroscopic work. It should be noted that the relative intensities of lines within an isolated  $S_0$ -,  $O_1$ -, or  $S_1$ -branch will be correct since the absolute value of the tensor invariants disappears in any ratio of  $\Phi(a^2, \gamma^2, \theta)$  values. This is also true of the  $Q_1$ -branch for the  $I(\frac{1}{2}; \parallel^s, \perp^i)$  and  $I(0;L^s, R^i) = I(0;R^s, L^i)$  polarisation regimes, and approximately true for the  $I(\frac{1}{2}; \perp^s, \perp^i)$  and  $I(0;R^s, R^i) = I(0;L^s, L^i)$  regimes since the constant  $(a')^2$  term tends to dominate over the term in  $b_{J,J}^{(2)}(\gamma')^2$ , which falls off rapidly with increasing  $J$ .

In this thesis, the modelling program *SpecGen* was used to investigate changes in relative intensity (usually between branches) with respect to gas mixture composition (i.e. relative number density) and polarisation regime. Since the calculation of these invariants is beyond the scope of this work (and in the absence of literature values), Raman spectra of hydrogen isotopomer mixtures containing the isotopes  $H_2$ ,  $HD$ , and  $D_2$  that were measured during the course of this work were used to fix the relative values of the invariants for these isotopomers to a leading order level of approximation. Further approximations that were made to simplify calculation and to obtain relative intensities are further discussed in Section 3.4.

In order to correctly fix the relative intensities between branches, it is necessary to measure all four branches ( $S_0$ ,  $O_1$ ,  $Q_1$ ,  $S_1$ ) so that an estimate of the relative values of the tensor invariants  $(a')^2$ ,  $(\gamma)_0^2$ , and  $(\gamma')^2$  can be made. It is important to take into account

---

<sup>††</sup> The  $I(\frac{1}{2}; \parallel^s, \perp^i)$  and  $I(0;L^s, R^i) = I(0;R^s, L^i)$  polarisation regimes are independent of the  $(a)_0^2$  and  $(a')^2$  tensor invariants.

variations in diffraction grating reflectivity and detector (quantum) efficiency with respect to wavelength. Further, if it not possible to simultaneously record the entire Raman spectrum (all four branches), then care must be taken that the experimental parameters (such as entrance slit width, exposure time, etc.) are the same for each measurement run.

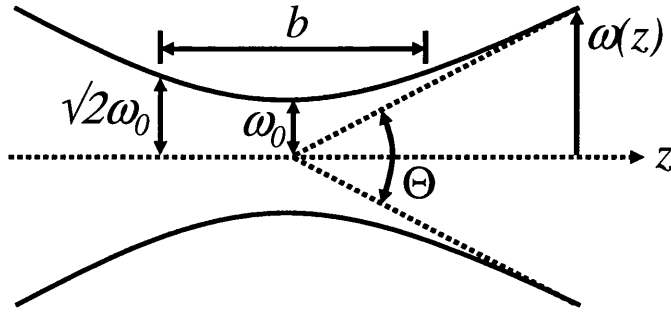
### 3.3.5 The irradiance $\mathcal{I}$

Since the incident radiation in experiments carried out for this thesis was the TEM<sub>00</sub> mode output of either a Nd:YAG or Nd:YVO<sub>4</sub> laser, one can reasonably approximate the beam profile by a Gaussian distribution. The intensity distribution of a Gaussian beam propagating through free space along the z-axis is given by the expression

$$I(r, z) = I_0 \left( \frac{\omega_0}{\omega(z)} \right)^2 \exp\left( \frac{-2r^2}{\omega^2(z)} \right), \quad (3.74)$$

where  $r$  is the radial coordinate,  $z$  is the axial coordinate,  $I_0 = I(0,0)$  is the intensity at the centre of the beam, and  $\omega(z)$  is the radius of the beam at a point  $z$  along the z-axis (also known as the 'spot size'), and  $\omega_0$  is the minimum radius of the beam. The beam radius is defined as the value of  $r$  at which the intensity  $I(r, z)$  is  $1/e^2$  of its peak value.

When such a Gaussian beam is focussed by a lens, the minimum radius  $\omega_0$  will be located at the (geometrical) focal point, commonly referred to as the 'beam waist'. The beam will therefore have a geometry as shown in Figure 3.8.



**Figure 3.8** The geometry of a focussed Gaussian beam. The red line represents the beam radius  $\omega(z)$  as previously defined. Also shown are the beam divergence  $\Theta$  and the confocal parameter  $b$ .

The function describing the beam radius is given by the expression

$$\omega(z) = \omega_0 \sqrt{1 + \left(\frac{z}{z_0}\right)^2}, \quad (3.75)$$

where – to simplify the expression – the origin is defined as the beam waist. The depth of focus,  $z_0$ , is defined as the distance from the beam waist at which the beam radius equals  $\sqrt{2}\omega_0$ . The confocal parameter is the length over which the radius is less than or equal to  $\sqrt{2}\omega_0$  and is thus simply twice the depth of focus, i.e.  $b = 2z_0$ . The depth of focus is defined as

$$z_0 = \frac{\pi\omega_0^2}{\lambda}, \quad (3.76)$$

where  $\lambda$  is the wavelength of the radiation.

In order to correctly calculate the irradiance,  $\mathcal{I}$ , an integration must be performed over the scattering volume, i.e. the range of  $z$  which is imaged onto the collection optics. Since the practical application of *SpecGen* is to calculate relative intensities, the absolute value of  $\mathcal{I}$  is irrelevant provided it is a positive real number. It should be borne in mind, however,

that if at some future time a requirement to calculate the absolute value of  $I(\theta; p^s, p^i)$  arises, this integration would need to be performed.

### 3.4 *SpecGen*

In this section we provide an overview of the structure of the *SpecGen* modelling program, a summary of the approximations that have been made so that relative intensities can be estimated between Raman branches, and examples of modelled spectra compared with real-life spectra of the same isotomeric composition. This section is concerned primarily with the approximations employed and the results obtained rather than the details of how the *LabVIEW* code was written. The reader is referred to Appendix A1 for a breakdown of the *LabVIEW* code.

#### 3.4.1 *Approximations currently employed in the SpecGen code*

Recall the expression for the absolute intensity of scattered radiation, due to a rotational or vibration-rotation transition:

$$I(\theta; p^s, p^i) = k_{\tilde{\nu}} (\tilde{\nu}_s)^4 N_i \Phi(a^2, \gamma^2, \theta) \mathcal{J}. \quad (3.77)$$

Of the terms in this expression,  $k_{\tilde{\nu}}$  and  $\mathcal{J}$  are constants and therefore we can set  $k_{\tilde{\nu}} = \mathcal{J} = 1$  for a relative intensity calculation. It will prove convenient here to explicitly include the statistical weight due to the nuclear spin degeneracy, which is normally included in the population factor term  $N_i$ . Equation (3.77) then simplifies to

$$I_{rel}(\theta; p^s, p^i) = (\tilde{\nu}_s)^4 g_i N_i \Phi(a^2, \gamma^2, \theta), \quad (3.78)$$

where  $g_i N_i$  should be considered a single term representing the value of  $N_i$  as defined in equation (3.56).

Apart from the statistical weight  $g_i$ , the important term in the population factor  $g_i N_i$  is the total number of molecules,  $N$ . Taking into account that the intensity of Raman scattering is linearly dependent on the total number of molecules present in the scattering volume, in a relative intensity calculation, the parameter  $N$  can now represent the *relative* number of molecules of a particular isotopomer in a gas mixture – e.g. when simulating the Raman spectrum of a 10:25:65 ratio mixture of H<sub>2</sub>:HD:D<sub>2</sub>, the parameter  $N$  is simply set to the relative values 10, 25, and 65 for the H<sub>2</sub>, HD, and D<sub>2</sub> calculation passes, respectively. In *SpecGen*, the value of the relative number density of each isotopomer is user-defined via a front panel object (see Section 3.4.2).

The line strength function  $\Phi(a^2, \gamma^2, \theta)$  term has three dependent parameters, namely the tensor invariants  $(a')^2$ ,  $(\gamma'_0)^2$ , and  $(\gamma')^2$ . Initially, the values of these invariants was set to  $(a')^2 = (\gamma'_0)^2 = (\gamma')^2 = 1$ , but in order to correctly estimate relative intensities between branches it was necessary to first fix the relative values of the invariants for each of the isotopomers individually by referring to measured spectra. In order for the estimates to be meaningful, the simulated spectral linewidths were matched as closely as possible to the measured linewidth of the spectrum under consideration.

In order to obtain the correct relative intensities between isotopomers, the relative values of each isotopomer's invariants were fixed against measured Raman spectra of isotopomer mixtures of known composition. Note that at the time of writing the only complete (i.e. all four branches) Raman spectra were those of the isotopomers H<sub>2</sub>, HD, and D<sub>2</sub>.

Table 3.12 summarises these preliminary estimates for the relative values of the tensor invariants  $(a')^2$ ,  $(\gamma'_0)^2$ , and  $(\gamma')^2$  for the hydrogen isotopomers H<sub>2</sub>, HD, and D<sub>2</sub>.

**Table 3.12** Leading order approximations of the relative values of the tensor invariants  $(a')^2$ ,  $(\gamma)_0^2$ , and  $(\gamma')^2$  for the hydrogen isotopomers H<sub>2</sub>, HD, and D<sub>2</sub>. Note the (arbitrary) normalisation relative to the  $(\gamma')^2$  value for the HD isotopomer following the format of these parameters in the *LabVIEW* code.

Tensor invariant	Isotopomer		
	H <sub>2</sub>	HD	D <sub>2</sub>
$(a')^2$	0.7105	0.6500	5.8400
$(\gamma)_0^2$	17.3950	13.4000	9.2000
$(\gamma')^2$	0.4900	1.0000	1.6000

The other approximation made in the code is mentioned in Section 3.2.5 – a modified version of Edlén’s formula is used to calculate the value of the refractive index of air with respect to absolute wavenumber in order to correct for the effect of the refractivity of air on the value of absolute wavenumber values (which are calculated for an isolated molecule in vacuum). Standard dry air parameters are assumed since the variation in the value of the refractive index of air due to expected deviations from standard dry air parameters are at least an order of magnitude less than the accuracy of the HTS / Spec-10 detector system used for the majority of this thesis.

### 3.4.2 *SpecGen* structure



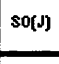
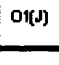
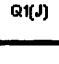
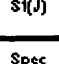
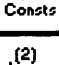
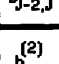
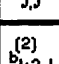
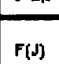
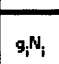
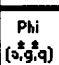


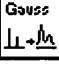

The structure of the *SpecGen* code is dictated by practical considerations such as ease of use and clarity in the block diagram code. The program works on three-tier system: the first and highest-level tier (Tier 1) is the user interface that handles the front panel<sup>##</sup> input of modelling parameters and the outputting of the modelled spectra to ASCII files, Tier 2 is a high-level handling of the subVIs (Tier 3) that greatly simplifies the first tier block diagram. The subVIs can be subdivided into three classes – those associated with calculating the line positions (Tier 3a), those associated with calculating the line intensities (Tier 3b), and a third class which contains the convolution subVI for lineshape simulation

---

<sup>##</sup> *LabVIEW* VIs consist of two parts – the front panel and the block diagram. The front panel is the user interface of the VI, if applicable, and the block diagram is the program’s graphical code. Some VIs used as subVIs, e.g. the subVIs used to calculate  $b_{j',j'}^{(2)}$ , have no front panel objects and therefore only have outputs.

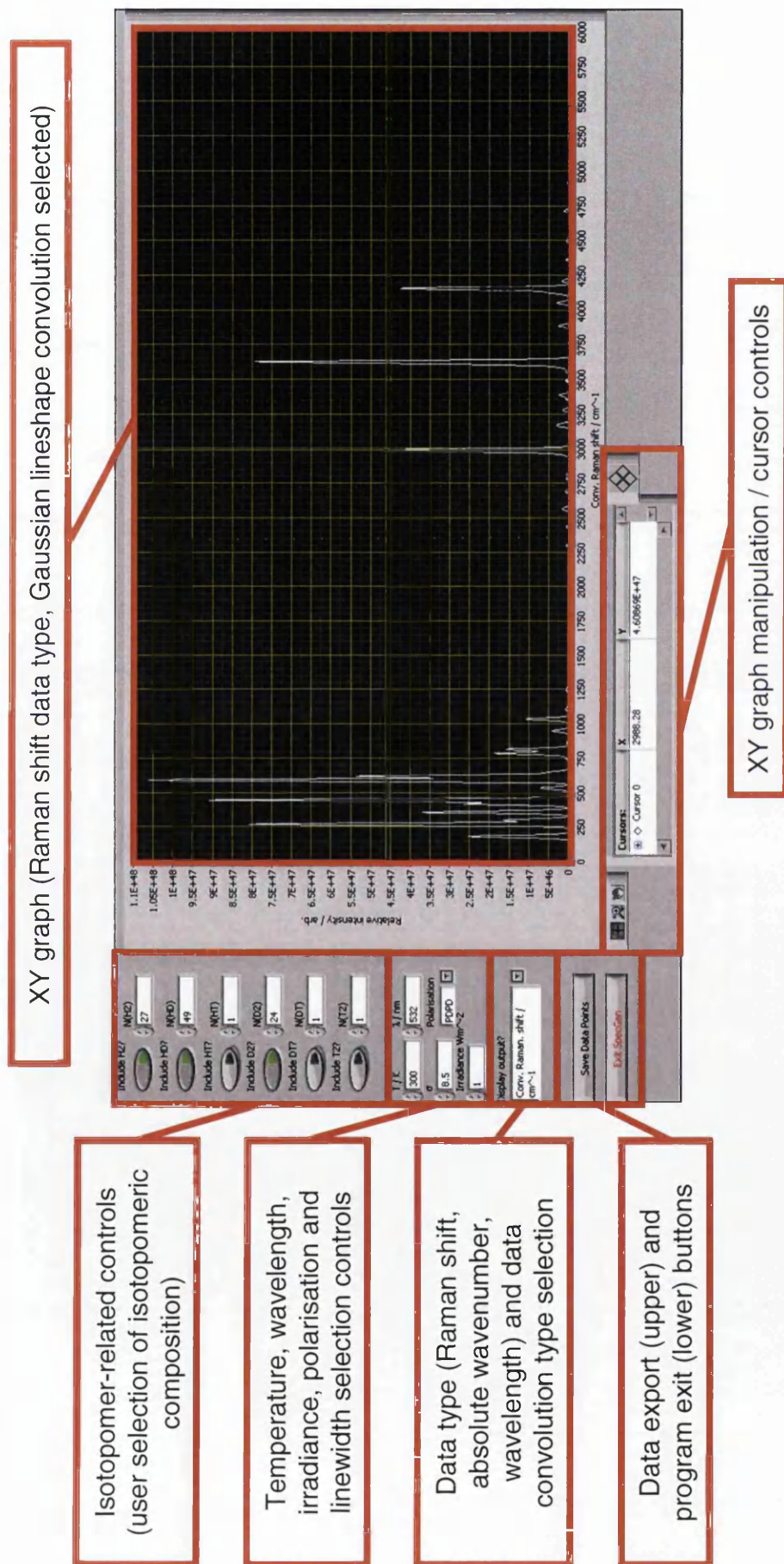
(Tier 3c). For a more detailed breakdown of the *SpecGen* code, the reader is referred to Appendix A1, but a summary is provided here in Table 3.13 and Figure 3.13.

**Table 3.13** The three-tiered hierarchy of the *SpecGen LabVIEW* code. The filename extension “.vi” is implied in the VI column. Note that even though the *SpecGen* code contains subVIs which are included as part of the base package, these are not proprietary and so are not included here (e.g. the “Write To Spreadsheet File.vi” node that handles ASCII file output).

VI	Icon	Tier	Purpose / calculates
SpecGen_Interface		1	User interface
SpecGen_SubVI_High_Raman_Spectrum		2	Tier 3 SubVI handling
SpecGen_SubVI_S0(J)		3a	S <sub>0</sub> -branch positions
SpecGen_SubVI_O1(J)		3a	O <sub>1</sub> -branch positions
SpecGen_SubVI_Q1(J)		3a	Q <sub>1</sub> -branch positions
SpecGen_SubVI_S1(J)		3a	S <sub>1</sub> -branch positions
SpecGen_SubVI_Spectroscopic_Constants		3a	$B_0, D_0, H_0, B_1, D_1, \tilde{\nu}_{vib}$
SpecGen_SubVI_b(2)J-2,J		3b	$b_{J-2,J}^{(2)}$
SpecGen_SubVI_b(2)J,J		3b	$b_{J,J}^{(2)}$
SpecGen_SubVI_b(2)J+2,J		3b	$b_{J+2,J}^{(2)}$
SpecGen_SubVI_F(J)		3b	$F(J)$
SpecGen_SubVI_giNi		3b	$g_i N_i$
SpecGen_SubVI_Phi(a^2_g^2_q)		3b	$\Phi(a^2, \gamma^2, \theta)$
SpecGen_SubVI_Tensor_Invariants		3b	$(a)_0^2, (a')^2, (\gamma)_0^2, (\gamma')^2$
SpecGen_SubVI_vs^4		3b	$(\tilde{\nu}_s)^4$
SpecGen_SubVI_Convolute_Gaussian		3c	Lineshape convolution



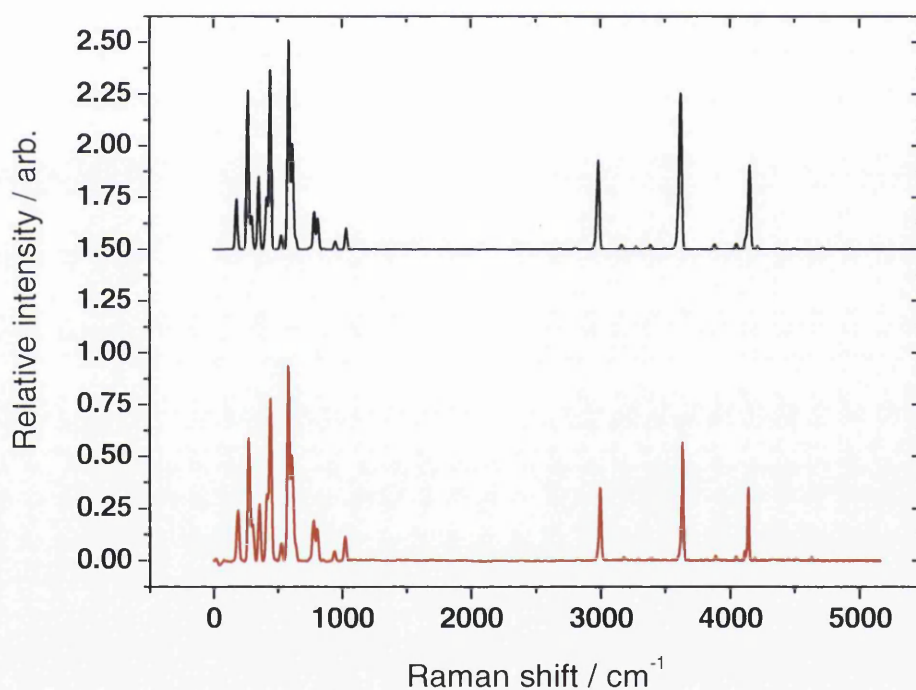
The front panel of *SpecGen* is shown in Figure 3.9. Which isotopomers to include in the simulation and their relative number densities are set via the controls to the upper left. The experimental parameters and convolution options are towards the mid left. The user can save the current spectrum via the “Save Data Points” button to the lower left. The simulated Raman spectrum is displayed in the XY graph to the right. The reader is referred to Appendix A1 for a more detailed breakdown of the front panel.



**Figure 3.9** SpecGen front panel. The major groups of controls and indicators are shown. The user-definable parameters and data convolution / export controls are located to the left, the XY graph displaying the current simulation is to the right.

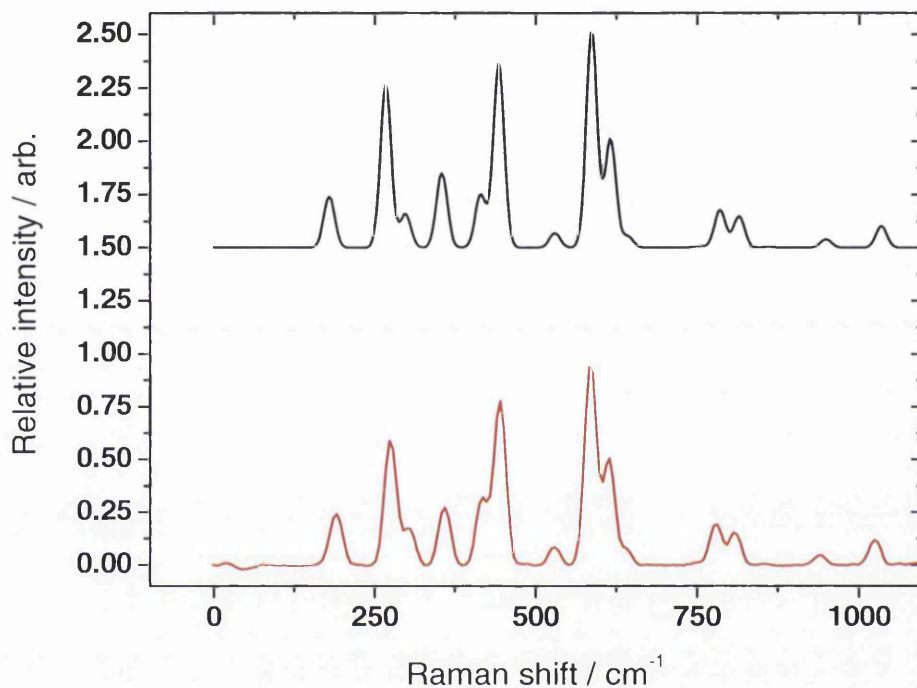
### 3.4.3 Simulated Raman spectra and comparison with measured spectra

In this section, examples of measured spectra of hydrogen isotopomer mixtures are compared with simulations of the same spectra in order to demonstrate the quality of the simulations currently achievable with the current implementation of *SpecGen*. Figure 3.10 shows the full Stokes Raman spectrum (the  $S_0$ -,  $O_1$ -,  $Q_1$ -,  $S_1$ -branches) of a 29:47:24  $H_2$ :HD: $D_2$  mixture. In the measured spectrum, the cosmic ray events have been removed and a flat baseline set via a function subtraction routine in *Origin*. The simulated spectrum has been generated without noise.



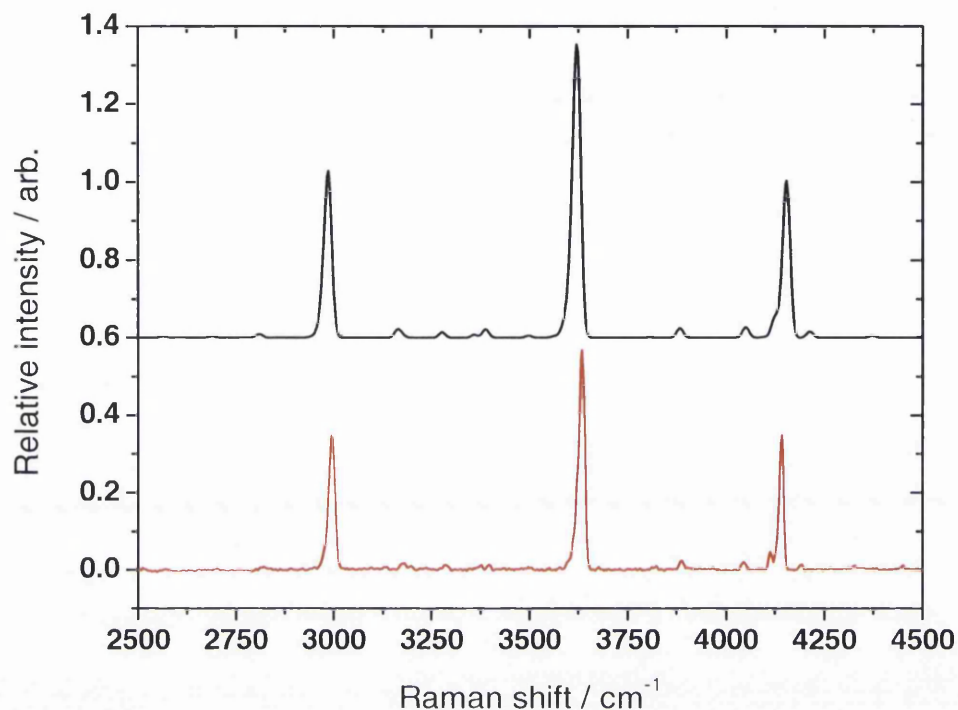
**Figure 3.10** Comparison of the measured (bottom, red) and simulated (top, black) Raman spectrum of a 29:47:24  $H_2$ :HD: $D_2$  mixture. Measured spectrum parameters: incident radiation wavelength = 512nm, entrance slit width = 25.4 $\mu$ m, temperature  $\sim$  300K. Simulated spectrum parameters: incident radiation wavelength = 512nm, Gaussian lineshape convolution standard deviation = 8.5, temperature = 300K. The polarisation regime in both cases is  $I(\pi/2; \perp^s, \perp^l)$ .

Concentrating on the pure rotational ( $S_0$ -) branches of the above spectra, one can see the excellent agreement between measured and simulated spectra with respect to both line position and the relative intensities of the Raman lines.



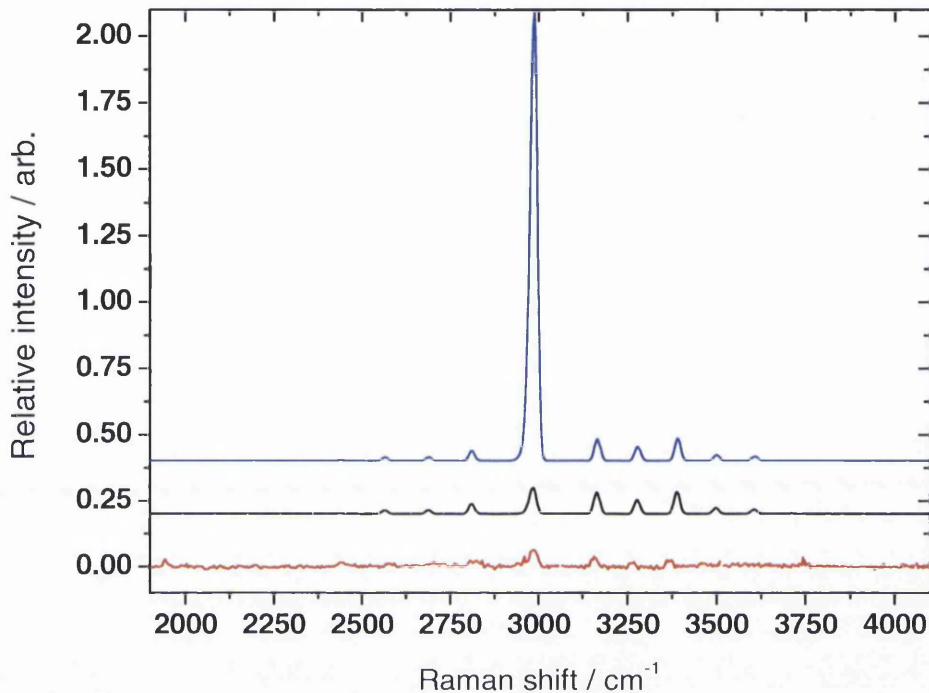
**Figure 3.11** Comparison of the measured (bottom, red) and simulated (top, black) pure rotational Raman spectra of a 29:47:24  $H_2$ :HD: $D_2$  mixture. Measured and simulated spectrum parameters are the same as for Figure 3.10. Note the excellent agreement between measured and simulated with respect to both line position relative intensity. The ‘negative peak’ at  $\sim 50\text{cm}^{-1}$  on the measured spectrum is an artefact of the function subtraction routine applied to the raw data in *Origin*.

The agreement is equally good for the vibration-rotation ( $O_1$ -,  $Q_1$ -, and  $S_1$ -) branches, as shown in Figure 3.12. One can see here an artefact of the simple Gaussian lineshape convolution routine employed in the current implementation of *SpecGen* – lines at longer wavelengths (higher Raman shift values) have slightly wider linewidths than those at shorter wavelengths (lower Raman shift values). The  $J'' = 3$  line of the  $Q_1$ -branch of  $H_2$  (at  $\sim 4125\text{cm}^{-1}$ ) is nearly resolved in the measured spectrum, whereas the  $J'' > 3$  lines in the simulated  $Q_1$ -branch of  $H_2$  are unresolved in the shoulder of the single  $Q_1$ -branch peak.



**Figure 3.12** Comparison of the measured (bottom, red) and simulated (top, black) vibration-rotation Raman spectra of a 29:47:24  $\text{H}_2$ :HD:D $_2$  mixture. Measured and simulated spectrum parameters are the same as for Figure 3.10. The three large peaks in each spectrum are the  $Q_1$ -branches of (left to right) D $_2$ , HD, and H $_2$ . The line spacing of the  $Q_1$ -branch of H $_2$  is great enough that the  $J''=3$  line is almost resolvable in the measured spectrum. This line is unresolved in the simulated spectrum due to the nature of the convolution routine. Note the arbitrary offset of the simulated spectrum has been set to 0.6 in this figure for clarity (the offset used in Figures 3.10 and 3.11 is 1.5).

Figure 3.13 shows how *SpecGen* was used to determine the polarisation regime of an 'anomalous' Raman spectrum. The example is taken from the investigation described in Chapter 6.



**Figure 3.13** Comparison of measured (lower, red), and simulated Raman spectra for the polarisation regimes  $I(\pi/2; ||^s, \perp^i)$  (middle, black) and  $I(\pi/2; \perp^s, \perp^i)$  (upper, blue). The isotopomeric composition in this case was 95:5 D<sub>2</sub>:H<sub>2</sub>. The spectrum intensities were all normalised to the most intense line of the S<sub>0</sub>-branch of D<sub>2</sub> to allow the spectra to be meaningfully compared. From this graph it is clear that the polarisation regime of the measured spectrum is closer to  $I(\pi/2; ||^s, \perp^i)$  than  $I(\pi/2; \perp^s, \perp^i)$ .

An unexpectedly low intensity of Q<sub>1</sub>-branches in measured spectra for a variety of isotopomeric compositions was observed when testing the HTS / Spec-10 detector system at the TILO experiment. Comparison of the measured spectra with simulations showed that the polarisation regime in which the spectra were measured was closer to  $I(\pi/2; ||^s, \perp^i)$  as opposed to the expected  $I(\pi/2; \perp^s, \perp^i)$ . The change of incident light polarisation from the expected perpendicular is likely due to the inclusion of a Faraday isolator in the incident beam path (see Sections 4.6.3 and 6.2.7).

### 3.5 *Summary and Outlook*

In this chapter we have demonstrated how to adapt the general theoretical principles describing Raman scattering outlined in Chapter 2 to the specific case of the Stokes Raman spectra of the hydrogen isotopomers, and have developed the theoretical framework on which *SpecGen* has been based.

The current implementation of *SpecGen* has proven to be a very useful tool for data analysis and investigation of ‘anomalous’ data. The agreement between measured and calculated line positions is excellent, and leading-order approximations for the relative intensities of the H<sub>2</sub>, HD, and D<sub>2</sub> isotopomers have been determined, which allow both qualitative and approximate quantitative comparison of simulated spectra with measured spectra.

Although the approximations made in developing the theoretical framework have currently limited *SpecGen* to calculating the relative intensities of Stokes Raman lines, the modular nature of *LabVIEW* allows the extension of the code to a full quantitative calculation should the need arise, although significant extra code would be required to simulate the power density geometry of the scattering region.

*SpecGen* is a work in progress, and improvements to the basic code outlined in this chapter and Appendix A1 are currently underway. The convolution routines are being updated to include Lorentzian and Voigt lineshape functions, and simulation routines to calculate the Raman spectra of possible trace contaminants of the tritium gas in the KATRIN source, such as methane isotopomers C<sub>n</sub>H<sub>x</sub>R<sub>y</sub> (R=H, D, T).

It is planned to develop a *LabVIEW* application that will handle the data acquisition, processing, analysis and reporting stages of the Raman monitoring system that is being developed for the KATRIN project. *SpecGen* provides a solid foundation on which to develop the analysis segment of that application.

### 3.6 References for Chapter Three

#### 3.6.1 Cited references

Bönsch, G. and Potulski, R. (1998). "Measurement of the refractive index of air and comparison with modified Edlén's formulae." Metrologia (35): 133-139.

Edwards, H. G. M., et al. (1978). "Pure rotational and vibration-rotational Raman spectra of tritium,  $^3\text{H}_2$ ." J. Chem. Soc. Faraday Trans. 2 (74): 1203-1207.

Herzberg, G. (1950). Molecular Spectra and Molecular Structure I. Spectra of Diatomic Molecules. New York (U.S.A.), Van Nostrand Reinhold Company.

Long, D. A. (2002). The Raman Effect - A Unified Treatment of the Theory of Raman Scattering by Molecules. Chichester (U.K.), John Wiley & Sons, Ltd.

#### 3.6.2 Further reading

Allen, H. C. and Cross, P. C. (1963). Molecular Vib-Rotors - The Theory and Interpretation of High Resolution Infrared Spectra. New York (U.S.A.), John Wiley & Sons, Inc.

Anderson, A. (1971). The Raman Effect. New York (U.S.A.), Marcel Dekker, Inc.

Beattie, D. R. and Cappelli, M. A. (2000). "Raman scattering measurements of molecular hydrogen in a low-density, arc-heated plasma." Appl. Phys. B(70): 419-427.

Collett, E. (1993). Polarized Light - Fundamentals and Applications. New York (U.S.A.), Marcel Dekker, Inc.

Hecht, E. (2002). Optics. San Francisco (U.S.A.), Addison Wesley.



Hollas, J. M. (2004). Modern Spectroscopy. Chichester (U.K.), John Wiley & Sons, Ltd.

Koningstein, J. A. (1972). Introduction to the Theory of the Raman Effect. Dordrecht (The Netherlands), D. Reidel Publishing Company.

Lefebvre-Brion, H. and Field, R. W. (2004). The Spectra and Dynamics of Diatomic Molecules. Amsterdam (The Netherlands), Elsevier Academic Press.

McCreery, R. L. (2000). Raman Spectroscopy for Chemical Analysis. New York (U.S.A.), John Wiley & Sons, Inc.

Person, W. B. and Zerbi, G. (1982). Vibrational Intensities in Infrared and Raman Spectroscopy. Amsterdam (The Netherlands), Elsevier Scientific Publishing Company.

Smith, E. and Dent, G. (2005). Modern Raman Spectroscopy - A Practical Approach. Chichester (U.K.), John Wiley & Sons, Ltd.

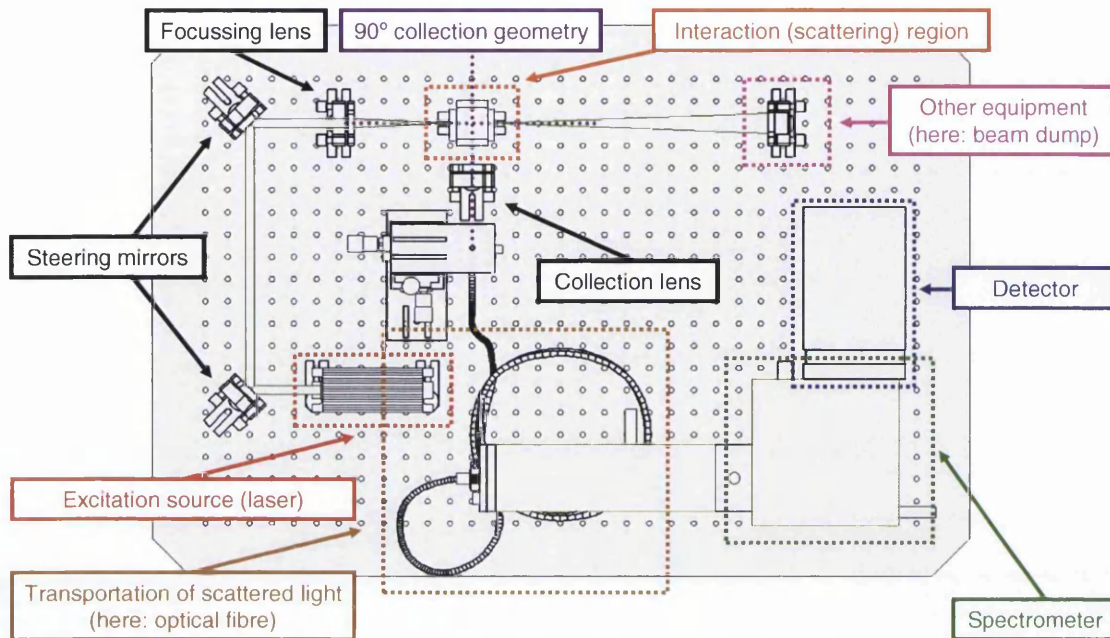
## CHAPTER FOUR

### INSTRUMENTATION AND SOFTWARE REQUIRED FOR LASER RAMAN SPECTROSCOPY OF GASEOUS SAMPLES

In this chapter we provide an overview of the most important instruments and software used in the research described in this thesis. First, the Raman scattering experiment is considered in general and divided into its main building blocks. These are then considered separately in dedicated sections, where a short general summary is provided of the relevant components. Thereafter, specific instruments or software employed in this work are described in detail. For brevity, only the most important and / or immediately relevant details of each instrument are given. For further details the reader is referred to the sources given in the references listed at the end of the chapter.

The principles of a general incoherent light scattering experiment was shown in Figure 2.1 in which the question was posed of how the set of parameters that characterise the scattered radiation could be linked to the parameters characterising the incident radiation and the properties of the scattering system. In practical applications, the questions posed are often less general. For our work, the desired information is the concentration of impurities in the tritium gas flow at the inlet to the WGTS. As such, a more specific case of the incoherent light scattering experiment can now be considered.

Figure 4.1 shows a typical Raman scattering experiment. The specific experimental arrangements described in this thesis are variations on this theme (the transportation of scattered light being the most-varied parameter). The only experimental design parameter that was fixed is the need for a sealed gas cell through which to pass the tritium gas flow, and the design for this cell was already determined, having been used in previous Raman experiments at TLK (see Taylor et al. (2001)). The design of the cell is most suited to a 90° collection geometry (i.e. setting  $\theta = \pi/2$  in the relevant equations discussed in Chapter 3), and this geometry was used throughout all Raman experiments described in this thesis.



**Figure 4.1** A typical  $90^\circ$  collection geometry Raman scattering experiment, showing important experimental design parameters (coloured labels).

Figure 4.1 highlights the parameters that are to a greater or lesser extent variable in the design of a Raman experiment. These are: the excitation source (red), the collection geometry (purple), the interaction (scattering) region (orange), the method of transportation of the scattered light (brown), the spectrometer type / model (green), the detector type / model (blue), and other auxiliary equipment such as beam dumps, enclosures, and interlocks (indigo). Not shown in the figure are the post-acquisition processing (software) routines that need to be applied to the raw data in order to perform meaningful spectroscopic analysis.

Each of these experimental setup parameters are discussed separately. A general case is considered first for each parameter, and then the specific experimental variations used in this work are described.

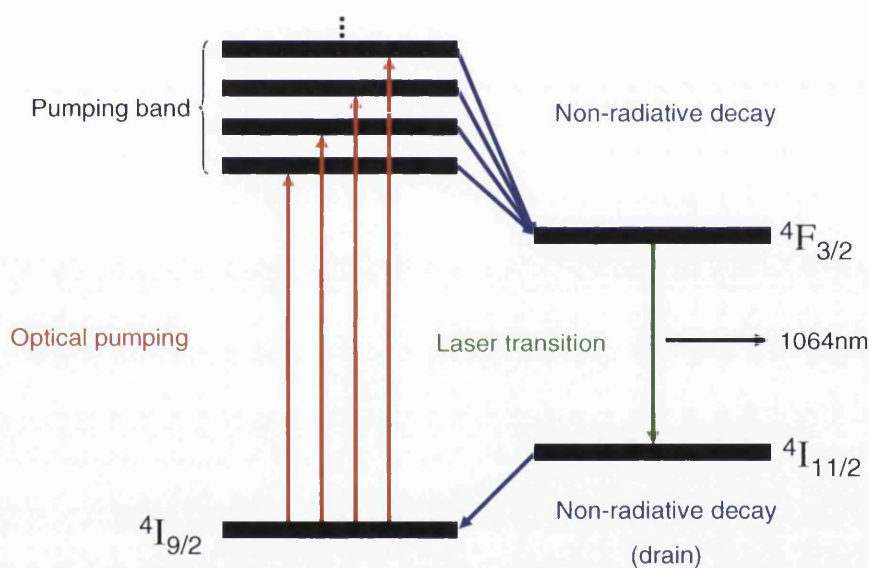
## 4.1 *Excitation Sources*

A variety of laser sources are used as excitation sources in modern Raman spectroscopy. Visible lasers are the most common choice for excitation with dispersive spectrometers. The peaks due to Raman scattering are sharper than absorbance and emission peaks in this region, and the inverse fourth-power wavelength dependence of the Raman scattering cross-section means that the scattered radiation will be more intense than compared with near infrared (NIR) excitation sources commonly employed with Fourier transform (FT) type spectrometers. In this latter case, the employment of NIR excitation is preferable if one wishes to ensure that as many samples as possible (whose composition is typically unknown beforehand) will give a Raman spectrum (McCreery (2000)). This is not true in our case, however, as the components of the gases in the tritium flow are known a priori – it is the (relative) number densities of isotopomer components that are the desired values. All experiments discussed in this thesis have been performed with dispersive (non-FT) spectroscopic systems, so visible laser excitation is the most appropriate.

Throughout this work, continuous-wave (CW) diode-pumped solid-state (DPSS) lasers have been employed. Proof-of-principle Raman measurements carried out at Swansea were performed using 10mW, 50mW and 100mW Nd:YAG (neodymium-doped yttrium aluminium garnate) lasers, while all measurements at TLK utilised a Coherent *Verdi V5* Nd:YVO<sub>4</sub> (neodymium-doped yttrium vanadate) laser which had a user-selectable power output of up to 5W. Both of these laser types use a particular method of second harmonic generation (frequency doubling) of the fundamental emission wavelength (1064nm) to produce the ‘working wavelength’ of 532nm. All lasers used in this work were (necessarily) single-mode and were linearly polarised vertically (with respect to the set-up breadboard plane).

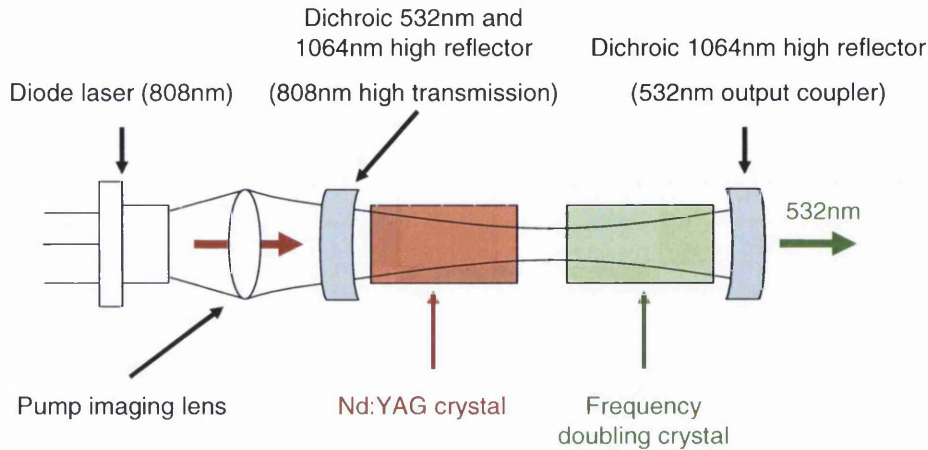
### 4.1.1 The Nd:YAG laser

The Nd:YAG laser is a very common choice for Raman spectroscopy, whether in flashlamp-pumped Q-switched (pulsed operation), arc-lamp-pumped CW, or diode-pumped CW form. Figure 4.2 shows a simplified energy level diagram for the  $\text{Nd}^{3+}$  ion, showing the fundamental (1064nm) laser transition  ${}^4F_{3/2} \rightarrow {}^4I_{11/2}$ . The Nd:YAG laser is a four-level system, with ground state  ${}^4I_{9/2}$ . The pumping band is between 300 and 900nm, with the strongest peaks at 750nm and 810nm.



**Figure 4.2** Simplified energy level diagram of the  $\text{Nd}^{3+}$  ion, showing the four-level system configuration. The 1064nm lasing transition is  ${}^4F_{3/2} \rightarrow {}^4I_{11/2}$ .

As noted above, the Nd:YAG lasers in our work were of the CW DPSS type. A standard diode pumping arrangement consists of using a diode laser operating at about 808nm to pump the Nd:YAG laser crystal (matching on of the strongest pump band peaks at about 810nm), with a pump imaging lens placed between the pump diode and laser cavity (Silvast (2004)). An intracavity frequency-doubling crystal is used to produce the visible output wavelength of 532nm. Figure 4.3 shows a typical arrangement of such a Nd:YAG laser cavity.



**Figure 4.3** Standard diode pumping arrangement of a Nd:YAG laser cavity, showing the intracavity frequency doubling crystal. Adapted from Silvast (2004)

Table 4.1 lists the Nd:YAG laser parameters which apply to all three modules used by us (10mW, 50mW, and 100mW modules).

**Table 4.1** Design parameters of the three Nd:YAG lasers used in this thesis.

Parameter	Value
Laser wavelength (doubled) / nm	532
Laser gain medium length / m	0.05
Doping density / $m^{-3}$	$1.4 \times 10^{26}$
Refractive index of gain medium	1.82
Operating temperature / K	300
Optical pumping method	Diode (808nm)
Output power / mW	10, 50, 100
Polarisation	Vertical (~100:1)
Mode	Single ( $TEM_{00}$ )

In addition to the fixed parameters, operating characteristics of the modules needed to be assessed, including output power variation, wavelength stability, beam divergence, and warm-up time.

Taking as an example the 10mW Nd:YAG module (model# JLM-10RB, of size 19dia  $\times$  74mm) used in the TLK / UWS system comparative review described in Chapter 5, the datasheet values for these more pragmatic parameters are listed in Table 4.2.

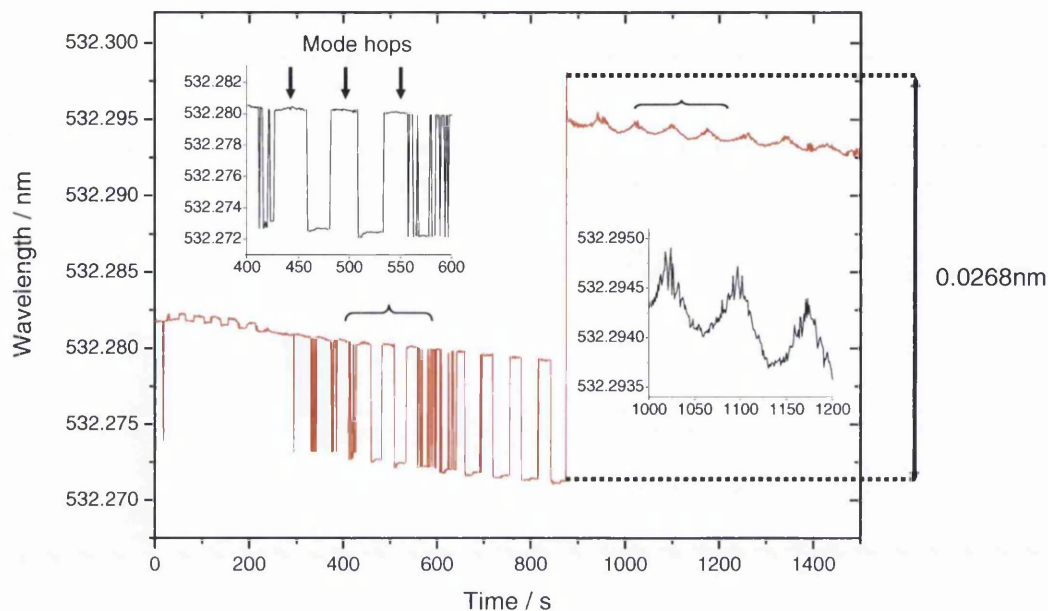
**Table 4.2** Manufacturer-specified operating parameters of the 10mW green Nd:YAG JLM-10RB module used in the TLK / UWS system comparative review described in Chapter 5.

Parameter	Value
Output power / mW	9 to 11
Power stability / %	$\pm 10$
Beam diameter / mm	3
Beam divergence / mrad	<1.2
Polarisation	Vertical (~100:1)
Warm-up time / min	<5
Operating temperature / °C	20 to 30
Expected life time / hrs	>3000

The power stability measurements are accurate for this module, but the total power output for this laser was found to be slightly lower, at ~7.1mW. Disparities between quoted and measured power outputs for the Nd:YAG lasers have been taken into account in Chapter 5 where signal-to-noise ratio estimates have been made on the basis of scaling up S/N values to estimate higher-power cases.

Wavemeter measurements of the output wavelength of the 10mW JLM-10RB module show a remarkably stable emission of  $\lambda_{\text{air}} = 532.054(3)\text{nm}$  in air. Using Edlén's formula to convert the air values to vacuum values yields a wavelength of  $\lambda_{\text{vac}} = 532.202(4)\text{nm}$ , and a corresponding absolute wavenumber of  $18789.8(42)\text{cm}^{-1}$ . The brackets represent the fluctuating decimal places. These fluctuations, of the order of  $10^{-2}\text{cm}^{-1}$ , are much less than the resolution of the HTS spectrometer system (of the order of  $\sim 3\text{cm}^{-1}/\text{pixel}$ ).

The three low-power Nd:YAG modules were all passively (air) cooled, and it should be noted that lasers reach stable output after a (relatively short) warm-up period during which the laser approaches its operating temperature. Figure 4.4 shows a warm-up curve for the 50mW Nd:YAG module (the curve for the 100mW module would be similar as they are variants of the same module design) – note that this module has a longer warm-up time of ~15min (compared with <5min for the 10mW module). One can clearly see the hops between longitudinal modes due to thermally-induced fluctuations in the cavity length.



**Figure 4.4** Warm-up curve for 50mW (red) Nd:YAG laser module showing mode hops (insets), and a large jump of 0.0268nm at ~900s (~15min). This jump corresponds to a wavenumber shift of  $\sim 1\text{cm}^{-1}$ . Note that 1500s = 25min.

During the warm-up period, the wavelength of the laser can fluctuate significantly. A fluctuation of 0.0268nm ( $\sim 1\text{cm}^{-1}$ ) is not much less than the resolution of the spectrometer systems used in this thesis ( $\sim 3\text{cm}^{-1}/\text{pixel}$ ), and a jump would only need to be slightly larger than shown in Figure 4.4 in order for it to adversely affect the quality of the Raman spectrum being recorded, i.e. to cause a broadening of the Raman lines (or multiple lines if the jump is especially large, or the system resolution is high enough).

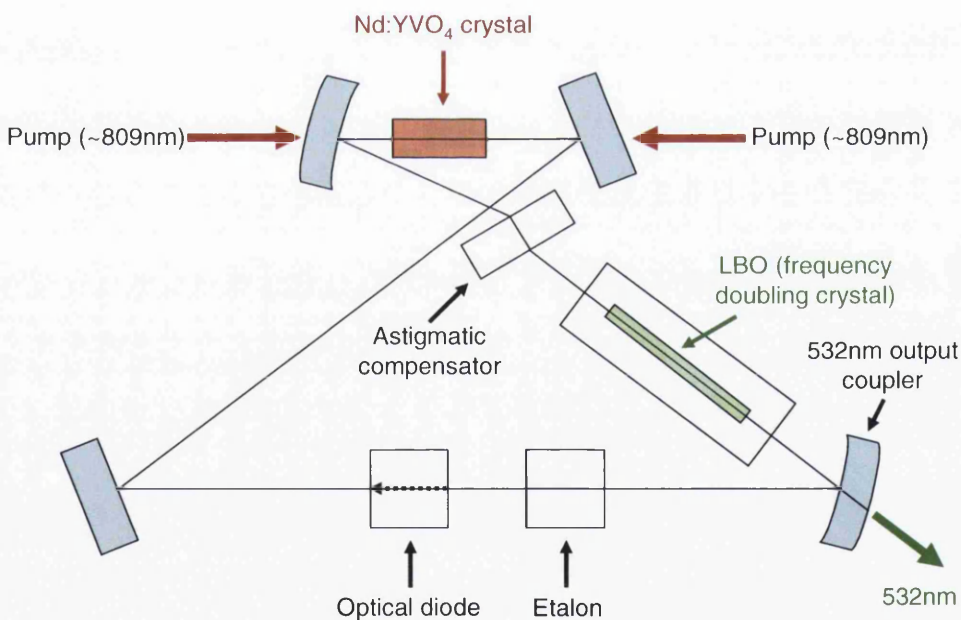
Typically, mode hops in these modules are much smaller than the large jump shown in Figure 4.4, and are of the order of  $\sim 0.0005\text{nm}$  ( $\sim 0.02\text{cm}^{-1}$  at 532nm). Once stabilised at its operating temperature, wavelength fluctuations of this size in a laser module's output would not be observed by the spectroscopic apparatus used in this work.



### 4.1.2 The Nd:YVO<sub>4</sub> laser

The Nd:YVO<sub>4</sub> laser operates at nearly the same wavelength as the Nd:YAG laser but has several advantages over the latter type that make it more amenable to diode pumping, namely a larger stimulated emission cross section and a wider pump absorption band centred at 809nm\*, which makes the laser more adaptable to temperature (and hence wavelength) changes of the laser pumping diode. The laser transition is  ${}^4F_{3/2} \rightarrow {}^4I_{11/2}$  (as for Nd:YAG), with an output wavelength of 1064.3nm

Figure 4.5 shows the layout of the Coherent *Verdi V5* Nd:YVO<sub>4</sub> laser head, which was used as the excitation source at TLK (see Chapters 5 and 6), and is typical of second-harmonic (532nm) Nd:YVO<sub>4</sub> lasers in general.



**Figure 4.5** Optical schematic of the Coherent *Verdi V5* Nd:YVO<sub>4</sub> laser head, showing the two pump and two end mirrors, the LBO crystal used for second harmonic generation, an etalon as the single-frequency optic, an optical diode to achieve unidirectional operation and an astigmatic compensator. Adapted from the Coherent *Verdi* Laser Operator's Manual (1997)

\* Pumping in Nd:YVO<sub>4</sub> occurs from the  ${}^4I_{9/2}$  ground state to the  ${}^4F_{3/2}$  pumping band. This band is less resolved in Nd:YVO<sub>4</sub> than in Nd:YAG, and so the absorption band at the pump wavelength of 809nm is much broader.

In the *Verdi V5*, the nonlinear medium used for second harmonic generation is a Type I, non-critically phase-matched LBO crystal. Due to the sensitive optical coatings on this crystal, the LBO has to be raised and lowered slowly to and from its operating temperature of approximately 142°C by a resistive heater. This element dictates the warm-up time of the laser system of at least 45min. Table 4.3 lists typical parameters for Nd:YVO<sub>4</sub> lasers of this type:

**Table 4.3** Design parameters for second-harmonic generating Nd:YVO<sub>4</sub> lasers.

Parameter	Value
Laser wavelength (doubled) / nm	532
Laser gain medium length / m	0.10
Doping density / m <sup>-3</sup>	1% atomic Nd
Refractive index of gain medium	1.958 at 1064nm 2.009 at 550nm
Operating temperature / K	300
Optical pumping method	Diode (809nm)
Output power / W	Up to 18W+
Polarisation	Vertical (>100:1)
Mode	Single (TEM <sub>00</sub> )

As discussed for the Nd:YAG lasers, more pragmatic parameters are usually of interest in experimental work. Table 4.3 lists these parameters for the purpose of comparison with those quoted for the 10mW Nd:YAG module in Table 4.2.

**Table 4.4** Operating parameters of the Coherent *Verdi V5*. Values taken from the Coherent *Verdi* datasheet (Coherent (2005)).

Parameter	Value
Output power / W	0.01 to 5.00 (user-selectable)
Power stability / %	±1
Beam diameter / mm	~2.25±0.23
Beam divergence / mrad	<0.5
Polarisation	vertical, >100:1
Warm-up time / min	~45
Operating temperature / °C	15 to 35
Head size / mm	139.7 × 108.8 × 464.3
Expected life time / hrs	Guaranteed for 5000

As one would expect for such a high-quality laser, the performance of the *Verdi V5* comfortably exceeds that of the smaller Nd:YAG modules. Of particular interest are the lower beam divergence, excellent polarisation characteristics.

The *Verdi* laser is, however, a large unit whose laser head is connected to the power supply via a bulky umbilical, requiring careful consideration of the experimental setup when available space is at a premium (as is the case at KATRIN, see Section 6.2.1). Further, the laser head generates over 30W of thermal energy, which is dissipated via the integrated heatsink on the underside of the module. It is therefore essential that the heatsink has good contact with the spacer that connects the head to the breadboard, and that the spacer itself should have a good contact with the breadboard in order to correctly dissipate the thermal energy.

## 4.2 *Interaction (Scattering) Region*

Before the laser light reaches the interaction region, it may be steered by one or more mirrors, and due to the low intensity of Raman scattered radiation, the beam will invariably need to be focussed down in order that sufficiently high power densities are achieved in the scattering volume. Since 532nm beams have been used throughout, all such beam path optics have either 532nm antireflection (AR) coatings (in the case of lenses) or suitable 532nm high reflectivity (HR) coatings (in the case of mirrors).

Both liquid (ethanol, propan-1-ol, etc.) and gaseous (hydrogen isotopomer mixture) samples have been used. Initially, the liquid samples were contained in a plain glass cell (no special coatings) since measurements on these samples were either for qualitative, 'proof of principle' investigations, or (in the case of ethanol) for alignment purposes (see Section 4.3.1). Later, for reasons of mechanical reproducibility (i.e. when switching from the alignment ethanol sample back to the target gas sample), a LARA cell was filled with ethanol. The gaseous samples were all probed in a LARA cell.

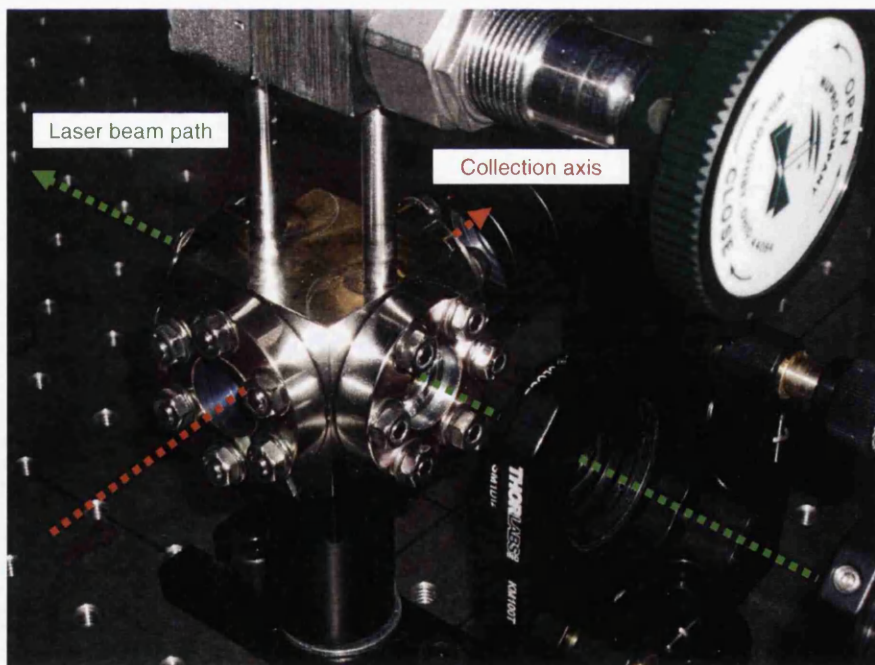
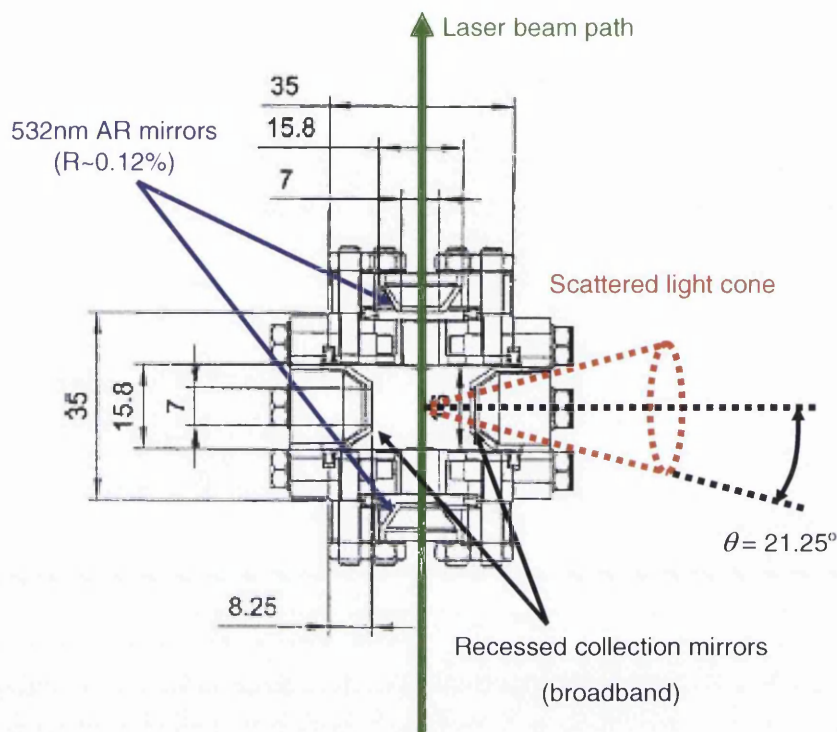


### 4.2.1 *The LARA cell*

Raman experiments typically employ one of two geometries:  $90^\circ$  or  $180^\circ$ . The  $180^\circ$  (backscattering) geometry is perhaps the most common geometry used in modern Raman spectroscopic instrumentation, particularly in Raman microscopes and fibre-optic probes. Since the excitation and collection axes coincide, the  $180^\circ$  geometry is easier to reproduce experimentally, which is essential if absolute measurements of intensity have to be made. The  $180^\circ$  geometry is also more flexible and in general easier to use than the  $90^\circ$  geometry, although at an expense of complication in the instrumentation (McCreery (2000)).

As mentioned in the preamble to this chapter the design of the gas cell used was essentially fixed as the LARA cell design used by Taylor et al. (2001) for use with the ASER signal enhancement apparatus at TLK. Figure 4.6 shows the design of the LARA cell, which apart from the windows and valve components is made entirely of stainless steel. Five LARA cells were in working order at the time of writing.

The cell windows in the beam path are spaced as far apart as possible in order to minimise the power density of the focussed beam at these windows and thus avoid damage to the antireflection coatings (see Section 4.2.2). The collection windows on the other hand are recessed into the cell in order to maximise the collection angle – the half angle is approximately  $21.25^\circ$ . In contrast to the beam path windows, the collection windows are broadband coated to maximise transmission. The valves atop the cell allow the cell to be connected to a gas loop.

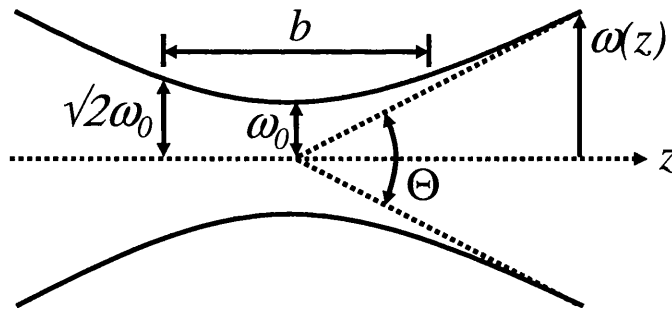


**Figure 4.6** The LARA gas cell used throughout this work for the containment of gaseous samples. Top: LARA cell design, showing the 532nm AR windows used in the beam path (spaced as far apart as possible in order to minimise the power density at the windows and avoid damage to the coatings) and the broadband collection mirrors, recessed into the cell in order to maximise the collection angle. Bottom: LARA cell in use, showing the beam and collection axes and the valves used to connect the cell to the gas loop.

### 4.2.2 Geometry of the interaction region

We will now briefly examine the (beam) geometry at the interaction region and the considerations that have to be made when designing a Raman scattering experiment given the need to use the LARA cell. Specifically, we wish to find the optimal balance between the desire to have a large confocal parameter (i.e. tending towards a long focal length) with the need to avoid exceeding the damage threshold of the antireflection coatings at the position of the beam path widows (i.e. tending towards a short focal length).

In Figure 4.7 the focal region of a focussed Gaussian beam is shown (see also Figure 3.7 in Chapter 3). This diagram represents the geometry of the scattering volume that we wish to image onto the CCD chip of the detector. Note that in order to simplify the numerical estimates (but without loss of generality), the point  $z = 0$  has been set to be the focal point. Here, the  $z$ -axis is the beam path axis as shown in Figure 4.6, and the focal point is taken to be at the centre of the cell on this axis.



**Figure 4.7** The geometry of a focussed Gaussian beam. The red line represents the beam radius  $\omega(z)$ ,  $\Theta$  is the beam divergence, and  $b$  is the confocal parameter.

The function describing the beam radius is given by

$$\omega(z) = \omega_0 \sqrt{1 + \left(\frac{z}{z_0}\right)^2}, \quad (4.1)$$

where, as defined in Section 3.3.5,  $z_0 = b/2$  is the depth of focus. We can calculate the spot size of a focussed laser beam at the beam waist,  $\omega_0$ , given the laser beam's wavelength and radius at the lens, and the focal length of the lens. Since the parameter  $\omega(z)$  approaches a straight line (geometrical optics limit) for  $z \gg z_0$ , the angle,  $\theta$ , between the beam axis and  $\omega(z)$  for large  $z$  is given by

$$\theta = \tan^{-1} \left( \frac{\lambda}{\pi \omega_0} \right). \quad (4.2)$$

Rearranging equation (4.2) to obtain an expression for  $\omega_0$  yields

$$\omega_0 = \frac{\lambda}{\pi \tan \theta} = \frac{\lambda f}{\pi R}, \quad (4.3)$$

where  $f$  is the focal length of the lens, and  $R$  is the radius of the laser beam at the lens.

An example from the experiments carried out at the TILO facility (see Chapter 6) is that of a 3mm diameter 532nm laser beam focussed by a lens with  $f = 175\text{mm}$ . In this case the spot size would be

$$\omega_0 = \frac{(532 \times 10^{-9})(175 \times 10^{-3})}{\pi(1.5 \times 10^{-3})} \approx 20 \mu\text{m}. \quad (4.4)$$

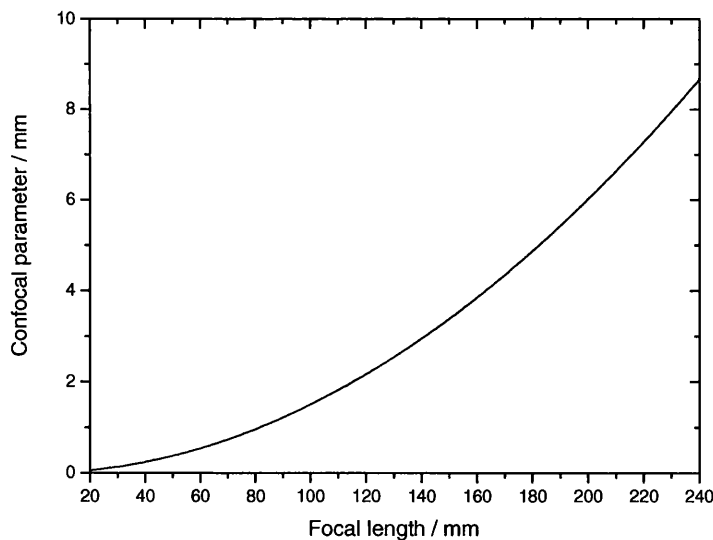
At the 3W output power typically used in those experiments, this corresponds to a power density of  $\sim 2.4 \times 10^9 \text{ Wm}^{-2}$  at the focal point. The corresponding confocal parameter given by equation (4.4) is

$$b = 2z_0 = \frac{2\pi\omega_0^2}{\lambda} \approx \frac{2\pi(20 \times 10^{-6})^2}{(532 \times 10^{-9})} \approx 5\text{mm}. \quad (4.5)$$

In order to maximise the sensitivity of the spectroscopic system as a whole, it is desirable to set the confocal parameter to match the height of the CCD chip (assuming 1:1 imaging, as is the case in this thesis throughout). In the case of the Spec-10 detector, the height of the CCD chip is 6mm. The above example might suggest that the 175mm focal length of the lens used is too short. However, one must also consider the power densities at the beam path windows. These are situated at  $\sim 9\text{mm}$  from the scattering volume. Substituting for  $\omega_0$  and  $z_0$  from equations (4.4) and (4.5), and setting  $z = 17.5 \times 10^{-3}$  into equation (4.1) yields

$$\omega(z) = 20 \times 10^{-6} \sqrt{1 + \left( \frac{17.5 \times 10^{-3}}{2.5 \times 10^{-3}} \right)^2} \approx 141 \mu\text{m}. \quad (4.6)$$

For a 3W laser beam this corresponds to a power density of  $\sim 0.05 \times 10^9 \text{ Wm}^{-2}$ , which is well below the damage threshold for the AR coating of the LARA cell. One can use equation (4.5) to construct a graph of confocal parameter with respect to focal length, as shown in Figure 4.8.



**Figure 4.8** Dependence of the confocal parameter with respect to the focal length of the focussing lens. The focal length at which the confocal parameter matches the CCD chip height of 6mm is about 200mm.

Over the range of focal lengths shown in Figure 4.8, the *Verdi V5* will not exceed the damage threshold of  $\sim 2 \times 10^{12} \text{ Wm}^{-2}$  for the antireflection coatings of the LARA cell



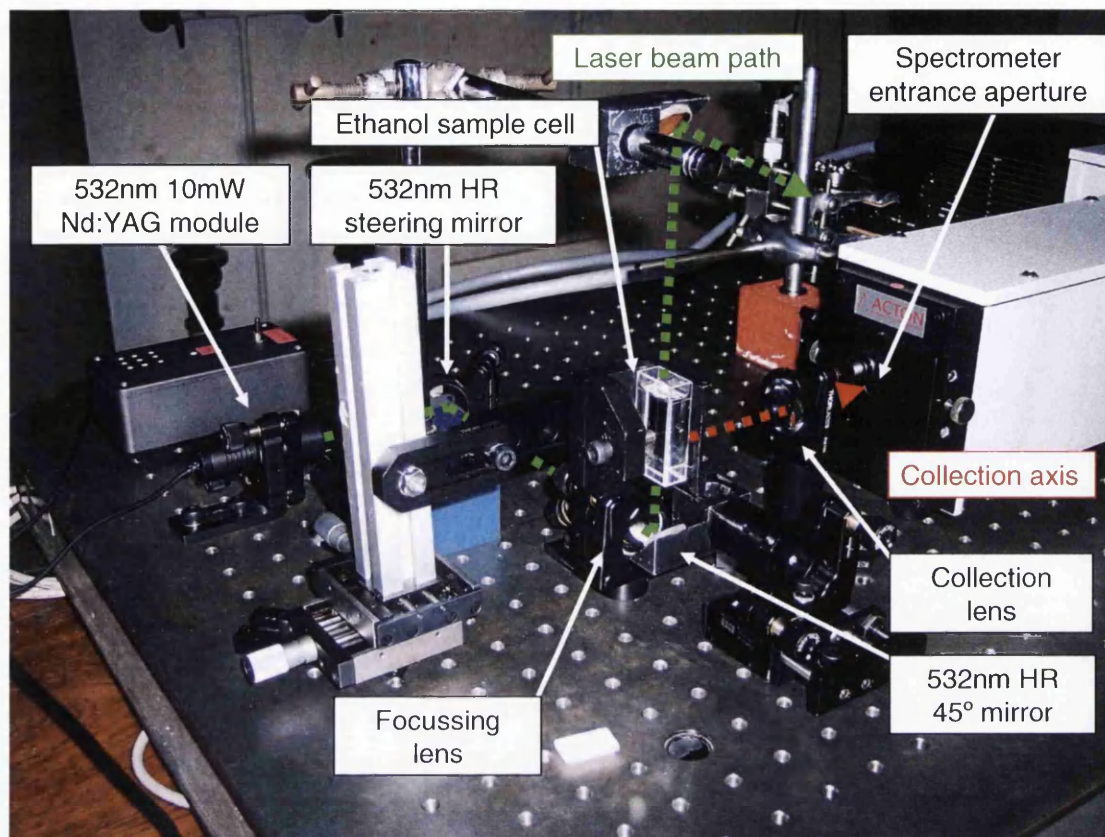
windows, even when running at its maximum power output of 5W. It would seem, therefore, that a ~200mm focal length lens would be the optimum, as the confocal parameter is then matched to the CCD chip height. One should bear in mind, however, that the system will be less sensitive to errors in CCD chip centreline alignments relative to the 1:1 image of the scattering volume. The 175mm lens currently used represents a sensible compromise, as it allows for slight errors in alignment, and has a confocal parameter nearly equal to the CCD chip height.

### *4.3 Transportation of scattered light*

Our experiments make use of three distinct techniques to transport a 1:1 image of the interaction region onto the CCD chip in the detector, namely direct-, translational- and fibre-coupled imaging. The goal of each imaging technique is the same, but there are specific advantages and disadvantages to each method that must be borne in mind when deploying a given technique. Of particular importance is the effect on the polarisation of the scattered light, as the efficiency of spectrometer gratings is dependent on the polarisation of the incident light.

#### *4.3.1 Direct imaging*

Direct imaging is perhaps the simplest technique. The laser beam is passed through the sample parallel to the entrance slit of the spectrometer. A lens is placed between the sample and the spectrometer such that the scattering volume and the entrance slit are positioned at the focal points of the lens. The optimal choice of lens focal length will depend on the available solid angle from the scattering volume (see Section 4.2.1) and the acceptance angle of the spectrometer (see Section 4.4). Figure 4.9 shows a typical direct imaging setup.



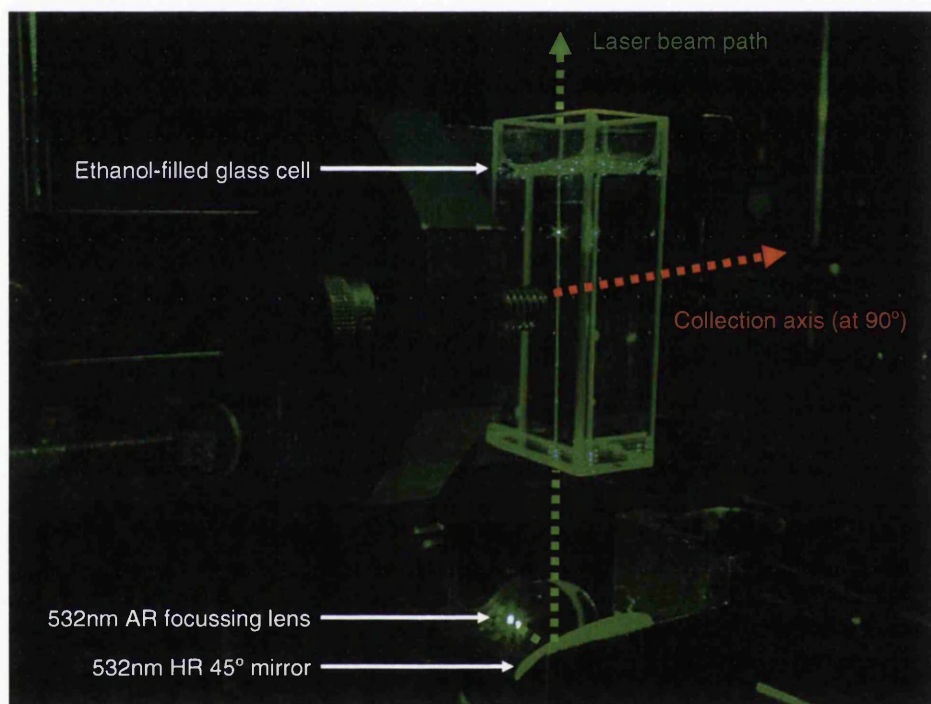
**Figure 4.9** Direct imaging setup at Swansea used to record the Raman spectrum of liquid ethanol (contained in the glass cell). The vertical section of the laser beam path (green dashed line) and the axis of the spectrometer entrance aperture are parallel, and are positioned at the focal points of the intervening collection lens along the collection axis (red dashed line). The imaging is clearly 1:1. The polarisation of the scattered light is unaffected by direct imaging.

A direct imaging setup does not affect the polarisation of the scattered light as the only intervening optical element is the lens. The lens itself should have a broadband anti-reflection coating to maximise transmission.

The only real point of concern with direct imaging is one of available space. Provided there is enough space to direct the beam vertically, to fit the sample holder and collection lens in front of the spectrometer, and to dump the laser beam, direct imaging is the easiest of the three arrangements to set up and align, at least in principle.

Direct imaging was used throughout the comparative review described in Chapter 5. Ethanol samples were used to align the systems. The acquisition software for both systems

was capable of taking short ( $<1s$ ), repeat measurements in quick succession, allowing for near real-time adjustment of the beam path and optimisation of the collection lens' position and / or orientation. Figure 4.10 shows an ethanol sample in a simple glass cell being used to align the UWS HTS/Spec-10 system. The Rayleigh scattering is visible to the naked eye.



**Figure 4.10** Ethanol sample in a simple glass cell being used to align the HTS/Spec-10 system used at Swansea. The Rayleigh scattering is clearly visible. The (relatively) strong Raman signal from liquid ethanol provides a convenient way to align the system by adjusting for maximum Raman signal strength.

A 2-axis mirror mount below the cell is used to steer the beam through the cell. The collection lens is on a moveable 2-axis mount to allow for adjustment of both position and orientation. The focussing lens has been set so that the focal point is at the height of the centre of the spectrometer entrance slit. Both the cell and the collection mirror are height-adjustable in order to align their centres to the height of the centre of the entrance slit.

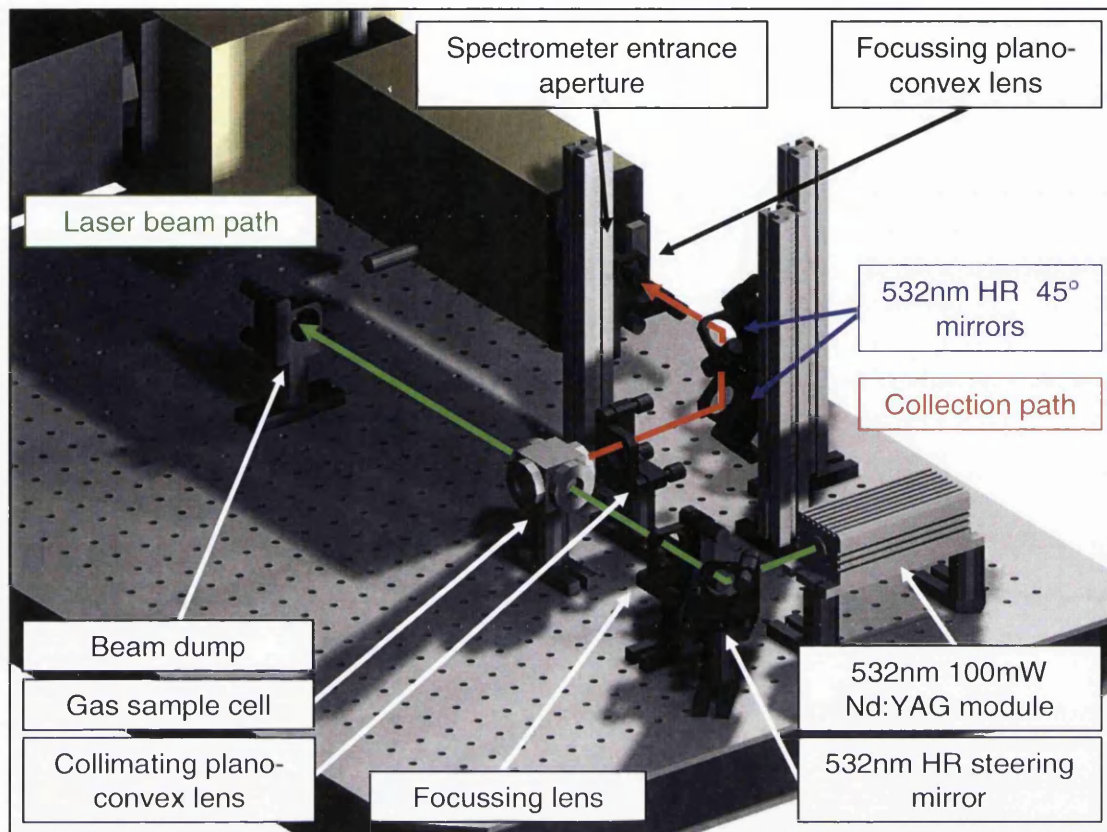
Note that direct imaging was not a feasible option with the TILO / KATRIN designs described in Chapter 6 due to the lack of available space. This type of imaging was used to

test the spectrometer parameters during the initial set-up phase, and so avoided the need for considering potentially complex parameters in the light transport system.

The space allocation was in fact the critical factor when designing the bench onto which the monitoring system was to be mounted when operating at TILO or (later) KATRIN. The important point is that the beam could only be safely used if it were kept in a horizontal orientation throughout its path from laser head to dump. With rotation of the spectrometer to orient the slit horizontally not a viable option, intervening optics would have been required to transport an image of the horizontally-oriented scattering volume to the vertically-oriented entrance slit of the spectrometer.

#### *4.3.2 Translational imaging*

Translational imaging is not too dissimilar from the direct-imaging technique. Instead of using a single convex lens to transport a 1:1 image directly onto the entrance slit of the spectrometer, two plano-convex lenses were used in conjunction with two mirrors. One lens collimates the scattered light onto a system of two mirrors oriented at  $45^\circ$  to the vertical and at  $90^\circ$  to each other; the mirror set rotates the image from the horizontal to the vertical. The second plano-convex lens is used to focus the now vertically-oriented image onto the entrance slit of the spectrometer. Thus, the two mirrors can be thought of as an image rotator between the faces of a single collection lens. The translational imaging arrangement used at Swansea is shown in Figure 4.11.



**Figure 4.11** Translational imaging setup used with the HTS/Spec-10 system at Swansea. The scattering volume is at the focal point of the collection (collimating) plano-convex lens, while the entrance slit of the spectrometer is at the focal point of the focussing (collection) plano-convex lens<sup>†</sup>. The two mirrors rotate the image of the scattering volume from horizontal to vertical.

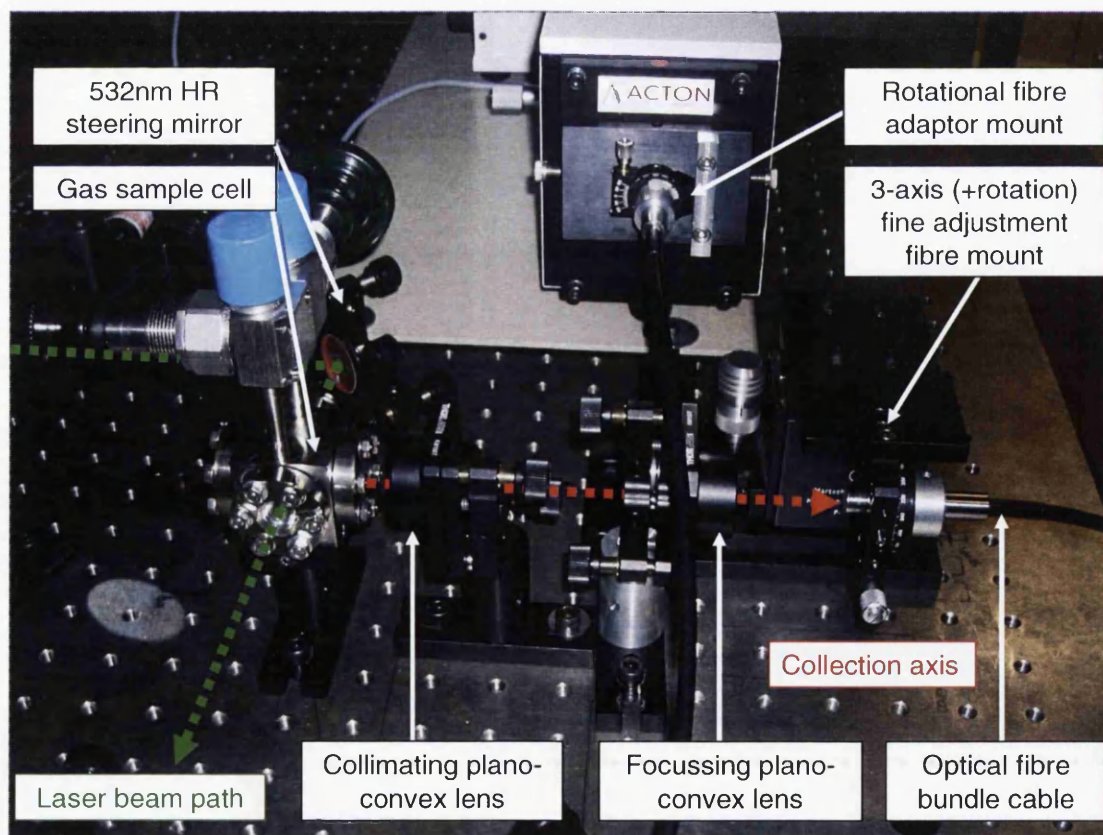
Unlike direct imaging, translational imaging rotates the image of the scattering volume by  $90^\circ$  and so rotates the plane of polarisation of the scattered light by  $90^\circ$  as well. This should be borne in mind when correcting for the grating efficiency, for example (see Section 4.7.6). Since a certain amount of space is required into which to allow adjustment of the  $45^\circ$  mirrors, it was necessary to raise the HTS/Spec-10 system by 50mm in order to comfortably fit the mirrors above the beam height of 75mm. The details of how the HTS/Spec-10 translational imaging system was aligned are given in Section 5.5.3,

<sup>†</sup> In the case of the HTS/Spec-10 system, the ‘entrance slit’ is the focal point of the collimation lens of a dedicated edge filter unit that is permanently attached in front of the spectrometer entrance slit (see Section 4.4.2). Since light focused onto this point will be in turn focussed onto the entrance slit of the spectrometer, the end result is the same regardless of whether we are referring to the ‘actual’ entrance slit or not.

although it can be noted here that alignment of the system was relatively straightforward, with no significant increase in difficulty when compared with the direct imaging method.

### 4.3.3 Fibre-coupled imaging

Coupling of the scattered radiation to the spectrometer by means of an optical fibre provides the greatest flexibility when designing an experimental setup, especially when space is limited, as is the case in the TILO / KATRIN monitoring system. A further advantage is that the fibre can be fixed at the spectrometer end (the HTS/Spec-10 system has a dedicated fibre mount), so the concerns regarding mechanical stability are confined to the collection end of the fibre. Figure 4.12 shows the setup of the fibre-coupled HTS/Spec-10 system used at Swansea to test the viability of this imaging technique.



**Figure 4.12** Fibre-coupled configuration of the HTS/Spec-10 system at Swansea. Due to the highly sensitive nature of the system alignment, the two plano-convex lenses are separated for flexibility of adjustment, and the optical fibre itself can be adjusted rotationally in mounts at both ends of the fibre.

The optical fibre cable used in the HTS/Spec-10 system is a 3m-long bundle of 48 100 $\mu\text{m}$  / 125 $\mu\text{m}$  (core / cladding) step-index multimode fibres arranged into a slit-shaped configuration (single file). The total length of the slit matches the height of the CCD chip in the Spec-10 detector (6mm), and the bundle is matched to the acceptance angle of the HTS spectrometer. Since the scattering volume is imaged 1:1 onto the slit-shaped bundle of the optical cable, it is absolutely essential to have high-precision 3-axis and rotational adjustment of the fibre position.

Note that there is no correlation in the sequence between individual fibres at one end of the bundle to the other. It should also be noted that in passing through the fibre bundle, the scattered light is essentially depolarised. When correcting for grating efficiency (see Section 4.7.6), therefore, one should use the average grating response.

Compared to the case of direct and translational imaging configurations, fibre-coupling the scattered light to the spectrometer is relatively involved. The main difficulty is associated with the collection end of the fibre bundle due to the narrow acceptance angle of the fibre. The numerical aperture, NA, of the fibre bundle is related to the critical angle (acceptance half-angle) by the expression (see, e.g., Goure and Verrier (2002)):

$$\text{NA} = \eta_{\text{air}} \sin(\theta_{\text{ca}}), \quad (4.7)$$

where  $\eta_{\text{air}}$  is the refractive index of air, and  $\theta_{\text{ca}}$  is the critical angle.

The NA of the fibre bundle can be determined from the refractive indices of the core and cladding and in this case is equal to  $0.22 \pm 0.02^\ddagger$ . Rearranging equation (4.7), and substituting for NA and setting  $\eta_{\text{air}} = 1$  yields

$$\theta_{\text{ca}} \approx \sin^{-1}(0.22) = 12.7^\circ. \quad (4.8)$$

---

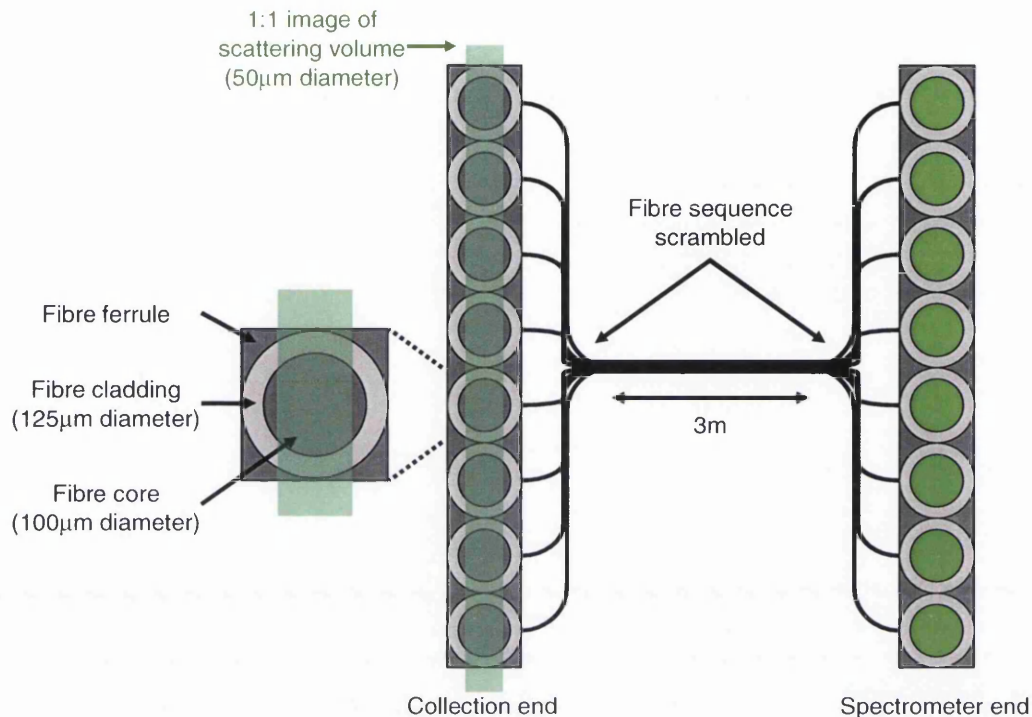
<sup>‡</sup> The uncertainty in the value of NA reflects the dependence of the refractive indices on wavelength. The value quoted is the value in the median of the fibre's useful wavelength range.

This value can be used to determine the optimum focal length for a given diameter of lens. All our beam path optics have been standardised to 25mm diameter. Simple trigonometry then yields an optimum focal length of ~55.5mm. In the system, plano-convex lenses of 50mm focal length are used, so the focussing is (slightly) too tight. This, however, has little overall effect on the sensitivity of the system. The primary difficulty with a small acceptance angle is the issue of keeping the fibre parallel with the optical axis in order to collect as much light as possible while at the same time being able to make the necessary 3-axis and rotational fine adjustments.

Another point of note with a fibre-coupled system is the introduction of loss in the signal. These losses can be categorised (broadly following the collection-transmission-collection order) as: geometrical losses (GL), reflection losses (RL), attenuation losses (AL), and diffraction losses (DL). These are considered separately below.

Geometrical losses are introduced at the collection end of the fibre due to the discontinuous nature of the slit-shaped bundle. When the continuous image of the scattering volume is focussed onto the discontinuous slit-shaped fibre bundle, only light that (correctly) enters the core of the individual fibres will be transmitted – light that falls onto the cladding or ferrule will be lost, as shown in Figure 4.13.





**Figure 4.13** 1:1 imaging of the scattering volume produced by a 25mm diameter,  $f = 175\text{mm}$  lens focussing a 3mm diameter laser beam onto the slit-shaped bundle of 48 100/125µm (core/cladding) fibres (8 of which are shown here). The scattering volume has been approximated as a cylinder of 50µm diameter. Light that falls onto the cladding or ferrule is lost, and there is also a significant portion of the core that is not utilised. The total loss is approximately 20% when compared with a (hypothetical) continuous collection of the scattered light.

Taking the example given in Section 4.2.4 of the scattering volume size produced by a 25mm diameter,  $f = 175\text{mm}$  lens focussing a 3mm diameter laser beam, we can reasonably approximate the scattering volume to be a cylinder of  $\sim 50\mu\text{m}$  diameter ( $1/e^2$  point in the intensity distribution) over the  $\pm 3\text{mm}$  axial displacement from the focal point. Assuming 1:1 imaging, and that the image falls along the line joining the centres of the fibres, it can be shown from geometrical considerations that the loss due to light falling onto the cladding is indeed approximately 20%.

For the light that enters the core of the fibre, one can expect losses (at both ends) due to reflection. Reflection losses at each end can be calculated to a good expression from the expression:

$$RL = \left( \frac{\eta_{\text{core}} - \eta_{\text{air}}}{\eta_{\text{core}} + \eta_{\text{air}}} \right)^2, \quad (4.9)$$

where  $\eta_{\text{core}}$  and  $\eta_{\text{air}}$  are the refractive indices of the fibre core and the air, respectively. The datasheet quotes  $\eta_{\text{core}} = 1.4571$  at 633nm in our case, so by setting  $\eta_{\text{air}} = 1$  we can estimate the total reflection losses,  $RL_{\text{total}}$ , by multiplying equation (4.9) by 2 and substituting in these values for  $\eta_{\text{core}}$  and  $\eta_{\text{air}}$ :

$$RL_{\text{total}} = 2RL \approx 2 \left( \frac{1.4571 - 1}{1.4571 + 1} \right)^2 \approx 0.07, \text{ i.e. } 7\%. \quad (4.10)$$

Attenuation (absorption) losses are generally only a serious problem for very long (>1km) fibres (in telecommunications, for example), whereas the fibre bundle in our case is only 3m in length. At ~600nm, one can expect an attenuation of approximately 10dB/km (~99.5% transmission / m) in an optical fibre. Therefore, over 3m, the attenuation loss is likely to be approximately 1.5 to 2%.

Diffraction losses can be difficult to accurately quantify in multi-mode fibres, as is the case here. One can, however, make a reasonable estimate by examining the equation for the intensity distribution at a circular aperture:

$$I(\theta) = I_0 \left[ \frac{2J_1(u)}{u} \right]^2, \quad (4.11)$$

where  $I_0$  is the peak intensity (pattern maximum),  $J_1$  is a Bessel function of the first kind (of order unity), and the parameter  $u$  is given by

$$u = \left[ \frac{\pi D}{\lambda} \right] \sin \theta, \quad (4.12)$$

where  $D$  is the aperture diameter,  $\lambda$  is the wavelength of the light, and  $\theta$  is the angular radius from the pattern maximum. The pattern produced consists of a series of circular maxima and minima. The angular positions of the maxima are given by

$$\theta_m = \sin^{-1}\left(\frac{n\lambda}{D}\right), \quad (4.13)$$

where  $m$  is the order of the maximum. The pattern maximum is the zeroth ( $n=0$ ) order maximum. For single-mode fibres, the angular radius of the first-order maximum is rather small. For a  $6\mu\text{m}$  diameter single-mode fibre at  $\lambda = 600\text{nm}$ , the angular radius of the first-order maximum,  $\theta_1$ , is

$$\theta_1 = \sin^{-1}\left(\frac{600 \times 10^{-9}}{6 \times 10^{-6}}\right) \approx 0.1 \text{ rad } (\sim 6^\circ). \quad (4.14)$$

In comparison, for a multi-mode fibre of  $100\mu\text{m}$  diameter at  $\lambda = 600\text{nm}$ ,  $\theta_1$  is an order of magnitude smaller:

$$\theta_1 = \sin^{-1}\left(\frac{600 \times 10^{-9}}{100 \times 10^{-6}}\right) \approx 6 \times 10^{-3} \text{ rad } (\sim 0.3^\circ). \quad (4.15)$$

Note that for a single-mode fibre (core diameter  $\sim 6\mu\text{m}$ ), due to the relatively large value of  $\theta_1$ , it is likely that only the pattern maximum ( $n=0$ ) would contribute to the signal. Integrating equation (4.11) up to the first minima shows that in this case  $\sim 84\%$  of the intensity will be transmitted.

In the case of multi-mode fibres, the value of  $\theta_1$  is much smaller, and it is likely that a few of the higher orders will also contribute to the signal. If we assume that the  $n=0,1,2$  maxima can contribute, then on integrating equation (4.11) we find that  $\sim 94\%$  of the intensity is observed (i.e. a  $\sim 6\%$  loss due to diffraction).

Using the above values for GL, RL, AL and DL, the total loss due to the inclusion of the fibre,  $FL_{\text{total}}$  can then be estimated as

$$FL_{\text{total}} = (1 - GL) \times (1 - 2RL) \times (1 - AL) \times (1 - DL) \approx 0.32, \text{ i.e. } 32\%. \quad (4.16)$$

This loss is significant, but can be tolerated, the more since it is partially offset by the reduction in scattered light entering the spectrometer. This loss in a fibre coupling arrangement stands in contrast to the direct and translational imaging techniques, where the exclusive use of HR mirrors and AR lenses between the scattering volume and spectrometer entrance slit means that losses are likely to be of the order of 2-3% only.

There are further complications in system alignment at the spectrometer end due to Fraunhofer / Fresnel regime transition. These are discussed along with the evaluation of the fibre-coupled system in Section 6.1.1. It should be noted that despite the difficulties in aligning the system and the diffraction losses incurred by the optical fibre bundle, once the system is set up correctly it is very robust (aided in part by the excellent pointing stability of the lasers employed) and needs little in the way of further adjustment.

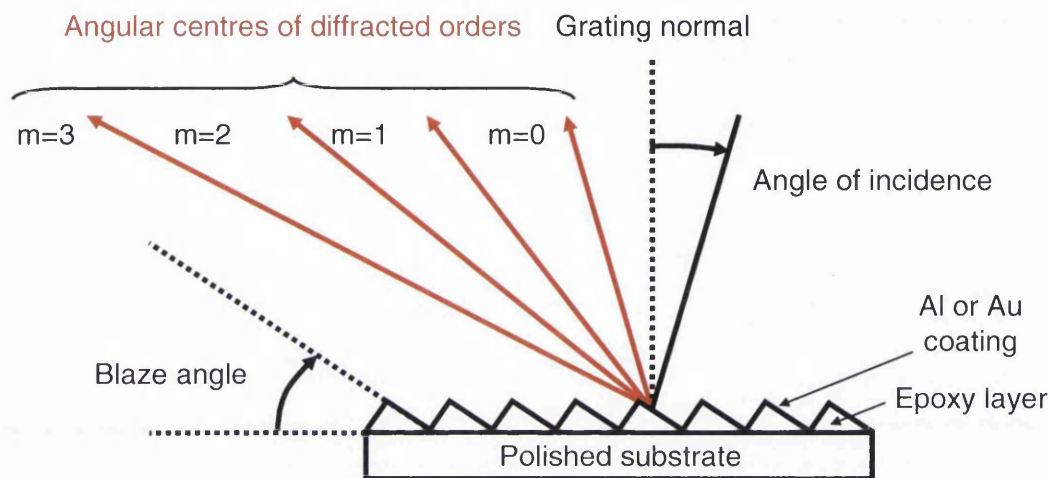
#### 4.4 Spectrometers

As briefly mentioned in Section 4.1, all spectrometers used in this work are of the spectrograph (large bandpass)<sup>§</sup> rather than the monochromator (narrow bandpass) type. These spectrometers can be roughly divided into two main types: the ubiquitous Czerny-Turner type which makes use of imaging mirrors in folded-pass configuration to reduce the overall length of the instrument, and the transmitting optics-type which use suitable lenses to achieve the same effect, but normally in rather smaller dimensions. Since only two spectrometers have been used in the whole of our work, and the comparative review deals with their performance in some detail, only a brief overview is given here.

---

<sup>§</sup> The bandpass is the wavelength range that is passed through the exit slit / plane of the spectrometer and onto the detector.

The basic principle behind all spectrometers is the dispersion of light by a diffraction grating, as shown in Figure 4.14.



**Figure 4.14** Dispersion of light by a (reflection) diffraction grating, showing the angular centres of several diffraction orders (the angular extent of higher orders will tend to overlap). In the case of the zeroth ( $m=0$ ) diffraction order, the grating acts as a mirror and there is no dispersion. The blaze angle is set to maximise the grating reflectivity in a particular (spectral) region of interest.

The physics of diffraction gratings is well-known, so only the following three relevant points need concern us here. Firstly, the reflectivity (or efficiency) of a diffraction grating is dependent on the polarisation of the incident light. This is a particularly important consideration when attempting to correct for the wavelength dependence of the grating efficiency (see Section 4.7.6). Secondly, the zeroth diffraction order is a specular reflection. In small transmitting optics-type spectrometers this reflection can potentially be passed through the system via a secondary reflection from one of the internal optical elements, for example if the diffraction grating is oriented with a near-normal angle of incidence (see Section 5.5.1). In Czerny-Turner spectrometers this is usually not a problem due to the much larger size of the instrument. Thirdly, the reflectivity response (efficiency) of the grating is wavelength dependent. This should be corrected for if full quantitative analysis is to be performed – see Section 4.7.6.

Many spectrometers have several gratings installed to vary the resolution range available to the user, as is the case in the *TRIA320* Czerny-Turner spectrometer used in the old TLK

system (see Section 5.1). The HTS used at Swansea (see Section 5.2) has only a single grating. The important parameter is the density of grooves, usually quoted as grooves per millimetre ( $\text{gr}\cdot\text{mm}^{-1}$ ). The higher the number of grooves, the higher the potential resolution, but the bandpass and intensity of the light are correspondingly lower. The resolution is also affected by the entrance slit width – the narrower the entrance slit, the narrower the observed linewidths will be (potentially down to the diffraction limit), but since less light is admitted to the spectrometer, the lines will be of lower intensity than at wider slit widths. The reader is referred to a standard textbook such as McCreery (2000) or Demtröder (2003) for more details.

A commonly-quoted figure on spectrometer datasheets will be the f-number. This number is related to the solid angle that the spectrometer can accept and is a useful indication of the light gathering power of the instrument. The f-number relates the effective diameter of the entrance pupil<sup>\*\*</sup>,  $D$ , to the focal length,  $f$ , of the instrument by the following expression:

$$f/\# = N = \frac{f}{D}. \quad (4.17)$$

The f-number is related to the solid acceptance angle of a spectrometer,  $\Omega$ , by

$$\Omega \propto \left( \frac{1}{f/\#} \right)^2. \quad (4.18)$$

One can therefore compare the light gathering power of two spectrometers A and B by evaluating the ratio

$$\frac{\Omega_A}{\Omega_B} \propto \left( \frac{f/\#_B}{f/\#_A} \right)^2, \quad (4.19)$$

---

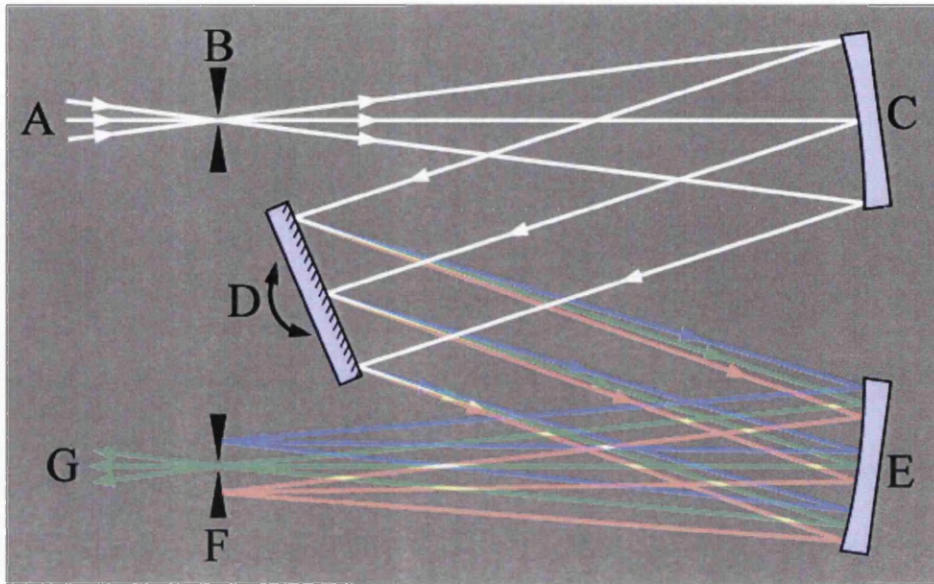
<sup>\*\*</sup> One can think of the entrance slit width of a spectrometer in the same way.

where  $\Omega_A$  and  $\Omega_B$  are the solid acceptance angles of spectrometer A and B, respectively, and  $f/\#_A$  and  $f/\#_B$  are the f-numbers of spectrometer A and B, respectively. For example, an  $f/2$  spectrometer will have a 16-fold greater light-collecting power than an  $f/8$  spectrometer.

#### 4.4.1 Czerny-Turner spectrometers

A typical Czerny-Turner spectrometer configuration is shown in Figure 4.15. The incident light (A) passes through the entrance slit (B) and is collimated by the spherical mirror (C). The dimensions of the spectrometer (B-C) determine the acceptance angle and hence the f-number of the system, while the entrance slit can be narrowed to decrease the linewidth of detected spectral lines (theoretically down to the diffraction limit, but mechanical considerations are usually the limiting factor) or widened to increase the light gathering power (at the expense of a wider detected linewidth, which might make resolving closely spaced lines more difficult).

The collimated light is dispersed by the diffraction grating (D) and is focussed on the exit slit / detector focal plane (F). The bandpass is the wavelength range that is detected at (G). The diffraction grating can usually be rotated to select the central wavelength of the bandpass, and it is common for Czerny-Turner spectrographs to have several different gratings installed on a turret.



**Figure 4.15** Typical Czerny-Turner spectrometer configuration, showing the incident light (A), the entrance slit (B), collimating mirror (C), diffraction grating (D), entrance slit (F) and bandpass (G).

The *TRIAX320* spectrometer used at TLK for use in the LARA experiments detailed in Taylor et al. (2001) and the comparative review in Chapter 5 is of this type, with two installed gratings (2400 and 600 $\text{gr}\cdot\text{mm}^{-1}$  densities, which can be switched and oriented via computer control), room on the grating turret for a grating, and has an f-number of  $f/8$ .

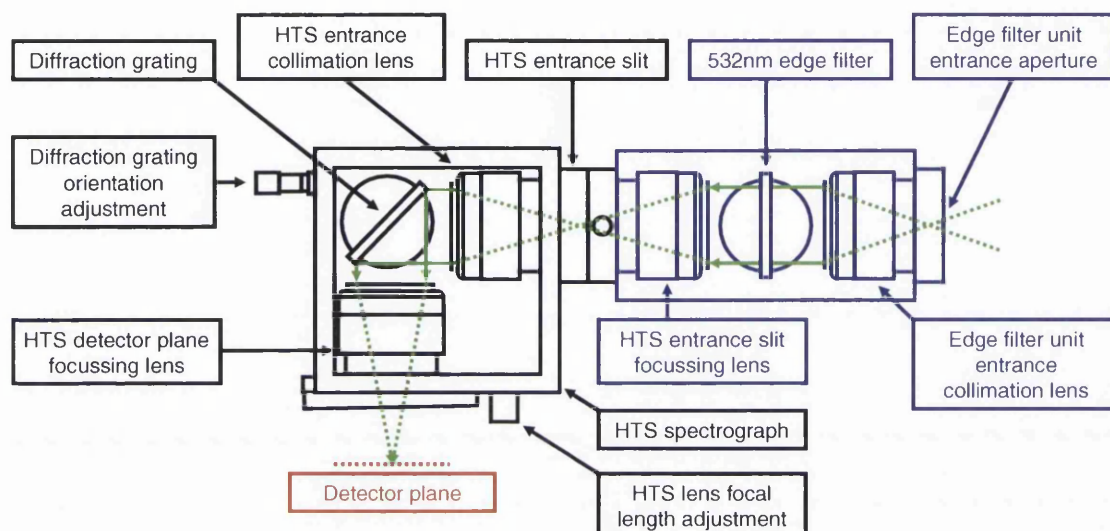
#### 4.4.2 Transmitting optics-type spectrometers

The spectrometer used for the majority of experiments in this thesis has been the PIActon HTS high-throughput lens spectrometer. In normal operation, the HTS is used in much the same way as a Czerny-Turner spectrometer in that the user is normally only concerned with setting the entrance slit width to the desired value and orienting the diffraction grating so that the wavelength range of interest is imaged onto the detector.

The HTS is quite different in principle, however, in the use of lenses rather than mirrors to handle the light passing through the system. The orientation of the grating relative to the paths of light incident and reflected from the grating; the HTS system has a  $90^\circ$  geometry, while the *TRIAX 320* has a near  $180^\circ$  geometry due to the large dimensions of the unit. Due to the small dimensions of the HTS, this  $90^\circ$  geometry has implications for near-



normal incidence orientations of the diffraction grating, as discussed in Section 5.5.1). The layout of the HTS is shown in Figure 4.16.



**Figure 4.16** The PIActon HTS (High Throughput lens Spectrometer, black unit). Note the dedicated edge filter unit (blue), and the path that is followed by light entering the system (green lines). The lenses are set to a focal length of 85mm, corresponding to an f-number of  $f/1.8$ . The HTS is much more compact (overall dimensions: 248×140×178mm) than a Czerny-Turner spectrometer of the same f-number.

Unlike the *TRIA320* Czerny-Turner spectrometer, the HTS has only a single  $600\text{gr}\cdot\text{mm}^{-1}$  diffraction grating installed (although gratings can be changed over manually) which has to be oriented manually via a lockable thumbscrew. The HTS has an f-number of  $f/1.8$ , and so has a >16-fold greater light collecting power than the *TRIA320*.

Due to the use of short focal length lenses, one expects severe astigmatism of the image of the entrance slit at the position of the detector plane. This can be corrected for by the application of a post-acquisition astigmatism correction routine, which provides significant improvements in peak intensity, linewidth and line position – see Section 4.7.1. Note that astigmatism is usually not such a problem with Czerny-Turner spectrographs since the astigmatism can generally be corrected for within the instrument itself by using aspherical mirrors.

## 4.5 Detectors

Both detectors (the Jobin-Yvon CCD2000 used at TLK and the PIActon Spec-10 used at Swansea) employed in our research have been Peltier-cooled 16-bit multi-channel back-illuminated<sup>††</sup> charge-coupled device (CCD) detectors. The performance of these two detectors relative to each other is discussed in Chapter 5. Problems common to both detectors arise from background noise, the efficacy of their cooling methods, and the quantum efficiency of the detector, which we shall now discuss separately.

### 4.5.1 CCD background noise

The background noise that one typically observes on a spectrum recorded with a CCD detector will be a combination of several different types of noise. Those of particular interest to us here are those that are directly linked to the operation of the CCD device, namely (i) dark current noise, (ii) readout noise, and (iii) cosmic ray event noise.

Dark current noise is due to the spontaneous generation of electrons within the solid-state detector, and is therefore strongly temperature dependent – both the CCD2000 and Spec-10 detectors employ Peltier stack coolers in order to minimise the temperature of the CCD chip (see Section 4.5.2). By taking multiple acquisitions of the same spectrum, one can reduce the standard deviation of the background noise due to dark current (the standard deviation decreases with the square root of the number of acquisitions), but in doing so one increases the contribution to the background noise due to readout noise.

Readout noise is related to the process of converting electrons from the detector into a digital signal that can then be interpreted by the controlling computer. It has contributions from the CCD to ADC amplifiers, and from thermal noise in electronic components. By minimising the number of acquisitions, one can minimise the readout noise, a single acquisition having the lowest contribution from readout noise. This however has to be

---

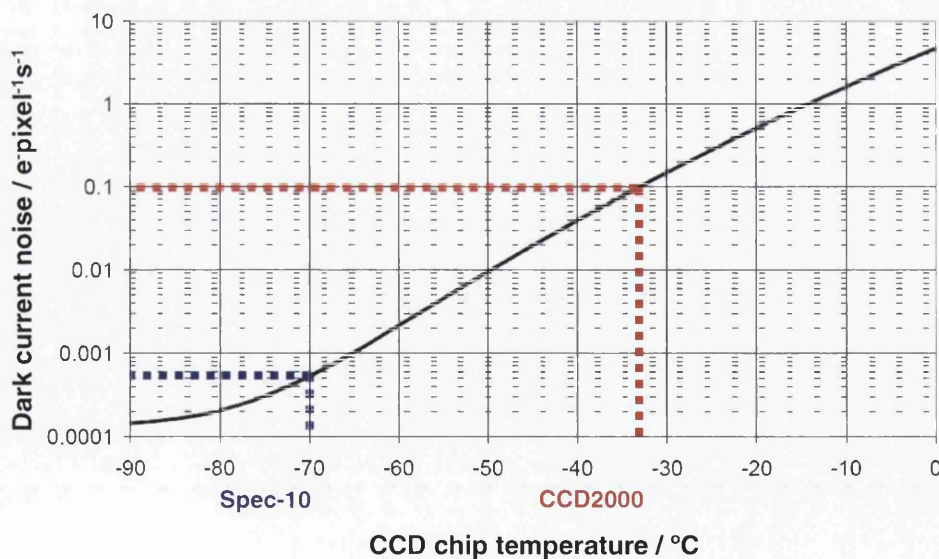
<sup>††</sup> The back-illuminated configuration maximises the detector quantum efficiency for low light applications.

balanced against the need to perform multiple acquisitions in order to minimise dark current noise.

Cosmic ray events are ‘spikes’ that appear on the spectral trace in ever-greater numbers as the acquisition time increases. As the name suggests, they are caused when energetic cosmic ray particles are stopped by the detector and liberate electrons from the detector material. Spectroscopy software packages such as *WinSpec/32* often have reasonably effective cosmic ray event routines built-in, but in order to best remove these events it is necessary to apply post-acquisition cosmic ray removal routines such as those developed for this work – see Sections 4.7.2, 4.7.3, and 4.7.4.

#### 4.5.2 CCD chip cooling

As mentioned in the last section, CCD cameras designed for high dynamic range and / or low intensity signal applications must cool their CCD chips in order to minimise dark current noise. A typical dark current curve is given in Figure 4.17, where the strong dependence on CCD chip temperature is shown.



**Figure 4.17** Dark current noise contribution to detector background as a function of the CCD chip temperature. The malfunctioning CCD2000 used at TLK (which could only reach about  $-33^{\circ}\text{C}$ ) is here compared with the Spec-10 used at Swansea, which operates at  $-70^{\circ}\text{C}$ . The CCD2000 has a dark current noise level 200 times that of the Spec-10.

The need to minimise the chip temperature is evident from this graph, as a  $\sim 17^{\circ}\text{C}$  increase in temperature corresponds to an order of magnitude increase in the dark current background noise level. In the case of the CCD2000, a faulty vacuum jacket around the Peltier stack effectively limited the detector to a minimum operating temperature of  $-33^{\circ}\text{C}$ . Since this was essentially a permanent fault, the CCD2000 was deemed unsuitable for use in a long-term Raman monitoring experiment (see Section 5.1).

Following the comparative review detailed in Chapter 5, the Spec-10 began to show signs of a cooling malfunction. A fault in the Peltier stack had limited the minimum operating temperature to  $-65^{\circ}\text{C}$ , which increased the background noise level by about a factor of 5. This was tracked to a fault in the batch of Peltier stacks that was used in the manufacture of our camera. The detector is currently being repaired by the manufacturer.

#### *4.5.3 CCD detector quantum efficiency*

The quantum efficiency of the CCD detector is, in practical terms, the analogue of the diffraction grating efficiency, in that the detector response is dependent on the wavelength of the incident light. This must be corrected for if full quantitative analysis of a Raman spectrum is to be performed – see section 4.7.6.

### *4.6 Other apparatus*

A wide variety of auxiliary equipment is often employed when conducting a Raman scattering experiment, including edge filters, optical diodes (Faraday isolators) and safety equipment such as beam dumps. A brief overview of these components is given here.

#### 4.6.1 *Safety equipment: enclosures, shutters, interlocks, and beam dumps*

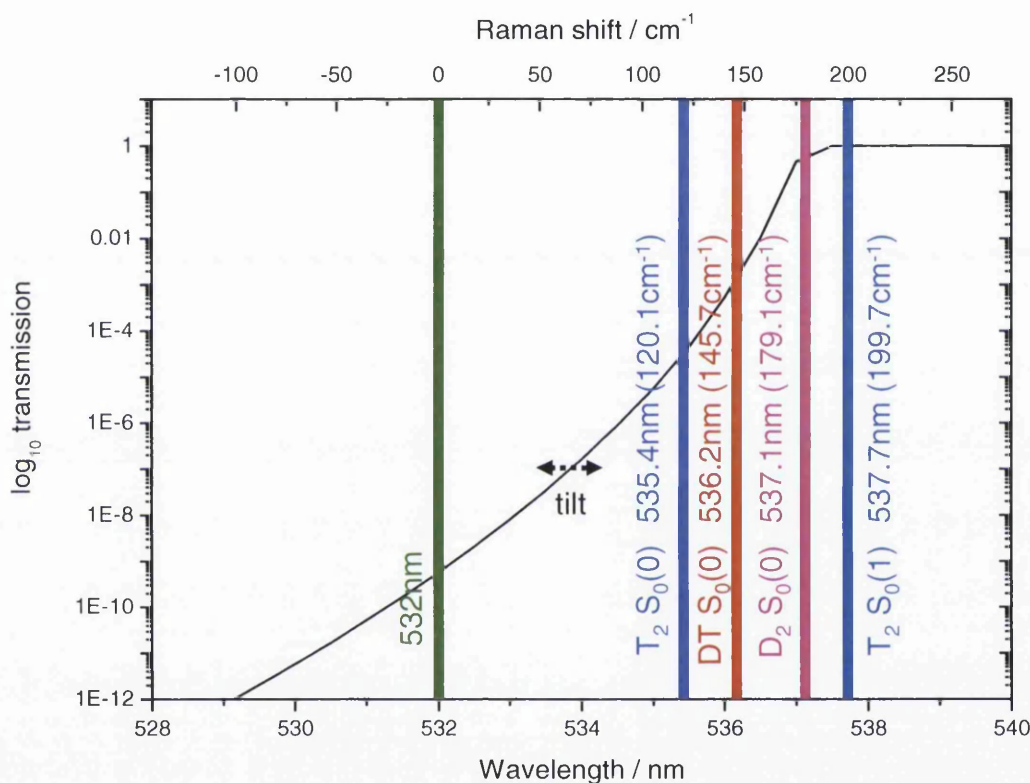
When high-power lasers are employed in a Raman scattering experiment (as is usually the case with gaseous samples), steps should be taken to ensure that the user is protected from accidental exposure to either the laser beam or scattered radiation. This is typically accomplished by enclosing the breadboard on which the experiment is located. The user should still be able to access the experiment, however, in order to perform alignment operations or to service / replace individual components. It is usual, therefore to have some provision such as lockable lids for the user to access the interior of the enclosure. Since the possibility exists of non-users removing the enclosure lids (or entering the room if the experiment is not enclosed), the lids (or door) should be linked to an interlock that will close a shutter in front of the laser head to prevent accidental exposure to the laser beam / scattered radiation. The shutter used for our experiments at TILO is the LaserMet LS-10-12, which has a fail-to-safe operation, to comply with current EU laser safety regulations.

Beam dumps are used at the end of a laser beam path in order to terminate the laser beam path safely. The dump used in our case at TILO is the Thorlabs BT500M, which can safely dump up to 40W of CW radiation with minimal backscatter (note that the *Verdi V5* has a maximum CW output of only 5W). The use of a beam dump can also be useful in experiments that utilise lower-power laser modules such as the 10mW green Nd:YAG JLM-10RB module used in the TLK / UWS system comparative review (see Chapter 5), since by this measure the amount of scattered light (background glow) in the enclosure is minimised.

#### 4.6.2 *Edge filters*

Edge filters are an absolute necessity when performing a Stokes (or anti-Stokes) Raman scattering experiment, especially if one wishes to observe the pure rotational  $S_0$ -branch lines that lie close the Rayleigh ( $Q_0$ ) line at the exciting laser wavelength. Without a filter in place, the Raman lines would at best be sitting upon a significant background from the Lorentz wing of the Rayleigh line, and in the worst case would be drowned out completely.

Good edge filters can suppress the laser line by a factor of  $10^8$  to  $10^9$ , while providing  $\sim 99\%$  transmission away from the laser line. The transition between full suppression and full transmission is quite sharp ( $<1\%$  of the laser wavelength is typical), and can be positioned very close to the laser line position. Figure 4.18 shows the transmission curve for the Semrock RazorEdge LP01-532RU line filter used in the HTS spectrometer set-up.



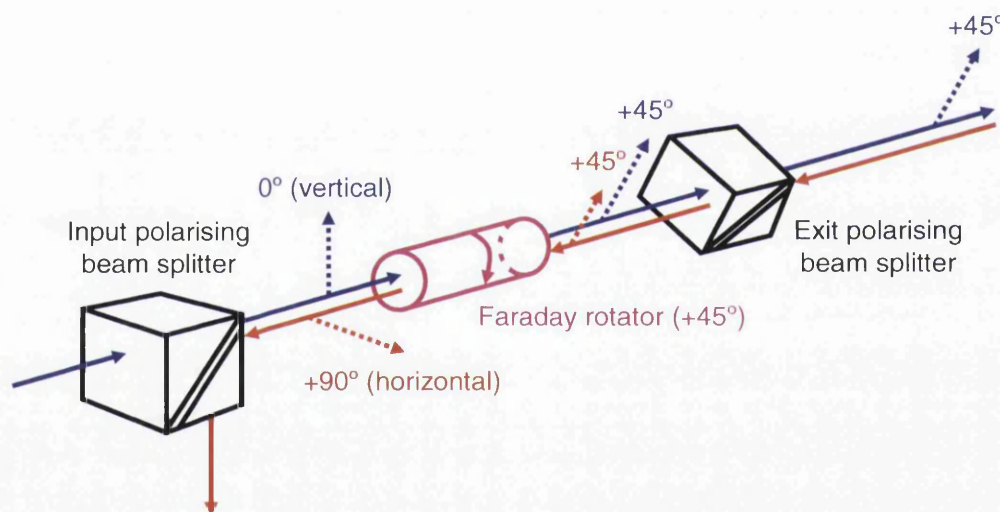
**Figure 4.18** Semrock RazorEdge LP01-532RU 532nm edge filter transmission curve, showing the position of the 532nm laser line (green), the first two T<sub>2</sub> S<sub>0</sub>-branch lines (blue) and the first DT and D<sub>2</sub> S<sub>0</sub>-branch lines (red and purple, respectively). The position of the edge transition is determined in part by the tilt of the filter with respect to the beam path. Information regarding the intensity of the first S<sub>0</sub>-branch lines of the T<sub>2</sub>, DT and D<sub>2</sub> isotopomers would be lost, but the T<sub>2</sub> S<sub>0</sub>(1) line should be usable. Note the logarithmic scale for the transmission axis. Transmission curve data: Semrock (2004).

The 532nm laser line is suppressed by a factor of  $10^9$ , while the transition from suppression at the laser line position to full transmission is quite sharp (about  $200\text{cm}^{-1}$ ). One can see, however, that even with this sharp transition, the T<sub>2</sub>, DT and D<sub>2</sub> S<sub>0</sub>(0) lines still lie on the transition region of the curve and are largely suppressed. The information regarding these lines will therefore be lost. The T<sub>2</sub> S<sub>0</sub>(1) line should be usable, but it should be noted that

the position of the transition region is determined in part by the tilt of the filter with respect to the laser beam. Necessary adjustment of the tilt may therefore even effect the  $T_2 S_0(1)$  line.

### 4.6.3 Faraday isolators

In order to ensure unidirectional operation in a laser beam path system, a Faraday isolator is often employed. A Faraday isolator allows the transmission of polarised light in only one direction. The device itself consists of two polarising beam splitters and a Faraday rotator<sup>‡‡</sup>, which makes use of the Faraday Effect to rotate the plane of polarisation, as shown in Figure 4.19.



**Figure 4.19** Operation of a typical Faraday isolator consisting of two polarising beam splitters and a Faraday rotator, showing light passing through in the allowed direction (blue line), but being blocked in the opposite direction (red line). Dashed lines indicate linear polarisation direction. The Faraday rotator applies a rotation to the polarisation direction of  $+45^\circ$  (insensitive to the light propagation direction).

The principle of the Faraday isolator is quite straight forward. Light leaving the input polarising beam splitter will have a vertical polarisation ( $0^\circ$ ). On passing through the Faraday rotator, the light acquires a  $+45^\circ$  polarisation. The exit polarising beam splitter is

<sup>‡‡</sup> The Faraday rotator in the unit used at TLK is a terbium gallium garnet crystal that is located between two powerful magnets.

set to only allow light of  $+45^\circ$  polarisation to pass, and so light passing in the allowed direction leaves the device unimpeded. Note that in order to ensure maximal transmission, the input light should be vertically polarised.

For light passing in the opposite, non-allowed, direction, the exit polarising beam splitter ensures that the light passing onto the Faraday rotator has a  $+45^\circ$  polarisation. This light then acquires a horizontal ( $+90^\circ$ ) polarisation on passing through the Faraday rotator. The light is then diverted by the input polarising beam splitter and dumped.

The Gsänger FR 532 HWP Faraday isolator was an essential component of the ASER system developed by Taylor et al. (2001) that prevented back-reflected laser light from entering cavity of the excitation laser. One should note, however, that initially vertically polarised light will acquire a  $45^\circ$  polarisation on passing through the device, and this has consequences for the intensity of the Raman scattering observed. The relative intensity of the  $Q_1$ -branches is particularly affected – see Section 6.2.7.

#### ***4.7 Post-Acquisition Spectra Processing Software***

As previously discussed, the low signal strength of the Raman signal dictates that every element of the Raman spectroscopic system, from the excitation source to the detector should be optimized for low losses and high sensitivity as far as is practicable. However, there is also much that can be done post-acquisition to further increase the available signal-to-noise ratio, such as correction of image astigmatism, cosmic ray event cleaning and routines to correct for variations in system transmission or detection efficiency with respect to wavelength.

In order to allow ease of integration, all of the routines discussed in this section have been written in *LabVIEW*. This industry-standard package allows the rapid development of effective software routines, as well as making it simple to apply several (or indeed all) correction routines in series and in any order desired. This is particularly important for a sequence involving the differential cosmic ray removal and astigmatism correction routines – in order for the differential routine to be maximally effective, the astigmatism routine



should be applied first. The following subsections deal with the principles behind the correction routines. The reader is referred to Appendix A2 for details regarding the *LabVIEW* code.

#### *4.7.1 Correction of image astigmatism in the HTS lens spectrograph*

As mentioned in Section 4.4.2, imaging errors are a notorious problem in all systems utilising collimating, i.e. curved optical components. In standard spectrographs many of the standard lens and mirror aberrations can be and typically are corrected for in order to minimise their effect on spectral resolution. In the widely used Czerny-Turner spectrometer design aspherical collimation mirrors are used to compensate for the astigmatism in the direction of dispersion. As such, astigmatism is a rarely quoted entity in spectrometer data sheets.

In the case of two-dimensional CCD array detectors, however, astigmatism may become an increasingly noticeable problem if it is necessary to maintain the highest spectral resolution. For very low light levels it is absolutely essential to average the measured signal over the entire height of the CCD chip.

The Acton HTS lens spectrometer targets ultra-low light level applications, incorporating transmitting optics (lenses). These allow for an extremely compact footprint and exhibit high light collection capabilities (with f-number  $f/1.8$ ), with astigmatic distortion quoted as  $< 100 \mu\text{m}$ . While this is a rather small value, the image of the entrance slit on the detector plane is highly distorted by astigmatism because of the very short focal length and the utilisation of spherical lenses. This aberration limits the number of useful pixel rows one can bin (average) before spectral resolution is compromised.

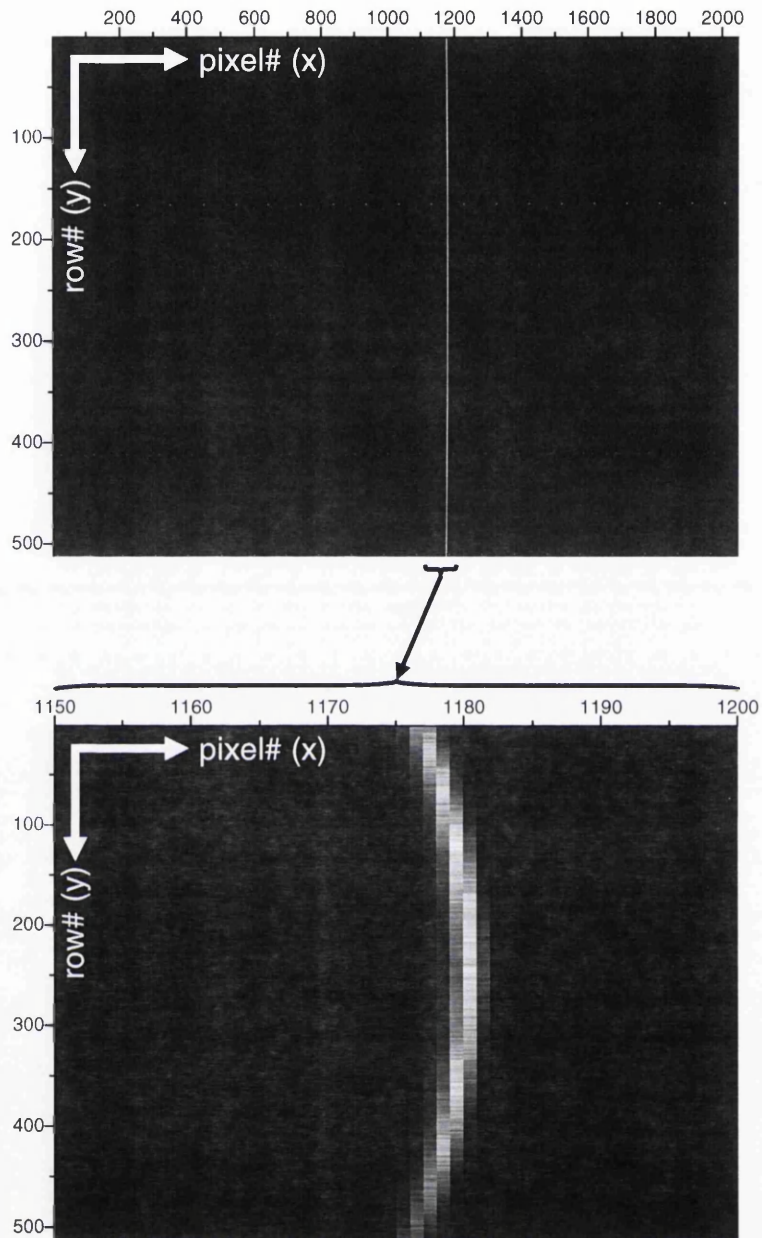
Correcting the astigmatism is especially important for the fibre-coupled case since the fibre will normally introduce extra losses into the system. While this is to some extent offset by the reduction in stray light entering the system, one should assume that there will be a loss of the order 30% due to the addition of a fibre to the system. As is demonstrated below, the astigmatism correction routine more than compensates for this additional loss.

Two *LabVIEW* programs have been developed to firstly determine the profile of the astigmatism function, and then to correct for the image distortion. The first, *AstCalc*, scans a spectrum with a prominent spectral feature and generates a file that characterizes the astigmatism; the second, *AstCorr*, uses that file to correct the astigmatism in measured 2D spectral images. The code for these programs is located in Sections A2.1.1 and A2.1.2, respectively. The source data is in ASCII format, exported from the relevant .SPE file in *WinSpec/32* (see Appendix A2 for the specific format used here). Since external calibrations are used, any internal calibration applied by *WinSpec/32* is ignored.

Using these programs, improvements in the signal-to-noise ratio in the region of 50% can be achieved, and line widths can be reduced to close to the diffraction limit. The line position errors caused by binning astigmatic spectra are effectively eliminated as well.

The profile of the trace of a spatially expanded beam image from a HeNe laser onto the Spec-10 CCD (2,048 pixels  $\times$  512 rows, pixel size  $13 \times 13 \mu\text{m}^2$ ) detector is shown in Figure 4.20, for a slit width of  $25.4 \mu\text{m}$ . While the full-chip view of the spectrum does not suggest a problem, on an expanded scale the astigmatism is clearly visible as a spectral line with gentle curvature, symmetric around the central pixels row (#256).

The spectrometer calibration is performed on the central strip, and the number of ‘useful’ rows is limited to about 50-75 rows on either side of the central row. ‘Useful’ is defined here as those rows with less than a pixel deviation from the central row position. The observed maximum deviation at the detector extremities (rows #1 and #512) is between 3 and 4 pixels, which is larger than the line width resolution of the system for minimal slit width of  $\sim 25 \mu\text{m}$ . The astigmatism therefore forces a compromise between light collection and spectral line width, both of which increase with the number of rows binned.



**Figure 4.20** Spec-10 chip exposed to HeNe laser at 632.816nm. Top: full chip map. Bottom: full chip height (full y-axis range), with the x-axis zoomed in to pixel# (column) 1150 to 1200, clearly showing the astigmatism of the entrance slit image over the CCD chip height.

If the binning is restricted to the “useful” rows, as per the definition given above, then only about 25% of the incident light is used – this will immediately halve the signal-to-noise ratio compared with the case where all pixel rows are available. However, using more rows will dramatically broaden the line width. In the case of a 25.4 $\mu\text{m}$  entrance slit,

binning all rows effectively doubled the line width, without significant gain in signal-to-noise ratio; furthermore, an error in the apparent line centre is introduced.

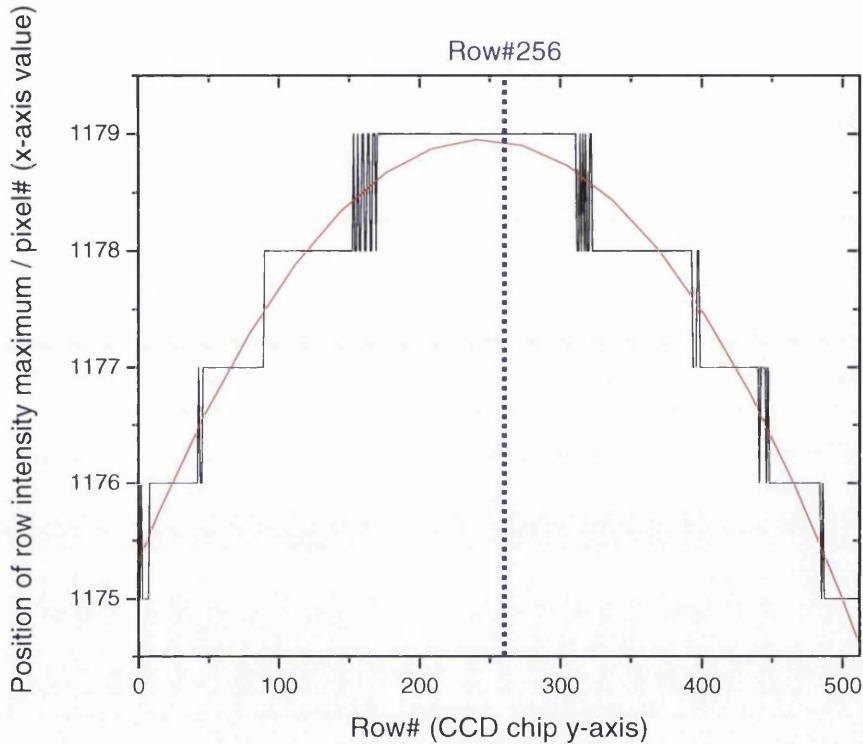
The correction method makes use of a simple idea. The rows either side of the central maximum can be thought of as being shifted from their 'correct' position with respect to the central row. As such, therefore it would be simply a matter of shifting these rows 'back' into line; thereafter, one can bin all rows without suffering the detrimental effects of astigmatic spectral lines. Of course, like with the majority of shifting procedures, a small price has to be paid for its implementation. In the example shown here, the outer rows (near rows #1 and #512) will be shifted by around 3 pixels, and so one loses the use of the three or so pixels (#1 to #3 or #2046 to #2048, depending on the orientation of the chip) at the extremities of these rows. However, for most applications this is an acceptable loss as one still has the use of the remaining 2045 pixels in these rows. Since the internal optics of the HTS are fixed, one only has to measure the astigmatism function once; it will remain valid as long as internal components are not moved or changed.

If one makes the reasonable assumption that all pixels in a row are displaced from their 'true' positions on the central row by the same amount then characterizing the astigmatism is quite simple. If a spectral feature is selected then all one has to do is measure its position (pixel#) relative to the 'true' position on the central row. Once this information is known, it is a simple matter of subtraction to determine how far each row needs to be shifted in order to line it up with the central row.

The routine *AstCalc* facilitates the characterisation of the astigmatism of a spectral line by recording the pixel# of the maximum intensity for each row and subtracting these values from the position of the maximum of the centre (#256) row. The output of *AstCalc* is an ASCII file which is used by the correction routine *AstCorr* to correctly apply the required shift to each row.

In the discussion presented here, the spectral feature utilized is the 632.816 nm emission from a HeNe laser. The 632.816 nm line is the most intense line in the HeNe laser emission spectrum, and as such it is easy to measure the position of the line on each row since all *AstCalc* has to do is scan the spectrum and record the most intense pixel in each

row in an array of (row#, pixel#) values. The line is also quite close to the central pixel column, may be therefore seen as representative of the average astigmatism across the whole chip. The result is a histogram as shown in Figure 4.21.



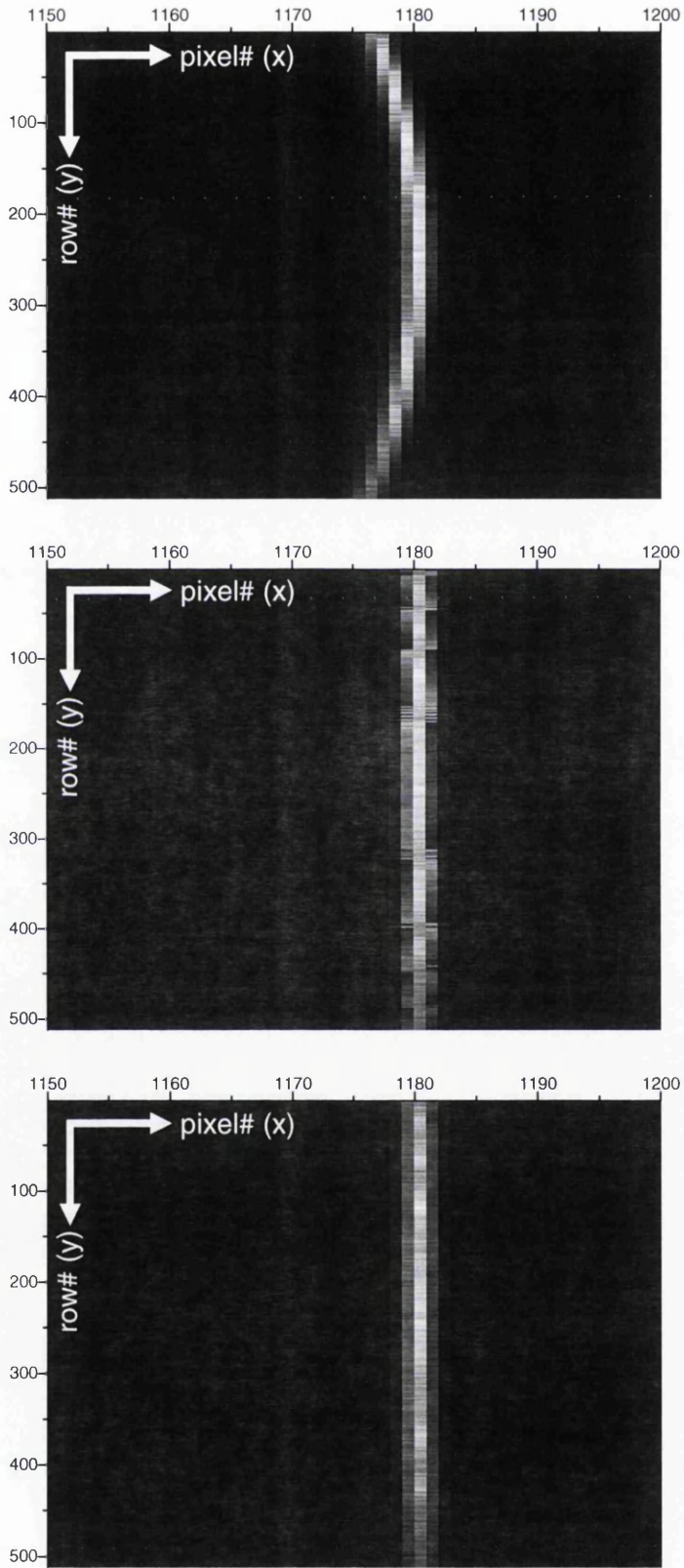
**Figure 4.21** Histogram of pixel# (column) positions of highest intensity in the line profile of the 632.816nm HeNe emission (black line) across the CCD chip height (pixel rows), showing the fitted parabolic function (red line) and the position of the central row (blue line). Note that the turning point of the parabola is slightly displaced from the central row due to minute inaccuracies in the internal alignment of the HTS components.

Note that the routine records the positions of the intensity maxima to the nearest pixel and so there are jump-like fluctuations in the recorded position in those rows where the line crosses pixel boundaries.

Using either *LabVIEW*'s curve fitting routines (access to which is built into *AstCalc*) or a data analysis program such as *Origin* it is possible to calculate the functional dependence of the parabolic astigmatism curve. Using this function, *AstCalc* then determines the (fractional) difference in position between each individual row and the central row. The generated array is a list of (row#, required shift) values. The shifts are fractions of a pixel

and as such it is not sufficient to simply shift each row by an integer number of pixels. It is the task of the second routine, *AstCorr*, to interpolate pixel intensity values and apply the necessary shift. Note that in the initial implementation of the idea of *AstCalc* and *AstCorr*, the simple subtraction of row maximum pixel# from the central row generated an array of integer pixel shifts for each row. This resulted in an imperfect alignment of rows, especially where the fluctuations along pixel boundaries occurred (see Figure 4.22 (middle)).

As stated above, each row needs to be shifted fractionally in order to achieve alignment as close to perfect as possible. For this, in the latest realization of *AstCorr*, *LabVIEW*'s 'Interpolate 1D Array' function is utilized to apply this fractional shift to each row, as specified by *AstCalc*. The result is a near-perfect alignment of all rows with respect to the central maximum, as shown in Figure 4.22 (bottom).



**Figure 4.22** Correction of HTS / Spec-10 astigmatism. Top: raw data, showing the 632.816nm HeNe line. Middle: integer-shift correction (using raw histogram data to apply integer pixel shifts). Bottom: fractional-shift correction (using fitted parabola to determine fractional pixel shifts).

The correction to the astigmatism allows one to bin / average the intensity from all rows of the detector, without affecting line position or line width; a marked improvement in peak intensity is observed, as summarized in Table 4.5. At the selected resolution with a 25.4 $\mu\text{m}$  entrance slit, the quality of the corrected data average is very close to that of a diffraction-limited image.

**Table 4.5** Numerical values for the influence of the shifting procedure on the data set averaged over the whole detector chip height. The peak fit was carried out using the Peak Fitting Module (PFM) in *Origin*.

Fit parameter	Raw data value	Corrected value	Difference / improvement
Line centre / nm	632.981	632.851	0.129nm
Peak intensity / arb.	44.6	68.5	54%
Linewidth / nm	0.427	0.274	36%

Note that the corrected line reading agrees with the actual value of  $\lambda_{\text{HeNe}} = 632.816\text{nm}$  to better than 1/3 of the resolution of 0.14 nm/pixel, as determined from the spectrometer wavelength calibration. The uncorrected line position is shifted by about 1 pixel (nearly half the linewidth value for this particular case). The improvement to the peak intensity is about 54%.

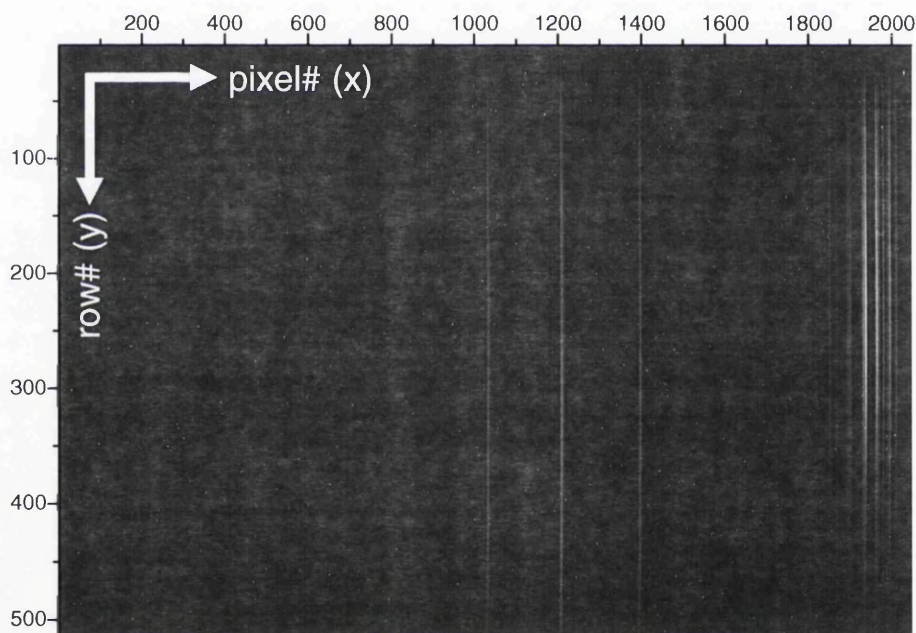
The correction of astigmatism is absolutely vital to allow the full use of the potential for high-throughput and high resolution in the HTS lens spectrograph. Even if weak signals were not the target, for optimum spectral resolution the astigmatism must be corrected to allow for precise determination of line positions when binning multiple rows, and to avoid the associated increase in line width. With these easily-implemented procedures in place, full use can be made of the excellent light collection capability of the HTS and line widths approaching that of diffraction-limited images can be achieved.

It should be noted that the methodology outlined in this section can be applied to any spectrograph system / 2D-array detector combination which may suffer the effects of vertical astigmatism.



### 4.7.2 Cosmic ray event removal: *TrigCRR*

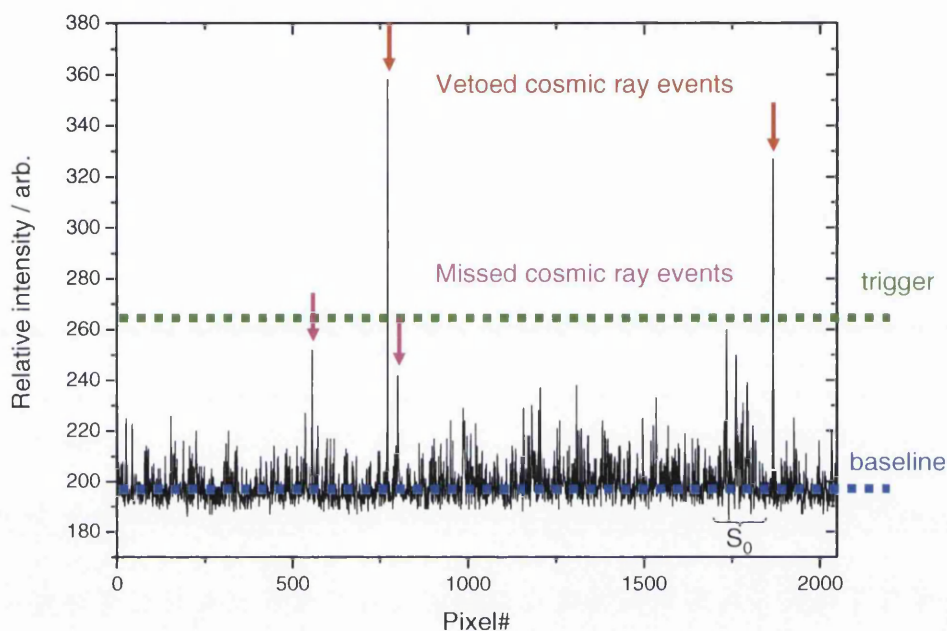
In order to compensate for the low signal strength of the Raman scattering, it is necessary to use long exposure times of up to 5000s (nearly 1.5hr) in order to achieve workable signal-to-noise ratios in the acquired spectra. This is especially true when using low-power lasers such as the 10mW-rated 532nm Nd:YAG unit, which provided a slightly lower power output of 7.1mW. The length of these exposures introduces a high number of cosmic ray events ('spikes') onto the traces, which for exposures of the order 1000s begin to dominate the noise contribution to the spectrum when the pixel rows are binned, as can be seen in Figure 4.23,.



**Figure 4.23** 5×1000s multiple exposure Raman spectrum of H<sub>2</sub>:HD:D<sub>2</sub> (1atm) cell as recorded by *WinSpec/32* from the HTS/Spec-10 system. The high number of cosmic ray events is quite evident. The three vertical lines between pixel# 1000 and 1400 are the Q<sub>1</sub>-branches of (left to right) H<sub>2</sub>, HD, and D<sub>2</sub>. The lines to the far right of the spectrum are the S<sub>0</sub>-branch lines of all three isotopomers.

The routine *TrigCRR* (acronym: “Trigger-value Cosmic Ray Removal”) is the simplest of the three cosmic ray event removal routines developed to date for the analysis of our hydrogen isotopomer Raman data, and is also the most limited in terms of general applicability. *TrigCRR* scans each pixel row and compares the intensity at each point with

a user-specified threshold value. If the intensity is above the threshold value, then *TrigCRR* replaces it with a user-specified substitution value. Figure 4.24 shows how *TrigCRR* would deal with a suitable Raman spectrum for a single pixel row.



**Figure 4.24** *TrigCRR* operation on suitable (ultra-low intensity) Raman spectrum with the necessary flat-line background for a single pixel row. The trigger (green line) is set just above the maximum signal intensity (here the  $S_0$ -branch lines of a  $H_2:HD:D_2$  gas mixture). Cosmic ray events that rise above the trigger value are vetoed (red arrows). Cosmic ray events that lie under the trigger value are missed, but will likely be diluted when all 512 rows are binned.

The simple principle behind *TrigCRR* is that the user should set the threshold value to be just above the expected signal maximum intensity, and any cosmic ray ‘spikes’ that rise above this level are replaced with the substitution value, which should be set to the level of the flat-line background<sup>§§</sup>. Due to the simplicity of the routine, *TrigCRR* is limited to ultra-low intensity level Raman spectra, and that the background level should be flat across the entire detector. This is, of course, exactly the situation that one has when using the

<sup>§§</sup> Care needs to be taken here when importing data to *TrigCRR* if a background subtraction or baseline scaling has been applied beforehand (see Section 4.7.5). The substitution value should be the baseline value of the *imported* data, which might not correspond to the baseline value of the raw data.

10mW Nd:YAG module to obtain Raman spectra of gases with the HTS/Spec-10 system. The performance of TrigCRR in this case is demonstrated in Section 5.2.2.

If the background is uneven (as is likely to be the case if there is much scattered light entering the detector, or if the detector chip is unevenly cooled) or the signal strength is comparable to the intensity of the majority of cosmic ray events (as is the case here with laser modules of power >50mW), then *TrigCRR* becomes ineffective. For more general use, more sophisticated routines are required.

### 4.7.3 Cosmic ray event removal: RCRR

The routine *RCRR* (acronym: “Row-comparison Cosmic Ray Removal”) makes use of a simple but effective idea. Rather than scanning along each pixel row (y-axis pixel row# held constant, x-axis scanned), *RCRR* scans along pixel columns (x-axis column# held constant, y-axis scanned), comparing the intensity value of each row with that of the row adjacent to it. The lower of the two values is passed to construct a new set of data that only contains the lowest values in each comparison. When the routine reaches the last row, it compares the intensity of the last row with that of the first in order to preserve the dimensionality of the input data.

One can visualise a spectrum recorded by a CCD chip as an  $i \times j$  matrix of values,  $\mathbf{A}$ , and thus the data set constructed by *RCRR* as described above will also be a matrix of the same dimensionality,  $\mathbf{P}$ . In the *LabVIEW* code, these matrices are represented by arrays of double-precision numbers. Each element of the passed matrix,  $\mathbf{P}_{ij}$ , can therefore be defined in terms of elements of the data matrix,  $\mathbf{A}_{ij}$ , as

$$\mathbf{P}_{ij} = \begin{cases} \mathbf{A}_{ij} & \text{if } \mathbf{A}_{ij} < \mathbf{A}_{i+1,j} \\ \mathbf{A}_{i+1,j} & \text{if } \mathbf{A}_{i+1,j} < \mathbf{A}_{ij} \end{cases}, \quad (4.20)$$

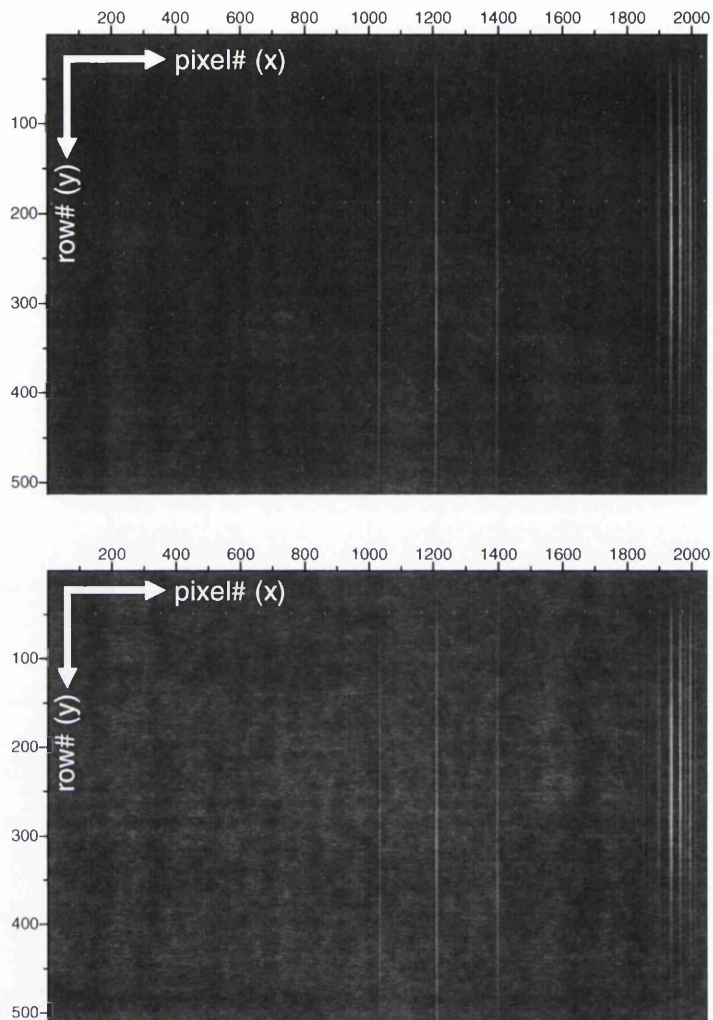
where  $i$  is the row (y-axis) index and  $j$  is the column (x-axis) index.

Since cosmic ray events tend to be of the order of a single pixel in width, this routine will remove events provided there are not more than two in adjacent pixels along the scanning direction. However, there are two caveats to bear in mind when using *RCRR*:

Firstly, the scan is performed along pixel columns (i.e. constant wavelength / wavenumber). It is therefore essential to perform astigmatism correction before using *RCRR* to ensure that the passed signal strength is not adversely affected by the passing of successively lower values. Since *RCRR* always passes the lower of the two values in a comparison, an isolated, narrow, astigmatic line can have zero intensity at the edges of the CCD chip since astigmatism in the HTS can be of the order of 3 pixels at the chip edge. As shown in Section A2.2.2, the astigmatism correction code was integrated into the *RCRR* subVI.

Secondly, even with relatively clean spectra there will be a loss of contrast between the signal and the background due to the fact that the lower of the two values in any comparison is passed. However, for a long exposure with many cosmic ray events this loss in signal-to-noise due to a lowering of contrast is more than offset by the gain in signal-to-noise due to the removal of the cosmic ray events when binning pixel rows.

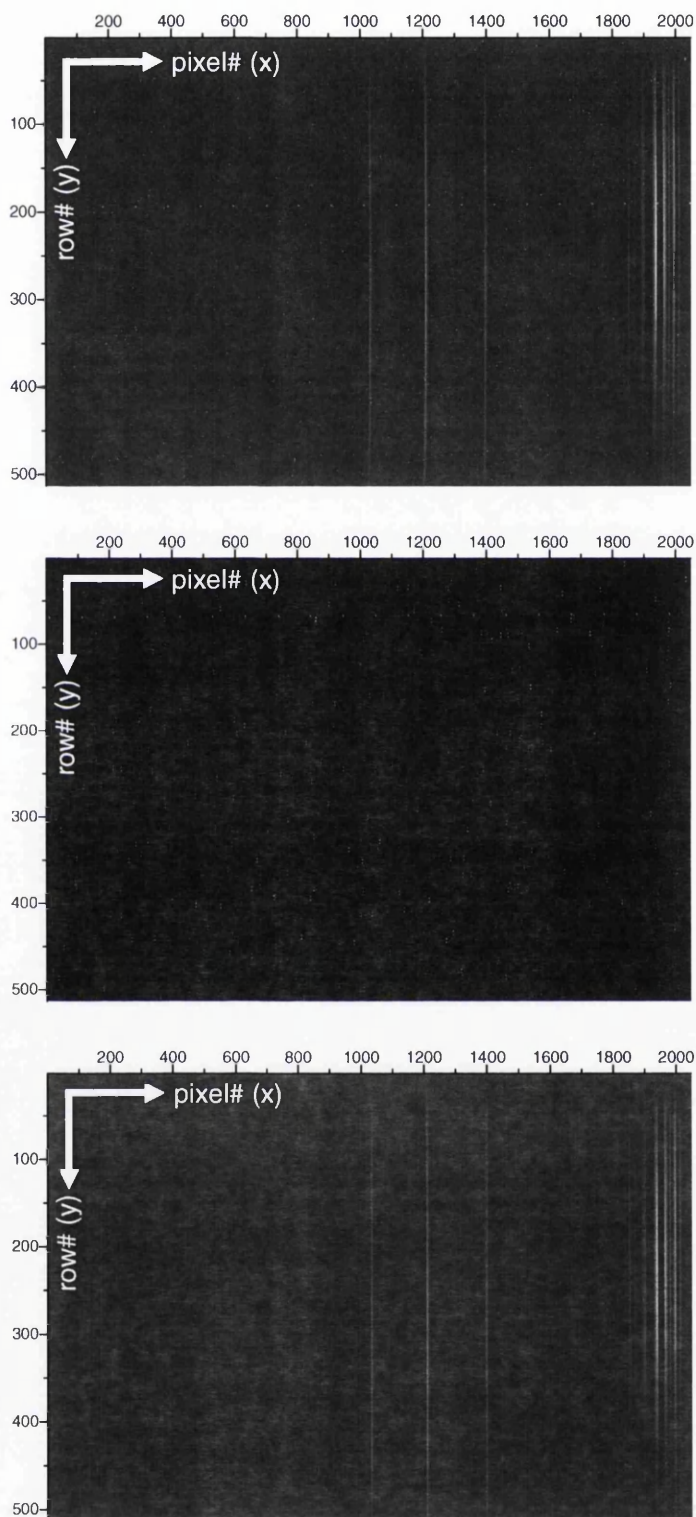
Since *RCRR* was replaced by the more sophisticated routine *DCRR* and therefore not extensively used in this work, it will suffice here to give a single example of *RCRR*'s performance. Figure 4.25 shows a 5×1000s-exposure Raman spectrum of a 29:47:24(±1) H<sub>2</sub>:HD:D<sub>2</sub> (1atm) sample recorded by the HTS/Spec-10 system in a direct-imaging configuration, with a 100mW Nd:YAG module as the excitation source, before and after application of *RCRR*.



**Figure 4.25** 5×1000s-exposure Raman spectrum of a 29:47:24(±1) H<sub>2</sub>:HD:D<sub>2</sub> (1atm) sample recorded by the HTS/Spec-10 system in a direct-imaging configuration, with a 100mW Nd:YAG module as the excitation source. Top: raw data, showing a high number of cosmic ray events. Bottom: *RCRR*-corrected data. There is a slight loss of contrast, but the cosmic ray events have mostly been filtered out.

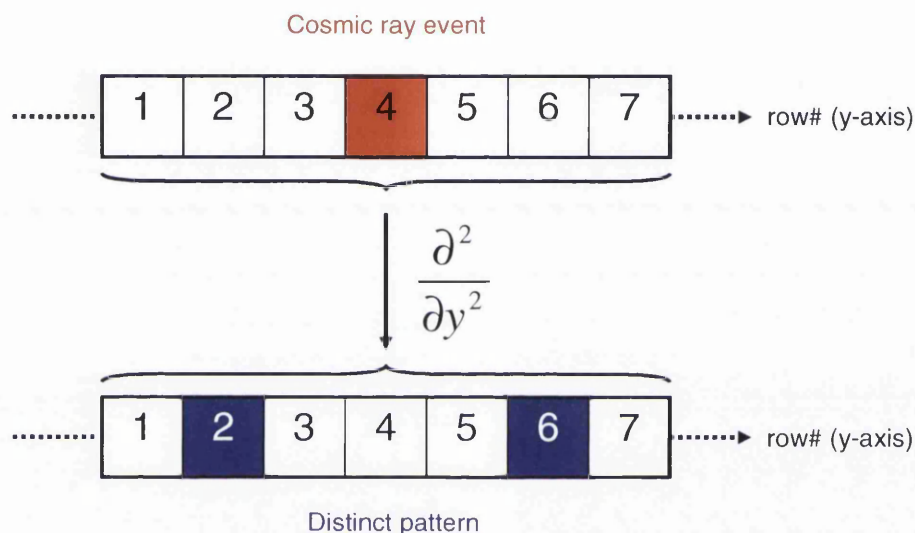
#### 4.7.4 Cosmic ray event removal: *DCRR*

*DCRR* (acronym: “Double-differential Cosmic Ray Removal”) is the most sophisticated of the cosmic ray event removal routines developed here. It can be applied to practically any spectrum, and can easily deal with large numbers of cosmic ray events. The principle behind *DCRR* is to reduce the problem of flagging pixels that contain cosmic ray event pixels to a simple threshold value exercise along the lines of *TrigCRR*. To this end, a double derivative is taken of the input Raman spectrum along the y-axis (constant column#, varying row#) as shown in Figure 4.26 (note that this is the same spectrum as shown in Figure 4.25).



**Figure 4.26** 5×1000s-exposure Raman spectrum of a 29:47:24(±1) H<sub>2</sub>:HD:D<sub>2</sub> (1atm) sample recorded by the HTS/Spec-10 system in a direct-imaging configuration, with a 100mW Nd:YAG module as the excitation source. Top: raw data, showing a high number of cosmic ray events. Middle: doubly differentiated data – the Raman lines have ‘dropped out’, but a distinct pattern around each cosmic ray event remains. Bottom: *DCRR* corrected data – the patterns were used to locate and replace each flagged cosmic ray event with a column average value.

Since the intensity of the Raman lines varies very slowly across rows (i.e. across spectral information of constant wavelength / wavenumber), their double derivative is essentially zero. Cosmic ray events, on the other hand, have large double derivatives, since they are ‘spikes’ of the order of 1 pixel across. As can be seen in Figure 4.26 (middle), the Raman lines are ‘invisible’ to the double derivative procedure, while the cosmic ray events form a distinct pattern around the location of the events themselves, as shown in Figure 4.27.



**Figure 4.27** The distinct pattern (blue pixels) of two high-value pixels formed when doubly differentiating a single-pixel (isolated) cosmic ray event (red pixel). The white pixels represent the background on which the cosmic ray event sits, whether the flat-line background or a Raman line (both are essentially invisible to double differentiation).

As mentioned above, the problem is now one of using a threshold value routine similar to *TrigCRR* to find the pattern of cosmic ray events across a chip. In the example shown in Figure 4.26, the background on which the post-differentiation cosmic ray patterns appear has a value between 0 and 10, with the majority of pixels being less than 5. Using 10 as a threshold value, *DCRR* scans each column (i.e. in the same direction as the differentiation) and looks for the pattern shown in Figure 4.27 in order to ‘flag’ the pixels that contain cosmic ray events. In the example shown, *DCRR* would detect the >10 values in pixels 2 and 6 and would therefore flag pixel 4 as a cosmic ray event.

Once a map of the positions of the cosmic ray events has been built up in this manner, the flagged pixel values can be replaced by a suitable value, again working along individual columns. In the *LabVIEW* code (see section A2.2.3), a harmonic mean value of the non-



flagged pixels in the column is used as the substitute value, although other types of mean might be suitable. It is essential to correct for astigmatism before applying the differentiation, since a form of mean along the column is being used to replace the flagged values, and this must be representative of the position (i.e. wavelength / wavenumber) of the column. As in *RCRR*, *DCRR* integrates the astigmatism code into its block diagram of the subVI.

Clearly, *DCRR* is extremely effective at removing cosmic ray events with no loss in contrast as was the case for *RCRR* (see Figure 4.26 (bottom)). With the exception of the spectra recorded at TLK (*Origin* was used instead, see Section 5.1) and spectra recorded with the 10mW module at Swansea (*TrigCRR* was satisfactory in that case, see Section 5.2), all Raman spectra in this thesis have been cleaned by *DCRR*. A few spectra were cleaned at the time they were acquired using *RCRR* while *DCRR* was in development, but these have been retroactively cleaned using *DCRR* for this work.

#### 4.7.5 *Background subtraction and baseline scaling*

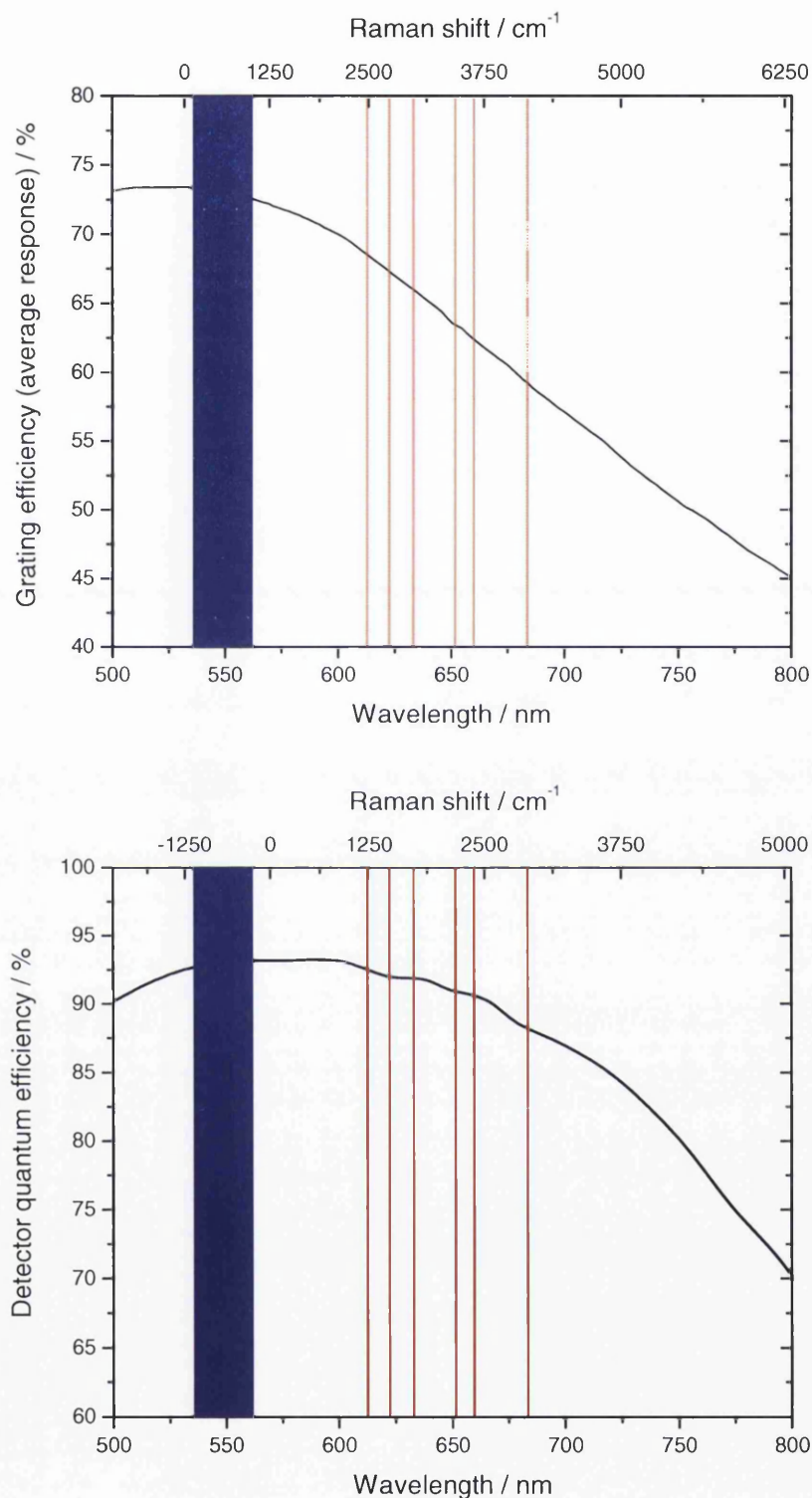
Background subtraction and baseline scaling routines serve to flatten uneven background such as in the case of an unevenly cooled CCD chip, or significant scattered light entering the system, and to set the flat-line background to zero. Background subtraction is easily achieved in *LabVIEW* code; since spectra are represented by arrays, one simply has to subtract a suitable background array from the spectrum array. Baseline scaling such as using the “baseline” tool in *Origin* can then be used to flatten any unevenness remaining in the spectrum and to set the flat-line level to zero, leaving only spectral lines (and possibly cosmic ray events) lying above the now-flat background. At the time of writing, all baseline scaling performed on spectra in this thesis was performed manually in *Origin* – a *LabVIEW* routine to perform this automatically is a currently outstanding task.

When subtracting a background spectrum it is obviously essential that the acquisition (exposure time, grating position) and post-acquisition (astigmatism correction, cosmic ray removal) parameters of the two files be the same. In particular, background files should be checked for any cosmic ray events that may have been missed by the removal routines

(although missed events are a rare occurrence when using *DCRR*). These should be removed (in *Origin*, e.g.) before using the background spectrum.

#### 4.7.6 *Grating efficiency and detector quantum efficiency correction*

The routines being developed to correct for the wavelength dependence of grating efficiency and detector quantum efficiency are still in the beta phase, and so will only be summarised briefly here. Note that the dependence on the polarisation (see Figure 5.26) of the incident light must be taken into account for the grating efficiency. Figure 4.28 shows the grating efficiency and detector quantum efficiency curves for the  $600\text{grmm}^{-1}$  grating of the Swansea HTS spectrometer and the attached Spec-10 CCD camera.



**Figure 4.28** Top: grating efficiency curve for the HTS 600grmm<sup>-1</sup> grating, showing the dependence on wavelength for an average response over vertical and horizontal polarisations (PIActon (2004)). Bottom: quantum efficiency curve for the Spec-10 detector, showing the dependence on wavelength. Also shown are the positions of the hydrogen isotopomer S<sub>0</sub>-branches (blue band) and Q<sub>1</sub>-branch lines (red). The Raman shifts are measured relative to 532nm (18797cm<sup>-1</sup>). The wavelength range shown is the region of interest for this thesis (PIActon (2004)).

Correction of this wavelength and / or polarisation dependence on efficiency is quite simple to implement. Provided the background has been properly subtracted and a 'zero'-baseline is set, one only has to multiply the values of each column (or equivalently, each point on the binned spectrum) by the appropriate factor given by the efficiency curve – the intensity at a wavelength (column) that is transmitted with 50% efficiency would be multiplied by a factor of 2, for example. Note again that astigmatism correction has to be applied beforehand for this correction to work correctly.

The code for such routines is elementary and will not be discussed here. The chief difficulty of this procedure is obtaining sufficiently high-resolution efficiency curves for the grating and detector in the region of interest that is being considered: manufacturers normally only supply 'typical' data, and not measurement data for a particular, installed grating. Less difficult, but still important is the need to be able to accurately ascertain the polarisation characteristics of the incident light, which will depend on the polarisation of the excitation source, the collection geometry, the depolarisation ratio of the relevant scattering mechanism, and the method of transportation of the scattered light.

Note that multimode fibres, as those utilised in our fibre bundle, scramble any input polarisation of the scattered light, and it is safe to use the 'average response' curve provided by the manufacturer. In all other cases, the polarisation composition of the light entering the spectrometer needs to be known in order to implement meaningful, quantitative efficiency corrections.

#### **4.8 Summary**

In order to take full advantage of the potential sensitivity of a given Raman spectroscopy experiment, it is necessary to optimise each element as far as is practicable. In this chapter we have summarised the main parameters that need to be considered at each point of the experimental process, from the mechanical setup and collection geometry of the system, to the specific equipment implemented, and the post-acquisition data processing that is vital in order to maximise the quality of the data and the amount useful information that can be

extracted from the spectral images. These aspects are taken into account in all data evaluation steps, which are described in the remainder of this thesis.

## ***4.9 References for Chapter Four***

### *4.9.1 Cited references (books and papers)*

Demtröder, W. (2003). Laser Spectroscopy – Basic Concepts and Instrumentation. Berlin Heidelberg (Germany), Springer-Verlag.

Goure, J. P., and Verrier, I. (2002). Optical Fibre Devices. London (U.K.). IOP Publishing Ltd.

McCreery, R. L. (2000). Raman Spectroscopy for Chemical Analysis. New York (U.S.A.), John Wiley & Sons, Inc.

Silvast, W. T. (2004). Laser Fundamentals 2nd Ed. Cambridge (U.K.), Cambridge University Press.

Taylor, D. J., M. Glugla, et al. (2001). “Enhanced Raman sensitivity using an actively stabilized external resonator.” Review of Scientific Instruments **72**(4): 1970-1976.

### *4.9.2 Cited references (manuals and datasheets)*

Coherent (1997). Operator’s Manual Verdi™ Diode-Pumped Laser. (U.S.A.) Part No. 0171-750-00, Rev. A

Coherent (2005). Verdi V2, V5 & V6. (U.S.A.) MC-107-02-2.5M0305, Rev. B

HTS grating datasheet master 3028, PIActon (2004)

[http://partners.gratinglab.com/products/efficiency/effFrame.asp?sku=010|53-\\*-260R](http://partners.gratinglab.com/products/efficiency/effFrame.asp?sku=010|53-*-260R)

Semrock RazorEdge transmission curve, Semrock (2004)

[http://www.semrock.com/spectra/LP01-532RU\\_DesignSpectrum.txt](http://www.semrock.com/spectra/LP01-532RU_DesignSpectrum.txt)

Spec-10 CCD array datasheet, PIActon (2004)

<http://architect.wwwcomm.com/Uploads/Princeton/Documents/Datasheets/2kbln.pdf>

### 4.9.3 *Further reading*

Hecht, E. (2002). Optics. San Fransisco (U.S.A.), Addison Wesley.

Hollas, J. M. (2004). Modern Spectroscopy. Chichester (U.K.), John Wiley & Sons, Ltd.

Person, W. B. and G. Zerbi (1982). Vibrational Intensities in Infrared and Raman Spectroscopy. Amsterdam (The Netherlands), Elsevier Scientific Publishing Company.

Sands, D. (2004). Diode Lasers. London (U.K.), IOP Publishing Ltd.

Smith, E. and G. Dent (2005). Modern Raman Spectroscopy - A Practical Approach. Chichester (U.K.), John Wiley & Sons, Ltd.

Wood, R.M. (2003). Laser-Induced Damage of Optical Materials. London (U.K.), IOP Publishing Ltd.

## CHAPTER FIVE

### DIRECT IMAGING SYSTEM CHARACTERISATION

In this chapter we summarise a comparative survey undertaken in early 2005 to determine the suitability of two laser Raman spectroscopic systems to monitor the isotopic purity,  $\epsilon T$ , of  $T_2$  in the Windowless Gaseous Tritium Source (WGTS) component of the Karlsruhe Tritium Neutrino (KATRIN) experiment (Lewis and Telle (2005)). The two systems under review are the 1998-vintage laser Raman system previously used at Tritiumlabor Karlsruhe (TLK) for Raman spectroscopy of hydrogen isotopomers (Taylor et al. (2001)), and the brand-new HTS / Spec-10 based system being designed and assembled at the University of Wales Swansea (UWS) to replace it.

The KATRIN design report (Drexlin, Weinheimer, et al. (2005)) specifies a required accuracy of  $\pm 0.2\%$  in the value of  $\epsilon T$ , with  $\pm 0.1\%$  being the 'gold standard' ideal in the long-term. The gas to be monitored is high purity ( $>95\%$ ) tritium,  $T_2$ , with possible impurities comprising all other hydrogen isotopomers ( $H_2$ , HD,  $D_2$ , HT, DT), and possibly trace amounts of methane isotopomers  $C_nH_xR_y$  ( $R=H, D, T$ ) from chemical reactions. Specifically, the determination of DT and HT is of high importance in the theoretical estimation of systematic error contributions.

The purity of the gas mixture needs to be measured in-line and in real-time in a small gas cell. The original design brief was to measure the purity of the tritium gas at a location near to the WGTS (after the pressure-controlled tritium buffer vessel) at a pressure of 10mbar, and the original estimates reflect this target. In 2006, the proposed position of the monitoring in the inner loop was changed. This was as a consequence of test measurements at the mock-up Test of Inner LOop facility (TILO), which showed that any alteration to the flow tube design (which would have been necessary to accommodate the Raman cell) was unacceptable for the controlled flow conditions. The pressure of the tritium flow at the new location between the main reservoir and the pressure-controlled buffer vessel is about 100mbar. This higher pressure reduces the laser power requirements

by a factor of 10, therefore we include in this chapter revised scaling estimates that reflect this newer probable operating pressure.

Since Raman signals are generally five to six orders of magnitude weaker than the exciting laser radiation, and the number density of the gas mixture at 100mbar is low, a target of  $\pm 0.1\%$  in the value of  $\epsilon T$  presents a significant technical challenge. However, this looks a feasible task, which would have been rather more challenging at the original pressure environment of  $\sim 10$ mbar.

Both the UWS and TLK systems exhibit a  $90^\circ$  collection geometry due to the design of the gas cell that both systems share (see Section 4.2.1). At the time of the review, both systems made use of direct imaging, i.e. the exciting laser beam path was parallel to the entrance slit of the spectrometer. The important features of both systems as used in the review are summarised in Table 5.1.

Overall, the description of experimental configurations and their results is broadly in line with the information provided in the interim report to the KATRIN collaboration (Lewis and Telle (2005)). Subsequent to the submission of said review report, further experiments were carried out on the UWS system using both direct and translational imaging methods. In addition, a higher resolution grating was tested, as well as more powerful lasers than the 10mW unit used in the review. The results of these experiments are summarised in Section 5.5 at the end of this chapter.



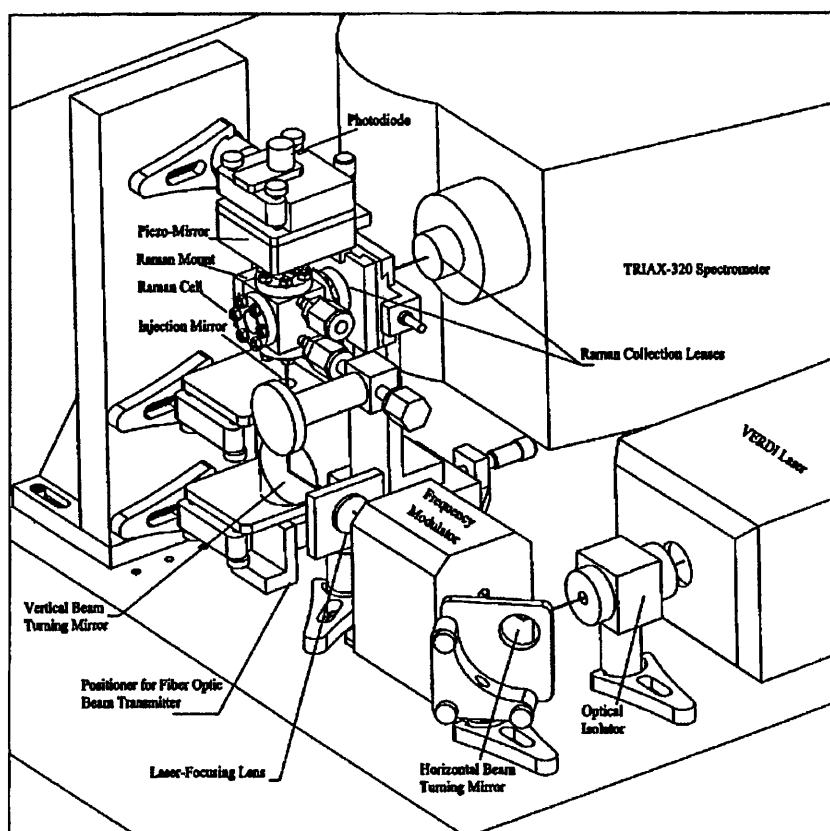
**Table 5.1** Summary of important features of the TLK and UWS Raman systems as evaluated in the comparative review.

Parameter	TLK Raman system	UWS Raman system
Excitation laser	Coherent <i>Verdi V5</i> Nd:YVO <sub>4</sub>	OEM Nd:YAG
Laser wavelength	532nm	532nm
Maximum laser power	5W (~10mW to 5W tuneable)	~7.1mW (10mW rated)
Laser power enhancement	Single back reflection (doubling of laser power)	None (beam dumped)
Spectrograph	Jobin-Yvon <i>Triax320</i>	Acton <i>High Throughput Spectrograph (HTS)</i>
Spectrograph type	Czerny-Turner	Transmitting
Spectrograph control	Computer control of slits and grating position (RS-232)	Micrometer control of entrance slit, manual setting of grating position (grating position lockable)
Installed gratings (gr·mm <sup>-1</sup> )	2400, 600	600
Maximum number of installed gratings	3	1
Spectrograph f-number	f/8	f/1.8
CCD detector	Jobin-Yvon <i>CCD2000</i>	Princeton Instruments <i>Spec-10</i>
CCD type	Back-illuminated 2000×800	Back-illuminated 2048×512
CCD cooling	Water-assisted Peltier	Air-cooled Peltier
A/D conversion	16-bit (65,536 dynamic range)	16-bit (65,536 dynamic range)
CCD interface	ISA (controller card required)	USB2 (via ST-133 controller)
Data acquisition / control software package	Jobin-Yvon <i>SpectraMAX</i> (Win/16)	Roper Scientific <i>WinSpec/32</i> (Win/32)
ASER unit	No	No

### 5.1 The TLK Raman System

A technique for boosting Raman signals from a gas sample is by using an Actively Stabilised External Resonator (ASER), which was demonstrated at TLK (see Taylor et al. 2001). For this, the length of an external high-Q cavity was actively matched to the excitation radiation (532nm) from a Coherent *Verdi V5 5W CW Nd:YVO<sub>4</sub>* laser, using the Pound-Drever locking technique (Drever et al. (1983)) to provide, in the ideal case, up to a 250-fold increase in the Raman signal.

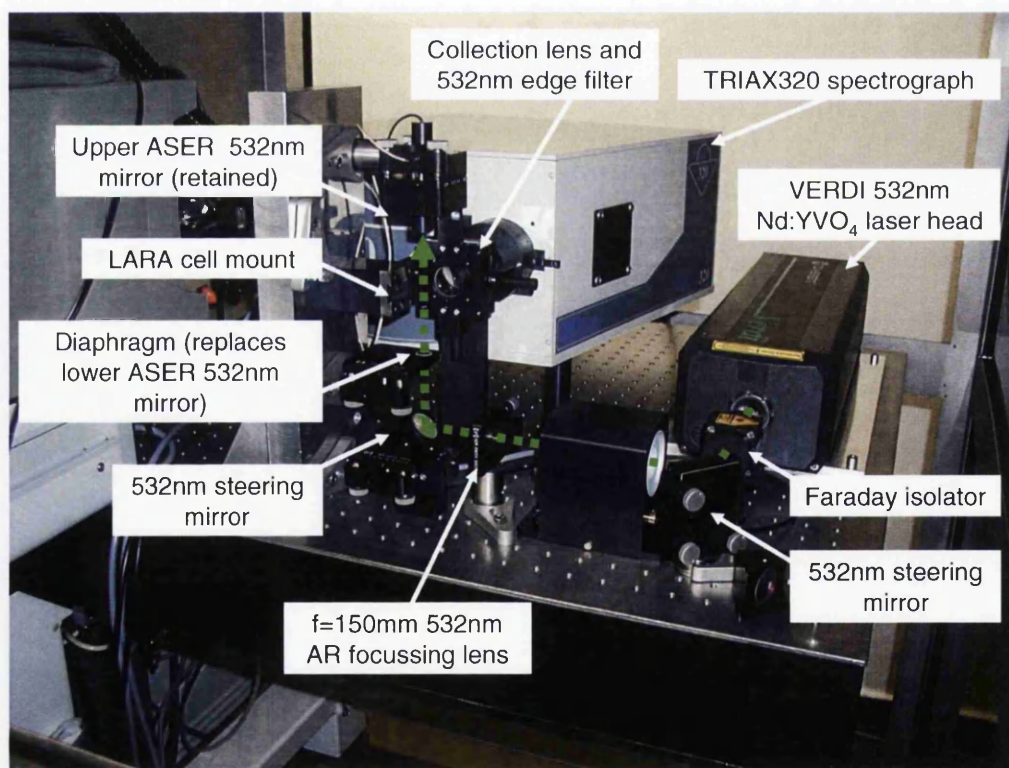
In the system at TLK a 50× enhancement was usually achieved. The scattered radiation (Rayleigh and Raman) from the measurement cell was imaged directly onto the entrance slit of a Jobin-Yvon TRIAX 320 spectrograph, equipped with a Jobin-Yvon 2000×800 CCD-array detector. The detector signal was converted by using a 16-bit A/D converter (with ISA-bus interface card) under computer control. The overall system layout was as shown in Figure 5.1.



**Figure 5.1** The TLK laser Raman spectroscopy system (LARA) with associated ASER for signal enhancement. (Taylor et al. (2001)).

### 5.1.1 The TLK system: overview and general remarks

The spectra obtained at TLK for this report were obtained using much of the LARA system, but without the ASER unit and its associated control system. The arrangement of the equipment is detailed in Figure 5.2. Note that the top ASER mirror was retained to provide a single back-reflection, which effectively doubles the laser power at the focal point – i.e. the scattering volume in the gas cell. A diaphragm aperture was placed in the position of the lower ASER mirror (itself removed) to prevent the broadened laser beam from scattering off the cell windows and metal surfaces. Note also that the optical isolator from the ASER system was retained to prevent back-reflection into the laser cavity, and that a 532nm edge filter was placed in an improvised mount between the scattered light collection lenses.



**Figure 5.2** The TLK laser Raman setup, with the LARA cell removed for clarity. Note the retention of the upper ASER mirror to provide a single back-reflection and hence a doubling of laser power at the focal point. The Faraday isolator prevents the back reflection from entering the laser cavity. The collection lens directly images the scattering region onto the entrance slit of the spectrometer.

In order to align the system, a small liquid cell filled with ethanol was used to provide a very high particle density environment for scattering and a visual reference of the beam path, as mentioned in Section 4.3.1. The detection system was set to record continuously, and the beam path was adjusted until the signal was at its maximum. The focussing did not need to be adjusted as the system has a fixed geometry and was already optimised for the intended beam path.

At the time of the review, both the TLK and UWS systems were aligned using this glass cell filled with ethanol. Following the review, the glass cell was replaced by an ethanol-filled LARA cell of the same design as the gas cells. The good mechanical reproducibility of the mounting dovetail-joint between the breadboard base and the cell considerably lessens the need for lengthy alignments of the beam path.

The Coherent *Verdi* laser used for the excitation was serviced prior to the recording of the spectra in the intermediate report. Although the output power is supposedly selectable between 10mW and 5W, in practice it was found that getting the laser to run at a desired output was more than a simple case of selecting the power on the laser controls. The laser was prone to jump unpredictably between power settings, and the only reliable way to realise a desired power output was to select a higher power than needed and then to lower the current slowly until the laser arrived at the desired output. There were also pointing stability and power output stability issues when attempting to run the laser at below 1W output. This effectively limited the system to  $>1W$  operation. Considering the application for which this system was designed, this does not constitute a restriction, although it would have been useful during the test phase to directly compare the TLK and UWS results both with 10mW laser power, rather than having to scale the data for comparison.

The spectrograph is a Triax320 Czerny-Turner spectrograph with light-collection ratio  $f/8$  and two installed gratings of  $2400\text{gr}\cdot\text{mm}^{-1}$  and  $600\text{gr}\cdot\text{mm}^{-1}$ , with the turret having room for a third (not installed) grating. It is controlled via a serial RS-232 link. The entrance slit width is controllable via the *SpectraMAX* software (see below) and the system includes a computer-operated shutter. The spectrograph was reliable enough once initialised and gave little trouble.

The CCD2000 detector is a discontinued model by Jobin Yvon (now Horiba / Jobin Yvon). It is based on a back-illuminated 2000×800 CCD array, which is cooled by a water-assisted Peltier system. This component proved to be the weak link of the hardware due to software control issues and an unreliable cooling system. When new, this type of detector should run at about 220K, with 230K being a reasonable expectation taking into account the device's age. However, the best operating temperature achievable with the device in its current state was only about 240K, with a steady upwards drift after initialisation to about 300K ("overheating") over the course of an hour. At these temperatures the CCD becomes unusable due to detector noise completely swamping any signal (in standard CCD devices, detector noise increases on average by an order of magnitude for every 20K), and had to be deactivated frequently to prevent damage.

In fact, the overheating of the chip was the single biggest problem of the system, as it limited both the time over which one could take useful readings and rendered the system, as it stands at this moment, unusable for continuous on-line monitoring in a critical situation like the KATRIN monitoring system.

One further remark should be made regarding the "recovery" time of the cooling system: after shutdown, the system has to be left for several hours to cool down completely before the entire start-up routine has to be repeated. The start-up routine, comprising of CCD initialisation, spectrograph initialisation and laser warm-up can take up to 45 minutes. Despite several attempts to repair the cooling system (including pumping out the vacuum in the Peltier jacket) this problem could not be resolved.

The spectroscopy software is a Win/16-based version of Jobin Yvon's *SpectraMAX* package. This is supplemented by DOS-based routines for CCD initialisation and Win/16 programs for setting up, initialising and controlling the Triax320 spectrograph. Due to the ISA interface for the CCD detector and the incompatibility of the software with Win/32 operating systems, it was necessary to conduct the experiments using an old 160MHz Pentium-based PC system running Windows 98. This severely affected reliability of operation and did not allow the use of modern Win/32-based data evaluation software.

Unfortunately, this aging software package constituted another weak point. The routines for initialising the CCD detector and the spectrograph were prone to failure and the *SpectraMAX* software itself was rather buggy, with frequent crashes, freezes, loss of data and the occasional inability to communicate with the spectrograph. Working in the time windows of an hour or so between the CCD being initialised and overheating, it was just about possible to record a few Raman spectra, but the need to constantly monitor the software for possible crashes and to reinitialise the system so often made this a very high-maintenance, hit-and-miss affair.

### 5.1.2 Raman spectra measured at TLK

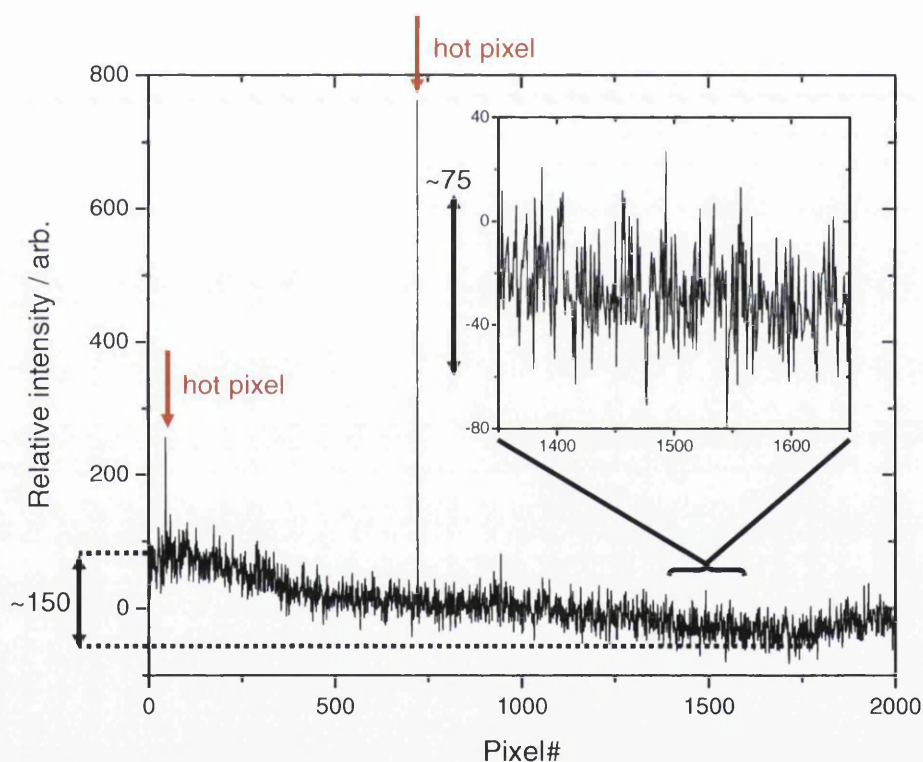
The rotational and vibration-rotation Raman spectra of a variety of gas mixtures were recorded – pure H<sub>2</sub>, pure D<sub>2</sub>, and a 29:47:24(±1) H<sub>2</sub>:HD:D<sub>2</sub> mixture. The gases were all analysed using the same design of gas cell as in the earlier studies at TLK, at 1atm pressure. In order to obtain a clear picture of the system's capabilities, spectra were recorded using both the 2400gr·mm<sup>-1</sup> and 600gr·mm<sup>-1</sup> grating, with exposure times of 30s and 60s. Longer exposure times tended to drive the CCD chip into saturation as a consequence of dark current accumulation – especially at elevated CCD temperatures.

The slit width was kept constant at 100µm when taking the Raman spectra, although it was closed nearly completely in order to record the dark current readings. The width of 100µm was chosen on the one hand as a compromise between light collection and line width, but on the other to simulate, as closely as possible, the expected line widths achievable by the current implementation of the UWS system.

Due to the far greater available laser power at TLK (up to 5W compared to the 10mW at Swansea), the presence of cosmic rays in the TLK Raman spectra was less of an issue than with the UWS system – exposure times were much shorter, being only 30s or 60s compared with up to 1000s at Swansea. The majority of the cosmic ray events during these short exposures were satisfactorily removed by the *SpectraMAX* software's internal 25% spatial cosmic ray removal routine. The very few cosmic ray events that remained

(perhaps one or two per spectrum) generally caused no problems during analysis, but even these events could be easily vetoed when the data analysis program *Origin* was used, by applying a suitable filter to the data.

Dark current readings are discussed in more detail later in this chapter, although it should be noted that the background for the TLK system was not flat at all (see Figure 5.3), and there were several ‘hot pixels’ in the CCD array that look like cosmic ray events in the spectra – but are always occurring in the same place.

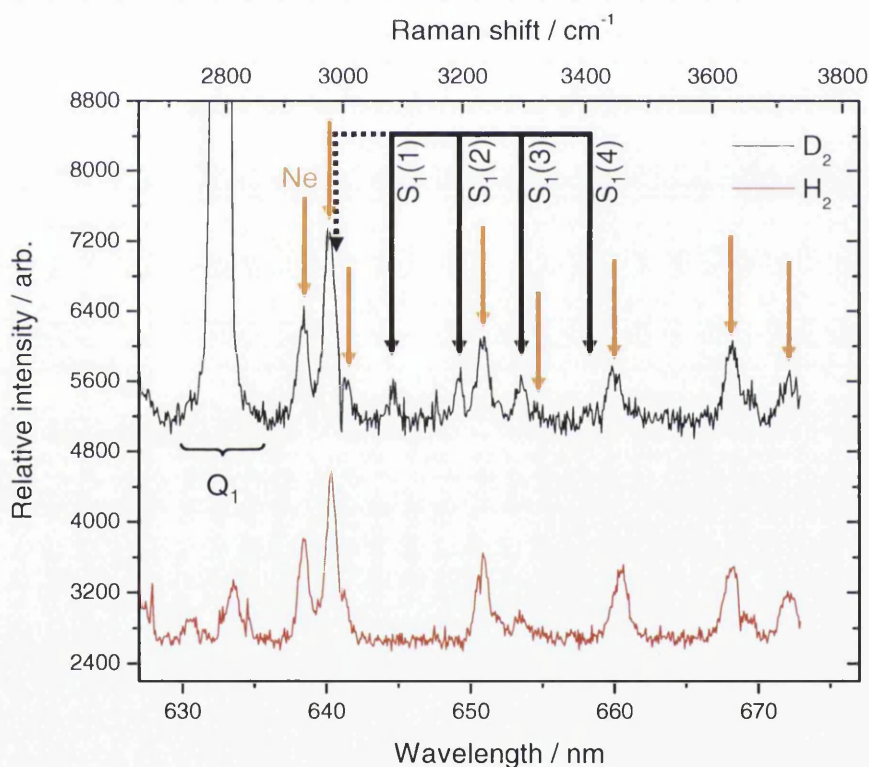


**Figure 5.3** Dark current background of the TLK CCD2000 detector for a 1s exposure – the 512 rows have been binned. The variation of the background level across the chip is of the order of 150 counts due to the uneven background across the chip, with typical local (near-flatfield) fluctuations of the order of 75 counts.

In addition to the steady increase in the background level, there was a tendency for the background to ‘jump’ occasionally more than the expected increase between readings before settling down again. This variation could be 1000 counts or more, or about 2-3% of the dynamic range of a 16-bit detector of 64,000 under ideal conditions. Because of the

very weak nature of Raman signals, this represents a serious handicap to the maximum signal-to-noise ratio possible before the detector saturates. Note that the spectra included in this chapter have been scaled to a zero baseline for clarity.

Despite its shortcomings, the TLK system proved sensitive enough to even pick up the emission from the computer LCD monitor (it was switched off during measurements once this problem had been identified), and the faint light from a small neon power indicator within the laser enclosure (which was taped over in the later experiments). The neon lines can clearly be seen superimposed on the recorded Raman spectra of  $D_2$  and  $H_2$  as shown in Figure 5.4.



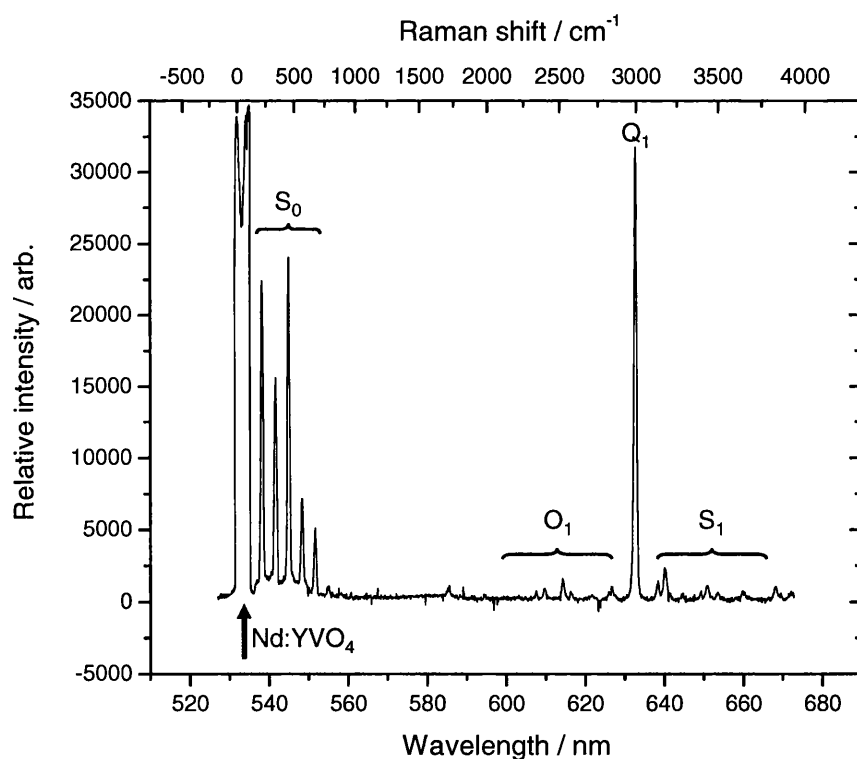
**Figure 5.4** Raman spectrum of  $D_2$  (top, black) and  $H_2$  (bottom, red), showing neon lines from a power indicator. The  $Q_1$ - and (visible)  $S_1$ -branch lines for  $D_2$  are labelled – the  $D_2$   $S_1(0)$  line at  $\sim 639$ nm is hidden by the neon lines. The rotation-vibration Raman spectrum of  $H_2$  has no lines in this region and is provided for comparison.

The first set of readings were taken with the  $600\text{gr}\cdot\text{mm}^{-1}$  grating, and this showed that the system was quite capable of recording both pure rotational and vibration-rotation Raman



spectra of the hydrogen isotopomers analysed ( $H_2$ ,  $HD$ ,  $D_2$ ). Note that all spectra recorded with the ASER system in the publication by Taylor et al. (2001) are vibration-rotation data; pure rotational spectra could not be recorded due to the absence of a Rayleigh suppression filter in those measurements.

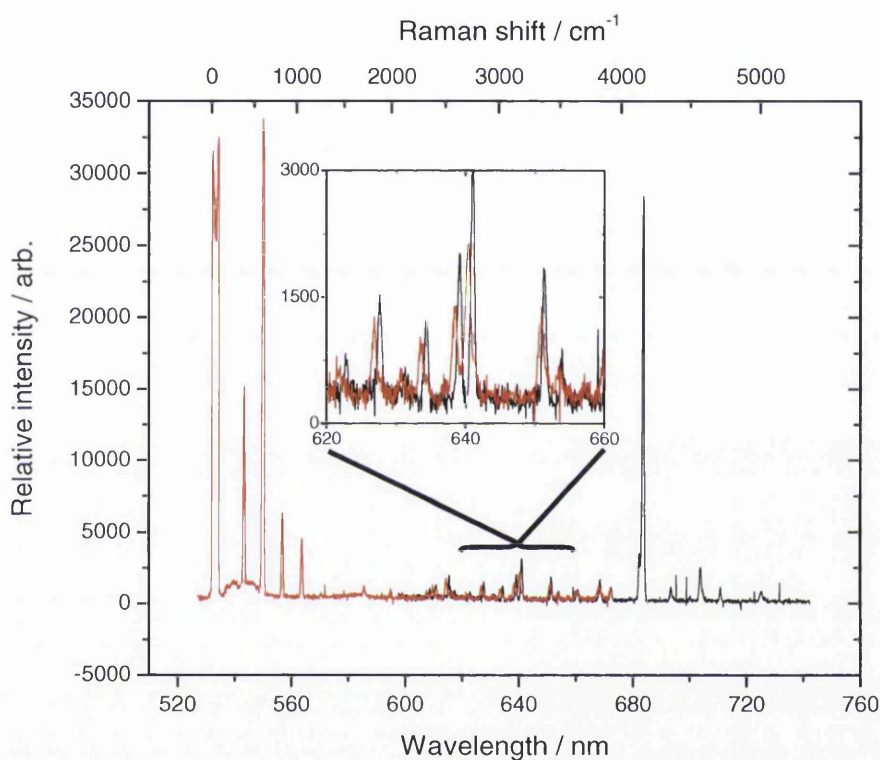
The spectral range of the  $600\text{gr}\cdot\text{mm}^{-1}$  grating at the operating wavelengths is about  $\pm 70\text{nm}$  either side of the central wavelength. While this is sufficient to resolve the whole spectral range (rotational and vibration-rotation) of  $D_2$  (see Figure 5.5), the spectrograph setting has to be adjusted to record both components in the  $H_2$  spectrum, and so they cannot be recorded simultaneously.



**Figure 5.5** Raman spectrum of  $D_2$ , exhibiting both pure rotational ( $S_0$ -branch) and vibration-rotation ( $O_1$ -,  $Q_1$ -, and  $S_1$ -branch) lines. Note the Lorentz wing from the 532nm laser line is still prominent even with the edge filter in place.

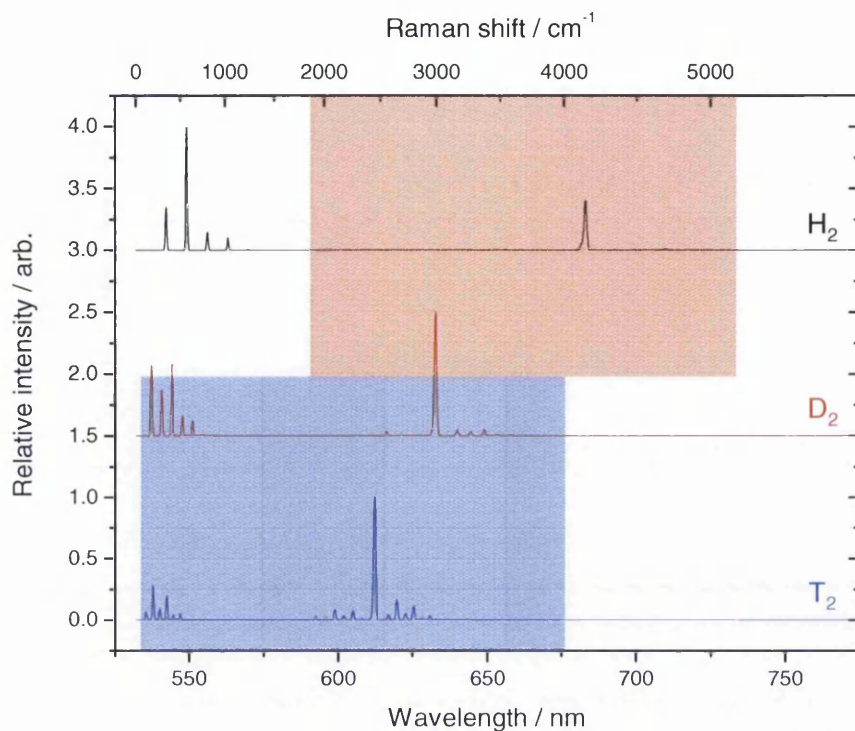
A software routine is provided with *SpectraMAX* to “stitch together” spectra from readings that overlap. As noted above, in order to record the whole spectrum of  $H_2$ , the central wavelength needs to be moved and sequential spectra taken – the program should then in

principle be able to stitch the two spectra together to give the whole range. Due to the non-linear nature of the background and the unpredictable variations in the background level, this was not possible using the proprietary routine. It was however, possible to achieve a fair overlap, scaled to the correct signal amplitudes, using the *Origin* data evaluation software. The result is shown in Figure 5.6.



**Figure 5.6** The Raman spectrum of  $\text{H}_2$ , recorded with the TLK Raman system. Note the slight intensity mismatch of the overlap between the two spectra, centred at 600nm (left, red) and 670nm (right, black), due to background inconsistencies.

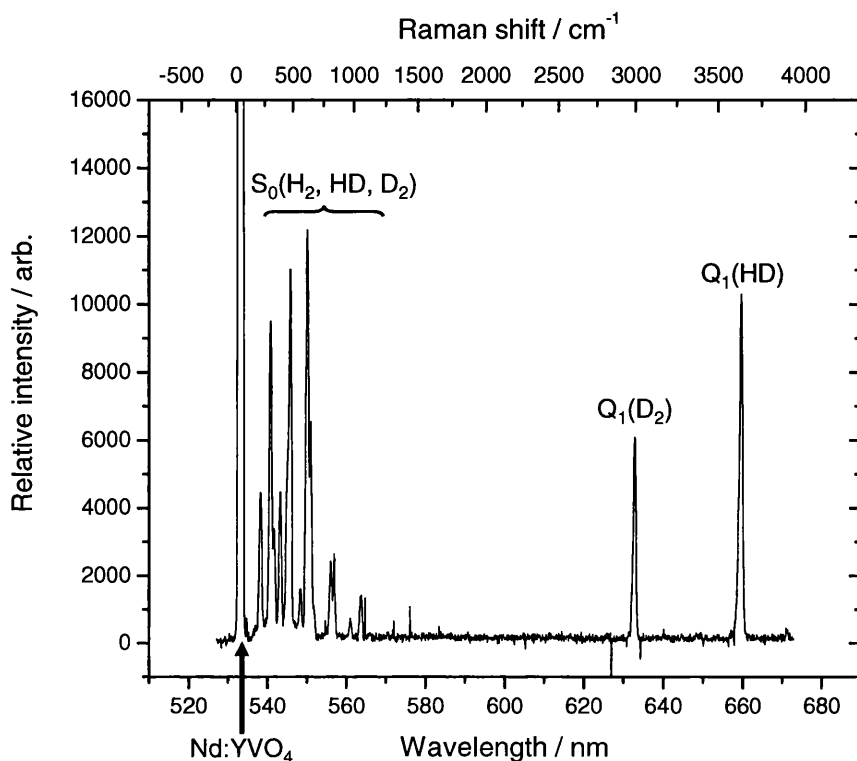
Calculations show that if centred at the 600nm position, the  $600\text{gr}\cdot\text{mm}^{-1}$  grating would be able to record the whole spectrum of  $\text{T}_2$ ,  $\text{DT}$ , and  $\text{D}_2$ , whereas in the spectra of  $\text{HT}$  and  $\text{HD}$  several vibration-rotation  $\text{S}_1$ -branch lines would be missing, although their  $\text{Q}_1$ - and  $\text{O}_1$ -branches would be visible. However, only the first few lines of the  $\text{H}_2$   $\text{O}_1$ -branch would be visible, with its  $\text{Q}_1$ - and  $\text{S}_1$ -branches missing completely. A summary for the spectral components of all hydrogen isotopomers is provided in Figure 5.7. The Raman spectra were calculated using the *SpecGen* program detailed in Chapter 3 (principle) and Appendix A1 (*LabVIEW* code).



**Figure 5.7**  $600\text{gr}\cdot\text{mm}^{-1}$  grating coverage for centre positions of  $600\text{nm}$  ( $\sim 2130\text{cm}^{-1}$ , blue block) and  $650\text{nm}$  ( $\sim 3412\text{cm}^{-1}$ , red block) with respect to the Raman spectra of  $\text{H}_2$  (top, black),  $\text{D}_2$  (middle, red), and  $\text{T}_2$  (bottom, blue). Simulations performed by *SpecGen*.

In order to record the spectrum of a hydrogen isotopomer mixture, a cell was refilled with a known mixture of  $\text{H}_2\text{:HD:D}_2$  at  $1\text{atm}$  in the ratio  $29\text{:}47\text{:}24(\pm 1)$ . The corresponding spectrum is shown in Figure 5.8. Note that in the vibration-rotation regions, only the  $\text{Q}_1$ -branches are clearly visible. Only the most intense lines of the  $\text{O}_1$ - and  $\text{S}_1$ -branches are just visible above the noise; as expected, these lines are very weak indeed.

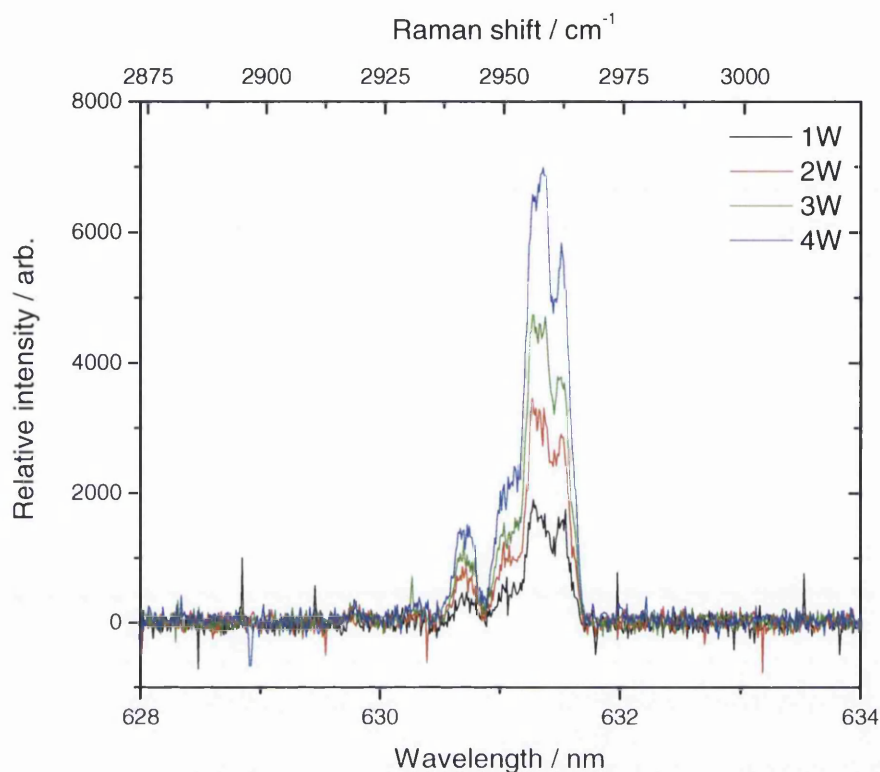
Using the  $600\text{gr}\cdot\text{mm}^{-1}$  grating the individual rotational lines of the  $\text{Q}_1$ -branch cannot be resolved. Although a handful of readings were taken with the  $2400\text{gr}\cdot\text{mm}^{-1}$  grating, at that stage of the test measurements the CCD overheating had become so severe when these measurements were attempted, that only the  $\text{Q}_1$ -branch of  $\text{D}_2$  at four different laser power outputs could be recorded before the system had to be shut down for the final time. These recordings are shown in Figure 5.9; they illustrate quite clearly the linear scaling of the Raman signal strength with the excitation laser power.



**Figure 5.8** Raman spectrum of the  $\text{H}_2:\text{HD}:\text{D}_2$  (1atm) cell, showing the pure rotational lines and the vibration-rotation lines of  $\text{D}_2$  (left) and HD (right).

Although the individual lines are not completely resolved, with a decrease in slit width it should be possible to resolve them reasonably well. It would also have been helpful to have spectra of the pure rotational bands of all three isotopomers using the  $2400\text{gr}\cdot\text{mm}^{-1}$  grating, but a combination of the overheating CCD and limited time at TLK made this impossible.

Signal-to-noise ratio estimates were difficult to extract from the data due to the unpredictable nature of the background, but ‘best-case’ numbers can be obtained by considering the very best spectra for a variety of exposure times / laser powers; these are summarised in Table 5.2. In the table,  $S(\text{rot})$  denotes the signal strength of the strongest pure rotational Raman line above the baseline (in this case the  $\text{H}_2$   $S_0(1)$  line),  $S(\text{vib})$  refers to the strength of the strongest HD  $Q_1$ -branch line,  $N$  is the noise level, with  $S/N(\text{rot})$  and  $S/N(\text{vib})$  being the signal-to-noise ratios for the rotational and vibration-rotation lines, respectively.



**Figure 5.9** The Raman vibrational  $Q_1$ -branch of  $D_2$  at laser excitation power: 1W (black), 2W (red), 3W (green) and 4W (blue). Note the almost perfect linear scaling of Raman signal strength with laser power and the high resolving power of the  $2400\text{gr}\cdot\text{mm}^{-1}$  grating.

Due to the aforementioned time restrictions, only the  $Q_1$ -branch of  $D_2$  was measured using the  $2400\text{gr}\cdot\text{mm}^{-1}$  and  $2\times 30\text{s}$  readings. Note that for the  $1\text{W } 600\text{gr}\cdot\text{mm}^{-1} 5\times 30\text{s}$   $D_2$  reading one notices that the vibration-rotation S/N is considerably greater than that for the rotational lines. This is most likely due to the strongest  $D_2$  rotational lines being strongly affected by the Lorentz wing of the Rayleigh line.

**Table 5.2** Estimates of ‘best-case’ signal-to-noise ratios achieved with the TLK laser Raman system, for 100 $\mu$ m entrance slit width. One can clearly see the wild variation in background noise from the CCD2000 detector. Note the doubling in laser power through the cell due to the single back reflection.

Sample (at 1atm)	Laser Power	Grating [gr·mm <sup>-1</sup> ]	Exposure [s]	S (rot)	S (vib)	N	S/N (rot)	S/N (vib)
H <sub>2</sub>	2× 1W	600	5× 30	33385	28033	225	<b>148</b>	<b>125</b>
D <sub>2</sub>	2× 1W	600	5× 30	23830	31523	100	<b>238</b>	<b>315</b>
H <sub>2</sub> :HD:D <sub>2</sub>	2× 1W	600	5× 30	12017	10124	70	<b>171</b>	<b>145</b>
H <sub>2</sub> :HD:D <sub>2</sub>	2× 1W	2400	2× 30		1680	200		<b>8</b>
H <sub>2</sub> :HD:D <sub>2</sub>	2× 2W	2400	2× 30		3234	200		<b>16</b>
H <sub>2</sub> :HD:D <sub>2</sub>	2× 3W	2400	2× 30		4469	200		<b>22</b>
H <sub>2</sub> :HD:D <sub>2</sub>	2× 4W	2400	2× 30		6723	200		<b>34</b>

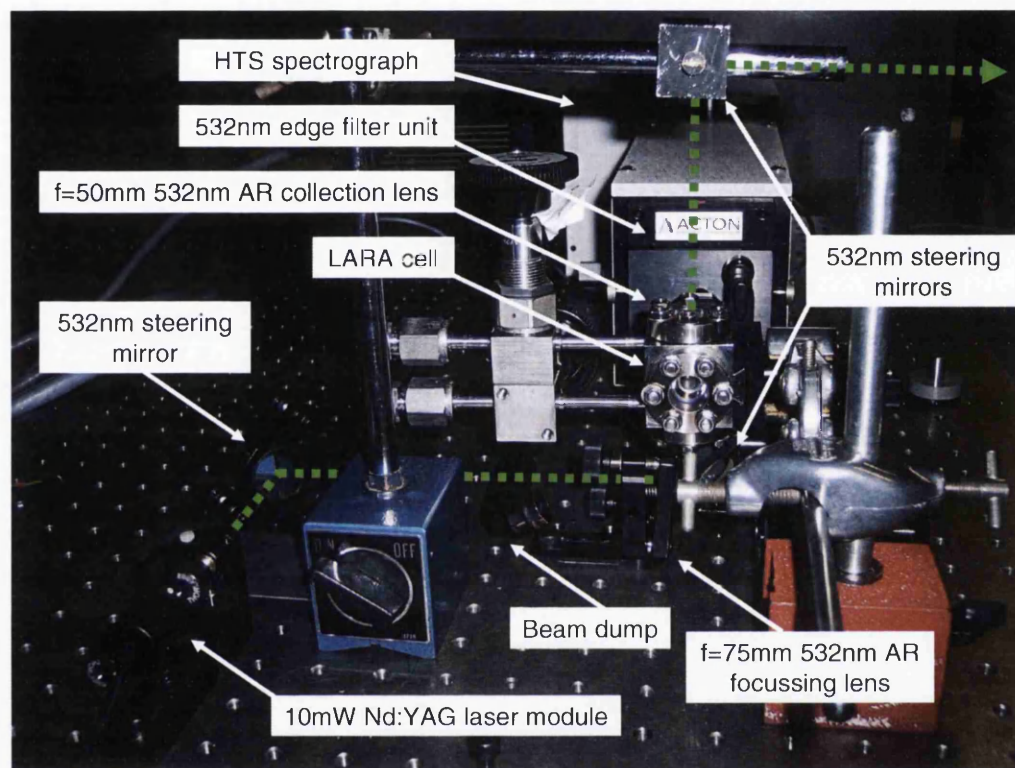
## 5.2 The UWS Raman System

### 5.2.1 The UWS system: overview and general remarks

The general configuration of the UWS Raman system is broadly similar to that of the TLK system. Both use a 90° geometry, direct one-to-one imaging of the scattering volume onto the entrance slit of the spectrometer. Apart from the newer spectrometer and detector, the main differences are the much lower power of the 532nm CW Nd:YAG laser (maximum output 10mW) employed in the UWS system, the once-through setup for the laser beam (no back reflection), and the dedicated filter unit. Due to the larger-diameter optics, compared with the TLK system, a larger diameter filter was required (1.5” diameter instead of 1” diameter). The UWS system is shown in Figure 5.10.

At the time of the review, the excitation laser employed in the UWS laser Raman system was a 532nm CW Nd:YAG laser (generic OEM module), with a maximum rated output power of 10mW. Measurements with a power meter have shown that the actual power reaching the cell is only about 7.1mW (due to the non-optimised beam-steering optics used in most of the test experiments). Wavemeter measurements (see section 4.1.1) have shown that this very rudimentary laser module exhibits remarkable stability with regards to

wavelength, remaining stable to six significant figures after a ‘warm-up’ time of ~15min (corresponding to much less than  $1\text{cm}^{-1}$  drift), although the laser is ready-for-use as soon as it is switched on.



**Figure 5.10** The UWS laser Raman setup, showing the dedicated filter unit and the single-pass configuration of the laser beam path (green dashed line). The steering mirrors are used to pass the laser beam through the LARA cell parallel to the entrance slit of the spectrometer and then away to a beam dump. The small beam dump near the focussing lens mount is used to dump any reflections from the lens (note orientation of lens mount).

The spectrograph is the first production model of the new Acton High Throughput Spectrograph (HTS). It differs from a standard Czerny-Turner spectrograph in its use of transmitting collimation optics, rather than reflective mirrors. The light-collection power of the HTS is also much higher than for standard spectrographs with an f-number of  $f/1.8$ . Compared to the TLK spectrometer’s f-number  $f/8$  this corresponds to a  $>16$ -fold increase in the light-collection power. The entrance slit of the spectrograph is manually controlled via a micrometer adjustment above the slit, although future HTS spectrographs will include

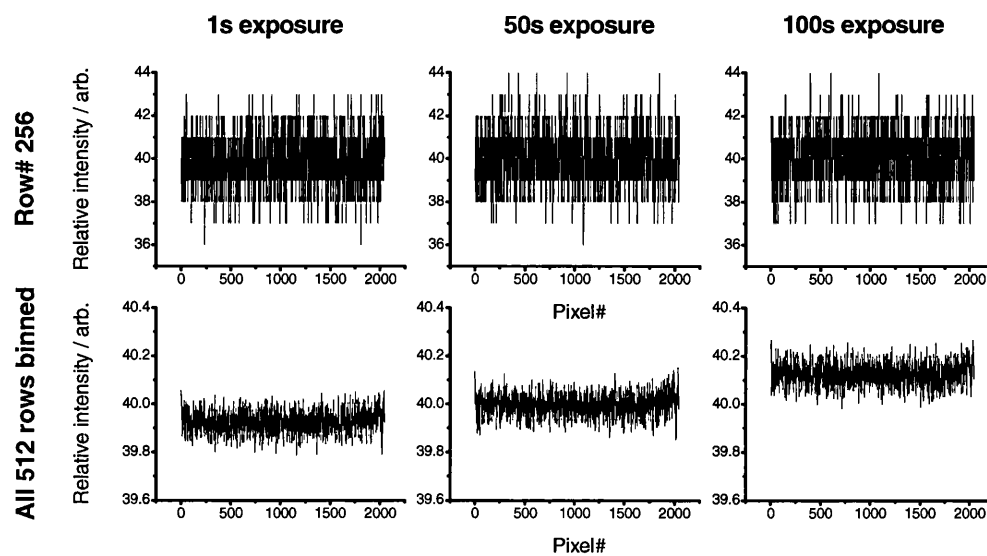
computer-controlled motors – this option may become available as an upgrade at a later date.

The installed  $600\text{gr}\cdot\text{mm}^{-1}$  grating is left in a ‘fixed’ position once it has been moved into the region of interest via a manual micrometer adjustment as each grating setting requires a recalibration. However, this doesn’t pose a problem in the current application. The unit is very rugged, and calibrations remain accurate for months at a time. The longest period over which a single calibration was used during the survey was for two months, and the calibration remained accurate to within a third of a pixel across the entire spectral range.

The CCD detector is a Spec-10:2K/B/NTE2 16-bit back-illuminated  $2048\times 512$  array (Princeton Instruments), cooled by an air-fed Peltier. Support for optional cryogenic cooling is provided, although this is not implemented. Based on the test measurements, it is thought that the incorporation of a cooling circuit, which requires regular service, would not be merited given the potential gain in S/N. The detector runs at 203K with a thermostatic precision of  $\pm 0.005\text{K}$ . The time from switch-on to operating temperature is of the order of 15 minutes, far superior to the sluggish response of the old Jobin-Yvon device at TLK. For further details on the detector, see the Spec-10 datasheet (Princeton Instruments (2004)).

In use at UWS the Spec-10 has proved to be extremely reliable and stable, with a very low and almost completely flat dark current noise across the whole chip, as the examples in Figure 5.11 illustrate. Note that the baseline level of 40 is an electronic offset that ensures stability and ease of data manipulation. The dark current noise is practically constant at  $\pm 2$  counts for a single pixel row at all (single) exposure times tested between 1s and 1000s. When all rows are binned the noise level is reduced to  $\pm 0.1$  counts for a single exposure. There is a slight upward drift of the baseline level (visible in the binned readings) as the exposure time is increased, but this is of the order of only 0.4 counts when increasing the exposure time from 1s to 1000s.





**Figure 5.11** Dark current noise across the UWS Spec-10 CCD for exposure times of 1s (left), 50s (centre) and 100s (right), for the central pixel row (top) and all 512 rows binned (bottom). The single-row noise for every exposure time is approximately  $\pm 2$  counts.

The Spec-10 was connected to the controlling PC (a Pentium III-based machine running Windows 2000) via a USB2.0 interface, and to the shutter via a proprietary cable. No incompatibility or communication issues were encountered during use.

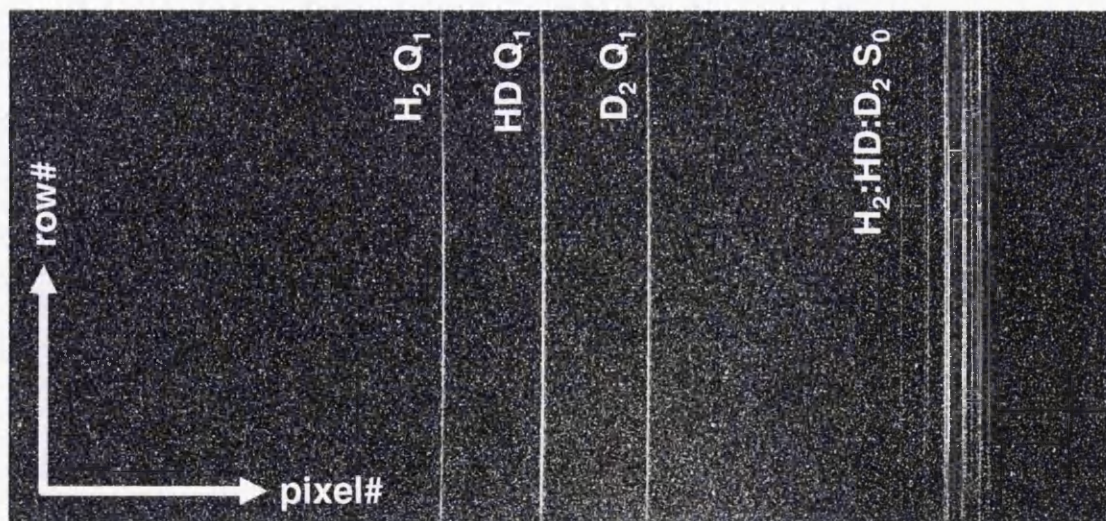
The acquisition software was version v.2.5.16.5 of Roper Scientific's *WinSpec/32* package, adapted for use with the HTS spectrograph, that runs equally well on Windows 2000 or XP SP1. The program is very stable and has regularly been run unattended over the period of days at a time, taking automated readings while the laboratory has been shut to keep out stray light.

After the survey was completed, it was found that there were problems in getting the Spec-10 to work under Windows XP SP2. In the meantime, this was fixed in *WinSpec/32* version v2.5.19.8. Under this newer version, the Spec-10 has been successfully run on both desktop and laptop systems running Windows XP SP2, without any problems. This flexibility is simply not possible with the ISA-based TLK system.

In order to align the system, the same method was used as for the TLK system, making use of the scattered light from a liquid cell filled with ethanol. By precisely manipulating the alignment mirrors an almost complete illumination of the CCD chip can be achieved, as shown overleaf in Figure 5.12. The alignment process was rather laborious as the setup used for the survey did not incorporate precision mounts for the optics. As mentioned earlier, this was remedied following the survey by replacing the generic glass cell with an ethanol-filled LARA cell.

### 5.2.2 Cosmic ray removal

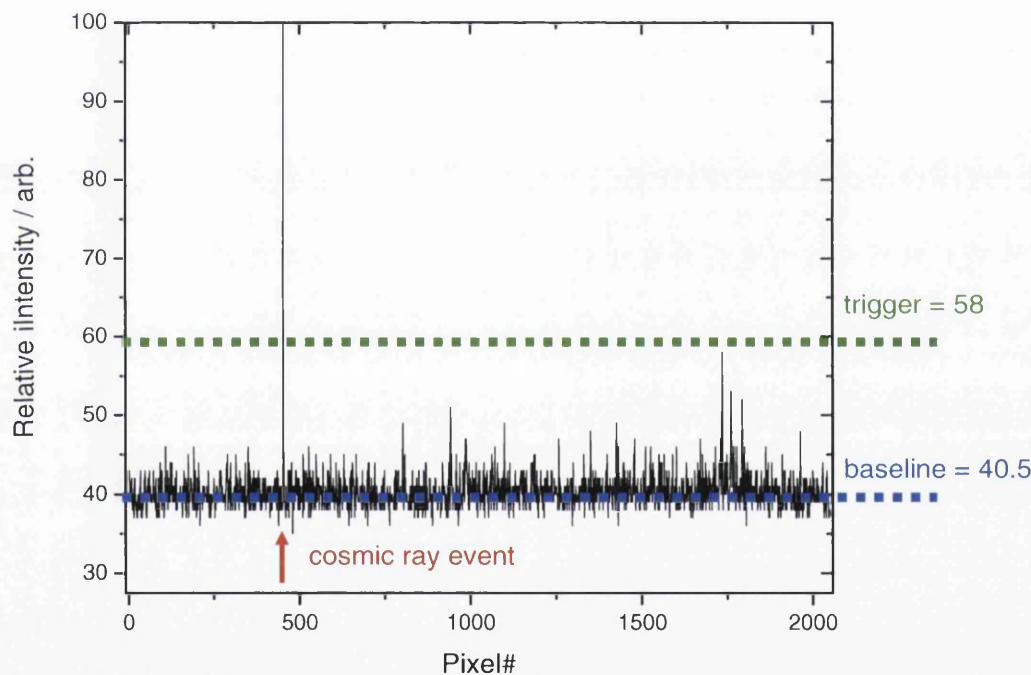
The low output power of the OEM Nd:YAG laser module used at UWS (typically 7.1mW passing through the cell) necessitated long exposure times of up to 500s, or more. Such long exposures mean that the number of cosmic ray events on the spectral traces is high, as shown in Figure 5.12. At the time of the survey, our initial, simplistic *LabVIEW* program *TrigCRR* (described in Section 4.7.2) was used to remove these events instead of *WinSpec/32*'s own internal cosmic ray event veto.



**Figure 5.12** Raman spectrum from the gas cell containing the 29:47:24( $\pm$ 1) H<sub>2</sub>:HD:D<sub>2</sub> mixture, showing near complete illumination of the CCD chip and the presence of cosmic ray events.

In use, *TrigCRR* scans each strip of a spectrum and replaces any pixel value above a manually-selected 'trigger' value with the baseline value of the trace (see Figure 5.13). The trigger value is set to be just above the maximum value of the strongest (rotational) line on the central (#256) row, as this is the row exhibiting the highest signal intensity (it is the centre of the Gaussian distribution of line intensities across pixel rows).

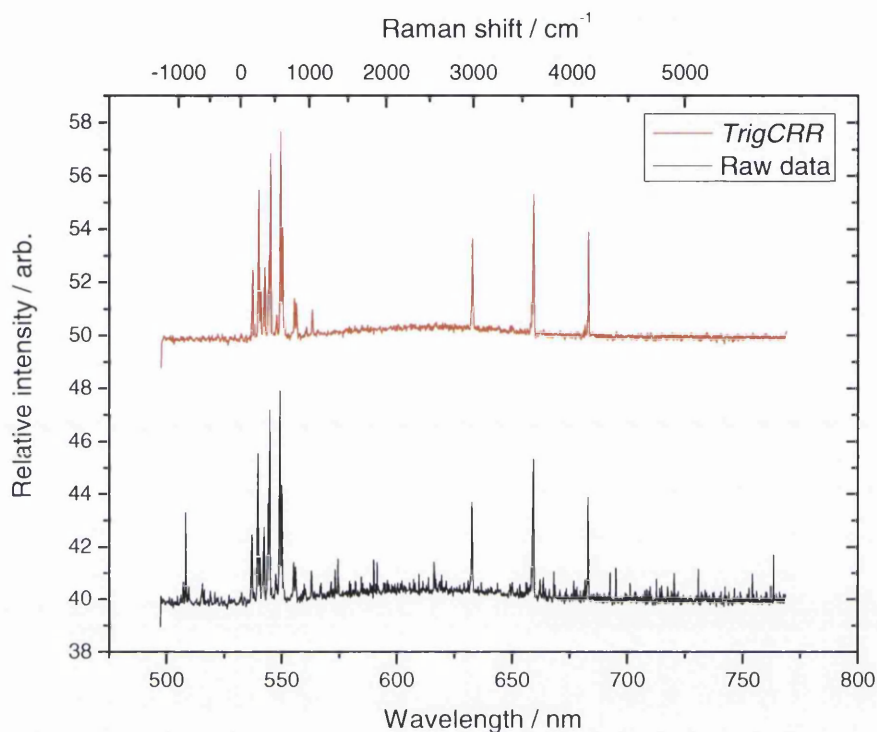
In the case of Raman spectra taken with the 10mW laser module, the maximum rotational line intensity never rose above about 55 counts, so the trigger was set at 58 counts. The replacement intensity was set at 40.5, which is the baseline value (see Figure 5.13 for an example).



**Figure 5.13** Row #256 of a Raman spectrum trace of the  $\text{H}_2\text{:HD:D}_2$  (1atm) cell, showing the baseline (40.5, blue) and trigger (58, green) values. The relative intensity values of the pixels comprising the cosmic ray event (red arrow) are replaced with the baseline value of 40.5.

When all 512 rows are binned, after execution of the cosmic ray removal routine, the spectrum is almost completely clean of cosmic ray events. In Figure 5.14 a Raman spectrum from a  $\text{H}_2\text{:HD:D}_2$  mixture at 1atm is shown before and after the application of

this routine – the events that were below the ‘trigger’ value are diluted in the binning process and are no longer visible.



**Figure 5.14** Raman spectrum of the  $\text{H}_2\text{:HD:D}_2$  (1atm) cell, before (bottom, black) and after (top, red) application of the cosmic ray removal routine *TrigCRR* – almost all the cosmic ray events have been eliminated. The corrected data has been offset for clarity.

It is worth restating that this rather crude procedure only gives satisfactory results because the Raman signals acquired using the 10mW laser lie only just above the background (dark current) noise level of roughly  $\pm 1$  counts above the baseline of 40.5 counts, but are much less intense than the cosmic ray events, which have a typical intensity of  $>100$  counts. Note that these numbers are per pixel row. The average background noise level is about  $\pm 0.03$  counts when all 512 pixel rows are binned.

Clearly this technique would not be suitable for the spectra obtained from the TLK system; those signals were much more comparable in intensity to the cosmic ray events themselves, as were the spectra taken with modestly increased (up to 100mW) laser power at UWS

following this review. In such cases, long exposures were cleaned by more sophisticated methods, i.e. row intensity comparison or (later) double derivative cosmic event vetoing.

### 5.2.3 Correction of HTS-system image distortion

As mentioned in Section 4.7.1, it is absolutely vital to correct for the astigmatism in the HTS spectrograph. The example given in that section demonstrated the improvements in line width and peak intensity, and corrections in line (centre) position for the 632.816nm emission from a HeNe laser. In that example, the corrections to the centre position, peak intensity and linewidth were 0.02%, 56%, and 36%, respectively.

The HeNe laser example used a slit width of 25.4 $\mu\text{m}$ , the same as for the spectra taken in the comparative survey with the UWS system. Since the  $Q_1$ -branches are unresolved with the 600gr $\cdot\text{mm}^{-1}$  grating in the HTS at any slit width, the slit can be opened to 76.2 $\mu\text{m}$  or even 127 $\mu\text{m}$  in order to improve the intensities of these lines. As these Raman lines are wider than the laser line, one would expect the improvements (in line position and linewidth at least) to become more modest when applying astigmatism correction with increasing slit width.

The improvements in linewidth and line position for a binned 5 $\times$ 1000s exposure of the 1atm 29:47:24( $\pm$ 1)  $\text{H}_2$ :HD:D<sub>2</sub> cell at  $\sim$ 7.1mW CW 532nm excitation with an entrance slit width of 25.4 $\mu\text{m}$  are summarised below in Table 5.3. Note that although the improvements are less dramatic than for the laser line example, at this power level it is absolutely necessary to make every correction and improvement possible to obtain spectra with optimal S/N ratio.

Note that although the correction to the line centres are roughly the same as for the laser line at about 0.02%, the improvements to the peak intensity and linewidth are not so dramatic, with the most intense lines ( $\text{H}_2$   $S_0(1)$  and HD  $Q_1$ ) showing rather less improvement in both parameters, at only a few percent. The  $S_0$ - and  $Q_1$ -branch lines for D<sub>2</sub> and  $\text{H}_2$ , however showed average improvements in peak intensity and linewidth of 31%

and 24.5%, respectively, which although modest in comparison with the improvements to the laser lines of 56% and 36%, respectively, these are nevertheless significant improvements.

**Table 5.3** Improvements to line position and linewidth for prominent Raman lines of a binned  $5 \times 1000$ s Raman spectrum of a 1atm 29:47:24( $\pm 1$ )  $H_2:HD:D_2$  sample, recorded at  $\sim 7.1$ mW CW 532nm excitation. The HTS entrance slit width was set to 25.4 $\mu$ m. The strongest rotational line of the  $H_2:HD:D_2$  Raman spectrum, (the  $H_2 S_0(1)$  line) was used to represent the rotational lines. *DCRR* was used to clean the spectra of cosmic ray events. The correction to the line centres is roughly even for all lines, less improvement in peak intensity and linewidth is noticed for the more intense lines.

Parameter	Spectral line			
	$H_2 S_0(1)$	$D_2 Q_1$	$HD Q_1$	$H_2 Q_1$
Line centre / nm (uncorrected)	549.187	632.624	659.275	683.116
Line centre / nm (corrected)	549.300	632.754	659.399	683.207
Correction to line centre / nm	0.113	0.130	0.124	0.091
Peak intensity / arb. (uncorrected)	36.7	13.2	21.9	14.4
Peak intensity / arb. (corrected)	37.7	16.7	23.3	19.5
Improvement in peak intensity / arb. (%)	1.0 (3%)	3.5 (27%)	1.4 (7%)	5.1 (35%)
Linewidth / nm (uncorrected)	0.475	0.623	0.664	0.474
Linewidth / nm (corrected)	0.456	0.505	0.632	0.332
Correction to linewidth / nm (%)	0.021 (4%)	0.118 (19%)	0.032 (5%)	0.142 (30%)

The correction to the line centre positions of  $\sim 0.1$ nm corresponds to almost a full pixel's width. This would be an essential correction if high-resolution spectroscopy was to be performed.

### 5.2.4 Raman spectra measured at UWS

A thorough study was conducted, in which Raman spectra of the cell containing H<sub>2</sub>:HD:D<sub>2</sub> (29:47:24±1 at 1atm) were recorded for several summations of exposure times, for a total of up to 5000s, at a slit width of 25.4μm. A summary for individual single exposures and repeated multiple exposure times is given in Table 5.4.

**Table 5.4** Exposure times for the UWS section of the TLK / UWS system comparative study. Spectra flagged with an asterisk (\*) are shown in this chapter.

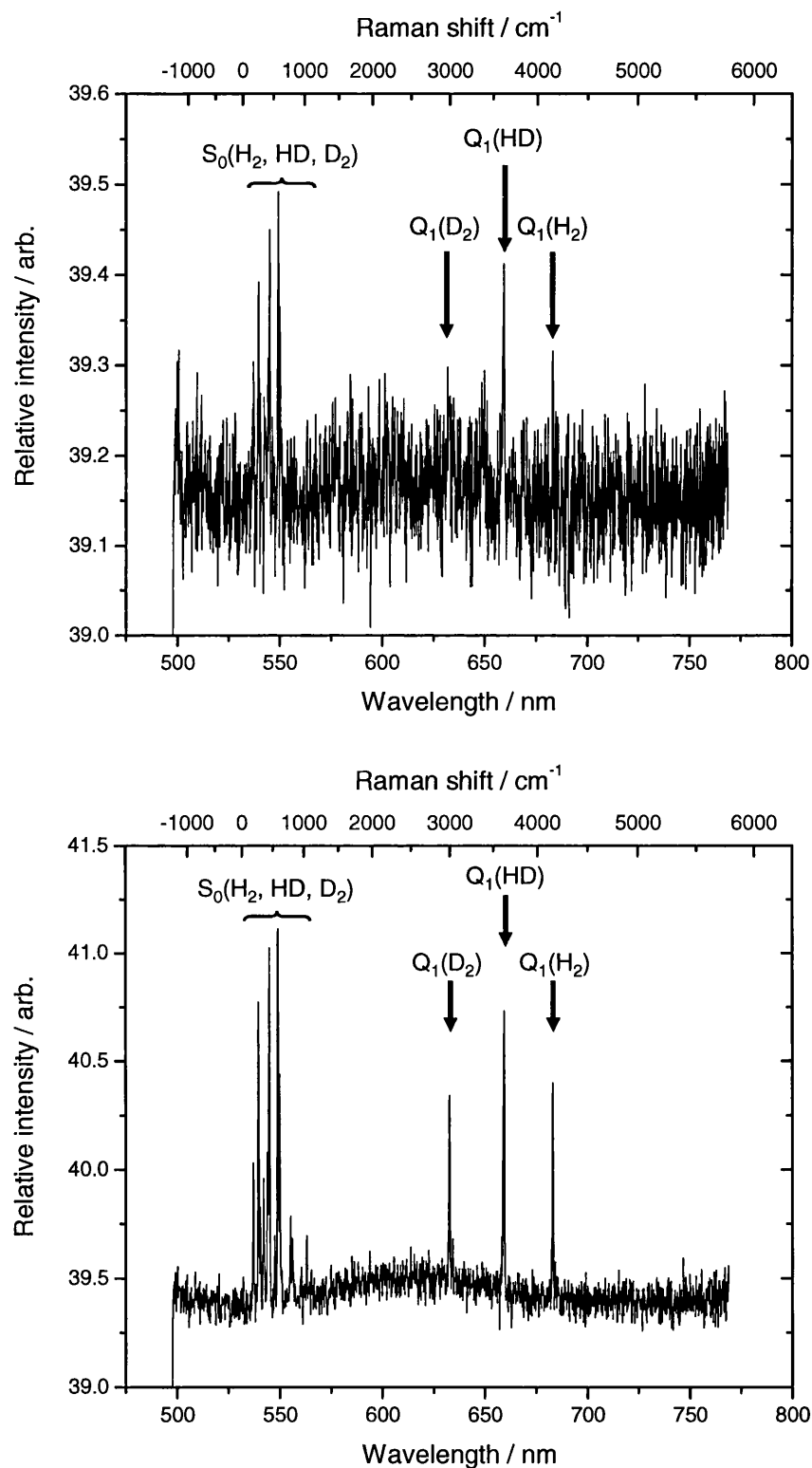
Multiple exposures (total of 5000s each)	Single exposures (s)
5 × 1,000s(*)	1 × 1,000s (*)
10 × 500s	1 × 500s
20 × 250s (*)	1 × 250s (*)
50 × 100s	1 × 100s
100 × 50s (*)	1 × 50s (*)

This study was conducted in order to obtain a better insight into the ideal balance between exposure time and number of exposures for a given total recording time.

With larger numbers of exposures, the random pixel-to-pixel response is averaged out, but the readout noise increases. The reverse is true for longer exposures: the random pixel-to-pixel response is more prevalent, but the readout noise is reduced. With longer exposure times, however, comes the added complication of cosmic ray events.

Figure 5.15 (top) shows that even at the shortest total exposure time (1×50s), the pure rotational lines and the vibration-rotation Q<sub>1</sub>-branch of HD are visible above the background noise. It is only just possible to see the Q<sub>1</sub>-branches of H<sub>2</sub> and D<sub>2</sub> above the noise, so this exposure time represents the lower limit for observing the H<sub>2</sub> and D<sub>2</sub> in the cell with the current laser power of ~7mW.

At 1×100s the Q<sub>1</sub>-branches for H<sub>2</sub> and D<sub>2</sub> are of similar intensity to the Q<sub>1</sub>-branch of HD for the 1x50s exposure, as expected, since the number densities of H<sub>2</sub> and D<sub>2</sub> are roughly half that for HD in the cell.



**Figure 5.15** Top: 1x50s-exposure Raman spectrum of the 29:47:24( $\pm$ 1)  $\text{H}_2$ :HD: $\text{D}_2$  (1atm) cell. The pure rotational lines and the vibration-rotation  $Q_1$ -branch of HD are visible. Bottom: 1x250s-exposure Raman spectrum of the same sample. The vibration-rotation  $Q_1$ -branches of all three isotopomers are now visible. Entrance slit width: 25.4 $\mu\text{m}$ , astigmatism correction: AstCorr, cosmic ray removal: TrigCRR.



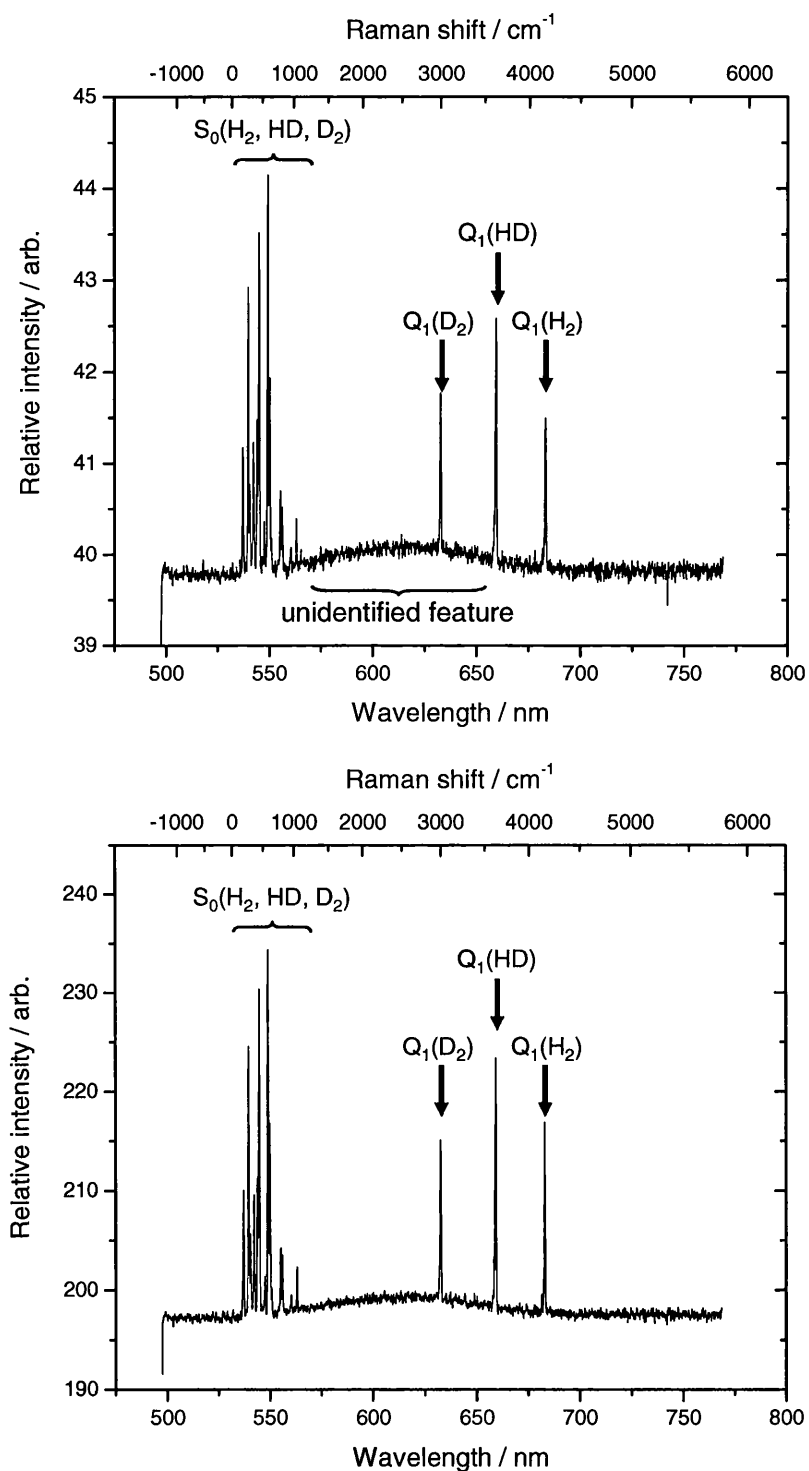
When the exposure time is increased to  $1 \times 250$ s, as shown in Figure 5.16 (bottom), it becomes possible to clearly recognise the  $Q_1$ -branches for  $H_2$  and  $D_2$ . Although one cannot yet completely resolve the pure rotational lines, it is just possible to identify and assign the strongest of the rotational lines. As expected, the vibration-rotation  $O_1$ - and  $S_1$ -branches are not visible.

The source of this hump-feature seen in Figure 5.15 (labelled as “unidentified” in Figure 5.16) has not been conclusively determined. Possible candidates include fluorescence (perhaps in the glass cell windows), effects of the grating spectral efficiency and detector array quantum efficiency, stray light entering the system, artefacts of the binning procedure (hardware and/or software), or a combination of the above. One candidate that was considered early on, namely that the feature was due to one of the weak transitions in the Nd:YAG crystal being doubled from the IR to the visible has been conclusively ruled out following experiments incorporating a laser line band-path filter into the beam path, which had no effect on the feature.

As expected, at the longest single exposure time of  $1 \times 1000$ s (see Figure 5.16 (top)), the situation is further improved, with  $1 \times 500$ s being an intermediate case. Despite the increases in signal-to-noise ratio, the  $O_1$ - and  $S_1$ - branches are still not visible. An unexpected fluorescence-like hump, centred roughly at 638nm, is observed for the longer exposure times of  $1 \times 500$ s and  $1 \times 1000$ s (just visible for  $1 \times 250$ s).

In Figure 5.16 (bottom) one notes that the multiple exposure  $5 \times 1000$ s looks much like the single  $1 \times 1000$ s trace, albeit with a superior signal-to-noise ratio. The multiple-exposure spectra show a pronounced distortion of the background shape with increasing numbers of exposures.

Specifically, as the number of exposures is increased, a distinct upturn towards the extremes of the spectrum is observed. Figure 5.17 (top) shows the effect for the  $20 \times 250$ s exposure – the  $10 \times 500$ s spectrum again being an intermediate case.



**Figure 5.16** Top:  $1 \times 1000\text{s}$ -exposure Raman spectrum of the  $29:47:24(\pm 1)$   $\text{H}_2:\text{HD}:\text{D}_2$  (1atm) cell. The cause of the fluorescence-like feature centred at  $\sim 638\text{nm}$  has not yet been determined. Bottom:  $5 \times 1000\text{s}$  multiple exposure Raman spectrum of the same sample. This spectrum demonstrates the highest S/N ratio of any of the UWS spectra of the original review, with  $S/N(\text{rot}) = 91$  and  $S/N(\text{vib}) = 63$  for the HD rotational  $S_0$ - and vibration-rotation  $Q_1$ -branch, respectively. Entrance slit width:  $25.4\mu\text{m}$ , astigmatism correction: AstCorr, cosmic ray removal: TrigCRR.

The effect becomes dramatic for the shortest exposures. In Figure 5.17 (bottom) the 100×50s spectrum is shown, in which the distortion is particularly pronounced. It is thought therefore that the fluorescence-like feature is mainly due to the hardware binning in the CCD itself (shot noise) when taking multiple exposures. The feature is reduced somewhat when (software) averages of multiple spectra are taken – i.e. averaging five 1×1000s spectra results in a much reduced feature with respect to a single 5×1000s.

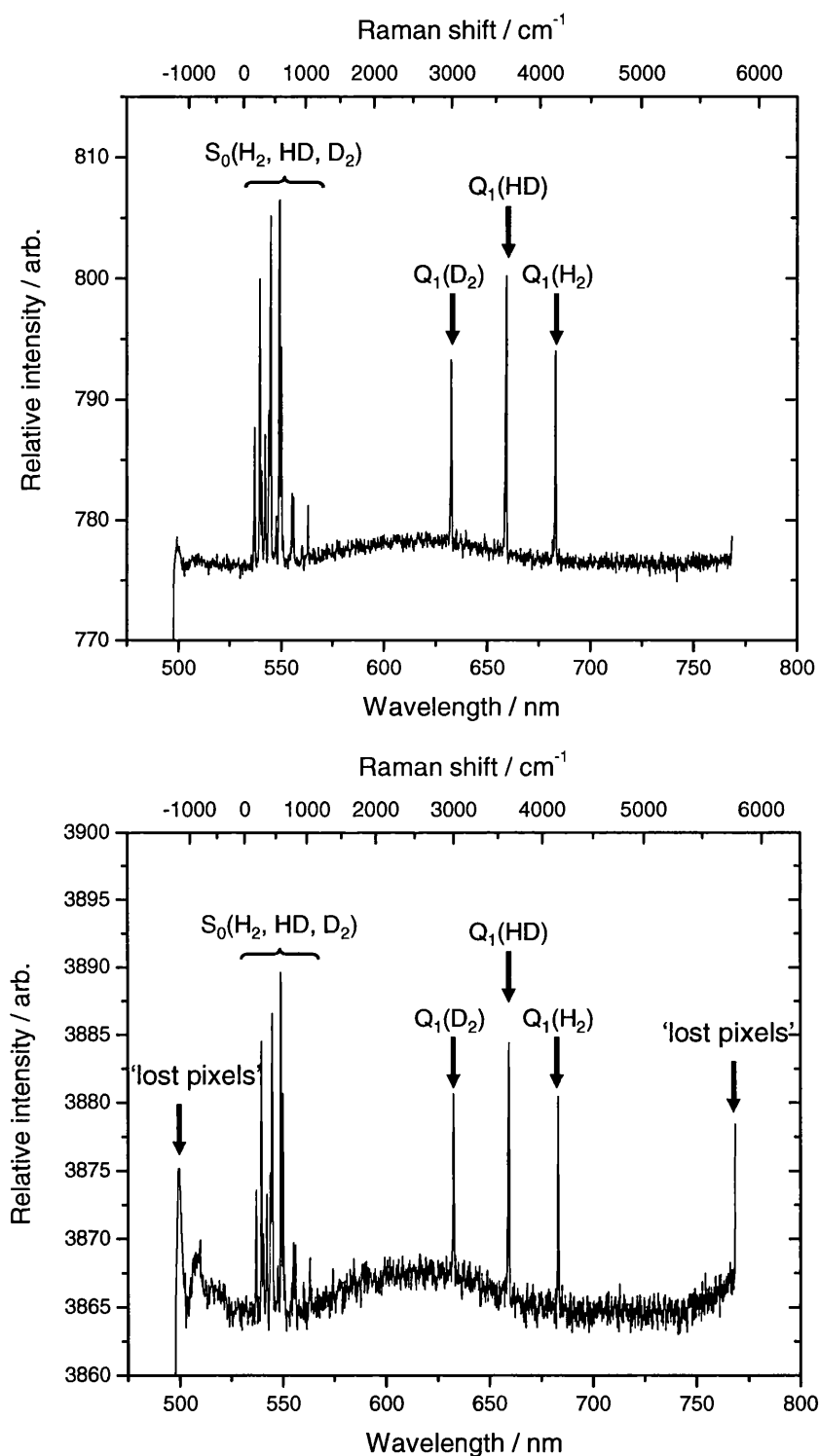
In none of the spectra recorded so far has it been possible to observe the vibration-rotation  $O_1$ - or  $S_1$ -branches for any of the isotopomers. However, comparison with the TLK spectra suggests that the  $O_1$ - and  $S_1$ -branches would be roughly at or below the noise level in the UWS system for the current laser power of ~7mW.

Table 5.5 summarises the signal-to-noise ratios measured for the  $H_2:HD:D_2$  cell at the various exposures.  $S(\text{rot})$  is the signal strength of the strongest pure rotational Raman line above the baseline\*,  $S(\text{vib})$  the strength of the maximum intensity line in the HD  $Q_1$ -branch,  $N$  is the noise level, with  $S/N(\text{rot})$  and  $S/N(\text{vib})$  being the signal-to-noise ratios for the rotational and vibration-rotation lines, respectively.

**Table 5.5** Summary of the best signal-to-noise ratios for the UWS system. Parameters:  $H_2:HD:D_2$  29:47:24±1 (1atm) cell, 7mW laser power at 532nm, 25.4μm entrance slit width, 600gr·mm<sup>-1</sup> grating.

Exposure		S (rot)	S (vib)	N	S/N (rot)	S/N (vib)
1×	50s	0.492	0.412	0.06	<b>8</b>	<b>7</b>
1×	100s	0.600	0.463	0.06	<b>10</b>	<b>8</b>
1×	250s	1.614	1.231	0.06	<b>27</b>	<b>21</b>
1×	500s	2.379	1.492	0.06	<b>40</b>	<b>25</b>
1×	1000s	3.649	2.086	0.06	<b>61</b>	<b>35</b>
100×	50s	24.60	19.40	1.20	<b>20</b>	<b>16</b>
50×	100s	22.80	17.40	0.90	<b>25</b>	<b>19</b>
20×	250s	28.98	22.69	0.70	<b>41</b>	<b>32</b>
10×	500s	23.06	15.48	0.50	<b>46</b>	<b>31</b>
5×	1000s	36.39	25.36	0.40	<b>91</b>	<b>63</b>

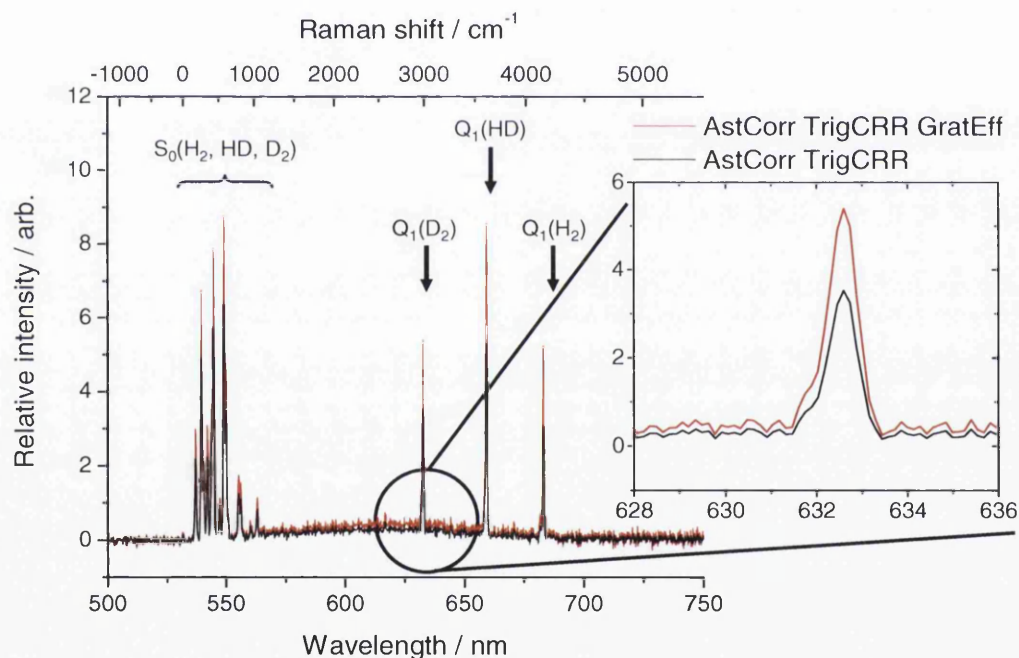
\* The average value of the relatively flat region at high  $\lambda$  (low Raman shift) was used for baseline purposes.



**Figure 5.17** Top: 20x250s multiple exposure Raman spectrum of 29:47:24(±1) H<sub>2</sub>:HD:D<sub>2</sub> (1atm) cell. Note the upturn at the high-wavelength (low pixel#) end of the spectrum. Bottom: 100x50s multiple exposure Raman spectrum of the same sample. The 'spikes' at the extremes of the spectrum are the 'lost pixels' from the astigmatism correction routine magnified by the pronounced background distortion. Entrance slit width: 25.4μm, astigmatism correction: *AstCorr*, cosmic ray removal: *TrigCRR*.

The difference in  $S/N$  for the rotational and vibration-rotation branches is interesting because one would expect from theoretical considerations that the rotational  $S_0$ -branch and the vibration-rotation  $Q_1$ -branch lines to be of roughly the same intensity. The observed discrepancy is most likely associated with the combined effects of the reduced grating efficiency and lower quantum efficiency of the CCD detector at the wavelength of the  $Q_1$ -branches.

A *LabVIEW* grating efficiency correction routine is currently at the beta testing stage. When applied to a 10mW-excited  $1 \times 1000s$  Raman spectrum of  $H_2:HD:D_2$ , as shown in Figure 5.18, the routine improves the  $S/N$  by approximately 43% in the case of the vibration-rotation branches.



**Figure 5.18**  $1 \times 1000s$  exposure Raman spectrum of  $H_2:HD:D_2$  (1atm) cell, after application of (beta) grating efficiency correction routine. The  $S/N$  (rot) = 61,  $S/N$  (vib) = 50. Entrance slit width:  $25.4\mu m$ , astigmatism correction: *AstCorr*, cosmic ray removal: *TrigCRR*.

In principle, the same technique can be implemented to correct for the variation in quantum efficiency of the CCD camera with respect to wavelength. This has not yet been carried out, but will become a high priority task once the HTS/Spec-10 system starts taking

its first proof-of-principle measurements at the TILO experiment at TLK. It is expected that the improvements due to correction of quantum efficiency variations will be of the same order as those for the grating efficiency corrections.

### 5.3 Comparison of the TLK and UWS Raman Systems

#### 5.3.1 Signal-to-noise ratio calculations

The target of  $\pm 0.2\%$  purity monitoring equates to a S/N in the Raman signal of at least 500, with the  $\pm 0.1\%$  'gold standard' requiring a S/N of 1000, or more. Estimates can be made from the current S/N ratios recorded for both the TLK and UWS systems as to the likelihood of reaching that target. At the time of the review, it was thought that the monitoring system would be positioned at the inlet of the WGTS, where a pressure of  $\sim 10$  mbar prevails. In order to perform Raman spectroscopy at such a low pressure (and hence molecular number density), it would have been necessary to purchase a laser of higher power than the 5W *Verdi* laser. Taking into account budgetary restrictions and damage thresholds of the optical components, a laser power of 8W was deemed optimal, with the option of a single back reflection to double the available laser power. These estimates are summarised below in Table 5.6.

**Table 5.6** Estimates of best S/N (rot) ratios attainable with the TLK and UWS systems as configured for the comparative review, without the use of the ASER. The S/N ratios are scaled to the WGTS inlet pressure of 10mbar, and laser operating powers of 8W and 16W.

System	Data parameters	Best observed S/N (rot) (1atm)	Scaled to 8W (10mbar)	Scaled to 16W (10mbar)
TLK	99 $\pm$ 1% D <sub>2</sub> Doubled 1W (2W)	315	13	26
UWS	47 $\pm$ 1% HD $\sim 7.1$ mW	91	1025	2050

Although the figures summarised in Table 5.6 are estimates, the numbers give a very clear idea as to the capabilities of the two systems. For the TLK system, as is, it cannot be hoped to reach the first target S/N of 500 without the use of the ASER. Even if an 18W laser (the most powerful commercially available) were run at full power, doubling up to 36W by a single back reflection into the cell, the scaled maximum S/N attainable would only be ~57. This is still short of the target of 500, not to mention the added complication of engineering the system against laser-induced damage.

The use of the ASER can provide a 50-fold boost to the signal with the Raman cell present (see Taylor et al. (2001)) for a total S/N of up to 1260 based on 16W input power. This would correspond to a maximum sensitivity of  $\pm 0.08\%$ , although it is unclear to what extent the addition of the ASER would affect the noise level of the system. Furthermore, the inclusion of the ASER configuration would constitute a significant increase in the complexity, and most likely long-term reliability of the system, and severely increase attendance and maintenance requirements. This could not be afforded in reliability-critical experiments, which run continuously for a few months at a time, over a period of a few years.

On the basis of the original estimates, the UWS system looked likely to exceed the long-term 'gold standard' S/N of 1000 even without using the ASER. In any case, the omission of the ASER from the final system specification was the much-preferred approach from the point of view of ease of optical path engineering, space requirements and maintenance.

Note that the UWS S/N estimates are from a single component of a gas mixture, representing  $\sim 47 \pm 1\%$  of the total number density, whereas the TLK estimates are from a near pure  $\sim 99 \pm 1\%$  sample. The S/N ratios can therefore be more meaningfully compared if the values in Table 5.6 are scaled not just to pressure and laser power, but to a hypothetical pure sample of the target gas. These revised estimates are presented in Table 5.7.

**Table 5.7** Estimates of best S/N (rot) ratios attainable with the TLK and UWS systems as configured for the comparative review, without the use of the ASER. The S/N ratios are scaled to the WGTS inlet pressure of 10mbar, and laser operating powers of 8W and 16W.

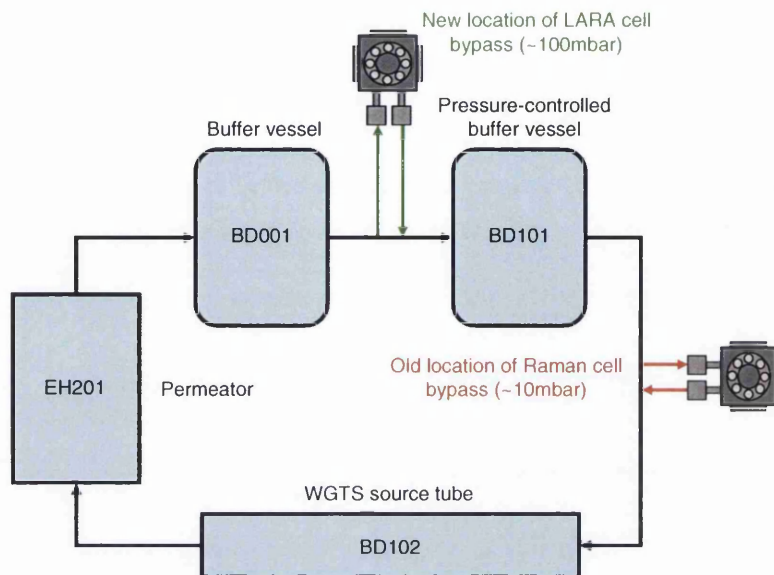
System	Data parameters	Best observed S/N (rot) (1atm)	Scaled to 8W (100% sample at 10mbar)	Scaled to 16W (100% sample at 10mbar)
TLK	99±1% D <sub>2</sub> Doubled 1W (2W)	315	13	26
UWS	47±1% HD ~7.1mW	91	2182	4363

When one applies the appropriate scaling, the disparity in the S/N between the systems is a factor of ~171 in favour of the UWS system. This value is in line with the expectation for S/N improvement of >100 when lowering the CCD chip temperature by ~40K (see Section 4.5.2), the remainder stemming from the higher quality of the new-generation Spec-10 camera compared with the CCD2000.

The proposed location of the gas cell was changed shortly after the submission of the results of the comparative survey. Crucially, the operating pressure at the new location is a factor of 10 higher at ~100mbar. The trade-off is that the pressure stability at this new location is not so precisely controlled at ±1mbar (~1% at ~100mbar), compared with the ±0.0005mbar (0.005% at 10mbar) stability at the originally proposed location. Figure 5.19 shows both of these locations on the TILO experiment. Note that TILO's gas handling provisions are identical with those of the final inner loop design – in fact, over 90% of TILO's components will be implemented in KATRIN's inner loop.

The original proposal for the excitation laser was to purchase a 10W (or higher) output unit and to run it at 8W. Running the laser at below maximum output would extend the life of the laser and provide a margin of reserve necessary to maintain a consistent 8W output as the laser degraded with age. Lasers systems under consideration included Coherent's *Verdi V10* and *V18* lasers (532nm Nd:YVO<sub>4</sub>) and ELS's *VersaDisk10* and *VersaDisk15* units (515nm Yb:YAG).





**Figure 5.19** Simplified gas flow diagram for TILO showing the original (red) and current (green) proposed locations for the LARA Raman cell bypass. The relevant TILO component numbers are shown.

The higher operating pressure of 100mbar relaxed the requirement for an excitation laser of greater than 5W output power. Since Raman signal intensities scale linearly with both laser power and number density of the scattering molecules, scaling estimates for direct imaging show that a laser need not be run much above 1W in order to achieve the ‘gold standard’ S/N of 1000 with the UWS system at this pressure. It was therefore decided to retain the *Verdi V5* for use in the final setup – at a financial saving of over £60K. As previously mentioned, running the *Verdi* laser below maximum power will provide the benefits of extended laser life and a margin of reserve.

In light of the revised pressure and operating power parameters, the S/N estimates have been rescaled to operating powers of 1 and 5W at 100mbar, and are presented in Table 5.8 for both the pure rotation and vibration-rotation lines. Note that the S/N ratios have also been scaled to a 100% pure sample of the target gas since the ‘gold standard’ KATRIN specification of S/N = 1000 is in reference to a hypothetically pure gas sample.

**Table 5.8** Estimates of best S/N ratios attainable with the TLK and UWS systems as configured for the comparative review, without the use of the ASER. The S/N ratios are scaled to the revised operating pressure specification of  $100\pm 1$  mbar, and laser operating powers of 1W and 5W. The S/N (rot) values are based on the pure rotational  $H_2 S_0(2)$  line, and the S/N (vib) values are based on the rotation-vibration HD  $Q_1$  line.

$H_2 S_0(2)$ (pure rotation )				
System	Data parameters	Best observed S/N (rot) (1atm)	Scaled to 1W (100% sample at 100mbar)	Scaled to 5W (100% sample at 100mbar)
TLK	99±1% D <sub>2</sub> Doubled 1W (2W)	315	16	80
UWS	47±1% HD ~7.1mW	91	2727	13635

HD $Q_1$ (vibration-rotation)				
System	Data parameters	Best observed S/N (vib) (1atm)	Scaled to 1W (100% sample at 100mbar)	Scaled to 5W (100% sample at 100mbar)
TLK	99±1% D <sub>2</sub> Doubled 1W (2W)	238	12	60
UWS	47±1% HD ~7.1mW	63	1888	9440

Note that in the case of the S/N (vib) values, the disparity between the TLK and UWS systems is smaller than for the S/N (rot) values. This difference most likely arises because the grating efficiency and detector quantum efficiency parameters for the two systems are different. Regardless of the reason, a disparity of over two orders of magnitude is decisive – the factor of 10 increase in pressure does not change the conclusion that the TLK system as it stands is incapable of meeting either S/N target specified by the KATRIN design report.

### 5.3.2 Interface and software issues

As it stands, the TLK system in its present status would not be suitable for use in a long-term, unattended on-line monitoring situation – even if the CCD detector cooling could be

repaired – due to the incessant software crashes and the limitations of the Win/16 / ISA-bus based control system. More likely than not, by the time the KATRIN measurements commence in 2007/8, motherboards supporting ISA-bus cards may not be available any longer (in which case system replacement of a failing PC main board might be required), and the support for Win/16 software / operating systems will definitely have ceased.

Over the course of the comparative review, the UWS system was run almost constantly since its full installation in early 2005, i.e. about six months, with only the occasional shut down when it was not being used for several days in a row. The system has been left to accumulate spectra of varying exposure times over a timescale of several days. Furthermore, the system has never crashed, or behaved in any way other than a completely predictable and reliable manner. The aforementioned issues when running *WinSpec/32* with Windows XP Service Pack 2 were all solved very quickly in a software update from Roper Scientific – support that any older Win/16 software would most likely lack.

The UWS system's flexibility is down in part to the USB2.0 interface connection, which makes it independent of changing bus standards, and a modern industry-standard Win32 software package. The plug-and-play nature of the connection, without the need for a dedicated interface card, means that the control / monitoring software could be installed on several computers (on a notebook, for example) and 'hot-swapped' in the event of a failure on the controlling computer. This flexibility is not an option with the ISA-bus based interface card and the (buggy) *SpectraMAX* software. Moreover, the use of an old Pentium-based system is mandatory due to the detector's ISA interface, and this would limit system resources available, specifically for software development integrating the Raman monitoring system with KATRIN's control room remote-control and monitoring system.

With respect to the latter software issue, the Roper Scientific software package used by the UWS system also includes *LabVIEW* support in the form of a software development kit. Since the drivers implemented in the kit are the same as those used by *WinSpec/32*, it is quite simple to write *LabVIEW* programs to control the Spec-10 and to automate data acquisition. Further, it is straightforward enough to include the astigmatism correction,

grating efficiency correction, quantum efficiency correction and cosmic ray removal routines into the software due to *LabVIEW*'s modular nature. The corrections could then be done in real-time with no input required from a human operator. The proposed KATRIN control-room software is to be based on *LabVIEW* as well; thus this factor will greatly ease software integration. Any software for the current ISA-based TLK system – including drivers – would have to be written from scratch.

### 5.3.3 *Modifications to the ASER design*

The current ASER design has the optical path oriented vertically, in order to facilitate direct imaging at the height of the Triax320's entrance slit. Although the Newport *IsoStation* optical table on which the components are mounted provides excellent vibration damping, the stability of the system could be greatly improved by changing the optical path from the vertical to the horizontal. This also would protect optical surfaces from contamination by dust particles settling on them from above.

Although the estimates from the comparative survey (and from experiments since then, see Section 5.5) show that the UWS system should have no problems in reaching the S/N targets specified by the KATRIN design report, it might be interesting to measure the gas composition at particle densities and temperatures closely resembling those at the WGTS inlet, or even within the WGTS itself – at pressures of 10mbar to  $10^{-2}$ mbar, respectively. At such low pressures, ASER enhancement would be required.

Thus, an ASER modification most likely would be in use in parallel test and calibration measurements, i.e. off-line, in which an updated version of the TLK detection system could be used in conjunction with a low-cost medium-power probe laser module.

Note that the design of the bench and enclosure onto which the final system is to be placed has already been finalised (see Section 6.2.1). In the space available, a horizontally-oriented ASER could only just be accommodated into the available space. In addition, such an arrangement would make optical fibre light collection mandatory. This method of

light collection has already been settled upon, however, as it provides excellent flexibility with a low loss of signal. This latter point, is therefore unlikely to cause additional problems should it become necessary to utilise the ASER at some point in the future.

#### *5.3.4 System footprint issues*

The design of the bench used to house the Raman components is described in Chapter 6. It should be mentioned here, however, that the UWS system has the further advantage of a very small footprint – the spectrometer, detector, filter box and cooling system can all be comfortably arranged in a footprint area of less than 500×500mm; the Triax320 spectrometer on its own is about that size already. At the time of the review, only a space of about 1200×800mm was provisionally allocated for the Raman system at the location of the inner loop. Still-open questions were the arrangement of laser beam delivery method (direct or fibre-launched), scattered light collection method (direct, translational or fibre-coupled), whether the ASER would be implemented or not, and the actual design of a T<sub>2</sub>-safe gas bypass into the cell.

In order to retain the maximum flexibility with respect to these design parameters, it was clear that the HTS system with its small footprint provided the best option. It would have been possible to use the TRIAX320, but the CCD2000 would have to be replaced by a Spec-10 or similar detector. The large size of the TRIAX320 would preclude it from practical mounting atop a Raman bench in-line with the beam path and/or horizontal ASER unit. Consequently, direct imaging would be difficult, essentially restricting the collection method to fibre-coupling (at the time unproved in this specific application). As shown in Chapter 6, the final arrangement is itself a fibre-coupled collection solution, but the HTS/Spec-10 unit can be mounted atop the breadboard. It also retains the option of reverting to translational imaging should some unforeseen factor render the fibre-coupled light collection solution untenable.

#### **5.4 *Concluding Remarks to the Comparative Survey***

It is perhaps indicative of the seven or so years of technological advancement that we see such a difference in the performance of the two systems: the TLK system was advanced for its day, but the necessity of using ISA-bus communication interfaces, and 1998-vintage operating system and software, means that it can never hope to match the rock-solid performance and stability of the state-of-the-art HTS/Spec-10 combination. Add to that the industry-standard *LabVIEW*-ready software, plug-and-play capability and small footprint of the HTS / Spec-10, and one has a clearly superior option for the spectrometer / detector combination for the KATRIN monitoring system.

While the equipment hardware will most likely be reasonably future-proof until the end of the KATRIN project, it looks prudent to place less confidence in the longevity of computer hardware and software. However, given the current flexibility afforded by the USB2.0 interface solution – a peripheral communication standard which is guaranteed for the next 10 years or so – such problems look less severe than those encountered in the leap from 1998 to 2005.

#### **5.5 *Post-Review Direct Imaging Experiments (UWS System)***

In this section we summarise the results of direct and translational imaging Raman measurements performed at Swansea that were carried out after the comparative review, but before the UWS system was transferred to the TILO experiment at FZK to perform in-line test measurements. These results are presented here in chronological order – note that the results of the fibre-coupled imaging investigations conducted prior to the transfer of the UWS system to TILO are not included here, but are summarised in Section 6.1.

### 5.5.1 $1200\text{gr}\cdot\text{mm}^{-1}$ HTS Grating Test

The  $600\text{gr}\cdot\text{mm}^{-1}$  grating installed in the HTS provides a spectral coverage of approximately 272nm when centred at 655nm<sup>†</sup> (as was the case for the comparative review), which corresponds to a median resolution of approximately 0.13nm/pixel. Although the broad spectral range permits the simultaneous observation of the  $S_0$ -,  $O_1$ -,  $Q_1$ -, and  $S_1$ -branches of all six hydrogen isotopomers, the relatively modest spectral resolution does not allow one to resolve the individual  $Q_1$ -branch lines. In addition, even with the relatively light isotopomers  $H_2$ , HD, and  $D_2$ , analysis of the  $S_0$ -branch lines can be difficult due to significant line overlap – the situation would be even worse with the tritium-containing isotopomers as their line spacing is narrower still.

In order to test the suitability of the HTS/Spec-10 system to a higher-resolution application, a  $1200\text{gr}\cdot\text{mm}^{-1}$  grating was acquired on loan from PIActon. The grating was loaned (and returned) before the acquisition of the higher-power laser modules (see Section 5.5.2), so the 10mW laser module was used as the excitation source. With the exception of the grating, the overall setup of the experiments was the same as for the comparative survey.

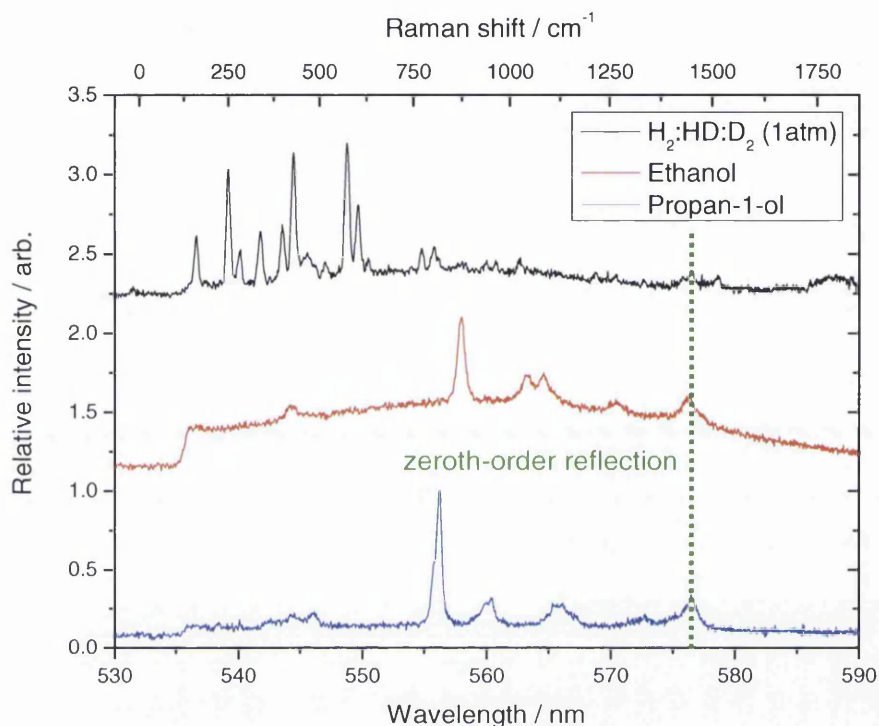
The  $1200\text{gr}\cdot\text{mm}^{-1}$  grating provides a spectral range of approximately 79nm when centred at 567nm for the purpose of investigating the  $S_0$ -branch lines, and the median resolution is approximately 0.04nm/pixel – a significant gain over the  $600\text{gr}\cdot\text{mm}^{-1}$  grating. In order to provide a direct comparison with spectra taken with the  $600\text{gr}\cdot\text{mm}^{-1}$  grating, the same exposure times and slit widths were used as for the comparative survey (see Table 5.4).

Figure 5.20 shows three Raman spectra measured using the  $1200\text{gr}\cdot\text{mm}^{-1}$  grating centred at ~567nm. Clearly visible towards the higher-wavelength end of the spectrum is a persistent feature that is present regardless of the exposure time, slit width or whether the Raman spectrum a gaseous or liquid sample is being observed. This is due to the zeroth-order

---

<sup>†</sup> The range when centred at 655nm is approximately 497nm to 768nm, corresponding to a Raman shift coverage of approximately  $-1324\text{cm}^{-1}$  to  $+5776\text{cm}^{-1}$  relative to the 532nm ( $\sim 18797\text{cm}^{-1}$ ) excitation line.

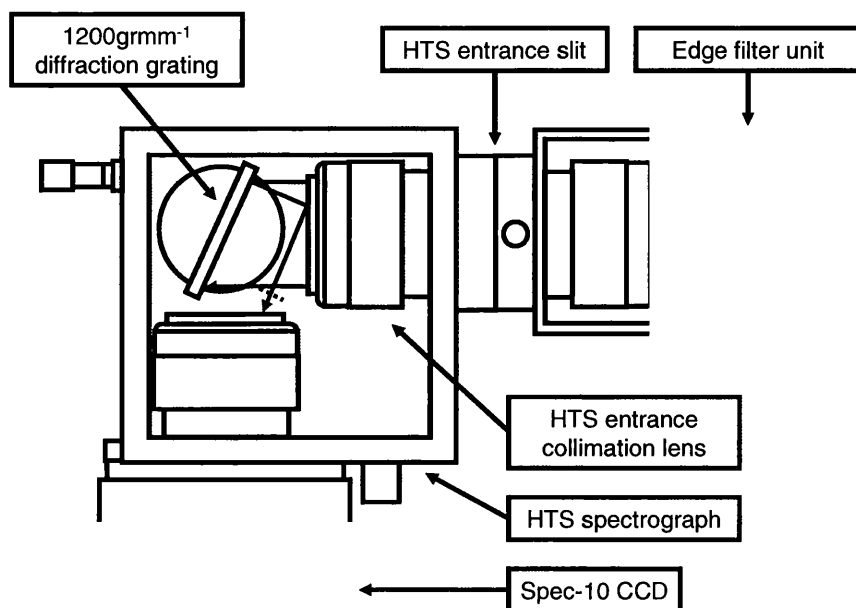
reflection from the diffraction grating being directed onto the CCD chip via a reflection from the entrance collimation lens, as shown in Figure 5.21 below.



**Figure 5.20** Raman spectra measured using the 1200gr·mm<sup>-1</sup> grating centred at ~567nm, clearly showing the zeroth-order reflection in all cases. This feature is present regardless of the sample and / or exposure time used – this figure shows a 5×1000s exposure pure rotational Raman spectrum of the H<sub>2</sub>:HD:D<sub>2</sub> (1atm) cell (top, black), a 1×1s exposure of liquid ethanol (middle, red), and a 1×1s exposure of liquid propan-1-ol (bottom, blue).

Note that if the orientation of the grating is changed, the position of the reflection feature will then move across the spectrum. When in isolation, the feature can be easily removed using a baseline tool (as in *Origin*). Difficulties arise, however if the feature lies close to – or on top of) a Raman line.





**Figure 5.21** Direction of the zeroth-order reflection onto the CCD chip via the entrance collimation lens. While a blank inserted at the position shown (red dashed line) could prevent the zeroth-order reflection from reaching the detector, it would also likely block a portion of the incoming light from reaching the diffraction grating.

Although it would probably be possible to insert a blank into the HTS in order to block this reflection, it would need to be carefully repositioned every time the grating was moved to observe a different part of the Raman spectrum. Further, for certain orientations of the grating it would be impossible to avoid blocking a portion of the incoming Raman scattered light from reaching the diffraction grating. Manual adjustment of a blank or the modification of the HTS grating turret to include a permanently mounted blank represents unacceptable additional complications to the system. The losses incurred at certain grating positions would be unacceptable in any case due to the already ultra-low levels of the Raman scattered light. Since neither the presence of the zeroth-order reflection on a Raman spectrum nor the modifications of the HTS are acceptable options, installation of a 1200gr·mm<sup>-1</sup> grating does not represent a viable high-resolution solution for the HTS/Spec-10 system.

It was shown in later investigations that fibre-coupled collection of Raman light is viable (see Chapter 6). At the time of writing, the HTS/Spec-10 system installed at the TILO

facility in FZK with the fibre-coupled collection system in place. It should therefore be possible to perform high-resolution Raman spectroscopy without seriously disrupting the current setup by sending the scattered light via the optical fibre into a second spectrometer which has a high-resolution grating installed. An Acton SP500i currently at Swansea has a  $2400\text{gr}\cdot\text{mm}^{-1}$  grating installed and would be suitable for this purpose. Due to the ultra-low intensities involved, it might prove necessary to dismount the Spec-10 and re-install it onto the second spectrograph. If the need for frequent high-resolution spectroscopy arises, however, a more practical option may be the acquisition of a second Spec-10 to minimise the disruption to the experimental setup and the possibility of damaging the Spec-10 during transfer between spectrographs.

### 5.5.2 Direct Imaging Survey (50mW and 100mW Excitation)

The Raman measurements performed with the 10mW laser module show that at atmospheric pressure, the pure rotational  $S_0$ - and vibration-rotation  $Q_1$ -branches are observable for a hydrogen isotopomer gas mixture at very low laser powers. The information that one can extract from such spectra is limited, however. For example, one cannot estimate a value for an isotopomer's transition polarisability tensor component  $(a')^{2\ddagger}$  without the  $O_1$ - and  $S_1$ -branch intensities (recall that this parameter essentially dictates the relative intensity of the  $Q_1$ -branch lines relative to the  $O_1$ - and  $S_1$ -branch lines – see Tables 3.10 and 3.11).

Although the Coherent *Verdi* laser at TLK provides a maximum of 5W, the maximum 532nm CW laser power available at UWS was originally only 10mW. Later, two medium-power (50mW and 100mW) modules were purchased to increase the signal-to-noise ratio in an attempt to obtain more useful spectra. For brevity, we shall only include

---

<sup>‡</sup> Note that further information would be required to correctly estimate values for the tensor invariants. One would want to measure as accurately as possible the intensity of the scattered light, and would therefore need to know the transmission / reflection curves of all optical elements, the quantum efficiency of the CCD detector, etc.

the results of experiments performed with the 100mW laser here – the 50mW results are broadly similar, with a roughly halved S/N ratio compared with the 100mW spectra.

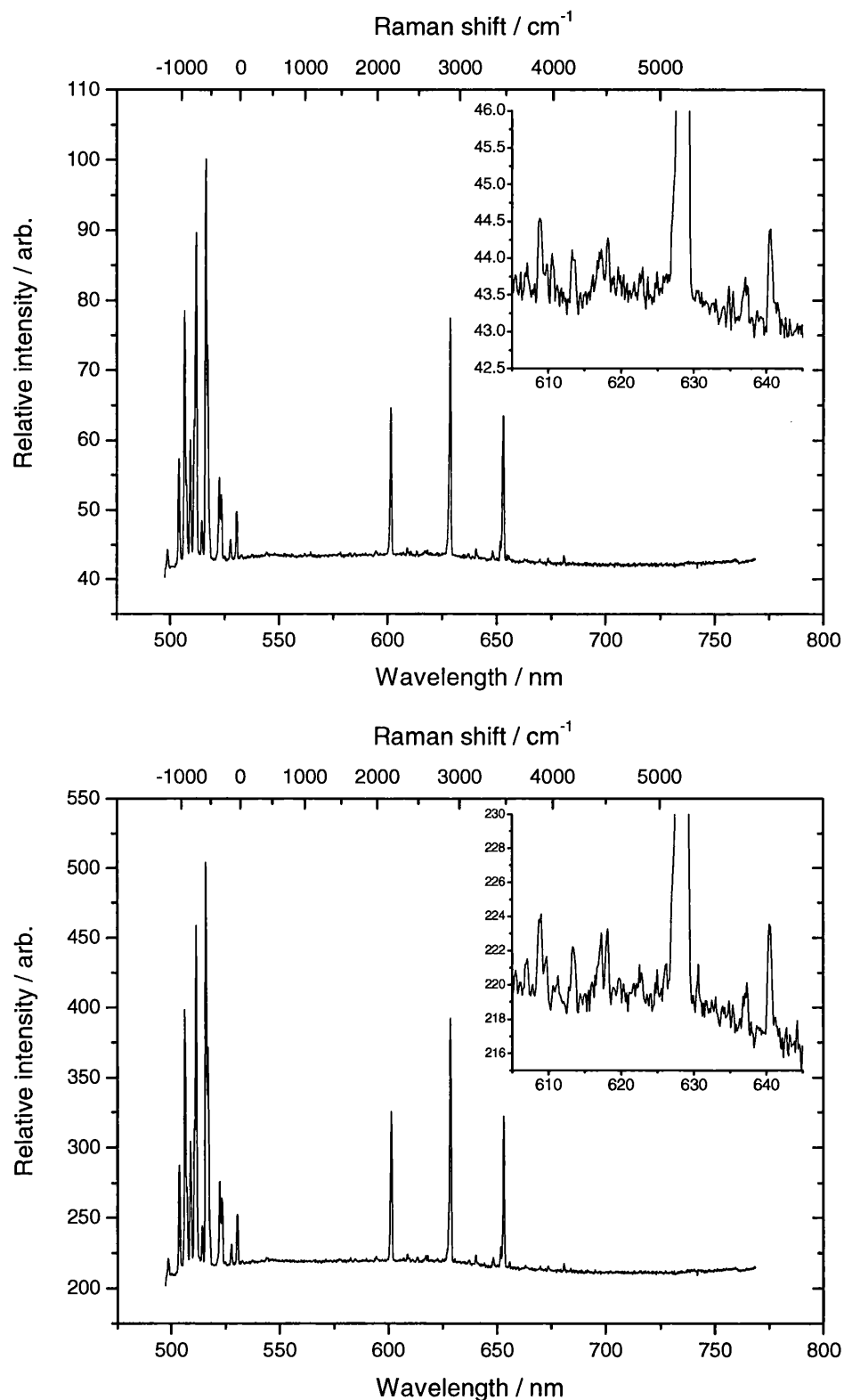
A survey to evaluate the performance of the UWS system with the 100mW laser module was undertaken, the exposure paralleling that of the TLK / UWS system comparative survey, as summarised in Table 5.10. Note that the entrance slit was set at 76.2 $\mu$ m, compared with the 25.4 $\mu$ m used in the survey.

**Table 5.9** Exposure times for the 100mW module Raman survey. Spectra flagged with an asterisk (\*) are shown in this chapter.

Multiple exposures (total of 5000s each)	Single exposures (s)
5 $\times$ 1,000s(*)	1 $\times$ 1,000s (*)
10 $\times$ 500s	1 $\times$ 500s
20 $\times$ 250s	1 $\times$ 250s
50 $\times$ 100s	1 $\times$ 100s
100 $\times$ 50s	1 $\times$ 50s

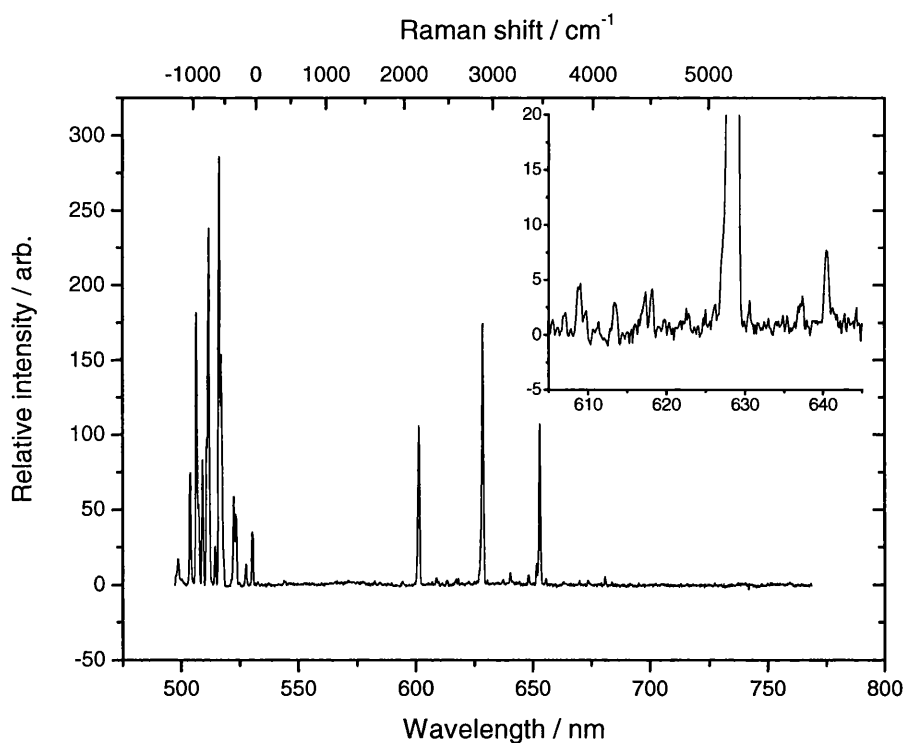
The increased laser power greatly improved the quality of the spectra for a given exposure time, as shown in Figure 5.22. Note that (as mentioned in Section 4.7.2), the Raman lines are now too intense to use the *TrigCRR* cosmic ray removal program. At the time of the review, the row-comparison routine *RCRR* was used to remove cosmic ray events, but the spectra shown here have been processed using the more sophisticated double-differentiation routine *DCRR*, which also incorporates the astigmatism correction code.

The quality of the spectra is much improved over those taken with the 10mW laser module. In Figure 5.22 (top), one can clearly see the O<sub>1</sub>- and S<sub>1</sub>- branches for the three isotopomers, although the HD lines are naturally the strongest. The fluorescence-like hump is still present, although it is far less prominent with the increased Raman signal strength. The noise level has remained at roughly the same values as for the comparative review for a given exposure time. One can just see the HD O<sub>1</sub>- and S<sub>1</sub>-branches down to single exposure times of 1 $\times$ 250s; these lines are not visible on the 1 $\times$ 50s or 1 $\times$ 100s exposures.



**Figure 5.22** Top: 1x1000s multiple exposure Raman spectrum of the 29:47:24( $\pm$ 1)  $\text{H}_2$ :HD: $\text{D}_2$  (1atm) cell. Bottom: 5x1000s multiple exposure Raman spectrum of the same sample. Entrance slit width: 76.2 $\mu\text{m}$ , astigmatism correction and cosmic ray removal: DCRR. The HD  $O_1$ - and  $S_1$ -branches are clearly visible in both spectra (insets).

As can be seen in Figure 5.22 (bottom), the quality of the multiple exposure spectra is similarly high, with the first few lines of all three isotopomer's  $O_1$ - and  $S_1$ -branches being clearly visible. As with the comparative review, there is a gradual distortion of the background as the number of exposures are increased. The  $5 \times 1000$ s spectrum shown in Figure 5.22 (bottom), however, shows only the fluorescence-like hump (no additional distortion), as for the single exposures. The background shape can be flattened using a baseline scaling routine in *Origin*, in which case the quality of the spectrum improves considerably, as shown in Figure 5.23.



**Figure 5.23**  $5 \times 1000$ s multiple exposure Raman spectrum of the 29:47:24( $\pm 1$ )  $H_2$ :HD: $D_2$  (1atm) cell. Entrance slit width:  $76.2 \mu m$ , astigmatism correction and cosmic ray removal: DCRR, baseline scaling: *Origin*. The HD  $O_1$ - and  $S_1$ -branches are more clearly visible with a flatter background (inset).

The S/N ratios for the best single ( $1 \times 1000$ s) and multiple ( $5 \times 1000$ s) exposure spectra measured with the 100mW module are summarised in Table 5.10. Note that the S/N ratios for the vibration-rotation lines are lower than those for the pure rotational lines. This is the case with the TLK system as well, and is expected due to the reduction of the grating

efficiency with increasing wavelength (see Figure 5.26 further below). The detector quantum efficiency falls off with increasing wavelength as well, but over the wavelength ranges considered in this work, the efficiency curve is relatively flat.

**Table 5.10** Summary of the best signal-to-noise ratios for the UWS system. Parameters: H<sub>2</sub>:HD:D<sub>2</sub> 29:47:24±1 (1atm) cell, 100mW laser power at 532nm, 25.4µm entrance slit width, 600gr·mm<sup>-1</sup> grating. As for the results in the comparative survey, the best pure rotational line (“S (rot)” column) was the H<sub>2</sub> S<sub>0</sub>(1) line, while the best vibration-rotation line (“S (vib)” column) is the HD Q<sub>1</sub> line.

Exposure		S (rot)	S (vib)	N	S/N (rot)	S/N (vib)
1×	1000s	57.52	34.21	0.06	<b>959</b>	<b>570</b>
5×	1000s	295.25	226.14	0.40	<b>738</b>	<b>565</b>

### 5.5.3 Translational Imaging Survey

The originally envisaged experimental design concept for the laser Raman monitoring system was to have a fibre-launched laser excitation and fibre-coupled scattered light collection system. The system would have been completely contained within an enclosure appended to the main tritium handling system, with both the laser and collection fibres directly ‘plugged in’ to mounts on the sides. Such a system would have been the simplest arrangement from the point of view of user interaction, since once aligned the system would need very little in the way of re-alignment, and would likely suffer little from vibrations due to pumps and other equipment in the vicinity since every component is rigidly mounted to the same unit.

While the original idea of launching the laser radiation through a fibre was abandoned due to concerns surrounding the robustness of single-mode fibres at high powers and long operating times, the goal of fibre-coupling the scattered light was retained. In the event that fibre coupling should introduce unacceptable losses in signal strength (e.g. Fresnel losses at the fibre ends) or prove impractical (e.g. alignment difficulties), a direct-imaging backup method was required.

Due to the constraint of a horizontal orientation of the gas cell, a true one-to-one imaging solution as used in the comparative survey would have been impractical, requiring a vertical orientation of the spectrometer. This would have introduced unacceptable stability problems, as well as requiring extensive modifications to the (now finalised) design of the Raman bench – i.e. either a modification of the enclosure to accommodate the extra height of the vertical spectrometer and its support or cutting a section out of the breadboard to allow the spectrometer to be mounted from underneath, which would require a second enclosure on the underside of the breadboard. The only practical solution in this case would be to employ a translational imaging method to rotate the horizontal image of the scattering volume into the vertical so that it can be imaged onto the entrance slit of the HTS.

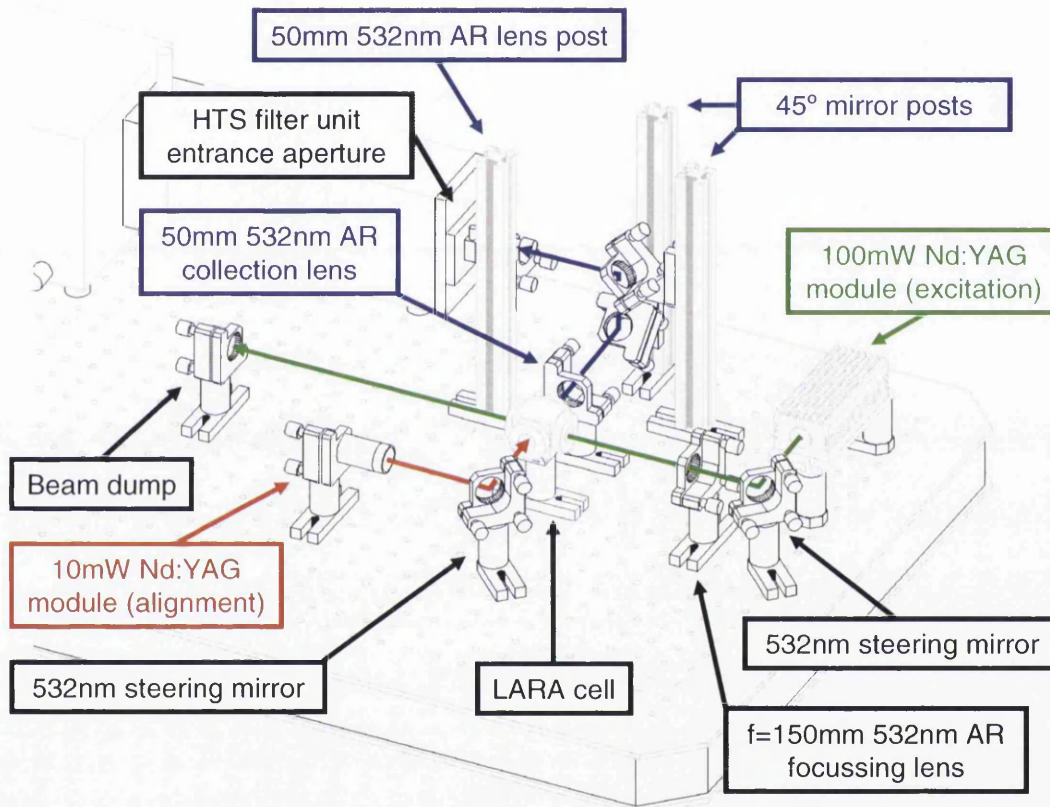
The concept of translational imaging is summarised in Section 4.3.2. The setup used to test the concept and to compare it with one-to-one direct imaging is shown in Figure 5.24. The laser beam remains horizontal through the cell, while the 50mm plano-convex collection lenses are the SM1 tube mounted units. The first lens collimates the collection through the translation, while the second lens focuses the light onto the entrance slit of the spectrometer.

The vertical pillars are standard 25mm aluminium extrusions mounted on Thorlabs BA1 bases. The two 532nm HR mirrors are mounted at  $45^\circ$  to the vertical and at  $90^\circ$  to each other using Thorlabs MA45-2 mounts. The mirrors were mounted in standard KM100 mounts to allow for fine adjustment in alignment. The vertical position of both mirror units was manually adjusted – the mirror units were affixed to the rail via a moveable nut and bolt.

The system was aligned in two stages:

Firstly, the 10mW Nd:YAG module was used to coarsely align the mirrors. The 10mW laser beam was sent through the cell at  $90^\circ$  to the path of the main laser beam parallel to the breadboard surface at the beam height of 75mm, i.e. in the same direction as the scattered light to be imaged. The beam was verified parallel to the breadboard by temporarily

placing diaphragms centred at 75mm height along the beam path, in much the same way that the main beam was aligned. With the 10mW laser in this location, it was possible to correctly locate the lower mirror in the horizontal and vertical axes. The upper mirror was then easily located by centering the vertical laser beam from the lower mirror onto the centre of the upper mirror.



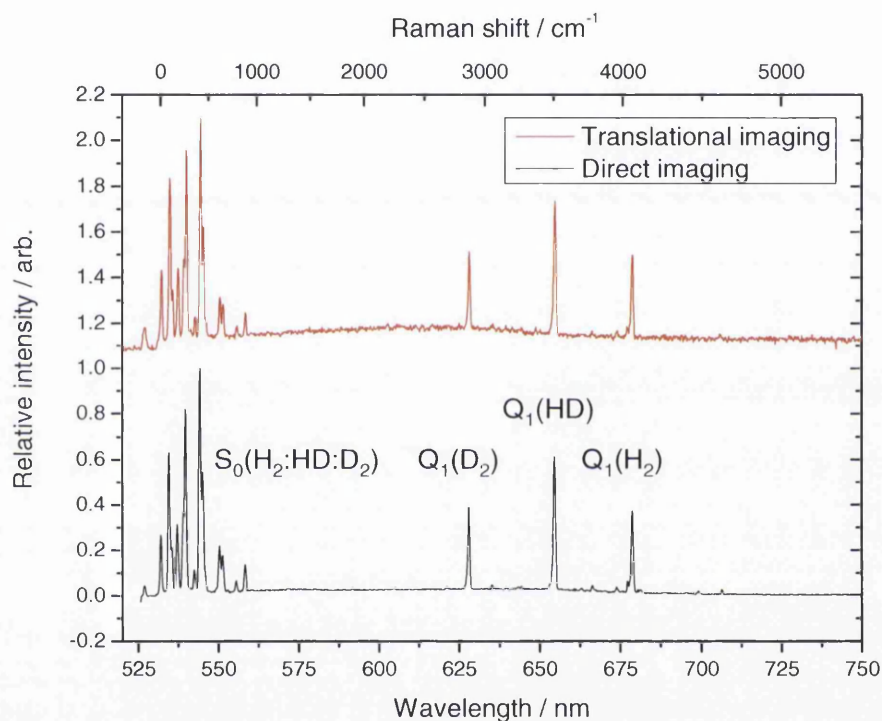
**Figure 5.24** Translational imaging setup at UWS. The excitation laser beam (green) is passed once through the LARA cell and dumped. The alignment laser beam (red) is oriented at  $90^\circ$  to the excitation beam path and is used to align the path of the scattered radiation (blue) onto the entrance slit of the HTS via the two  $45^\circ$  mirror posts.

Secondly, the 50mm collection lenses were installed in their respective locations and the mirrors were adjusted to centre the laser spot on the entrance slit. The 10mW laser was then deactivated and the 100mW laser beam sent through the alcohol-filled gas cell. Fine adjustment of the mirror orientation was then a simple matter of maximising spectral coverage on the 2D representation of short exposure (1s) images in *WinSpec/32*. The



system proved to be very stable and required very little further adjustment when the  $\text{H}_2:\text{HD}:\text{D}_2$  cell was installed to begin the translational imaging survey.

For brevity, only one spectrum is included here for comparison with a direct-imaging result. Figure 5.25 shows a  $5 \times 1000\text{s}$  spectrum of the  $29:47:24(\pm 1)$   $\text{H}_2:\text{HD}:\text{D}_2$  (1atm) cell for both imaging techniques.

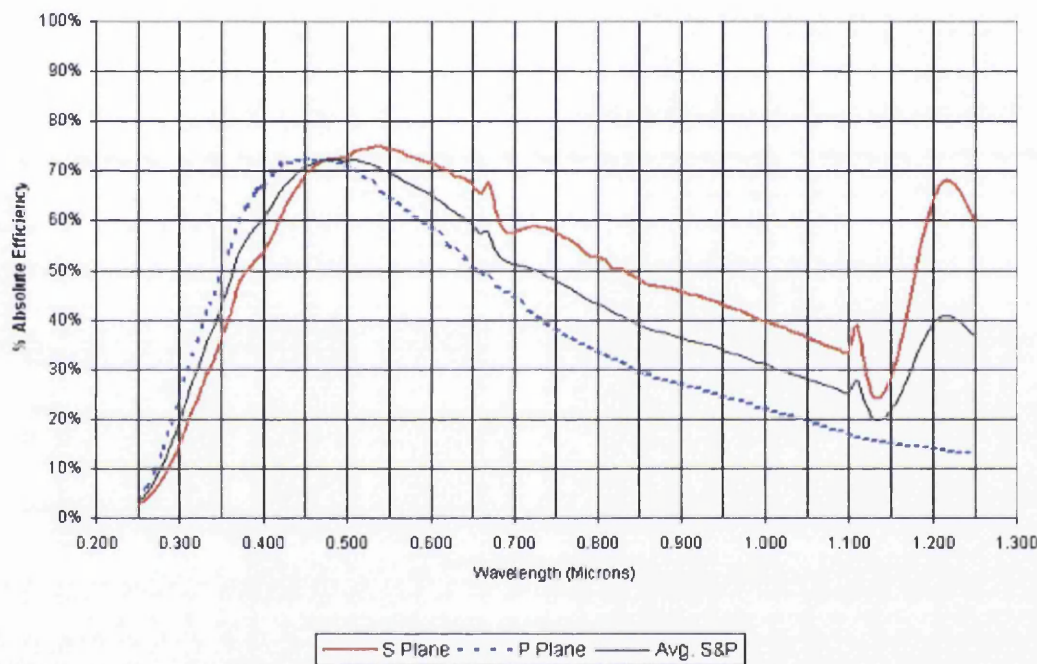


**Figure 5.25** Comparison of  $5 \times 1000\text{s}$  multiple exposure Raman spectra of the  $29:47:24(\pm 1)$   $\text{H}_2:\text{HD}:\text{D}_2$  (1atm) cell for direct- (bottom, black) and translational- (top, red) imaging cases. Entrance slit width:  $76.2\mu\text{m}$ , astigmatism correction and cosmic ray removal: *DCRR*, no baseline scaling. The two spectra are very similar, although the translational-imaging trace has a more pronounced background, most likely due to the slight overheating of the Spec-10 CCD.

The measured spectra are very similar to those acquired with direct imaging, as would be expected. Slight differences between the direct imaging and translational imaging intensity distributions for the same gas mixtures and acquisition parameters are most likely due to the change of polarisation of the scattered light due to the orientation of the two  $45^\circ$

mirrors since the  $600\text{gr}\cdot\text{mm}^{-1}$  grating has different transmission coefficients for parallel and perpendicularly polarised light entering the system, as shown in Figure 5.26.

It should also be mentioned that at the time the translational-imaging spectra were taken, a slight overheating of the CCD chip in the Spec-10 camera was observed, leading to increased background noise levels and an uneven background. This overheating issue is discussed more fully in Chapter 6.



**Figure 5.26** Absolute HTS grating efficiency for s- (perpendicular, red) and p- (parallel) polarisation with respect to incident wavelength in micrometres. The average efficiency is shown in black. From HTS grating datasheet master 3028 (PIActon (2004)).

## 5.6 Summary

In this chapter we have shown that although the TLK system can potentially be used for off-line high resolution spectral analysis (due to its  $2400\text{gr}\cdot\text{mm}^{-1}$  grating), it cannot compete with the UWS HTS / Spec-10 in terms of signal quality or reliability. Further, we have shown that the HTS / Spec-10 combination is quite capable of resolving quality Raman spectra with laser powers down to 10mW. The scaled estimates for performance

in-line at TILO (and in the future at KATRIN) are well within requirements, and have significant overhead in terms of both S/N and available extra laser power.

Although the  $1200\text{gr}\cdot\text{mm}^{-1}$  grating tests showed that such a grating is not viable for use in the ultra-compact HTS spectrograph, it is not thought that this represents a significant shortcoming. Since the target application is only concerned with relative intensities of Raman lines, and that it is most likely that only the vibration-rotation lines will be of interest (due to their wide spacing), it is not necessary to resolve the  $Q_1$ -branches in order to obtain the desired information. As such, a higher-resolution spectrometer such as the SpectraPro SP500i at Swansea could be used for off-line analysis. Since the mountings for both the fibre adaptor and the Spec-10 camera are common to both the HTS and the P500i, this would be a simple procedure, with minimal disruption to the on-line system.

Finally, although a fibre-coupled version of the UWS system has been shown to be viable, and was chosen for the setup for KATRIN (see Chapter 6), the translational-imaging experiments have provided a useful backup method should insurmountable complications arise with the fibre-coupled system. Initial results for the fibre-coupled approach are promising, however, and it is unlikely that the translational-imaging system will be used in practice.

## ***5.7 References for Chapter Five***

### ***5.7.1 Papers***

Drever R.W.P., Hall J.L., Kowalski F.V., Hough J., Ford G.M., Munley A.J., Ward H. (1983). "Laser phase and frequency stabilization using an optical resonator." Applied Physics B: Lasers and Optics **31**(2): 97-105.

Drexlin G., Weinheimer C., et al. (2005). KATRIN Design Report 2004. Wissenschaftliche Berichte FZKA 7090, ISSN 0947-8620

Lewis, R. J. and Telle, H. H. (2005). „Hydrogen Isotopomer Raman Spectroscopy for KATRIN - Intermediate Report 2005.” KATRIN BSCW (Internal) 10-ME-3200-0.

Taylor D.J., Glugla M., Penzhorn R.-D. (2001). “Enhanced Raman sensitivity using an actively stabilized external resonator.” Review of Scientific Instruments **72**(4): 1970-1976.

### 5.7.2 Datasheets

HTS grating datasheet master 3028, PIActon (2004)

[http://partners.gratinglab.com/products/efficiency/effFrame.asp?sku=010|53-\\*-260R](http://partners.gratinglab.com/products/efficiency/effFrame.asp?sku=010|53-*-260R)

Spec-10 CCD array datasheet, PIActon (2004)

<http://architect.wwwcomm.com/Uploads/Princeton/Documents/Datasheets/2kbIn.pdf>.

## CHAPTER SIX

### IN-LINE FIBRE-COUPLED RAMAN MEASUREMENTS AT THE TILO EXPERIMENT

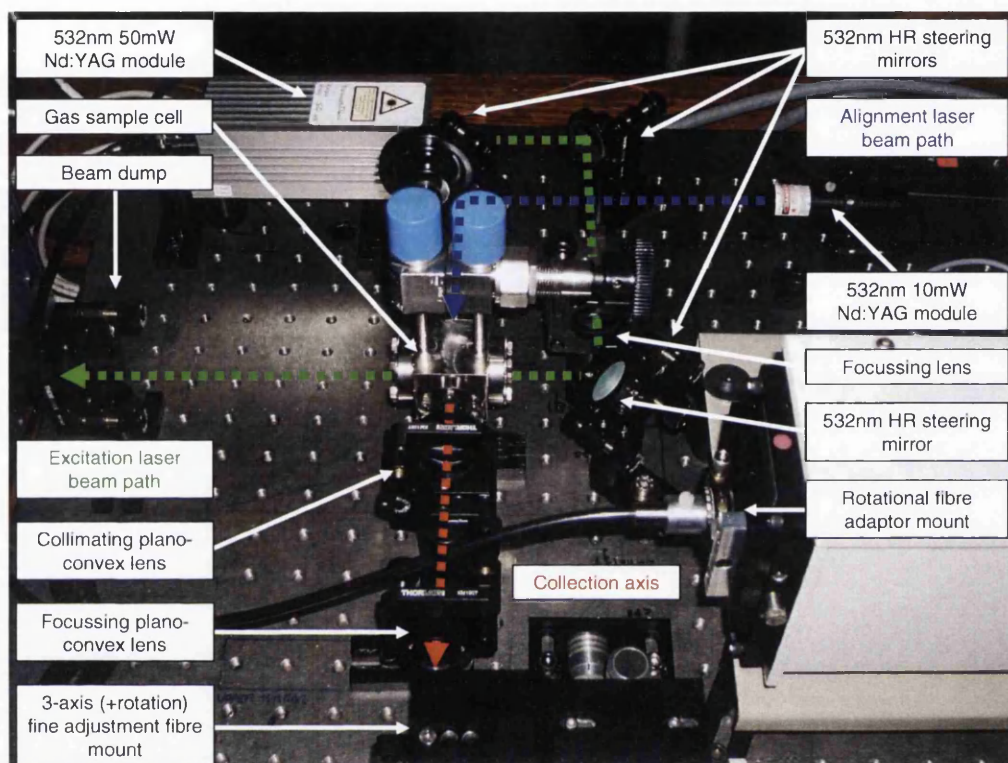
In this chapter we summarise the preliminary fibre-coupled Raman experiments performed at Swansea prior to the transfer of the system to the Test of Inner Loop (TILO) experiment at FZK in July 2006 and the first run of Raman measurements that were done in-line at TILO in October 2006 with flowing gas mixtures of the hydrogen isotopomers  $D_2$  and  $H_2$ . The issues relating to system setup and operation are discussed for each case, and the areas that require further development are identified.

#### *6.1 Preliminary Fibre-Coupled Raman Measurements at UWS*

The principle of fibre-coupled imaging was described earlier in Section 4.3.3. The setup used to test the viability of the fibre-coupled imaging in our case is shown in Figure 6.1. Unfortunately, after the conclusion of the translational imaging experiments detailed in Section 5.5.3, the 100mW Nd:YAG module failed; it was replaced by a 50mW Nd:YAG module of same reference design (i.e. differing only in power output) for the fibre-coupled experiments. The technique of passing a second laser beam from the 10mW Nd:YAG module through the LARA cell windows at  $90^\circ$  coaxial with the collection axis was adapted from the translational imaging technique to coarsely align the fibre centreline position.

As previously mentioned in Section 4.3.3, the optical fibre cable is a 3m-long bundle of 48  $100\mu\text{m}/125\mu\text{m}$  (core / cladding) step-index multimode fibres arranged into a slit-shaped configuration (single file). The bundle is matched to the acceptance angle of the HTS spectrometer, and the total slit height of 6mm matches the height of the CCD chip in the Spec-10 detector. The ferrules at both ends of the fibre are of 10mm diameter. Although the utilisation of a fibre cable means that this setup is very robust once aligned, the system

is quite sensitive to even very small errors in alignment of the fibre bundle in all three axes and in rotation at both ends of the optical cable, which dictates that high-precision mounts be used throughout.



**Figure 6.1** Fibre-coupled imaging setup at UWS. The 50mW laser beam path (green line) is sent through the centre of the LARA cell by means of two steering mirrors. The 10mW laser beam (blue line) is sent through the cell at  $90^\circ$  to the excitation beam path to coincide with the collection axis (red line). The position of the fibre is coarsely aligned on the alignment laser beam and finely aligned on the Raman spectrum of a liquid ethanol sample. The fibre mount has provision for 3-axis and fine rotational adjustment.

Unlike the translational imaging setup, the fibre-coupled system requires that the ‘pre-alignment’ of the system be very precise. The 50mW laser beam is steered by two 532nm HR mirrors to allow for adjustment of both beam height and direction. Diaphragms are used to ensure that the beam leaving the second steering mirror is as close to horizontal as possible. The beam is directed through the centre of the LARA cell windows and terminated with a beam dump. As mentioned above, the 10mW module is retained for coarse alignment of the fibre centreline – the 10mW beam is passed through the centre of the LARA cell at  $90^\circ$  to the excitation beam to provide a reference to the collection axis.

Since the 10mW module is mounted on a Thorlabs KM100 mount, which allows for tilt adjustment, a single steering mirror suffices to correctly guide the beam through the LARA cell coaxial with the collection axis. As for the excitation beam path, diaphragms are used to ensure that the beam is horizontal.

Initial fibre-coupled setups used a single collection lens to focus the scattering volume onto the slit of the fibre bundle, but this arrangement lacks flexibility. In such an arrangement, with the lens fixed in position, it becomes difficult to correct for vertical displacements in the imaging, since tilting the lens moves the collection axis on both sides of the lens. A much more flexible configuration is to employ two plano-convex lenses, which can be separated by a convenient distance along the collection axis. Tilt errors can then be corrected for each lens independently. This is crucial, as the fibre mount has only a limited range of adjustment of  $\pm 1\text{mm}$  in the vertical axis. The two-lens setup is also easier to coarsely align, since both lenses can be separately moved to their correct locations, with the LARA cell and fibre mount having been fixed in location. In contrast, a single-lens setup would require the fibre mount itself to be moved into the correct location, and this would have to be done quite accurately because of the rather limited  $\pm 1\text{mm}$  range of adjustment in each axis.

The fibre bundle is initially positioned using the beam of the 10mW laser to locate the collection axis. An ethanol-filled LARA cell is then used to provide a strong Raman spectrum to image onto the horizontally-oriented fibre bundle. In low ambient light, the image of the Rayleigh scattering can be seen directly on the fibre ferrule, allowing for relatively straightforward initial alignment. As for the translational imaging alignment procedure, fine adjustment of the fibre position is achieved by maximising chip coverage and signal intensity on the 2D representation of short exposure (1s) images in *WinSpec/32* while making fine 3-axis and / or rotational adjustments. Due to the small acceptance angle of the fibre bundle, it is imperative that the collection axis be as close to horizontal as possible (achieved as mentioned above by using diaphragms). The fibre mount is set so that the face of the fibre ferrule is very close to the vertical. Optimisation of the signal strength is therefore achieved by a combination of 3-axis and rotational adjustments on the

mount, and vertical displacement corrections are achieved by appropriately tilting the plano-convex lenses.

Before any Raman spectra can be recorded, however, the fibre must be correctly mounted at the spectrometer end of the system. At the collection end, the fibre is mounted on a micrometer-drive high-precision 3-axis lockable mount, which has been modified to include a Thorlabs CRM1P/M micrometer-drive high-precision rotation lockable mount. As such, the 3-axis and rotational adjustments at the collection end are very precise.

### *6.1.1 Spectrometer-end fibre alignment issues*

At the spectrometer end, alignment is less straightforward. Firstly, the small dimensions of the adaptor plate of the edge filter unit limits the size (and hence precision) of the components that can feasibly be mounted onto the faceplate to provide the necessary adjustments.

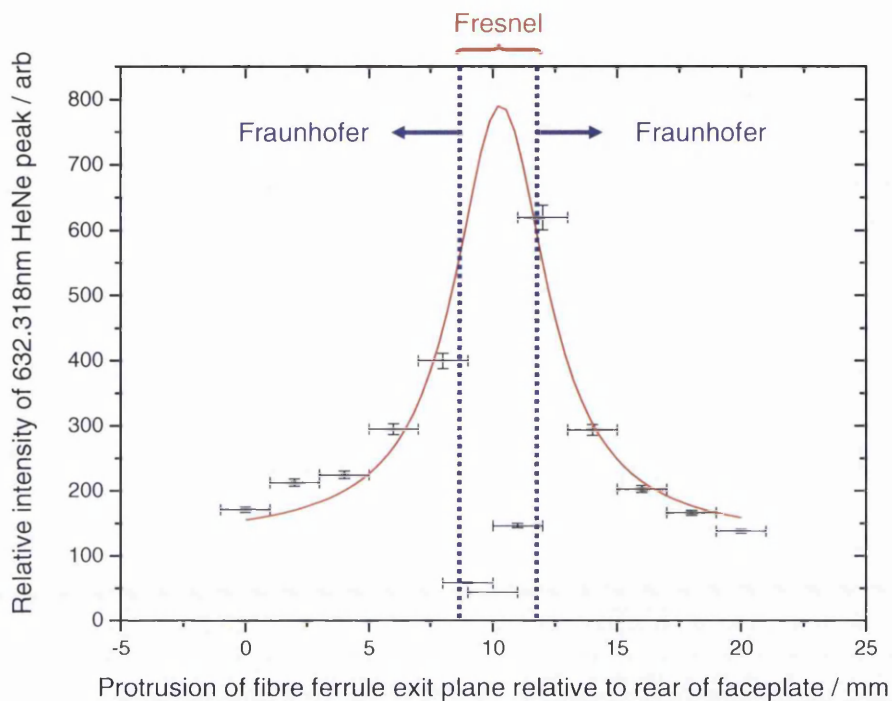
Secondly, the fibre positioning is highly sensitive to even small variations in the fibre location when the object plane (i.e. the end of the fibre ferrule) and the focal plane of the filter unit collection lens are close to coincidence. The rotation mount used on the faceplate is a Thorlabs PRM05/M; although less precise than the larger CRM1P/M used at the collection end, it provides adequate precision for rotational adjustment of the fibre bundle with the entrance slit. Vertical adjustment is performed manually by loosening four fastening screws at the corners of the plate and shifting the entire faceplate along the track of the four corner holes. The holes have been lengthened to provide  $\pm 5$ mm adjustment in the vertical axis. Aligning the fibre bundle in the vertical axis is quite simple. The fibre bundle is rotated so that the fibre slit and entrance slit of the spectrometer are firstly perpendicular to each other, and by using a white light source one can then adjust the faceplate until the narrow image is centralised in a 2D spectral representation in *WinSpec/32*. Since a white light source (such as a lamp) is rather bright, one can use very short (<1s) repeat measurements to adjust the vertical position in real-time.



After returning the fibre bundle orientation back to vertical, horizontal adjustment of the fibre is provided by two thumbscrews on the filter unit faceplate. Although not as precise as a micrometer driven arrangement, it is relatively simple to align the fibre bundle with the centre of the entrance slit once the vertical and rotational adjustments have been made. Although manual adjustment of the vertical and horizontal alignment is less than ideal, it presented no real shortcoming in practice.

The difficulty at the spectrometer end is the lack of micrometer adjustment along the collection axis of the filter unit (i.e. how close the fibre ferrule is to the filter unit collection lens). Currently, this is done manually – the fibre ferrule is held in the rotation mount by a simple adaptor tube which has a single grub screw to secure the fibre. Since rotational orientation is typically disturbed when the ferrule is moved in this direction, the rotational alignment must be reset every time the fibre is adjusted in this way.

A further complication arises when attempting to position the fibre near the focal plane of the filter unit collection lens. Intuitively, one would assume that positioning the fibre bundle exit plane near the focal plane of the imaging lens would provide the optimum result. However, as the fibre ferrule is gradually pushed into the unit and passes through the focal plane, there will be a region where the near-field (Fresnel) diffraction pattern from the individual fibres (i.e. small circular apertures) is imaged onto the entrance slit of the spectrometer. The diffraction pattern imaged onto the entrance slit can result in lower than expected signal strength, when relating it to the total light intensity emerging from the fibre. This is shown in Figure 6.2 for the case of the 632.318nm HeNe laser emission. While the decrease for larger distances is intuitive (the image moves out of focus), when nearly in focus the intensity drops in an erratic manner. The actual Fresnel intensity pattern from the 100 $\mu$ m fibre can be calculated in principle (see for example the treatment given in Hecht (2002)), but shall not be provided here. An excellent applet for calculating and visualising Fresnel intensity patterns is provided on-line by Wyatt (2007).



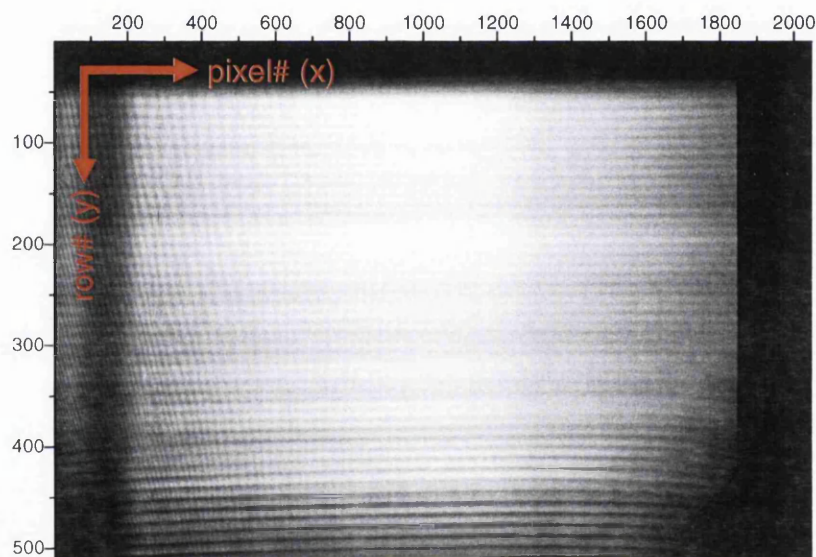
**Figure 6.2** Maximum relative intensity measured for the 632.318nm HeNe laser emission line as a function of the protrusion of the end of the fibre ferrule from the rear of the spectrometer fibre adaptor plate. A dramatic loss of signal strength is observed as the near-field (Fresnel) regime is crossed. The red line shows a Lorentzian-type fit of the far-field (Fraunhofer) regime data points.

One can see from Figure 6.2 that not only is the intensity much lower near the ‘true’ focal point of the lens, but that the far-field (Fraunhofer) regions of the signal strength curve are slightly asymmetric about the focal point. In order to maximise signal strength through the fibre it is necessary to position the fibre ferrule slightly closer to the lens than the focal point. Due to the high sensitivity of the observed signal strength on this position, it is planned to fit a lockable micrometer-drive z-axis to improve the accuracy of fibre placement relative to the focal plane.

### 6.1.2 General fibre-related issues

The inclusion of the fibre bundle into the collection path introduces losses of ~32%, as was discussed in Section 4.3.3. It should be mentioned again here that the sequence of fibres at

either end of the optical cable are random. This has the consequence that spectral lines exhibit a patchiness in the y-axis direction that was not present for the direct and translational imaging arrangements. Also, as can be seen in Figure 6.3, the fibre boundaries are clearly visible. Note that both of these factors affect the double-derivative of a given y-axis interval, even if no cosmic rays events are present. Despite this, the cosmic ray removal routine *DCRR* suffered no ill effects and was used on all of the Raman spectra presented in this chapter.



**Figure 6.3** Spec-10 CCD chip image of a white light source. The fibre boundaries and scrambling of the fibre sequence are clearly visible. The vertical, sharply defined dark boundary towards the right of the image is due to the edge filter (near 532nm). The horizontal band towards the top of the image is due to a slight vertical misalignment. The barrelling effect towards the bottom of the image is due to the fibre exit plane and the focal plane not being exactly parallel.

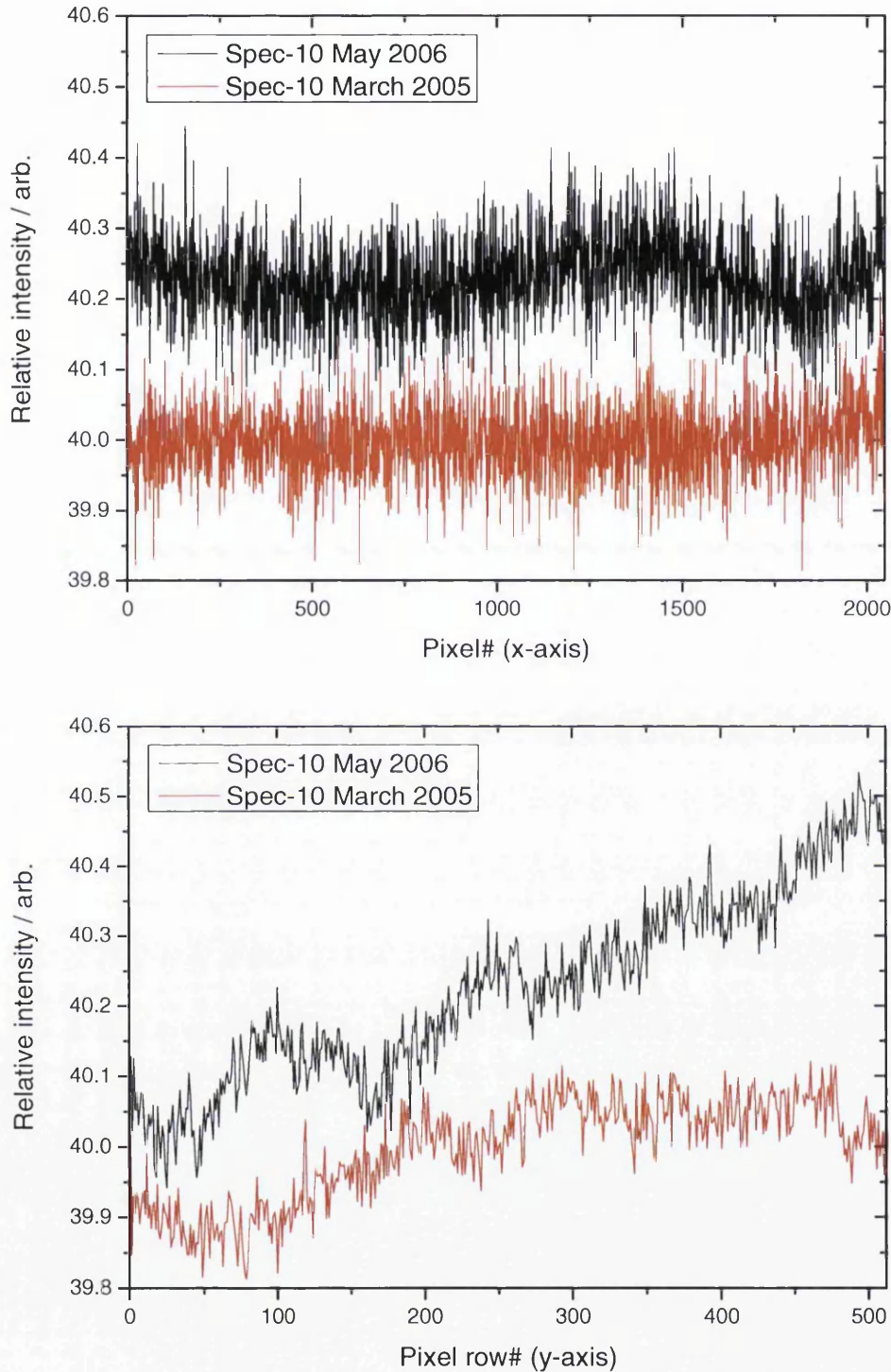
One can see in Figure 6.3 that there is a rather pronounced barrelling effect towards the bottom of the spectral image due to the fibre exit plane and the focal plane not being exactly parallel. Although this distortion did not seem to have an adverse effect on the quality of the Raman spectra measured with this system, it may be the case that at higher resolutions this distortion would have to be corrected for. The astigmatism correction routine *AstCorr* that is integrated into *DCRR* could be easily modified to apply shifts in the y-axis direction in the future should such a requirement arise. All Raman spectra shown in

this chapter have been cleaned of cosmic ray events with *DCRR* and have undergone baseline scaling using the data evaluation package *Origin*.

### 6.1.3 *Detector noise issues*

Dark current measurements taken at the time of these preliminary fibre-coupled experiments reveal that the Spec-10 was beginning to show first signs of deterioration. As will be discussed more fully in Section 6.2.3, the batch of Peltier stacks to which the unit installed in our Spec-10 detector belonged was faulty (private communication, PIActon (2006)). Although the effect is quite small, the background noise is nevertheless noticeably greater than for the Raman spectra measured at the time of the comparative review detailed in Chapter 5. Since the fibre-coupled and translational imaging experiments were carried out at the same time, the remarks made here apply equally to the translational imaging system described in Section 5.5.3.

Figure 6.4 compares the average background noise in the Spec-10 in cross section between the time of the comparative review (March 2005) and the time of the translational and fibre-coupled imaging experiments (May 2006). The increase in baseline values is probably due to a drift in the electronic offset, but there is a clear increase in the unevenness of the background in both horizontal and vertical directions, with the overall variation in background level more than doubling in the case of the y-axis cross section (bottom).



**Figure 6.4** Comparison of Spec-10 dark current noise between March 2005 (red) and May 2006 (black) for a  $1 \times 50$ s exposure. Top: averaged cross section along the y-axis (pixel row#). Bottom: averaged cross section along the x-axis (pixel column#). The dark current noise traces in the x-axis direction (top) are comparable, but there is an obvious increase in the overall variation of the dark current noise in the y-axis direction (bottom). The difference in the baseline value is probably due to a drift in the electronic baseline offset that has occurred over the 14 months that separate these two measurements.

#### 6.1.4 Raman spectra measured with the fibre-coupled HTS/SPEC-10 system

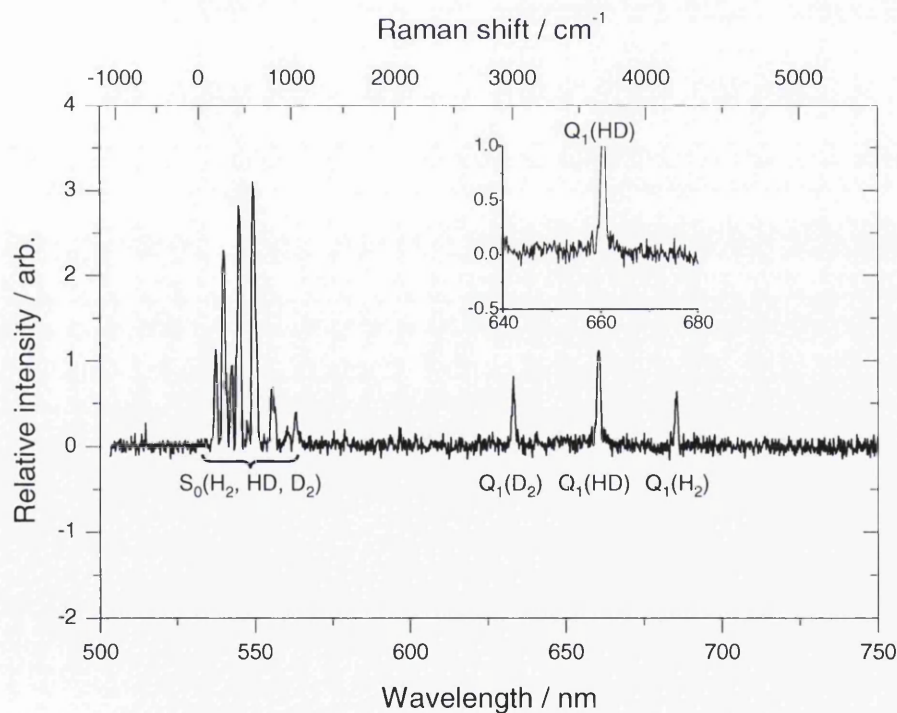
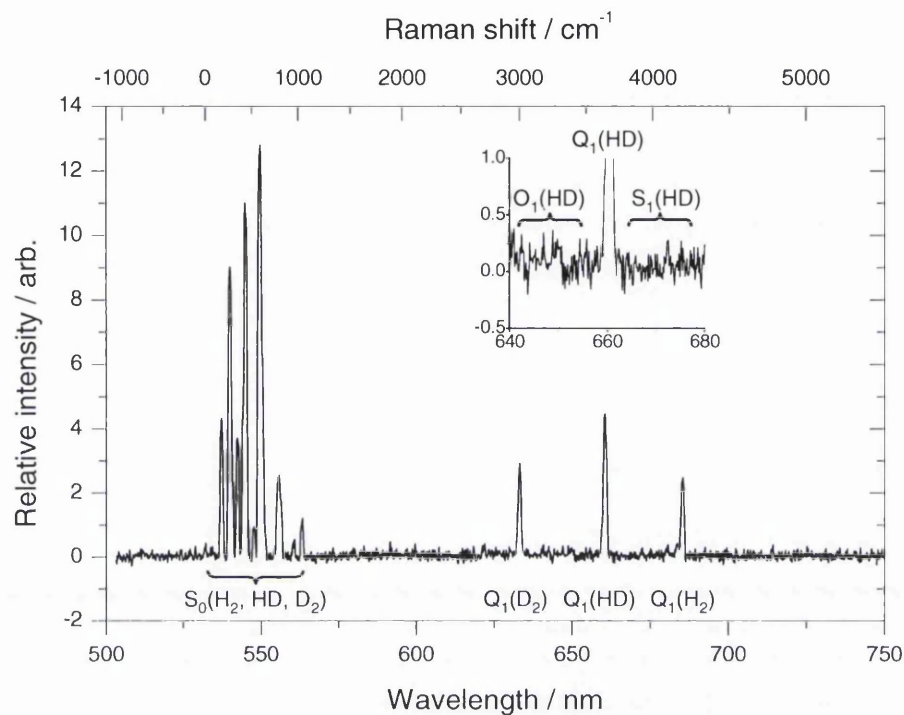
As for the direct and translational imaging cases, The Raman spectrum of the H<sub>2</sub>:HD:D<sub>2</sub> (29:47:24±1 at 1atm) cell was recorded for a variety of acquisition times and exposure multiples in order to test the performance of the fibre-coupled system. These times match those used in the other HTS/Spec-10 system surveys included in this thesis and are summarised in Table 6.1. In order to ensure that as close as possible to all the light transmitted by the fibre was used, the entrance slit of the spectrometer was set to 127µm.

**Table 6.1** Exposure times investigated to evaluate the fibre-coupled HTS/Spec-10 system viability. Spectra flagged with an asterisk (\*) are shown in this chapter.

Multiple exposures (total of 5000s each)	Single exposures (s)
5 × 1,000s (*)	1 × 1,000s
10 × 500s	1 × 500s
20 × 250s	1 × 250s
50 × 100s	1 × 100s
100 × 50s (*)	1 × 50s

Figure 6.5 shows the Raman spectra of the 29:47:24(±1) H<sub>2</sub>:HD:D<sub>2</sub> (1atm) cell for two multiple exposure times, namely 5×1000s and 100×50s. Even though the laser power has been reduced by a factor of two, relative to the direct and translational imaging experiments which utilised a 100mW Nd:YAG module, and notwithstanding the ~32% loss of signal due to the optical fibre, in the case of the 5×1000s exposure (top) the strongest lines of the HD O<sub>1</sub>- and S<sub>1</sub>-branches are just visible above the background noise. In all other exposure configurations, however, these branches were not observed.

In the case of the 5×1000s exposure, the S/N ratio for the strongest S<sub>0</sub>-branch line is approximately 45, while the S/N ratio for the HD Q<sub>1</sub>-branch is approximately 16. This translates into 'scaled up' estimates of 270 and 96 for the S<sub>0</sub>-branch and Q<sub>1</sub>-branch lines at 3W operating power and 100mbar pressure, respectively. It is likely that in addition to the slight overheating problem with the Spec-10, there was also a slight error in the highly-sensitive fibre placement at the filter unit faceplate, as described in Section 6.1.1, because the S/N values derived here are not in line with estimates from the other reviews described in Chapter 5.



**Figure 6.5** Top:  $5 \times 1000s$  multiple exposure Raman spectrum of the 29:47:24( $\pm 1$ )  $H_2$ :HD: $D_2$  (1atm) cell. The HD  $O_1$ - and  $S_1$ - branches are just visible above the background noise (see inset). Bottom:  $100 \times 50s$  multiple exposure of the same sample. The HD  $O_1$ - and  $S_1$ - branches are not visible for this exposure configuration (see inset). Entrance slit width:  $127\mu m$ , astigmatism correction and cosmic ray removal: *DCRR*, baseline scaling: *Origin*.

## 6.2 *Fibre-Coupled Raman Measurements at TILO*

The fibre-coupled HTS/Spec-10 system was transferred to the TILO experiment at FZK shortly following the first run of ‘proof-of-principle’ measurements at Swansea described above. As mentioned in Section 5.3.1, TILO shares over 90% of its components with the KATRIN inner loop for the tritium flow, and therefore provides an ideal, highly realistic mock-up scenario in which to test the HTS/Spec-10 system. Although TILO cannot be run with tritiated isotopomers, due to its lack of a secondary enclosure, mixtures of H<sub>2</sub>, HD, and D<sub>2</sub> can be run through the system at any desired composition. In this section we summarise the design of the system and the first run of in-line Raman scattering experiments that were performed at TILO in October 2006.

### 6.2.1 *Laser Raman system mounting bench design*

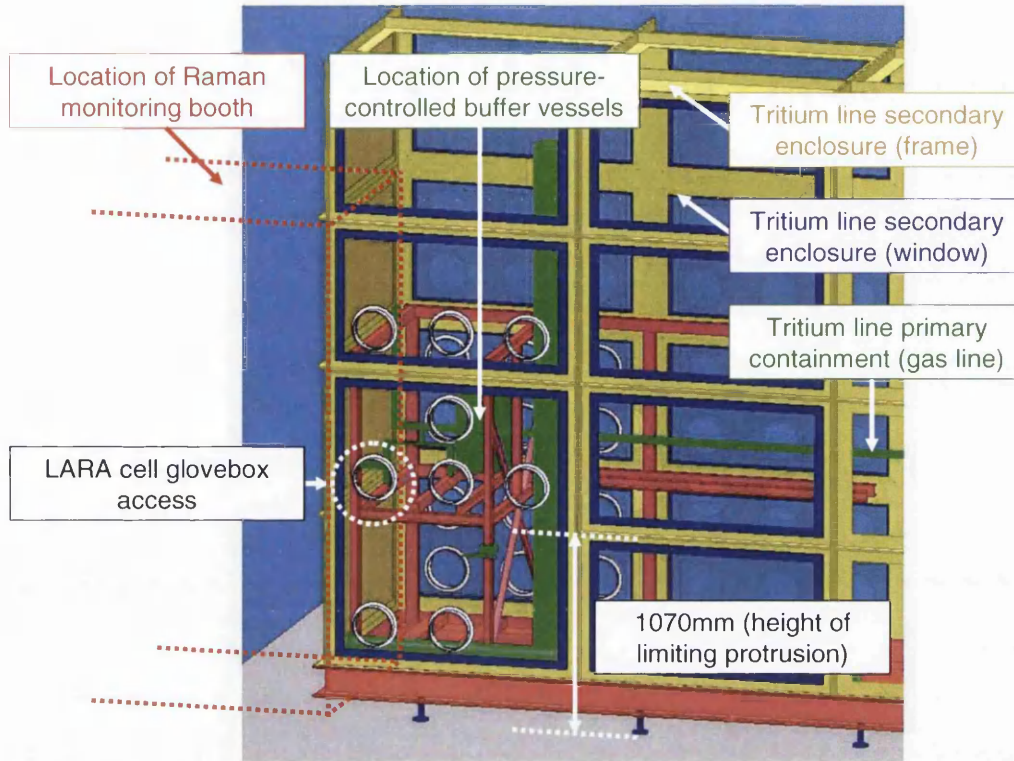
Allocation of floor space at the KATRIN experiment is at a premium. The floor space allocated to us for the laser Raman monitoring system is 1.2x1.8m maximum. To ensure that other experiment staff members are not accidentally exposed to laser radiation while the monitoring system is in operation, the allocated floor space will be enclosed in an interlocked booth. A mobile bench has been designed to house the monitoring system, and to facilitate both transport from TILO to KATRIN and wholesale removal should the requirement to move the bench out of the enclosure arise.

The designated location of the Raman monitoring booth is shown in Figure 6.6 abutted to one end of the HVT-TLK R 195 glovebox. The location of the booth is dictated by the position of the pressure-controlled buffer vessels (BD001 and BD101) between which the LARA cell bypass must be located and the requirement that the LARA cell must be reachable via a glove box access in the secondary enclosure\*.

---

\* The tritium gas path at KATRIN will be contained in a double-enclosure system. The primary enclosure is the gas line through which the tritium gas flows. The secondary enclosure surrounds the primary enclosure and provides a leak-tight space which can be purged in the event of a tritium gas leak.



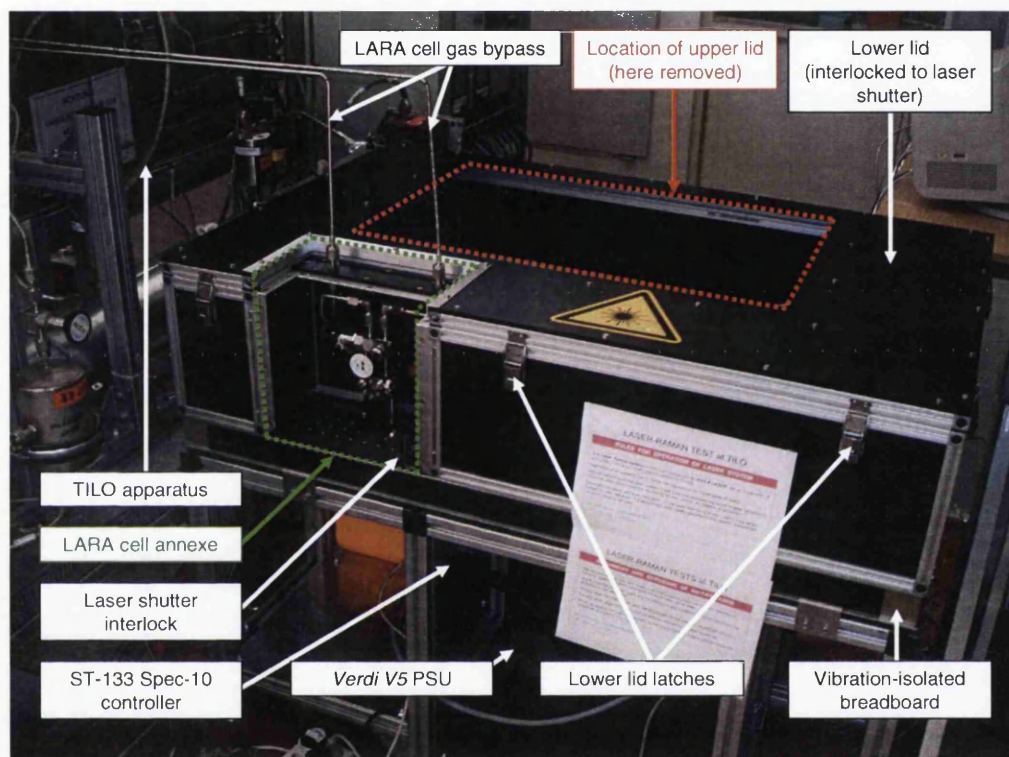


**Figure 6.6** Designated location of the Raman monitoring booth abutted to one end of the HVT-TLK R 195 glovebox. The location of the booth is determined by the position of the buffer vessels BD001 and BD101 (shown) and the requirement for access to the LARA cell via a glovebox window. Adapted from drawings by Stern (2006).

The bench is shown in Figure 6.7 with the LARA cell connected to the TILO experiment via a bypass between the two buffer vessels. All measurements described in the remainder of this chapter were made with the system in place on the bench and in-line at TILO. The dimensions of the bench were selected for it to fit into the floor space allocated by KATRIN, while still allowing sufficient space for an operator to sit at a desk within the enclosed booth. A further consideration was that the bench should be able to be moveable through standard doors which constrained the maximum width of the short side of the bench (and hence the breadboard) to 750mm.

The main lid is made from two segments – the lower section encloses the laser beam path, which is linked to the shutter in front of the *Verdi V5*'s exit aperture, and can be locked to the bench via catches on the upper rails of the laser enclosure. The lower section has a large hole to allow access to the alignment optics and the HTS/Spec-10 system. An upper

lid is placed over this hole to exclude light from the laboratory from the collection area. Since the only access to the beam path in the collection area is via a 25mm diameter hole in the enclosure panel next to the LARA cell, this upper lid is not linked to the laser shutter. Both lids are dust- and light-tight.



**Figure 6.7** Laser Raman system bench designed to enclose the optical path and provide a darkened space for the fibre-coupled HTS/Spec-10 system and associated optics, here shown in-line at TILO. The annexe for the LARA cell is positioned to provide maximum access from the secondary enclosure glovebox and has a light-tight cover (removed in the picture). The main lid is in two parts to allow access to the collection optics and the HTS/Spec-10 system, while still enclosing the laser beam path.

The lower section of the bench provides adequate space for a 19-inch rack in which to fit the *Verdi V5* laser power supply, and a controlling PC. Also located in the lower section is a shelf for the ST-133 Spec-10 controller. The design of the secondary enclosure glove

box and the requirement to have at least 180mm<sup>†</sup> available height above the breadboard in order to house the necessary components of the fibre-coupled system dictates that the vibration-isolated breadboard is located at a height of 700mm from the laboratory floor. The LARA cell is located in an annexe that allows for access from the secondary enclosure glove box without compromising the laser beam path enclosure.

### 6.2.2 *TILO system setup and alignment*

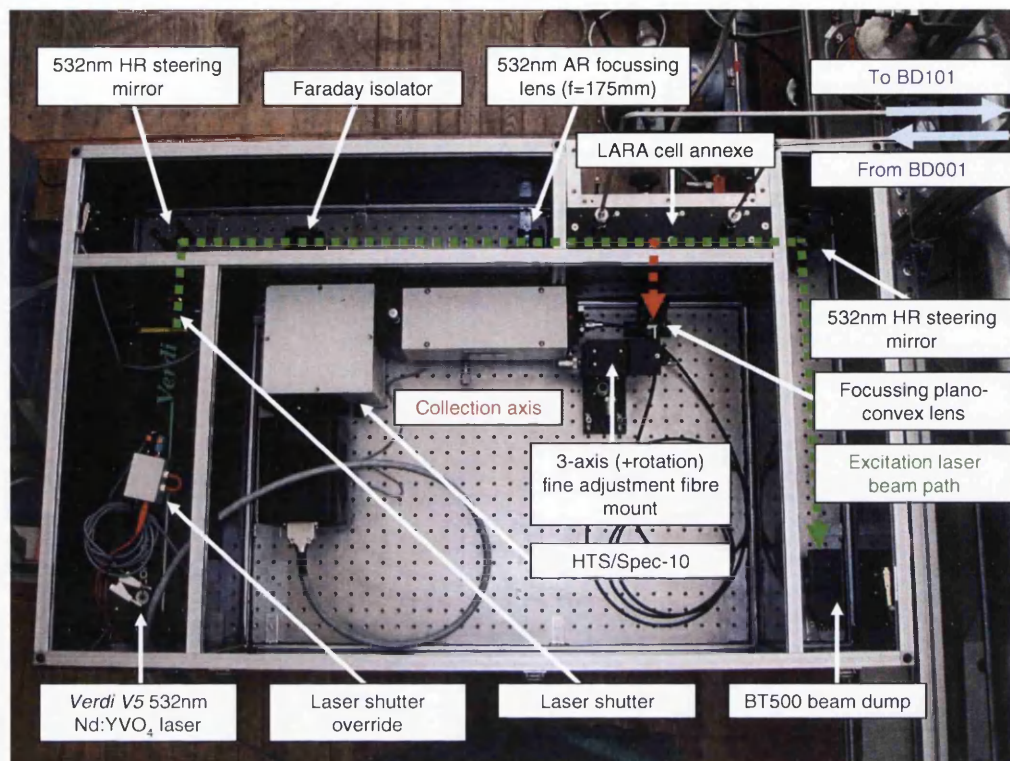
The fibre-coupled HTS/Spec-10 system is shown in-line at TILO on its mounting bench in Figure 6.8. The gas bypass for the LARA cell is inserted at the new proposed location between the pressure-controlled buffer vessels BD001 and BD101, as mentioned previously in Chapter 5.

The procedure for aligning the system on the bench is much the same as for the setup at Swansea, although on the bench there is only room for a single steering mirror for the *Verdi* laser, and no room at all for a low-power laser module to act as a coarse alignment aid. This has not proved to be a problem, however, as the system was pre-aligned to a high degree of accuracy, and the single steering mirror was adequate to align the laser beam path. As for the other configurations, an ethanol-filled LARA cell was used as an alignment aid. Due to the very high strength of the ethanol Raman spectrum when operating at laser powers of the order 1W, fine alignment proved relatively straightforward, so the loss of the coarse-alignment laser module was not critical.

Note that after the beam has passed through the LARA cell, a second steering mirror is used to send the beam down a long distance to a beam dump. This ensures that the laser beam has diverged significantly by the time it reaches the beam dump. Although the BT500 beam dump used here is rated to operate safely at up to 70Wcm<sup>-2</sup>, a laser beam of 5W power needs to have a diameter of at least 3mm at the beam dump surface.

---

<sup>†</sup> The HTS is the tallest component at 178mm. 180mm is therefore a practical minimum to allow between the breadboard and the underside of the lower enclosure lid. In the design implemented, the available height above the breadboard is 200mm.

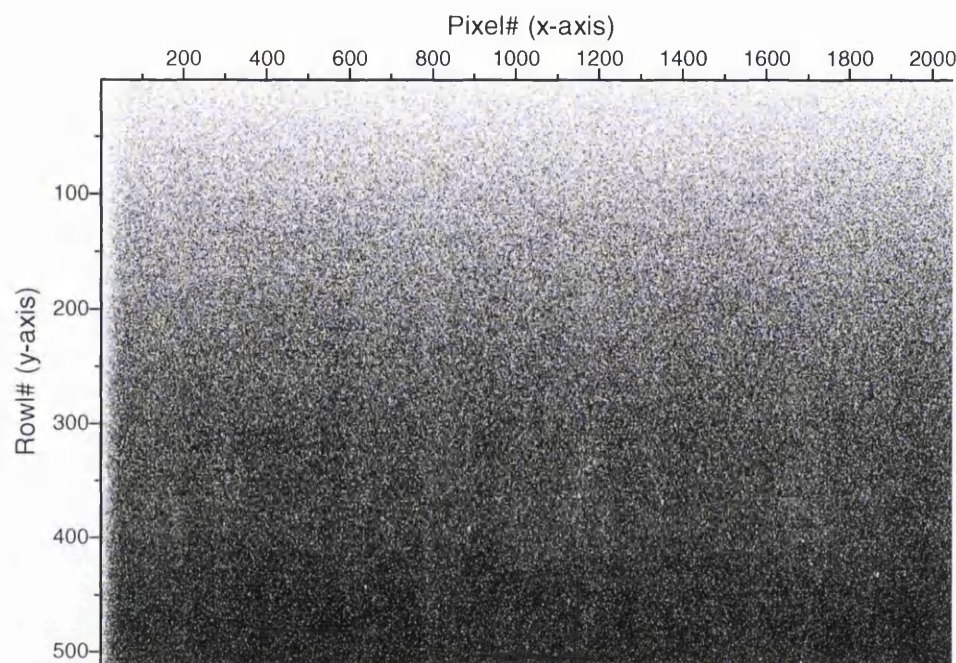


**Figure 6.8** Fibre-coupled imaging setup of the HTS/Spec-10 system at TILO. The *Verdi* laser beam (green line) is steered by a single 532nm HR mirror, but has a very good pre-alignment at the required beam height. A second mirror steers the beam down the long arm to the right of the figure to the beam dump. The two-mirror collection configuration is identical to the Swansea setup, but there is no low-power laser module for coarse alignment. The LARA cell is located in an annexe to the enclosure connected to the gas bypass between buffer vessels BD001 and BD101 (blue).

### 6.2.3 Detector noise issues

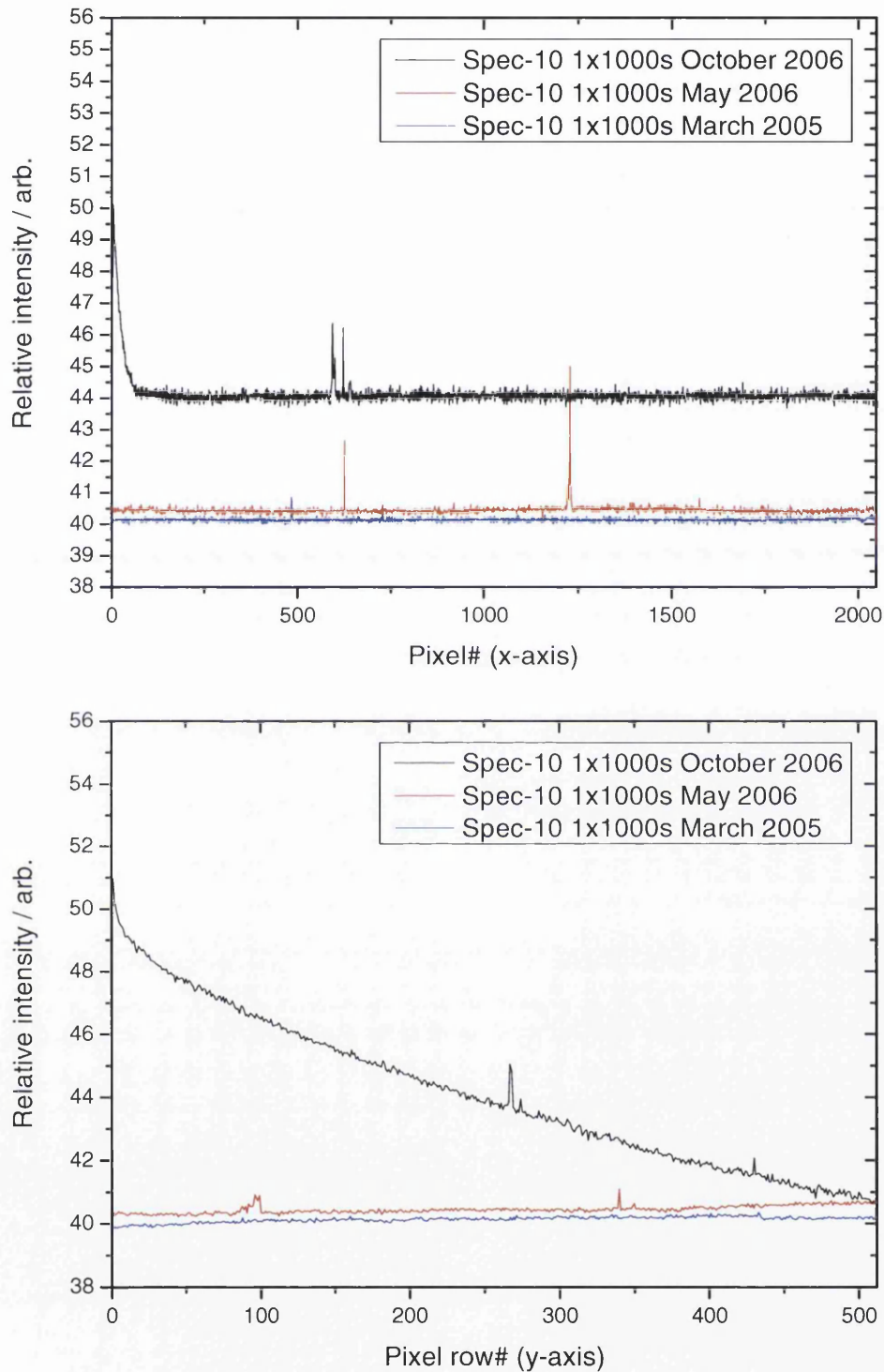
During the equipment checks following the transfer of the HTS/Spec-10 system to FZK, a severe increase in the dark current noise of the detector was noticed. The Spec-10 was returned to the UK distributor, but attempts to fully rectify the problem were unsuccessful. The engineers were able to minimise the overheating problem to a level that the Spec-10 could be used for proof of principle measurements at TILO. The problem was identified as a manufacturing fault in the Peltier stack, and this problem was a common one to an entire batch of systems that were shipped to Europe in 2005. A gradual degradation of the thermal contact of the Peltier stack to the CCD array evolved over time, which in turn

gradually increased the thermal noise. Figure 6.9 shows the background noise of the Spec-10 for a  $1 \times 1000$ s acquisition time during the October 2006 experimental trials – the Peltier stack has lost thermal contact with the CCD chip particularly along two edges (towards the left and top of the figure).



**Figure 6.9** Spec-10 detector background noise for a  $1 \times 1000$ s acquisition. The loss of thermal contact between the Peltier stack and the CCD chip array is particularly noticeable towards the top and left edges of this figure.

Figure 6.10 shows the above spectral image in averaged x- and y-axis cross section and compares it with  $1 \times 1000$ s exposures taken in May 2006 (the time of the preliminary fibre-coupled imaging tests at Swansea) and in March 2005 (two months before the time of the UWS/TLK system comparative survey). The increase in the noise level between March 2005 and May 2006 is slight when compared with the dramatic increase between May 2006 and October 2006.



**Figure 6.10** Comparison of Spec-10 dark current noise between March 2005 (blue), May 2006 (red), and October 2006 (black) for a 1×1000s exposure. Top: averaged cross section along the y-axis (pixel row#). Bottom: averaged cross section along the x-axis (pixel column#). The Peltier stack has lost thermal contact along the two edges pixel#=0 and pixel row#=0. The increase in pixel-to-pixel noise, cross section unevenness, and baseline level is quite significant in both graphs.

The March 2005 dark current measurements show a nearly flat response across the entire 2048×512 pixel array. In these measurements the Spec-10 is operating correctly at its normal operating temperature of -70°C. The thermal noise contribution to the pixel-to-pixel fluctuations is therefore minimal, with the contributions from readout and digitisation noise being of roughly the same magnitude. The pixel-to-pixel fluctuation along a single column is approximately  $\pm 0.05\text{mV}$  in this ideal case.

Due to the sloping background of the October 2006 measurements, it is more difficult to evaluate a statistical (thermal) average for this value. If the slope is removed (i.e. scaled in *Origin* using the baseline tool), the pixel-to-pixel fluctuation is found to be approximately  $\pm 0.8\text{mV}$ . Using the argument that the pixel-to-pixel fluctuations will average out following a  $\sqrt{N}$  dependence, where  $N$  is the number of pixels averaged, then one can estimate that the signal variance in October 2006 was more than a factor of 10 worse than for the ideal, flat response case of March 2005. One should also bear in mind that the highly uneven background introduces further difficulties when binning spectra – the October 2006 background varies by nearly two orders of magnitude more than the March 2006 background. To further complicate matters, the temperature of the Spec-10 CCD chip varied quite significantly during operation when spectra were taken in October 2006

In order to assess the effect of the increased dark current noise on the Raman spectra measured at TILO, and to ascertain meaningful comparison to results from previous experimental surveys at TLK and Swansea, dark current readings were taken at each of the exposure times investigated for the in-line measurements (1×10s, 1×100s, 1×1000s), and the temperature of the Spec-10 chip was noted before and after each run. Using the graph of dark current noise dependency on CCD chip temperature (see Figure 4.17), it is possible to estimate the effect of the average temperature on the measured S/N ratios of a given spectrum, and to obtain a more realistic estimate of system performance.

The Spec-10 was returned to the UK distributor in January 2007 for shipping back to PIActon in the United States where a replacement cooling system will be fitted. The camera should be available for a second run of experiments at TILO in the second quarter of 2007. With the Spec-10 performing to specification, it will finally become possible to

make quantitative comparison of the results with previous experiments described in Chapter 5.

#### *6.2.4 Raman spectra measured in-line at TILO*

The experiments described in the remainder of this chapter were carried out during the week 23-27<sup>th</sup> October 2006. The initial results of these experiments have been submitted to the KATRIN collaboration in the form of a preliminary report (Lewis and Telle (2006)). These experiments were designed to test the performance of the system in-line under various realistic operating conditions and with different compositions of flowing hydrogen isotopomer gas mixtures, albeit limited to the non-tritiated species.

Table 6.2 summarises the experiments performed during that week, and highlights the purpose of each of the experiment runs performed on each day. Raman spectra were measured in each run with single acquisition times of 10, 100, and 1000s, but only the 1000s spectra are shown in this chapter.

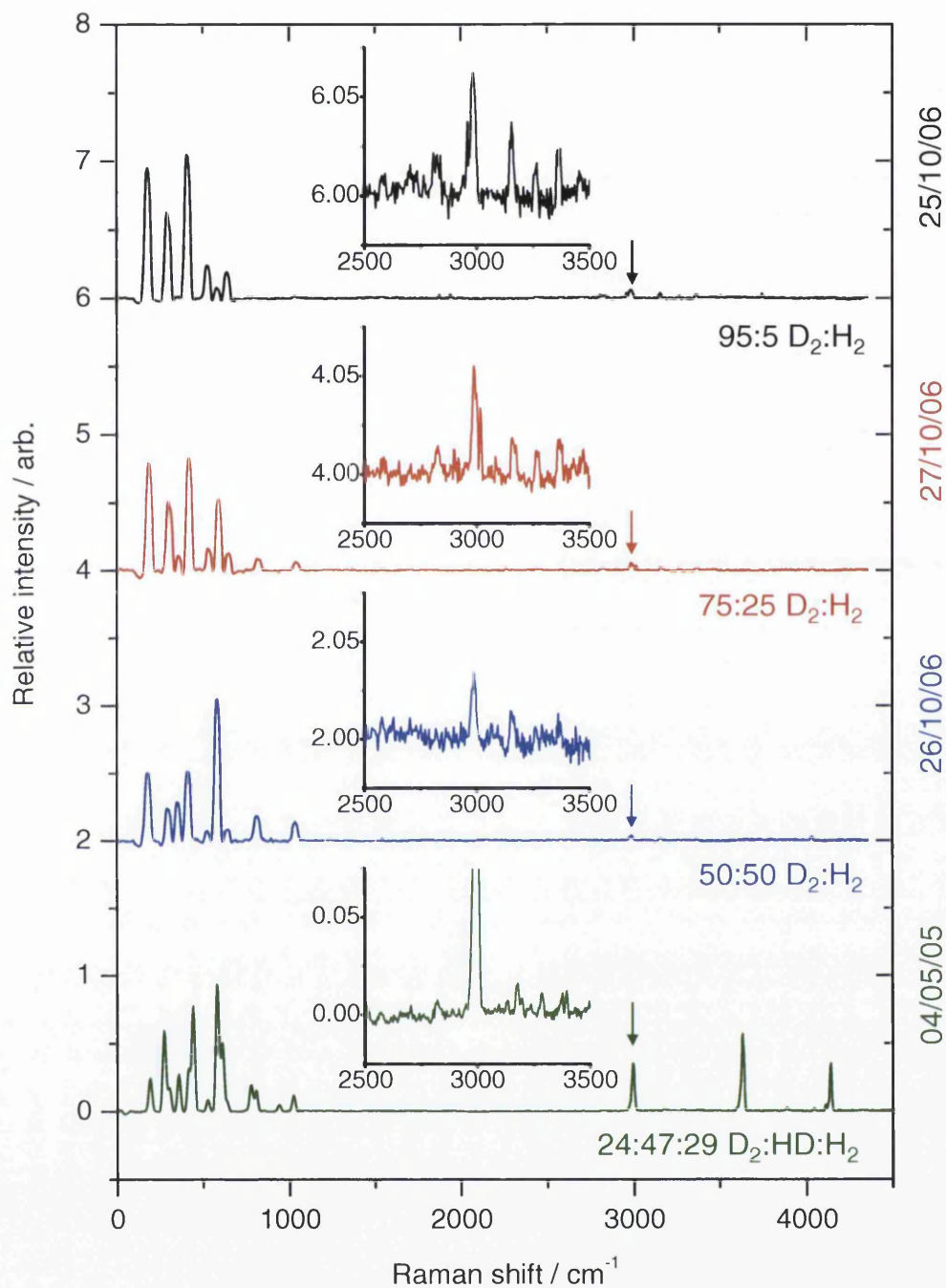


**Table 6.2** Summary of the Raman scattering experiments performed in October 2006 in-line at TILO. The entrance slit of the HTS was set at 127 $\mu$ m for all experiments. Gas loop flow rate values are averages over each run.

Date	Target of experiments	Sample / spectral source	Laser power (W)	Sample pressure (mbar)	Gas loop flow rate (cm <sup>3</sup> min <sup>-1</sup> )
23/10/06	Spec-10 dark current characterisation	None	N/A	N/A	N/A
24/10/06	Alignment of fibre coupling	Liquid ethanol	0.25, 0.5	N/A	N/A
25/10/06 (i)	Spec-10 dark current characterisation	None	N/A	N/A	N/A
25/10/06 (ii)	In-line Raman spectra (high flow rate)	95:5 D <sub>2</sub> :H <sub>2</sub>	1	110	271
25/10/06 (iii)	In-line Raman spectra (low flow rate)	95:5 D <sub>2</sub> :H <sub>2</sub>	1,2,3	110	92
26/10/06 (i)	Wavelength calibration of HTS/Spec-10 system	Hg, Ne lamps	N/A	N/A	N/A
26/10/06 (ii)	In-line Raman spectra (low flow rate)	50:50 D <sub>2</sub> :H <sub>2</sub>	1,2,3,4	110	102
27/10/06	In-line Raman spectra (high flow rate)	75:25 D <sub>2</sub> :H <sub>2</sub>	1,2,3,4	140	270

Figure 6.11 shows a representative selection of Raman spectra measured in-line at TILO with a 3W excitation laser power, comparing the three compositions measured (95:5, 75:25, and 50:50 D<sub>2</sub>:H<sub>2</sub>), and a Raman spectrum of a 29:47:24 $\pm$ 1 (1atm) H<sub>2</sub>:HD:D<sub>2</sub> mixture measured in a static (zero flow) cell at Swansea with the 100mW direct-imaging system. These spectra contain a great deal of information about the performance of the system at TILO, and several points are immediately apparent (with further discussion below):

- i. Flow rate apparently makes no difference to the system sensitivity.
- ii. There is no contribution to the TILO spectra from the HD isotopomer.
- iii. The Q<sub>1</sub>-branches of the TILO measurements are heavily suppressed.



**Figure 6.11**  $1 \times 1000\text{s}$  single exposure Raman spectra measured in-line at TILO with the fibre-coupled system. Black: 95:5  $\text{D}_2$ : $\text{H}_2$  at  $\sim 110\text{mbar}$ ,  $92.5\text{cm}^3\text{min}^{-1}$  flow rate, 3W laser power. Red: 75:25  $\text{D}_2$ : $\text{H}_2$  at  $\sim 140\text{mbar}$ ,  $270.47\text{cm}^3\text{min}^{-1}$  flow rate, 3W laser power. Blue: 50:50  $\text{D}_2$ : $\text{H}_2$  at  $\sim 110\text{mbar}$ ,  $101.5\text{cm}^3\text{min}^{-1}$  flow rate, 3W laser power. Included for comparison is a  $1 \times 1000\text{s}$  single exposure Raman spectrum of 24:47:29  $\text{D}_2$ : $\text{HD}$ : $\text{H}_2$  at 1atm, static cell, 100mW laser power measured at Swansea with direct imaging. The spectra have been normalised to the first  $\text{D}_2$   $\text{S}_0$ -branch line according to the respective  $\text{D}_2$  content and offset for clarity. The insets show the  $\text{D}_2$  vibration-rotation branches for each spectrum.

### 6.2.5 Invariance of system performance under high / low flow conditions

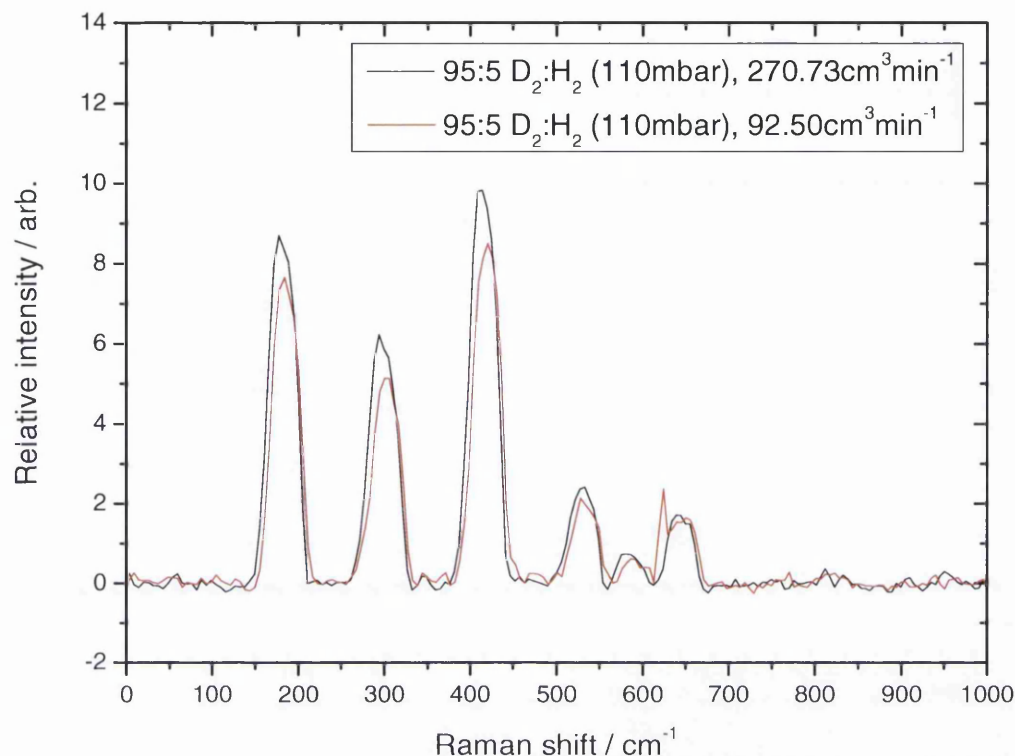
The TILO mock-up has provision for circulating the gas through the mock-up WGTS source tube in two modes, namely low flow and high flow. In the low flow mode, the pressure of the buffer vessels BD001 and BD101 are actively stabilised, and the gas is passed through a 4mm inner diameter pipe (HV111) into the source tube (BD102). In this mode, the pressure of the gas in the buffer vessels (and hence the circulating gas at the location of the LARA cell bypass) can be precisely defined ( $\pm 0.005\text{mbar}$ ), but the flow rate will vary (by as much as  $\pm 1\text{cm}^3\text{min}^{-1}$ ) as the active stabilisation seeks to keep the buffer vessels at their design pressures. In high-flow mode, the gas is passed through a 7.1mm inner diameter pipe (HV112)<sup>‡</sup>, and the active pressure stabilisation of the buffer vessels is deactivated. In this mode, the flow rate is well defined ( $\pm 0.005\text{cm}^3\text{min}^{-1}$ ) but the pressures at the buffer vessels (and hence at the LARA cell bypass) becomes less certain.

From Figure 6.11 one can see that the relative intensities of the 50:50 D<sub>2</sub>:H<sub>2</sub> trace, which was recorded at a high ( $270.47\text{cm}^3\text{min}^{-1}$ ) flow rate compare well with those of the 95:5 D<sub>2</sub>:H<sub>2</sub> and 75:25 traces, which were recorded at low (92.5 and  $101.5\text{cm}^3\text{min}^{-1}$ , respectively) flow rates, and to 24:47:29 D<sub>2</sub>:HD:H<sub>2</sub> trace, measured in a static cell (zero flow rate).

In Figure 6.12 a direct comparison is made between two  $1\times 1000\text{s}$  single exposure Raman spectrum of the 95:5 D<sub>2</sub>:H<sub>2</sub> sample, for high and low flow regimes. The two traces are practically identical. The slight difference between the two traces is probably due to the difference in the Spec-10 CCD detector temperature from one measurement to the next. Due to the poor thermal contact of the Peltier stack and the relatively high ambient temperature of the laboratory, the temperature of the CCD chip tended to increase the longer the camera was run. In this case, the measurements are sequential, but the high flow trace was recorded first. For all practical purposes, one can assume the flow rate to have no measurable effect on system performance.

---

<sup>‡</sup> The thin (low flow rate) line HV111 is the line that KATRIN will use to circulate the tritium gas. The thick line HV112 is a krypton line, and has been employed here solely to test the invariance of the system performance under varying flow rate conditions.



**Figure 6.12**  $1 \times 1000$ s single exposure Raman spectrum of 95:5  $D_2:H_2$  (110mbar) gas mixtures for high (black) and low (red) flow rates through the TILO system, with an excitation laser power of 1W. The lines obtained in the high flow rate measurements are slightly higher due to the lower temperature of the CCD chip ( $-62.75^\circ\text{C}$ ) compared with when the low flow rate measurements were made (at  $-61.5^\circ\text{C}$ ). The temperatures quoted here are averages over each  $1 \times 1000$ s run.

### 6.2.6 Missing contributions from the HD isotopomer

One can see quite clearly in Figure 6.11 that there are no HD lines in the spectra recorded at TILO. Note that for an isotopic gas mixture in thermodynamic equilibrium, one would expect that a mixture of  $H_2$  and  $D_2$  generates a quantity of HD based on the stoichiometric rate equation



If one neglects the difference in the binding energies of the different isotopomers, one would expect the equilibrium constant,  $K_C$ , to be given by

$$K_C = \frac{[\text{HD}]_e^2}{[\text{D}_2]_e \cdot [\text{H}_2]_e} = 4, \quad (6.2)$$

where the subscript  $e$  denotes the thermal equilibrium limit of the particle concentration. More correctly, the different binding energies have to be taken into account. With these, one arrives at the theoretical prediction that  $K_C = 3.28$ . Experimentally, one finds that  $K_C = 3.3$  at 25°C (Levine (2001)).

Starting from arbitrary concentrations for  $\text{H}_2$  and  $\text{D}_2$ , i.e.  $[\text{H}_2]_0 \equiv a$  and  $[\text{D}_2]_0 \equiv b$ , one finds for the gas mixture approaching thermodynamic equilibrium that

$$K_C = \frac{[\text{HD}]_e^2}{[\text{D}_2]_e \cdot [\text{H}_2]_e} = \frac{[2c]^2}{[a-c] \cdot [b-c]} = 3.3. \quad (6.3)$$

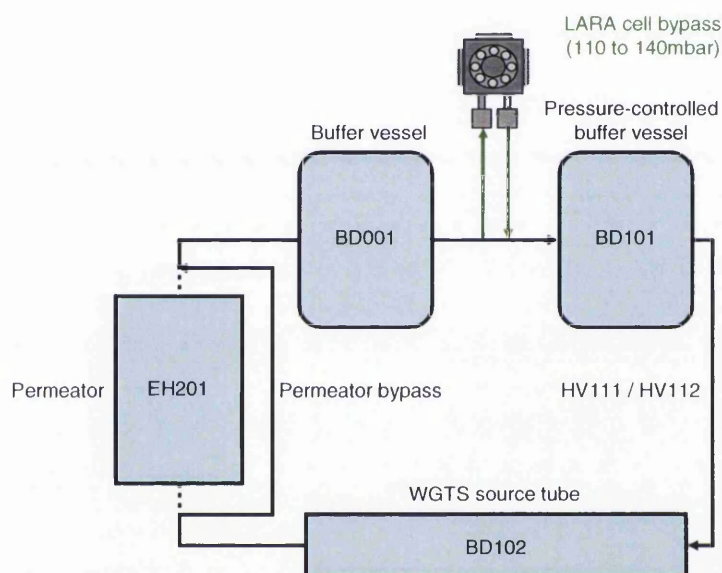
Thus, when this quadratic equation in  $c$  is solved, one obtains the values summarised in Table 6.3 below. These values suggest that substantial quantities of HD should be present in the gas mixtures, sufficiently high to be measurable.

**Table 6.3** Concentrations of hydrogen isotopomer mixtures used in the October 2006 measurements in thermodynamic equilibrium.

Component	Mixture / %		
	D <sub>2</sub> :H <sub>2</sub> / 95:5	D <sub>2</sub> :H <sub>2</sub> / 75:25	D <sub>2</sub> :H <sub>2</sub> / 50:50
D <sub>2</sub>	90.3	56.9	26
HD	9.4	36.2	48
H <sub>2</sub>	0.3	6.9	26

Recalling Figure 5.19, the assumption was made at the time of the measurements that the gas mixture passes through a permeator (EH201), in which the diffusion process atomises the molecules and then allows them to recombine. Hence, one would expect

thermodynamic equilibrium of the circulating gas mixture, once the whole gas volume has been processed in this way. Taking into account the flow rates used in the experiments at TILO (between  $\sim 100$  and  $\sim 270 \text{ cm}^3 \text{ min}^{-1}$ ), and the  $\sim 15 \text{ min}$  allowed for the gases in the two buffer vessels to mix before commencing measurements, the gas mixture should have been circulated long enough to provide complete exchange through the permeator. However, on checking the actual circulation path, it was found that the permeator had in fact been bypassed during our measurements, as shown in Figure 6.13.



**Figure 6.13** Gas circulation path for the Raman measurements at TILO in October 2006. The permeator unit (EH201) was bypassed for these experiments, and so isotopic exchange reactions occurred only at a very slow rate.

Without the permeator in the circulation path, one expects that the isotopic exchange reactions are too slow to have produced measurable quantities of HD in the  $\sim 15 \text{ min}$  allowed for before commencing measurements, since thermodynamic equilibrium is reached in this case only by collisional exchange reactions in the low-pressure gas. The time it takes to reach equilibrium in the TILO gas mixtures,  $\tau$ , can be calculated from the rate constants  $k_1$  and  $k_{-1}$ , which govern the exchange reaction



Taking  $k_1$  and  $k_{-1}$  together with the number densities,  $a$ ,  $b$ , and  $c$ , of  $\text{H}_2$ ,  $\text{D}_2$ , and  $\text{HD}$ , respectively, we can write

$$\tau = \frac{1}{k_1 \cdot (a) \cdot (b) + k_{-1} \cdot c} . \quad (6.5)$$

Due to the low pressure of the gases flowing through the TILO circulation path,  $a$  and  $b$  are much smaller than at atmospheric pressures. The number density  $c$  is initially zero and will increase over time. One would expect that the time to reach thermodynamic equilibrium,  $\tau$ , to be much larger than the ~15min allowed for the gases to mix in the loop. However, estimation of  $\tau$  requires accurate literature values for rates of the various exchange reactions in hydrogen isotopomer mixtures. This has not yet been followed up at the time of writing, but it will be a high priority task following the submission of this thesis.

Although the inclusion of the permeator into the circulation path would have allowed unequivocal confirmation of the validity of Raman spectroscopy for in-line monitoring of isotopic purity in at TILO, one very interesting and extremely valuable conclusion can be drawn from the results described in this section. It is clear that even over the individual measurement periods of order 1000s, no noticeable exchange reactions are observed. Therefore, it becomes a reasonable assumption that the isotopomeric composition measured between the two buffer vessels will be representative of that which is injected into the source tube, since the flow time from the measurement point to the source tube inlet is significantly shorter (of the order of a few seconds) than the measurement times used in these experiments.

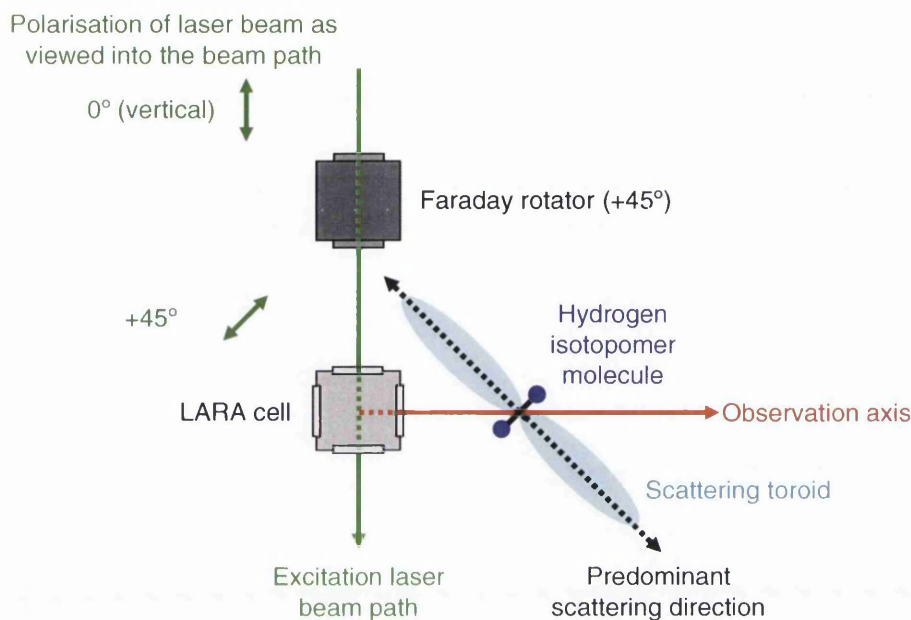
### 6.2.7 'Anomalously' low $Q_1$ -branch intensities

The spectra measured at TILO have a particularly striking characteristic in that the  $Q_1$ -branches of  $H_2$  and  $D_2$  are substantially lower than one would expect from simple theoretical predications, or from comparison with hydrogen isotopomer spectra previously measured at TLK or Swansea. The  $S_0$ -,  $O_1$ -, and  $S_1$ -branches, however, appear to be unaffected. As discussed in Chapter 3, the polarisation of the incident light can have a profound effect on the intensity of Raman scattering, and close scrutiny reveals that it affects individual branches differently.

As was shown in Figure 6.8, the Faraday isolator used in the older ASER experiments at TLK (Taylor et al. (2001)) was retained in the setup at TILO, and it is the retention of this component that has caused the 'anomalously' low intensities of the  $Q_1$ -branches that are observed in all experiments performed in October 2006. The principle of the Faraday isolator was described in Section 4.6.3. The key property of this component is that the polarisation direction of the laser beam leaving the isolator is rotated by  $45^\circ$  to the original vertical orientation. The polarisation direction at the position of the scattering volume will therefore also be oriented at  $45^\circ$  to the vertical. Although this  $45^\circ$  tilt does not affect the total intensity of the Raman scattered light, it has a profound effect on the scattered light intensity distribution observed by the fibre, which is oriented horizontally and at  $90^\circ$  to the direction of the laser beam propagation.

As shown in Figure 6.14, both the Rayleigh and Raman scattered light components are predominantly scattered into an axially-symmetric toroid which is oriented at  $90^\circ$  to the bond axis of the hydrogen isotopomer molecule. This means that the majority of the  $\pi$ -component of the scattered light will not enter the collection optics, and hence will not be recorded.





**Figure 6.14** Effect of the 45° tilt to the initially vertically polarised light on the strength of the observed Raman scattering. The orientation of the  $\pi$ -scattering toroid means that the majority of the scattered light does not enter the collection optics and is therefore not observed.

If the Faraday isolator had been removed from the beam path, the laser beam passing through the LARA cell would have been vertically polarised, and the resulting spectra would have been in agreement with theoretical predictions for the  $I(\pi/2; \perp^s, \perp^i)$  regime. The low intensity of the  $Q_1$ -branches in the spectra measured at TILO with the isolator in place, however, more closely resemble the intensity distribution for the  $I(\pi/2; \parallel^s, \perp^i)$  regime. Table 6.4 summarises the value of the line strength function  $\Phi(a^2, \gamma^2, \theta)$  for these two polarisation regimes.

**Table 6.4** The values of the line strength function  $\Phi(a^2, \gamma^2, \theta)$  for the linear polarisation regimes  $I(\pi/2; \perp^s, \perp^i)$ ,  $I(\pi/2; \parallel^s, \perp^i)$ , together with the depolarisation ratio  $\rho(\pi/2; \perp^i)$  for diatomic molecules, based on isotropic averages of squares of transition polarisability tensor components with  $\Lambda = 0$  and  $S = 0$  for rotational and vibration-rotation transitions. Normal Stokes Raman branches are shown. As has been standardised throughout this work,  $J = J' = J''$ . Adapted from Long (2002).

Type of scattering	Branch	Selection rules		$\Phi(a^2, \gamma^2, \theta)$		$\rho(\pi/2; \perp^i)$
		$\Delta v$	$\Delta J$	$I(\pi/2; \perp^s, \perp^i)$	$I(\pi/2; \parallel^s, \perp^i)$	
Rayleigh	Q <sub>0</sub>	0	0	$(a)_0^2 + \frac{4}{45} b_{J,J}^{(2)}(\gamma)_0^2$	$\frac{1}{15} b_{J,J}^{(2)}(\gamma)_0^2$	$\frac{3b_{J,J}^{(2)}(\gamma)_0^2}{45(a)_0^2 + 4b_{J,J}^{(2)}(\gamma)_0^2}$
Raman (pure rotation)	S <sub>0</sub>	0	+2	$\frac{4}{45} b_{J+2,J}^{(2)}(\gamma)_0^2$	$\frac{1}{15} b_{J+2,J}^{(2)}(\gamma)_0^2$	$\frac{3}{4}$
Raman (vibration-rotation)	O <sub>1</sub>	+1	-2	$\frac{4}{45} b_{J-2,J}^{(2)}(\gamma')^2$	$\frac{1}{15} b_{J-2,J}^{(2)}(\gamma')^2$	$\frac{3}{4}$
	Q <sub>1</sub>	+1	0	$(a')^2 + \frac{4}{45} b_{J,J}^{(2)}(\gamma')^2$	$\frac{1}{15} b_{J,J}^{(2)}(\gamma')^2$	$\frac{3b_{J,J}^{(2)}(\gamma')^2}{45(a')^2 + 4b_{J,J}^{(2)}(\gamma')^2}$
	S <sub>1</sub>	+1	+2	$\frac{4}{45} b_{J+2,J}^{(2)}(\gamma')^2$	$\frac{1}{15} b_{J+2,J}^{(2)}(\gamma')^2$	$\frac{3}{4}$

$$\text{Note: } b_{J,J}^{(2)} = \frac{J(J+1)}{(2J-1)(2J+3)}, \quad b_{J+2,J}^{(2)} = \frac{3(J+1)(J+2)}{2(2J+1)(2J+3)}, \quad b_{J-2,J}^{(2)} = \frac{3J(J-1)}{2(2J-1)(2J+1)}$$

From the formulae in Table 6.4 one can see that the main difference in the value of  $\Phi(a^2, \gamma^2, \theta)$  for the Q<sub>0</sub>- and Q<sub>1</sub>-branches between the  $I(\pi/2; \perp^s, \perp^i)$  and  $I(\pi/2; \parallel^s, \perp^i)$  polarisation regimes is due to the presence (or absence) of the terms  $(a)_0^2$  (in the case of Rayleigh scattering) and  $(a')^2$  (in the case of Raman scattering). In the  $I(\pi/2; \parallel^s, \perp^i)$  regime, where these factors are omitted, the Q<sub>0</sub>- and Q<sub>1</sub>-branches are less intense than for the  $I(\pi/2; \perp^s, \perp^i)$  regime by a factor of the depolarisation ratio  $\rho(\pi/2; \perp^i)$ . In the case of the Q<sub>0</sub>- and Q<sub>1</sub>-branches, the terms  $(a)_0^2$  and  $(a')^2$  tend to dominate the expression for  $\Phi(a^2, \gamma^2, \theta)$  as  $J$  increases.

The 45° tilted polarisation case encountered at TILO represents an intermediate between these two extremes. Unfortunately, one cannot simply follow the standard textbook

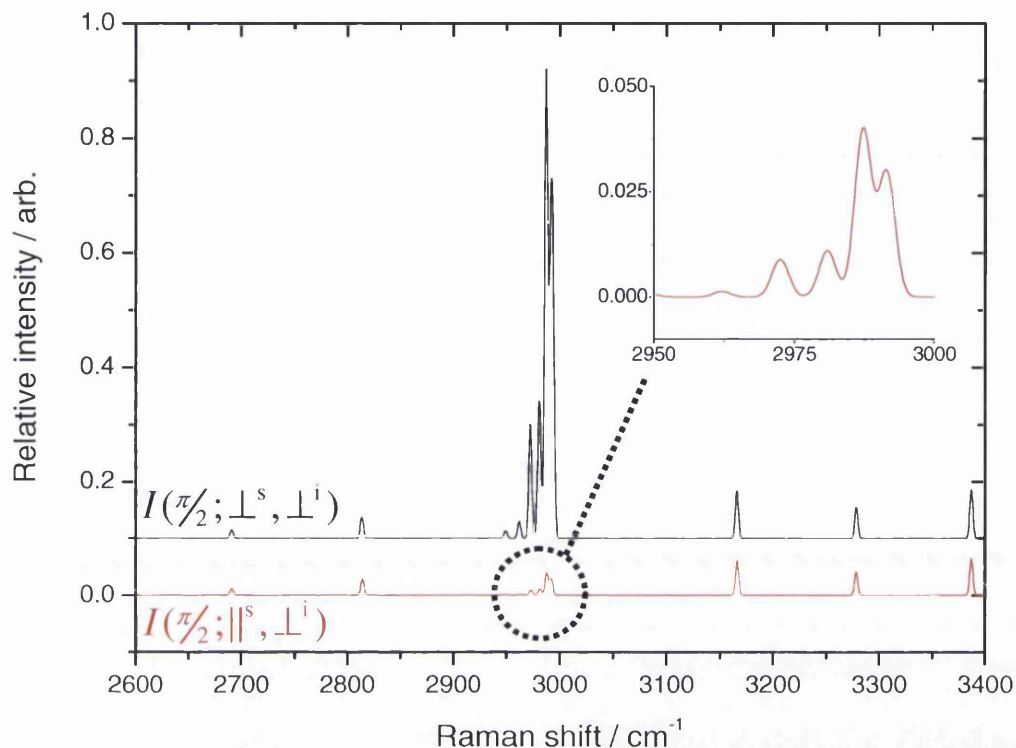
approximation of applying a simple  $\cos^2$  interpolation between the two polarisation regimes of a dielectric medium. In our case since the spatially inhomogeneous molecular polarisability of the hydrogen isotopomer molecules results in a higher-order  $\cos^n$  dependence, and consequently a larger angular asymmetry, as exemplified by, e.g. Garret (2004).

In spectra observed prior to the TILO measurements, the  $I(\pi/2; \perp^s, \perp^i)$  regime has been the norm<sup>§</sup>. In this case, Q<sub>1</sub>-branch lines of a given isotopomer have been observed to have comparable intensity to the corresponding S<sub>0</sub>-branch lines. These measurements confirm that the  $(a')^2$  term dominates the expression for  $\Phi(a^2, \gamma^2, \theta)$  and is therefore relatively large. In the  $I(\pi/2; \parallel^s, \perp^i)$  regime where this term is absent, one would thus expect a dramatic reduction in the intensity of the Q<sub>1</sub>-branch. All other lines would be correspondingly lower at 75% of their  $I(\pi/2; \perp^s, \perp^i)$  regime intensity.

Note that in the Raman spectra observed at TILO, the relative intensities of the spectral lines have been close to the  $I(\pi/2; \parallel^s, \perp^i)$  regime intensity pattern. Figure 6.15 shows the effect on the vibration-rotation Raman spectrum of D<sub>2</sub> in a simulation performed by *SpecGen* (see Chapter 3 and Appendix A1); these are used in the comparison with the experimental data.

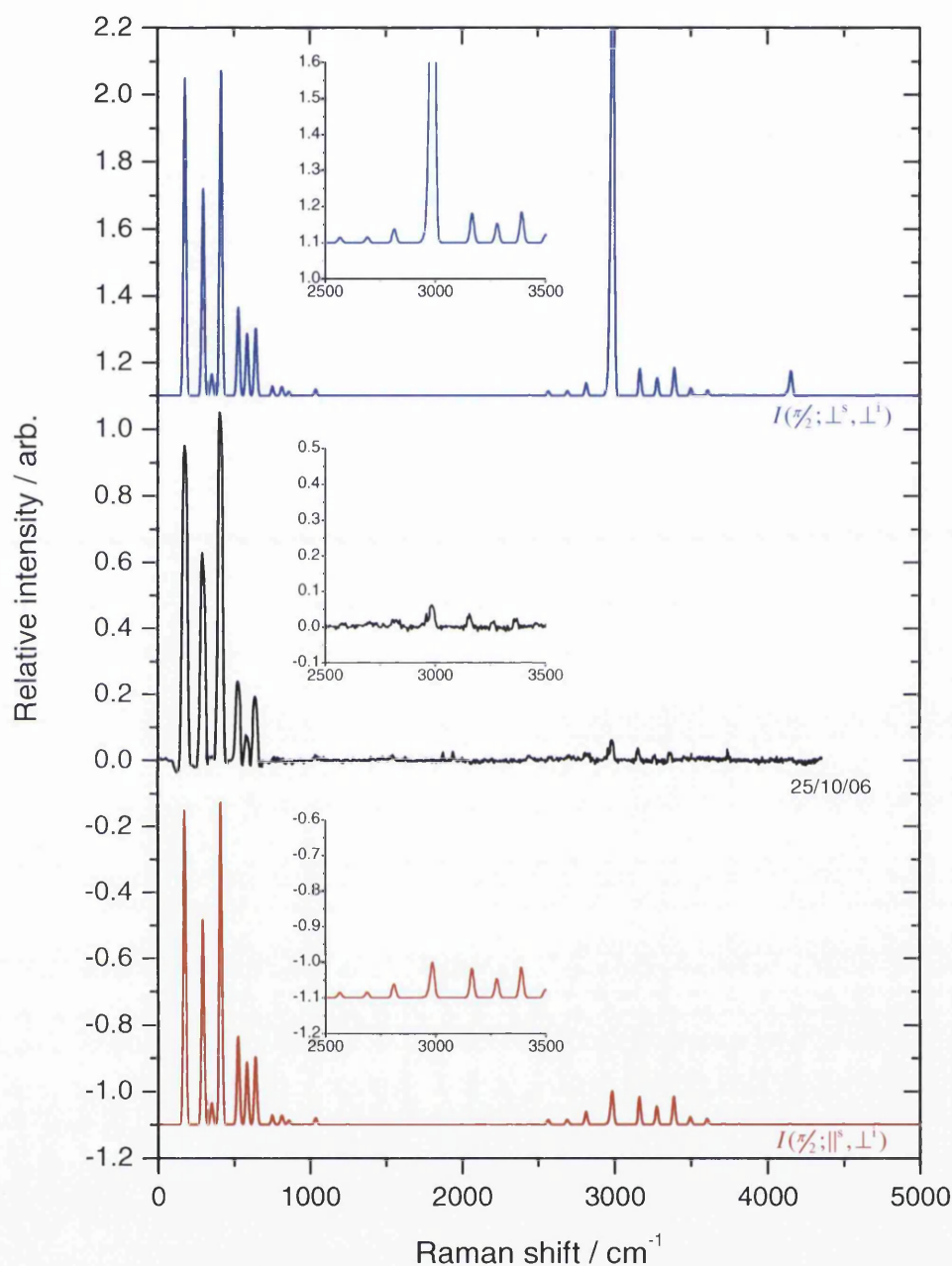
---

<sup>§</sup> Note that the polarisation regime is a function only of the observation geometry (i.e. the angle between excitation beam path and the collection axis), and is not normally affected by the imaging method. In all experiments performed for this work, the laser beam has been vertically polarised and so the intensity pattern of the scattered light has been predominantly of the  $I(\pi/2; \perp^s, \perp^i)$  form. Effects of the collection method on the polarisation of the scattered light will only manifest themselves in the difference in the polarisation response of the diffraction grating in the analysing spectrometer.

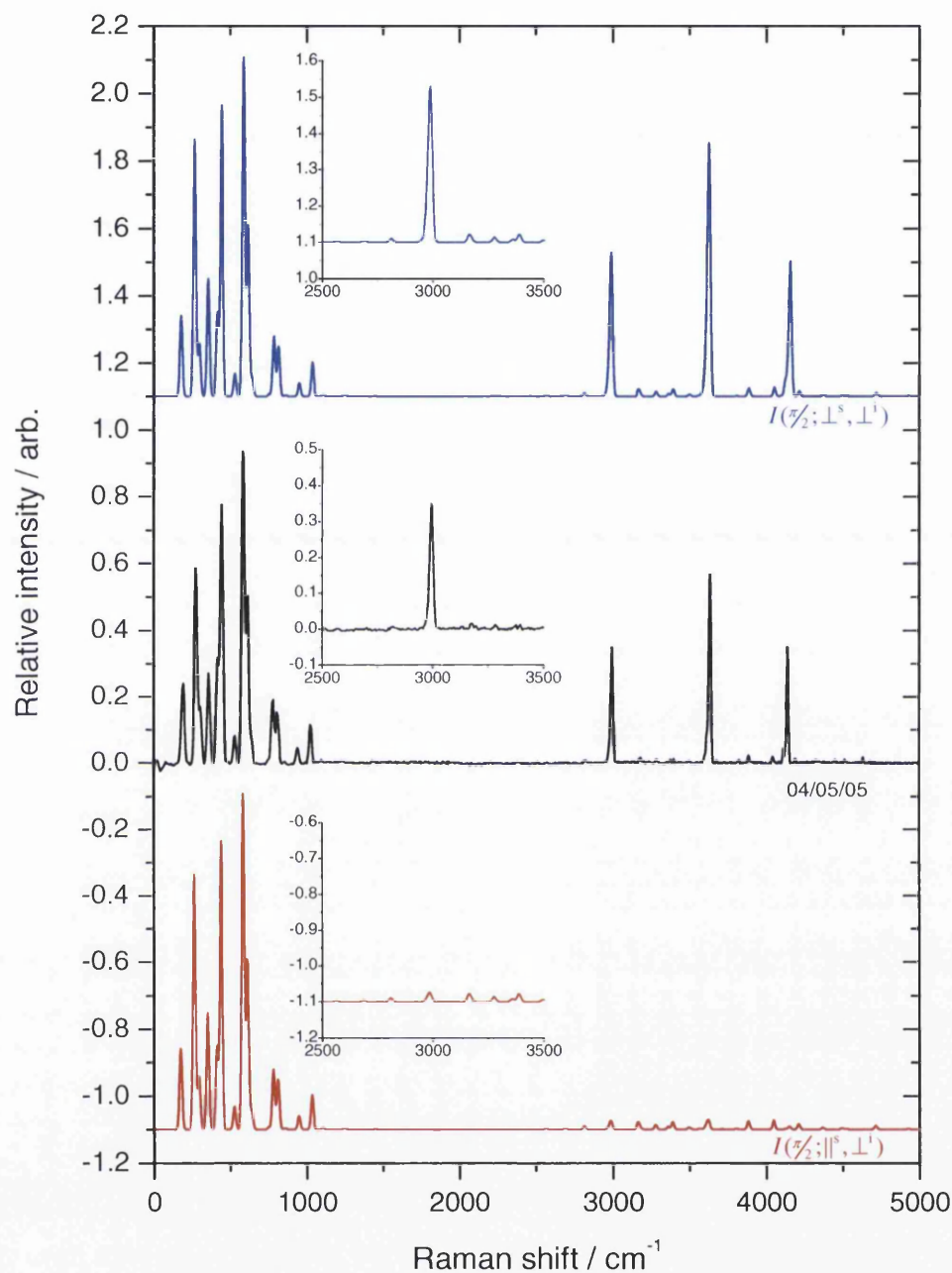


**Figure 6.15** Simulated vibration-rotation Stokes Raman spectrum of  $D_2$  in the  $I(\pi/2; \perp^s, \perp^i)$  (top, black) and  $I(\pi/2; \parallel^s, \perp^i)$  (bottom, red) polarisation regimes. The  $Q_1$ -branch intensity is much reduced in the latter case. The intensity of the  $O_1$ - and  $S_1$ -branches in the  $I(\pi/2; \parallel^s, \perp^i)$  regime are 75% that of those in the  $I(\pi/2; \perp^s, \perp^i)$  regime. Simulation performed by *SpecGen* using an estimate for the tensor invariant  $(a')^2 \cong 5.84$  (see Section 3.4.1). Both spectra are normalised to the strongest  $S_0$ -branch line and are offset for clarity.

In Figure 6.16, the Raman spectrum of the 95:5  $D_2:H_2$  mixture recorded during the TILO measurement campaign is compared with theoretical predictions for the two polarisation regimes. The same procedure has been carried out for the 24:47:29  $D_2:HD:H_2$  as previously measured at Swansea in Figure 6.17. For brevity, only the 95:5  $D_2:H_2$  and 24:47:29  $D_2:HD:H_2$  compositions are considered here, but the observations and conclusions that are made from this example investigation hold for the other compositions measured (and presumably would hold for arbitrary compositions).



**Figure 6.16** Comparison of the Raman spectrum of a 95:5 mixture of  $D_2:H_2$  measured at TILO in October 2006 (middle, black) with theoretical predictions for the  $I(\pi/2; \perp^s, \perp^1)$  (top, blue) and  $I(\pi/2; \parallel^s, \perp^1)$  (bottom, red) polarisation regimes, showing the vibration-rotation region of the spectra (insets). The measured spectrum in this case closely resembles the  $I(\pi/2; \parallel^s, \perp^1)$  regime simulation due to the inclusion of a Faraday isolator in the excitation laser beam path. Simulations performed by *SpecGen*.



**Figure 6.17** Comparison of the Raman spectrum of a 24:47:29 mixture of D<sub>2</sub>:HD:H<sub>2</sub> measured at Swansea in May 2005 (middle, black) with theoretical predictions for the  $I(\pi/2; \perp^s, \perp^i)$  (top, blue) and  $I(\pi/2; \parallel^s, \perp^i)$  (bottom, red) polarisation regimes, showing the vibration-rotation region of the spectra (insets). The measured spectrum in this case closely resembles the  $I(\pi/2; \perp^s, \perp^i)$  regime simulation due to the vertical polarisation of the excitation laser beam and 90° collection geometry. Simulations performed by *SpecGen*.

As can be readily seen in Figure 6.17, the Raman spectrum of the 24:47:29 D<sub>2</sub>:HD:H<sub>2</sub> cell agrees well with the simulation for the expected  $I(\pi/2; \perp^s, \perp^i)$  regime intensity pattern. The relative intensities of the lines within each branch of the measured spectrum in particular mimic the simulated spectrum. There is a slight discrepancy between simulated and measured spectra in the relative intensities of the pure rotational S<sub>0</sub>- and vibration-rotation S<sub>1</sub>-branches. This is to be expected, however, since the dependency of the diffraction grating and detector efficiencies on wavelength is currently not taken into account in either the post-acquisition data processing stages or in the *SpecGen* simulation code. The difference in signal efficiency between the wavelengths at which the S<sub>0</sub>- and S<sub>1</sub>- branches are observed is roughly 20-25%, which agrees with the observed discrepancy.

In the case of the 95:5 D<sub>2</sub>:H<sub>2</sub> spectra in Figure 6.16 the above observations still hold, only here the measured data agrees more closely with the  $I(\pi/2; \parallel^s, \perp^i)$  regime simulations. In the measured spectrum, the Q<sub>1</sub>-branch line is stronger relative to the O<sub>1</sub>- and S<sub>1</sub>-branch lines than for the simulation, but this is to be expected since the polarisation of the incident laser beam is at 45° to the vertical and not at 90° as is the case for the simulated data in the  $I(\pi/2; \parallel^s, \perp^i)$  regime. The fact that the intensity pattern is very close to the  $I(\pi/2; \parallel^s, \perp^i)$  limiting case confirms the assertion previously made that the directionality of the scattering process, for the  $\pi$ -component (associated with the  $(a')^2$  term), is strongly asymmetric.

A note should be made here regarding the Raman spectra recorded by Taylor et al. (2001) in whose experimental setup a Faraday isolator was necessarily incorporated. In their spectra, the recorded intensity distribution is much closer to the  $I(\pi/2; \perp^s, \perp^i)$  regime, as was the case for the majority of the spectra measured in this thesis prior to the TILO measurements. In their setup, however, a fortuitous arrangement in the beam steering geometry (the steering mirror is positioned below the LARA cell and oriented at 45° to the vertical which directs the laser beam out of the horizontal plane and into the vertical) partially corrects for the 45° shift applied by the Faraday isolator (see Figure 5.1). Had the ASER unit been oriented horizontally and the collection optics arranged as for the TILO measurements, the intensity pattern would have been the same – i.e. highly suppressed Q<sub>1</sub>-branches and a significantly lower apparent measurement sensitivity.

A final note should be made here regarding a possible different approach to analysing these effects. Since a linearly polarised beam of  $45^\circ$  orientation can be represented by a suitable superposition of counter-rotating co-propagating circularly polarised components, one can use the values for  $\Phi(a^2, \gamma^2, \theta)$  that are stated in Section 3.3.4 for the circularly polarised regimes  $I(0; R^s, R^i) = I(0; L^s, L^i)$  and  $I(0; L^s, R^i) = I(0; R^s, L^i)$ . Although these are  $180^\circ$  geometry cases, the results are broadly in line with those for the linearly polarised regimes, since the  $I(\pi/2; \perp^s, \perp^i)$  and  $I(0; R^s, R^i) = I(0; L^s, L^i)$  have quite similar intensity patterns. The same holds for the  $I(\pi/2; \parallel^s, \perp^i)$  and  $I(0; L^s, R^i) = I(0; R^s, L^i)$  regimes.

### 6.3 Summary

Had the Spec-10 detector been working to specification in October 2006, it is likely that the measured spectra would have unequivocally demonstrated the viability of the fibre-coupled HTS/Spec-10 system for in-line laser Raman monitoring of the tritium gas purity for the KATRIN experiment. Nevertheless, despite the shortcomings in the data associated with the imperfect performance of the Spec-10 detector, these first tests of the system in a realistic in-line environment have proven that with fully functional equipment the specifications for the laser Raman monitoring of the gas flow injected into the WGTS will be comfortably met. Although full systematic investigation of all operating parameters could not be performed in the October 2006 measurements, a number of very valuable conclusions can be drawn from the data that it was possible to obtain.

- (i) The Raman spectra obtained from the small range of  $D_2:H_2$  gas mixtures have shown that Raman signal strengths scale linearly with respect to the excitation laser power over the range of powers investigated (1 to 4W), which is in line with theoretical calculations and with direct imaging experimental results (see Figure 5.9).
- (ii) The October 2006 measurements were made with the gas flow bypassing the permeator, which will be a feature of the KATRIN inner loop. While this may be judged as not an ideal arrangement for the purposes of predicting the system performance in the



final implementation of the KATRIN inner loop, the omission of the permeator from the gas loop provided an ideal – albeit accidental – proof that the isotopic gas composition measured at the Raman monitoring location (between the buffer vessels BD001 and BD101) should accurately reflect the composition of the gas injected into the WGTS. This can be deduced from the fact that under the 110 to 140mbar pressure range conditions at the location of the LARA cell no discernable chemical exchange reactions of the form  $H_2 + D_2 \rightleftharpoons 2HD$  were observed over the duration of a measurement series (~1.5hr) for each gas composition.

(iii) The inclusion of the Faraday isolator into the beam path reduced the overall observed Raman intensity by 25% in the case of the  $S_0$ -,  $O_1$ -, and  $S_1$ -branches, and introduced near-full collapse of the  $Q_1$ -branch intensity. Since the role of the Faraday isolator was initially overlooked, the reduction in system intensity and the suppression of the  $Q_1$ -branches in particular\*\* was a perplexing and worrying observation. This result is now understood and has been modelled theoretically.

Note that in order to make full use of the  $Q_1$ -branches, the Faraday isolator will be removed from the beam path in future experiments. Although necessarily included in the ASER setup of Taylor et al. (2001) to prevent back-reflected light from the ASER from re-entering the laser cavity, the Faraday isolator can be safely removed from the beam path in our case – the small amount of radiation back-reflected from the 532nm AR-coated focussing lens (<0.25%) can be directed to an off-axis beam dump by slightly tilting the lens away from the beam axis. This procedure has been tested at Swansea in previous experiments with no adverse effects to the overall alignment of the system.

(iv) The thermal noise background of the Spec-10 detector was found to be at least a factor of 10 worse in October 2006 than at the time of the comparative review experiments described in Chapter 5, and there is evidence to suggest that the thermal contact between the Peltier stack and the CCD array had begun to deteriorate by May 2006 at the latest.

---

\*\* Recall that the  $Q_1$ -branches had been decided upon over the  $S_0$ -branches as the best choice for isotopomeric composition monitoring.

The measurements performed in October 2006 suggest that the minimum measurable isotopomer concentration variation under the prevailing noise-limited conditions was approximately  $\pm 1\%$  (i.e. a maximum S/N of  $\sim 100$ ). Clearly, with the detector working to specification, the current system configuration can meet the original KATRIN design report specifications of  $\pm 0.2\%$  (Drexlin, Weinheimer, et al. (2005)), and closely approach the ‘gold standard’ of  $\pm 0.1\%$  (i.e. a S/N of 1000) at an excitation laser power of  $\sim 3\text{W}$ .

(v) The planned improvements to the monitoring setup, namely the removal of the Faraday rotator and the upgrade of the filter faceplate z-axis adjustment to a lockable micrometer-drive system will, possibly in combination with a higher operating laser power (up to 5W is currently available), will likely result in the  $\pm 0.1\%$  target being surpassed by a considerable margin. The acquisition time of 1000s can therefore likely be reduced to allow for more frequent control measurements, and therefore a faster response of the monitoring system.

## ***6.4 References for Chapter Six***

### *6.4.1 Cited references (books and papers)*

Drexlin G., Weinheimer C., et al. (2005). KATRIN Design Report 2004. Wissenschaftliche Berichte FZKA 7090, ISSN 0947-8620

Garret S.H., Wasey J.A.E., Barnes W.L. (2004). “Determining the orientation of the emissive dipole moment associated with dye molecules in microcavity structures” Journal of Modern Optics **51**(15): 2287-2295

Hecht, E. (2002). Optics 4<sup>th</sup> Edition. Reading (U.S.A), Addison-Wesley.

Levine, I.N.(2001). Physical Chemistry 5<sup>th</sup> Edition. New York (U.S.A.), McGraw Hill Higher Education.

Lewis R.J. and Telle H.H. (2006). “Hydrogen Isotopomer Raman Spectroscopy for KATRIN – Raman test measurements at TILO (Preliminary Report).” KATRIN BSCW (Internal) 10-ME-3201-0.

Long, D. A. (2002). The Raman Effect - A Unified Treatment of the Theory of Raman Scattering by Molecules. Chichester (U.K.), John Wiley & Sons, Ltd.

Taylor D.J., Glugla M., Penzhorn R.-D. (2001). “Enhanced Raman sensitivity using an actively stabilized external resonator.” Review of Scientific Instruments 72(4): 1970-1976.

#### 6.4.2 *Cited internet resources*

Stern, D. (2006). Drawing of Glovebox HVT-TLK R 195 KATRIN BSCW (Internal) 060131\_DS\_Glovebox\_1.JPG

Wyant, J.C. (2007). “Fresnel Diffraction Pattern for Circular Aperture” webMathematica applet, <http://wyant.optics.arizona.edu/fresnelZones/fresnelZones.htm>

## CHAPTER SEVEN

### SUMMARY AND OUTLOOK

#### *7.1 Summary*

Since detailed summaries have been given at the end of each chapter, only the major themes covered in this thesis are summarised in this section. The progress made towards developing a laser Raman monitoring system for the KATRIN experiment is broadly divided into the areas of hardware and software development.

##### *7.1.1 Summary of hardware development*

It has been demonstrated that measuring the Stokes Raman spectrum of hydrogen isotopomers is possible with the HTS/Spec-10 system even with an ultra-low power 10mW Nd:YAG laser module as the excitation source in a single-pass configuration. The HTS/Spec-10 system has been shown to be superior to the older TRIAX320/CCD2000 system previously used at TLK for measurement of hydrogen isotopomer Raman spectra in conjunction with an ASER signal enhancement cavity. It has also been shown that the HTS/Spec-10 system can be operated satisfactorily with direct, translational, and fibre-coupled imaging methods.

Estimates of system signal-to-noise ratios suggest that the target minimum specified system sensitivity of  $\pm 0.2\%$  with respect to changes in the isotopomeric composition of the WGTS tritium gas flow can be easily met, and that the 'gold standard' sensitivity level of  $\pm 0.1\%$  will likely not only be reached, but exceeded by a comfortable margin. The extra overhead in terms of system sensitivity and laser power (up to 5W compared to the 3W used in these experiments) will prove invaluable to the monitoring system in general due to the ability to reduce acquisition times and thus increase the number of control measurements that can be made in any given time interval.

The initial in-line tests of the fibre-coupled HTS/Spec-10 system at the TILO experiment in October 2006 have shown great promise. Had the Spec-10 detector been operating to specification at the time, it is probable that we could have unequivocally shown the performance of the system to be well above the level specified for the KATRIN experiment. Detector problems notwithstanding, the system has been proven to operate satisfactorily in a fibre-coupled configuration in-line at TILO, for realistic gas sample pressures, laser operating powers, and with acceptably short acquisition times. Further, the accidental bypass of the permeator has resulted in data which demonstrated that the composition of the gas mixture measured at the location of the LARA cell bypass can be relied upon to be representative of the composition injected into the source tube.

### 7.1.2 Summary of software development

The KATRIN experiment will operate under overall system control in a *LabVIEW* software environment. It has thus been an aim of our work to develop a corpus of *LabVIEW* software on which a master control application for the laser Raman monitoring system could be built. The software developed and described in this thesis has laid a solid foundation for the post-acquisition processing and data analysis stages of this planned application.

The simulation program *SpecGen* has become an invaluable tool for identifying spectral features in hydrogen isotopomer spectra, and was instrumental in identifying the role of the Faraday isolator in causing the initially perplexing suppressed Q<sub>1</sub>-branch intensities observed at TILO in October 2006.

The integrated cosmic ray removal and astigmatism correction routine *DCRR* has proven vitally important in optimising the quality of data recorded with the HTS/Spec-10 system at relatively long acquisition times (>1000s). *DCRR* has allowed clean spectra to be obtained from the binning of long-acquisition spectral images that would otherwise be dominated by noise caused by cosmic ray events, while the astigmatism correction segment of the routine yields significant improvements in observed linewidths, peak intensities and line positions.

## 7.2 Outlook

The Spec-10 detector is currently undergoing maintenance to replace the faulty Peltier stack that prevented full investigation of the operating performance of the fibre-coupled HTS/Spec-10 system in October 2006. It is planned to perform a second run of in-line experiments at TILO in March 2007 with the repaired detector operating at its ultra-low noise level specification. The repair of the detector, combined with the planned upgrade of the filter unit faceplate, to incorporate z-axis adjustment to eliminate errors in fibre ferrule / focal plane relative placement, and the removal of the Faraday isolator from the excitation laser beam path, will finally allow direct demonstration of the high performance of the fibre-coupled HTS/Spec-10 system in a realistic mock-up of the WGTS inner loop environment.

The next logical step following the test of a fully functional monitoring system at TILO will be to perform measurements at TLK with the tritiated isotopomers HT, DT, and T<sub>2</sub> flowing through either the TILO system or the WGTS inner loop itself. Since the inclusion of the tritiated isotopomers would necessitate the use of a secondary enclosure around the primary gas line, it is probable that the latter scenario is more likely. It is foreseen, however, that even if these measurements have to be made using the final WGTS inner loop system (TILO will be dismantled in 2007), there will be sufficient time between the inner loop being built and the switch-on of KATRIN to resolve any remaining issues with either the system operation or the mechanical considerations of accessing the LARA cell gas bypass.

A final note should be made here regarding an investigation of potentially vital importance that is to be performed in parallel with the general system development and testing, namely the determination of the values of the tensor invariants  $\langle a' \rangle^2$  for each of the hydrogen isotopomers by accurate measurement of the intensity pattern of their Raman spectra. An accurate evaluation of the tensor invariants would provide an invaluable insight into the structure of the derived polarisability tensor and greatly aid the experiments planned to measure the ortho / para ratio of the hydrogen isotopomers. The ortho / para ratio is a determining factor in the population of the even / odd rotational levels of the molecules in

the tritium gas flow. Since the intensity of a given Raman line is directly proportional to the population of the initial level of the corresponding transition, these shifts in the relative intensities of Raman lines within a spectral branch are in principle measurable.

In order to observe these effects, it will be necessary to utilise a higher-resolution spectrometer than the HTS in order to also resolve the individual lines of the vibration-rotation  $Q_1$ -branches. Since the Spec-10 and the filter unit incorporate standard mounting brackets, it is planned to simply switch the fibre and detector over to a suitable high-resolution spectrometer such as the *SpectraPro* SP500i available at Swansea. Since the ortho / para ratio of the tritium gas injected into the WGTS source tube is an important parameter in determining systematic uncertainties in the KATRIN experiment as a whole, it can be said that the laser Raman monitoring system is promising to contribute much more to KATRIN than was initially envisioned.

*Richard James Lewis*  
*Department of Physics*  
*Swansea University*



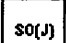

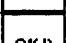

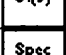
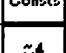
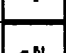

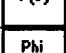
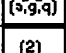
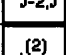
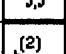
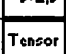
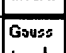
## APPENDIX A1

SPECGEN – A HYDROGEN ISOTOPOMER STOKES  
RAMAN SPECTRUM MODELLER

## (LABVIEW CODE)

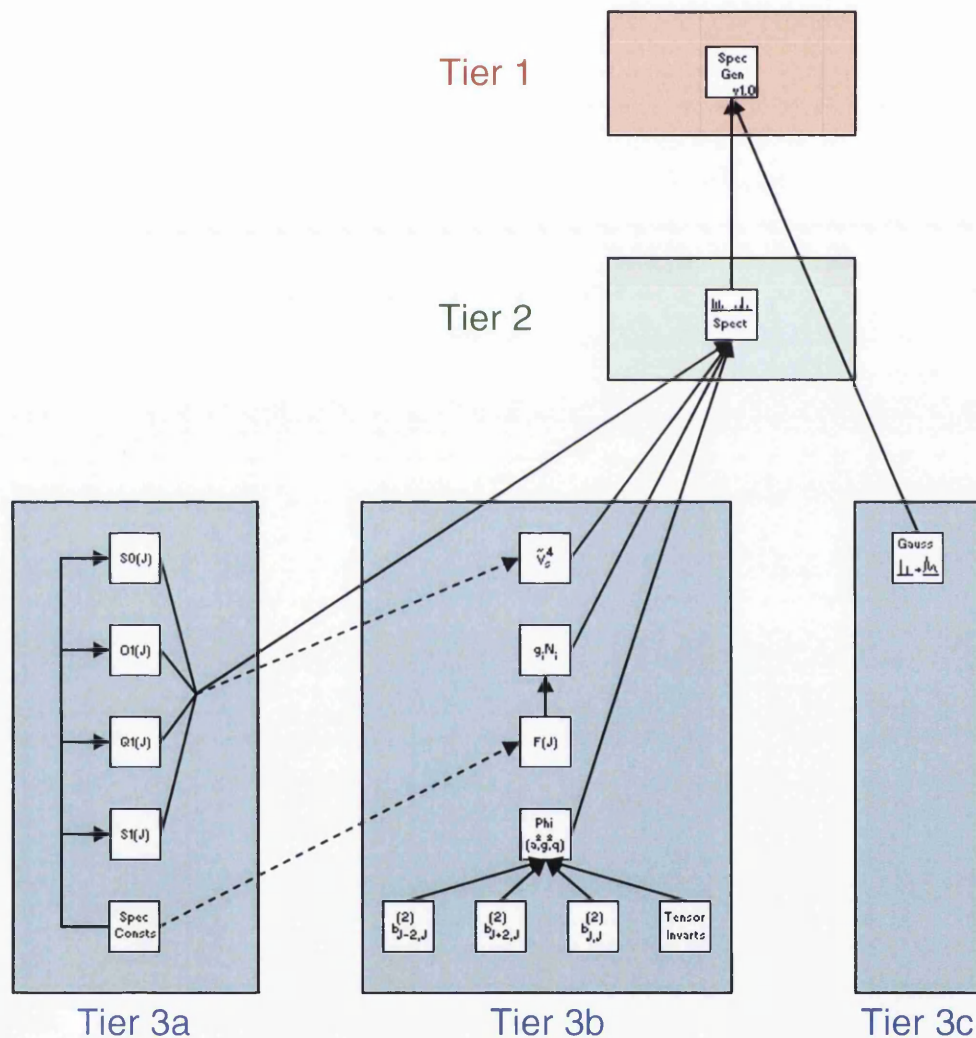
A1.1 *SpecGen Architecture*

*SpecGen* is a three-tier program consisting of a user interface (tier 1), a high-level subVI handler (tier 2), and a number of calculation- and simulation-specific subVIs (tier 3). The table below is a list of all VIs that form the current build (v1.0) of the *SpecGen* package.

VI	Icon	Tier	Purpose / calculates
SpecGen_Interface		1	User interface
SpecGen_SubVI_High_Raman_Spectrum		2	Tier 3 SubVI handling
SpecGen_SubVI_S0(J)		3a	S <sub>0</sub> -branch positions
SpecGen_SubVI_O1(J)		3a	O <sub>1</sub> -branch positions
SpecGen_SubVI_Q1(J)		3a	Q <sub>1</sub> -branch positions
SpecGen_SubVI_S1(J)		3a	S <sub>1</sub> -branch positions
SpecGen_SubVI_Spectroscopic_Constants		3a	$B_0, D_0, H_0, B_1, D_1, \tilde{\nu}_{vib}$
SpecGen_SubVI_vs^4		3b	$(\tilde{\nu}_s)^4$
SpecGen_SubVI_giNi		3b	$g_i N_i$
SpecGen_SubVI_F(J)		3b	$F(J)$
SpecGen_SubVI_Phi(a^2_g^2_q)		3b	$\Phi(a^2, \gamma^2, \theta)$
SpecGen_SubVI_b(2)J-2,J		3b	$b_{J-2,J}^{(2)}$
SpecGen_SubVI_b(2)J,J		3b	$b_{J,J}^{(2)}$
SpecGen_SubVI_b(2)J+2,J		3b	$b_{J+2,J}^{(2)}$
SpecGen_SubVI_Tensor_Invariants		3b	$(a)_0^2, (a')^2, (\gamma)_0^2, (\gamma')^2$
SpecGen_SubVI_Convolute_Gaussian		3c	Lineshape convolution



The hierarchy of *SpecGen* is shown in Figure A1.1. Note that with the exception of the tier 3c subVI *SpecGen\_SubVI\_Convolute\_Gaussian.vi* (handled by tier 1), all tier 3 subVIs are handled from tier 2. Direct dependencies (dependency sink connector to dependent source connector) are shown in solid lines, indirect dependencies (dependency sink connector to direct dependent block diagram node to indirect dependent source connector) are shown in dashed lines.




**Figure A1.1** *SpecGen* VI hierarchy.

With the exception of *SpecGen\_SubVI\_Convolute\_Gaussian.vi*, all tier 3 subVIs are handled by the tier 2 high-level subVI, *SpecGen\_SubVI\_High\_Raman\_Spectrum.vi*. Solid lines represent direct dependencies, dashed lines represent indirect (crosstalk) dependencies handled by the tier subVI.








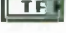












The *SpecGen* package is designed to calculate the first (ten) lines of each of the four normal Stokes Raman branches of interest in this thesis for a mixture of hydrogen isotopomers of a user-specified composition and temperature, and in any of the following four polarisation regimes for the exciting radiation relative to the observation direction:  $I(\pi/2; \perp^s, \perp^i)$ ,  $I(\pi/2; \parallel^s, \perp^i)$ ,  $I(0; R^s, R^i)$ , and  $I(0; L^s, R^i)$ . The wavelength of the exciting radiation is set by the user, although *SpecGen* can output data in wavenumber shift (wavelength-independent) if desired. The output format can either be in non-convoluted (“x,y”) format or convoluted with a Gaussian lineshape function. Support for Lorentzian and Voigt profiles are to be added in the next revision of the package. The reader is referred to Chapter 3 for details regarding the underlying theory of Raman scattering from hydrogen isotopomers.



### A1.2 Tier 1: *SpecGen* User Interface


The tier 1 VI *SpecGen\_Interface.vi* is the highest-level tier of the *SpecGen* package. Whereas all other VIs are dedicated calculation or simulation modules, the front panel *SpecGen\_Interface.vi* is where the user selects desired calculation and simulation parameters, can view the simulated data and export the data to an ASCII file.

VI filename	SpecGen_Interface.vi	
Icon		
Dependencies	N/A	
Dependents	SpecGen_SubVI_High_Raman_Spectrum.vi	

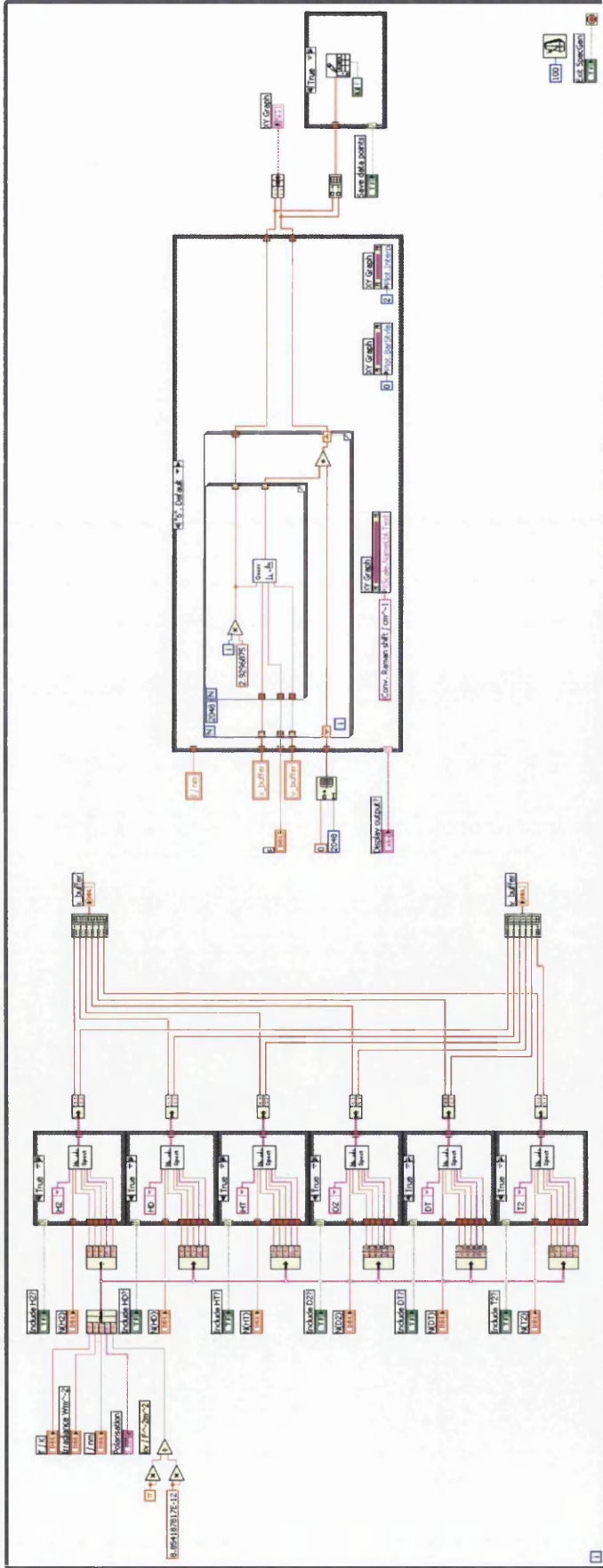
As mentioned above, the user has no direct front panel interaction with the tier 2 and 3 subVIs. The inputs listed below are directly inputted by the user via front panel objects in the tier 1 VI. For the tier 2 and 3 subVIs, the input / output tables will specify the source or sink subVI of the listed parameter.

User-defined input (front panel control)	Purpose / calculation / simulation parameter
 “Include H2?” (SWP)*	Includes / excludes H <sub>2</sub> Raman spectrum
 “Include HD?” (SWP)	Includes / excludes HD Raman spectrum
 “Include HT?” (SWP)	Includes / excludes HT Raman spectrum
 “Include D2?” (SWP)	Includes / excludes D <sub>2</sub> Raman spectrum
 “Include DT?” (SWP)	Includes / excludes HT Raman spectrum
 “Include T2?” (SWP)	Includes / excludes T <sub>2</sub> Raman spectrum
 “Save data points?” (LWR)	Governs case structure that exports data stored in local variables “x_buffer” and “y_buffer” to tab-delimited ASCII file. Case structure is called once if TRUE.
 “Exit SpecGen” (LWR)	Governs while loop that contains the <i>SpecGen</i> code. <i>SpecGen_Interface.vi</i> is stopped if TRUE.
 “N(H2)”	Relative number density of H <sub>2</sub> molecules
 “N(HD)”	Relative number density of HD molecules
 “N(HT)”	Relative number density of HT molecules
 “N(D2)”	Relative number density of D <sub>2</sub> molecules
 “N(DT)”	Relative number density of DT molecules
 “N(T2)”	Relative number density of T <sub>2</sub> molecules
 “T / K”	Temperature of the gas mixture, <i>T</i> / K
 “Irradiance / Wm <sup>-2</sup> ”	Irradiance of the incident radiation on the gas mixture, $\mathcal{I}$ / Wm <sup>-2</sup>
 “λ / nm”	Wavelength of the incident radiation, λ / nm
 “σ”	Standard deviation of the Gaussian lineshape convolution, σ / cm <sup>-1</sup>
 “Polarisation” (Combo box)	Specifies the polarisation regime
 “Display output?” (Combo box)	Specifies the form of the XY graph display and thus the form of exported data

Local variable	References
 “x_buffer” (1D array)	Concatenated wavenumber shift arrays for specified “Include <isotopomer>?” Booleans
 “y_buffer” (1D array)	Concatenated relative intensity arrays for specified “Include <isotopomer>?” Booleans

Simulation display (front panel indicator)	Displays
 “XY Graph”	Simulated Raman spectrum for specified “Include <isotopomer>?” Booleans in the form specified by the “Display output?” combo box

\* The acronyms “(SWP)” and “(LWR)” stand for “Switch When Pressed” and “Latch When Released”, respectively. They represent the appropriate “mechanical action” of the controls they qualify.



**Figure A1.2** Block diagram for SpecGen\_Interface.vi. Note the use of bundles to simplify the transport of front panel object values to the tier 2 nodes.

As can be seen in Figure A1.2, the block diagram of SpecGen\_Interface.vi is split roughly into two halves. The left hand side of the block diagram deals with calculation of the Raman spectrum following the user-specified parameter, while the right hand side is concerned with display and output of the simulated spectrum.

Extensive use has been made of bundling, in both tiers 1 and 2, in order to simplify the block diagram. Note that the output bundle from tier 2 “Spectrum / (cm<sup>-1</sup> / Wsr<sup>-1</sup>)” are unbundled to allow concatenation of the x and y arrays. The calculated x and y arrays are stored in the sinks “x\_buffer” and “y\_buffer”, respectively. These are hidden front panel objects that are referenced by local variables, which feed into a case structure governed by the “Display output?” combo box. The use of local variables is not strictly necessary in this build (the array wires could have connected directly to the case structure), but since they are a feature of builds currently in progress (e.g. for recalling previously calculated spectra for comparison on a double plot), the local variables have been left on the block diagram.

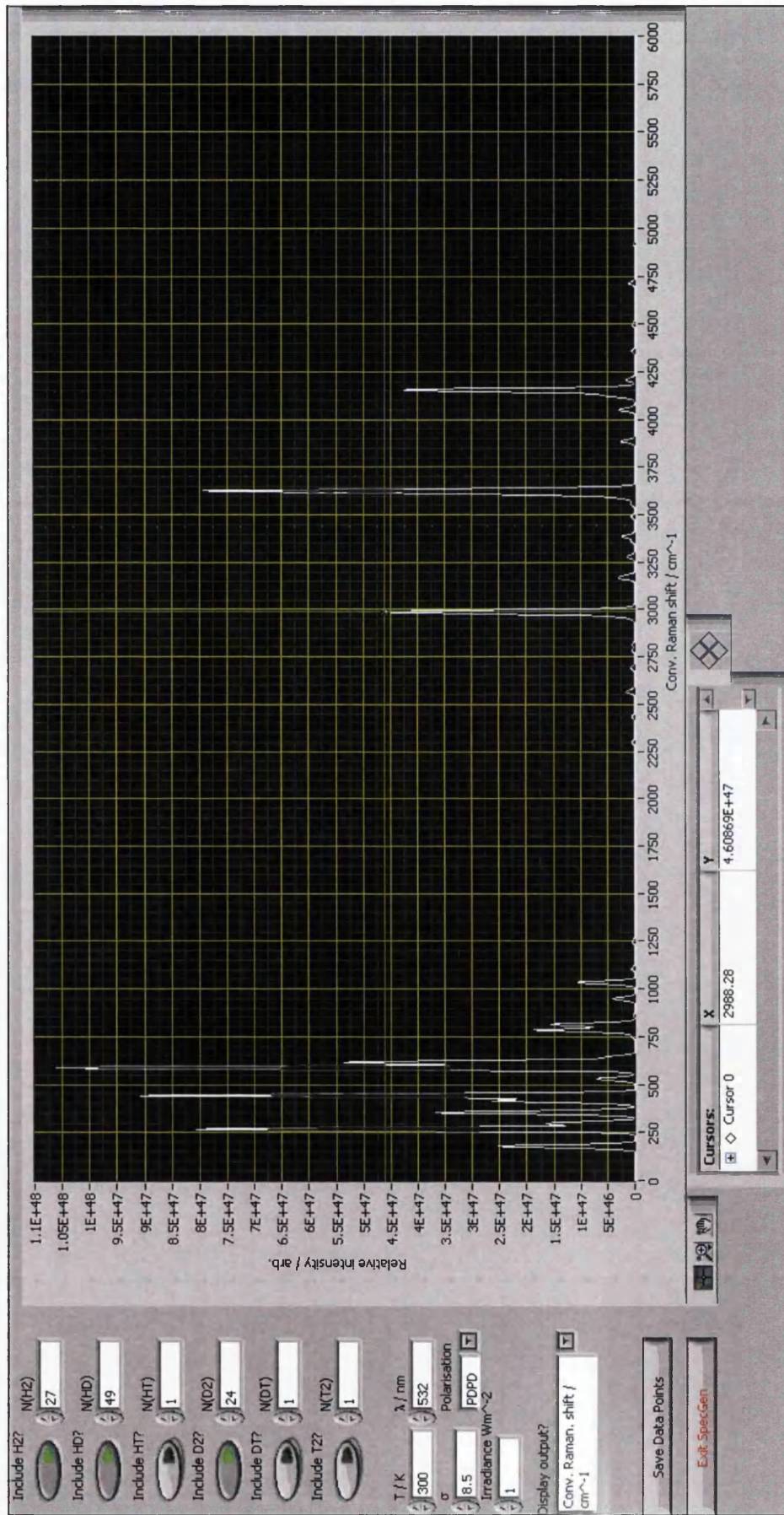
The current range of available XY graph display formats for data is somewhat limited. Via the combo box “Display output?” one can select from non-convoluted (i.e. “(position, relative intensity)”) format (combo box entries 1 to 3) or a convoluted format that simulates approximately the range of the 600grmm<sup>-1</sup> grating installed in the HTS (the simulated range is from 0 to 6000 cm<sup>-1</sup>)<sup>†</sup> and the 2048-pixel format of the Spec-10 CCD detector (combo box entries 4 to 6). The case structure governed by the combo box “Display output?” contains property nodes that correctly set the x-axis label and select the appropriate data point and interpolation style for the selected display format.

The exporting is performed by a case structure governed by the “Save data points?” Boolean. Note the TRUE constant wired to the “transpose?” connector of the Write to Spreadsheet File.vi node. This is to set the exported columns to be arranged vertically.

---

<sup>†</sup> i.e. from 532 to 781nm if the incident radiation is chosen to have a wavelength of 532nm.

Figure A1.3 shows the front panel of the tier 1 VI. The user controls are to the left, with the XY graph on the right. The simulation pictured is the  $I(\pi/2; \perp^s, \perp^i)$  regime Raman scattering from a 27:49:24 mixture of H<sub>2</sub>:HD:D<sub>2</sub> at 300K, with incident radiation of wavelength 532nm displayed in convoluted Raman shift format (combo box entry 6). The hidden indicators “x\_buffer” and “y\_buffer” are located (but not visible) to the lower right of the XY graph.



**Figure A1.3** Front panel of SpecGen\_Interface.vi. A simulation of a 27:49:24 mixture of H<sub>2</sub>:HD:D<sub>2</sub> at 300K, with incident radiation of wavelength 532nm is shown. The Gaussian lineshape has been convoluted to the (x,y) data. The Boolean controls on the left specify which isotopomers are present. The isotopomeric composition (relative number density of each isotopomer) is specified by the numeric controls to the right of the Boolean controls. Other simulation parameters are handled by the controls below the Boolean and composition numeric controls.

### A1.3 Tier 2: High-Level SubVI Handling & Lineshape Convolution








The tier 2 subVI, SpecGen\_SubVI\_High\_Raman\_Spectrum.vi, is used for high-level handling of the tier 3 subVIs. It greatly simplifies the block diagram of the main (tier 1) VI, SpecGen\_Interface.vi. The main tasks of the tier 2 subVI are to coordinate the calculation of line position and intensities, to provide the necessary cross-talk between tiers 1, 3a, and 3b (e.g. for the correct calculation of  $(\tilde{\nu}_s)^4$  values), and to output the (position, relative intensity) values in a convenient form.

Each running instance of the tier 2 subVI calculates the Raman (wavenumber) shifts of the first ten S<sub>0</sub>-, O<sub>1</sub>-, Q<sub>1</sub>-, and S<sub>1</sub>-branch lines and their relative intensities for a single isotopomer specified by the input string “Isotopomer”. Valid inputs for this string are “H2” (default), “HD”, “HT”, “D2”, “DT”, and “T2”. The output bundle “Spectrum / (cm<sup>-1</sup> / Wsr<sup>-1</sup>)” consists of two 40-element 1D arrays of double precision numbers.


Lineshape convolution is not handled by this subVI, but rather is carried out by the dedicated tier 3c subVI, SpecGen\_SubVI\_Convolute\_Gaussian.vi, which is a dependent of the main VI.

VI filename	SpecGen_SubVI_High_Raman_Spectrum.vi
Icon and connector pane	
Dependencies	SpecGen_Interface.vi
Dependents	SpecGen_Interface.vi SpecGen_SubVI_S0(J).vi (embedded) SpecGen_SubVI_O1(J).vi (embedded) SpecGen_SubVI_Q1(J).vi (embedded) SpecGen_SubVI_S1(J).vi (embedded) SpecGen_SubVI_Spectroscopic_Constants.vi (embedded) SpecGen_SubVI_giNi.vi (embedded) SpecGen_SubVI_F(J).vi (embedded) SpecGen_SubVI_Phi(a^2_g^2_q).vi (embedded) SpecGen_SubVI_Tensor_Invariants.vi (embedded)



Input	Source
 "N"	SpecGen_Interface.vi
 "T / K"	SpecGen_Interface.vi
 "Lambda / nm"	SpecGen_Interface.vi
 "Irradiance Wm <sup>-2</sup> "	SpecGen_Interface.vi
 "kv / F <sup>-2</sup> m <sup>2</sup> "	SpecGen_Interface.vi
 "Isotopomer"	SpecGen_Interface.vi
 "Polarisation"	SpecGen_Interface.vi

Output	Sink
 "Spectrum / (cm <sup>-1</sup> / Wsr <sup>-1</sup> )" (bundle of two 1D arrays)	SpecGen_Interface.vi

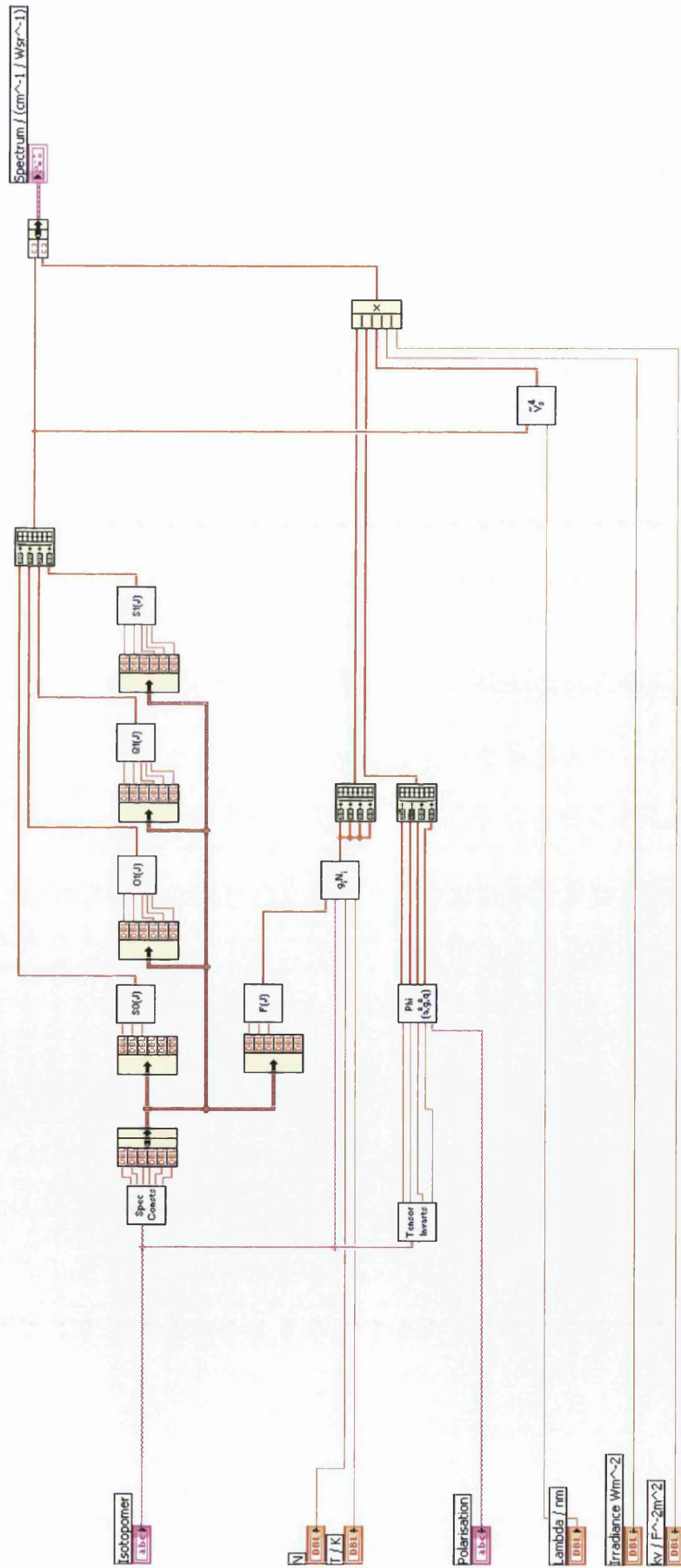


Figure A1.4 Block diagram for SpecGen\_SubVI\_High\_Raman\_Spectrum.vi

### A1.4 Tier 3a: Calculation of Raman Line Positions

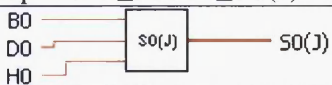
The tier 3a subVIs are handled by SpecGen\_SubVI\_High\_Raman\_Spectrum.vi and are used to calculate the wavenumber shifts of the first ten ( $J = J'' = 0, 1, \dots, 9$ ) lines of the  $S_0$ -,  $Q_1$ -, and  $S_1$ -branches and the first eight ( $J = J'' = 2, 3, \dots, 9$ ) lines of the  $O_1$ -branch for the isotopomer being handled by the running instance of the tier 2 VI.





#### A1.4.1 SpecGen\_SubVI\_S0(J).vi

This subVI calculates the wavenumber shifts,  $S_0(J)$ , of the first ten ( $J = J'' = 0, 1, \dots, 9$ ) pure rotational Stokes Raman  $S_1$ -branch lines from the specified spectroscopic constants  $B_0$ ,  $D_0$ ,  $H_0$ , according to the expression:

$$S_0(J) = (4B_0 - 6D_0 + \frac{27}{4}H_0)(J + \frac{1}{2}) - (8D_0 - 34H_0)(J + \frac{1}{2})^3 + 12H_0(J + \frac{1}{2})^5.$$

The output is a ten-element array of double-precision numbers, "S0(J)". The index of the array matches the  $J''$  value. Note that the isotopomer correspondence is handled by SpecGen\_SubVI\_High\_Raman\_Spectrum.vi. The units of the wavenumber shifts are reciprocal centimetres.

VI filename	SpecGen_SubVI_S0(J).vi
Icon and connector pane	
Dependencies	SpecGen_SubVI_Spectroscopic_Constants.vi
Dependents	SpecGen_SubVI_High_Raman_Spectrum.vi

Input	Source
 "B0"	SpecGen_SubVI_Spectroscopic_Constants.vi
 "D0"	SpecGen_SubVI_Spectroscopic_Constants.vi
 "H0"	SpecGen_SubVI_Spectroscopic_Constants.vi
Output	Sink
 "S0(J)" (1D array)	SpecGen_SubVI_High_Raman_Spectrum.vi

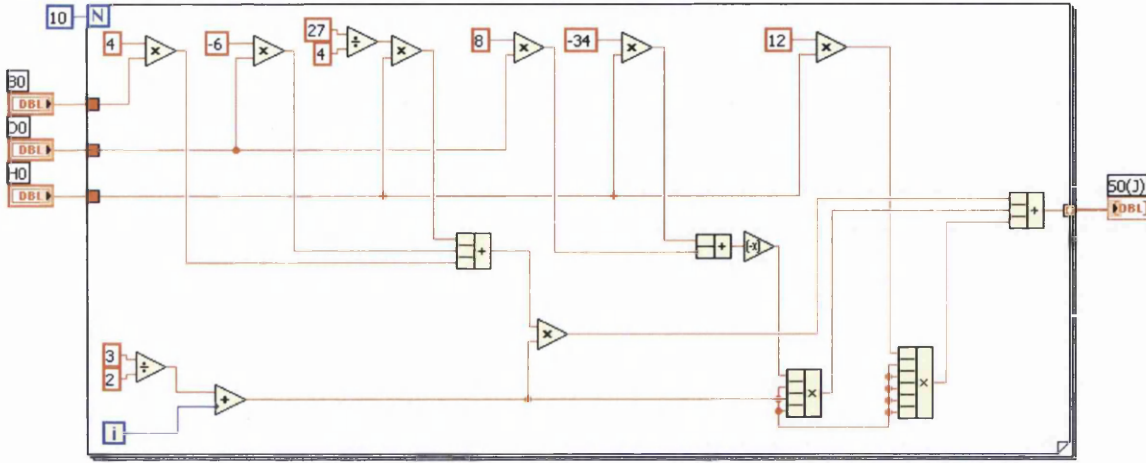


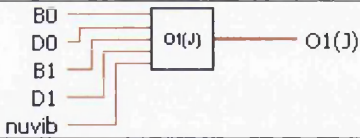
Figure A1.5 Block diagram for SpecGen\_SubVI\_S0(J).vi






### A1.4.2 SpecGen\_SubVI\_O1(J).vi


This subVI calculates the wavenumber shifts,  $O_1(J)$ , of the first ten ( $J = J'' = 2, 3, \dots, 11$ ) vibration-rotation Stokes Raman  $O_1$ -branch lines from the specified spectroscopic constants  $B_0$ ,  $D_0$ ,  $B_1$ ,  $D_1$ , and  $\tilde{\nu}_{vib}$  according to the expression:

$$O_1(J) = \tilde{\nu}_{vib} + 2B_1 - (3B_1 + B_0)J + (B_1 - B_0)J^2 - \frac{9}{16}(D_1 - D_0) + \frac{3}{2}(D_1 + D_0)(2J - 1) - \frac{11}{2}(D_1 - D_0)(2J - 1)^2 + \frac{1}{2}(D_1 + D_0)(2J - 1)^3 - \frac{1}{16}(D_1 - D_0)(2J - 1)^4$$

The output is a ten-element array of double-precision numbers, "O1(J)". The index of the array is equal to  $J'' - 2$ , i.e. index 0 (first element) corresponds to  $J'' = 2$ , etc. The isotopomer correspondence is handled by SpecGen\_SubVI\_High\_Raman\_Spectrum.vi. The units of the wavenumber shifts are reciprocal centimetres.

VI filename	SpecGen_SubVI_O1(J).vi
Icon and connector pane	
Dependencies	SpecGen_SubVI_Spectroscopic_Constants.vi
Dependents	SpecGen_SubVI_High_Raman_Spectrum.vi

Input	Source
 "B0"	SpecGen_SubVI_Spectroscopic_Constants.vi
 "B1"	SpecGen_SubVI_Spectroscopic_Constants.vi
 "D0"	SpecGen_SubVI_Spectroscopic_Constants.vi
 "D1"	SpecGen_SubVI_Spectroscopic_Constants.vi
 "nuvib"	SpecGen_SubVI_Spectroscopic_Constants.vi

Output	Sink
 "O1(J)" (1D array)	SpecGen_SubVI_High_Raman_Spectrum.vi

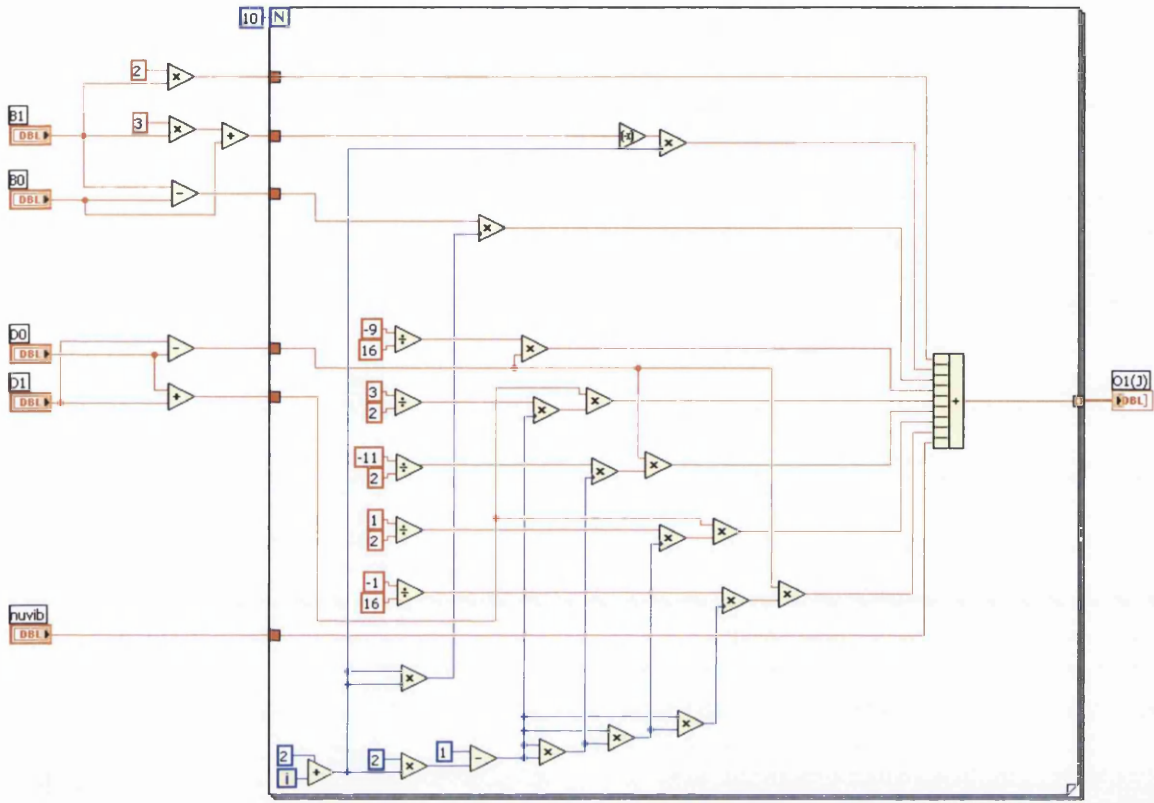


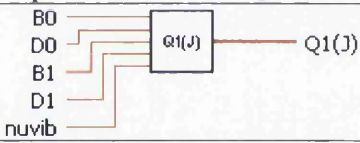
Figure A1.6 Block diagram for SpecGen\_SubVI\_O1(J).vi






### A1.4.3 SpecGen\_SubVI\_Q1(J).vi


This subVI calculates the wavenumber shifts,  $Q_1(J)$ , of the first ten ( $J = J'' = 0, 1, \dots, 9$ ) vibration-rotation Stokes Raman  $Q_1$ -branch lines from the specified spectroscopic constants  $B_0$ ,  $D_0$ ,  $B_1$ ,  $D_1$ , and  $\tilde{\nu}_{\text{vib}}$  according to the expression:

$$Q_1(J) = \tilde{\nu}_{\text{vib}} + (B_1 - B_0)J(J+1) - (D_1 - D_0)J^2(J+1)^2.$$

The output is a ten-element array of double-precision numbers, “Q1(J)”. The index of the array matches the  $J''$  value. Note that the isotopomer correspondence is handled by SpecGen\_SubVI\_High\_Raman\_Spectrum.vi. The units of the wavenumber shifts are reciprocal centimetres.

VI filename	SpecGen_SubVI_Q1(J).vi
Icon and connector pane	
Dependencies	SpecGen_SubVI_Spectroscopic_Constants.vi
Dependents	SpecGen_SubVI_High_Raman_Spectrum.vi

Input	Source
 “B0”	SpecGen_SubVI_Spectroscopic_Constants.vi
 “B1”	SpecGen_SubVI_Spectroscopic_Constants.vi
 “D0”	SpecGen_SubVI_Spectroscopic_Constants.vi
 “D1”	SpecGen_SubVI_Spectroscopic_Constants.vi
 “nuvib”	SpecGen_SubVI_Spectroscopic_Constants.vi

Output	Sink
 “Q1(J)” (1D array)	SpecGen_SubVI_High_Raman_Spectrum.vi

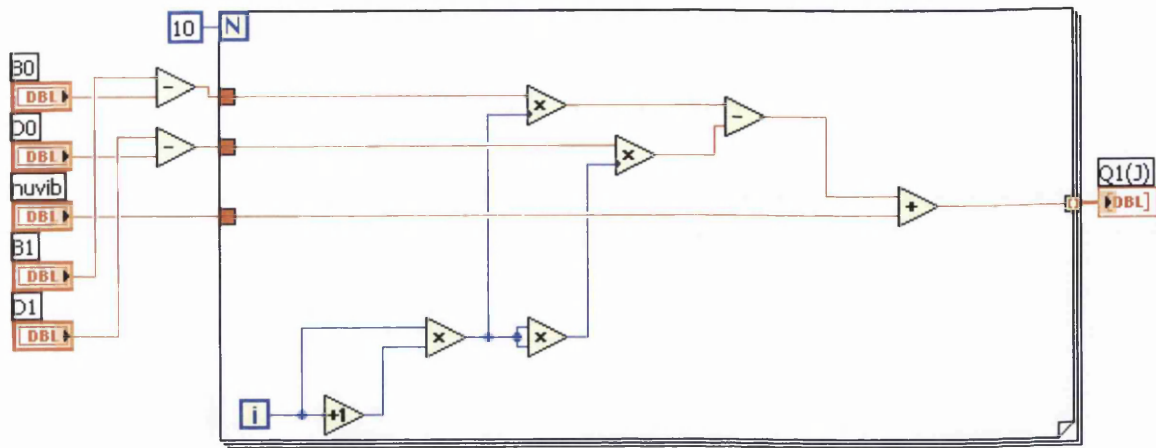


Figure A1.7 Block diagram for SpecGen\_SubVI\_Q1(J).vi

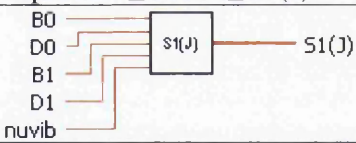







## A1.4.4 SpecGen\_SubVI\_S1(J).vi


This subVI calculates the wavenumber shifts,  $S_1(J)$ , of the first ten ( $J = J'' = 0, 1, \dots, 9$ ) vibration-rotation Stokes Raman  $S_1$ -branch lines from the specified spectroscopic constants  $B_0$ ,  $D_0$ ,  $B_1$ ,  $D_1$ , and  $\tilde{\nu}_{\text{vib}}$  according to the expression:

$$S_1(J) = \tilde{\nu}_{\text{vib}} + 6B_1 + (5B_1 - B_0)J + (B_1 - B_0)J^2 - \frac{9}{16}(D_1 - D_0) - \frac{3}{2}(D_1 + D_0)(2J + 3) - \frac{11}{8}(D_1 - D_0)(2J + 3)^2 - \frac{1}{2}(D_1 + D_0)(2J + 3)^3 - \frac{1}{16}(D_1 - D_0)(2J + 3)^4$$

The output is a ten-element array of double-precision numbers, “S1(J)”. The index of the array matches the  $J''$  value. Note that the isotopomer correspondence is handled by SpecGen\_SubVI\_High\_Raman\_Spectrum.vi. The units of the wavenumber shifts are reciprocal centimetres.

VI filename	SpecGen_SubVI_S1(J).vi
Icon and connector pane	
Dependencies	SpecGen_SubVI_Spectroscopic_Constants.vi
Dependents	SpecGen_SubVI_High_Raman_Spectrum.vi

Input	Source
 “B0”	SpecGen_SubVI_Spectroscopic_Constants.vi
 “B1”	SpecGen_SubVI_Spectroscopic_Constants.vi
 “D0”	SpecGen_SubVI_Spectroscopic_Constants.vi
 “D1”	SpecGen_SubVI_Spectroscopic_Constants.vi
 “nuvib”	SpecGen_SubVI_Spectroscopic_Constants.vi

Output	Sink
 “S1(J)” (1D array)	SpecGen_SubVI_High_Raman_Spectrum.vi

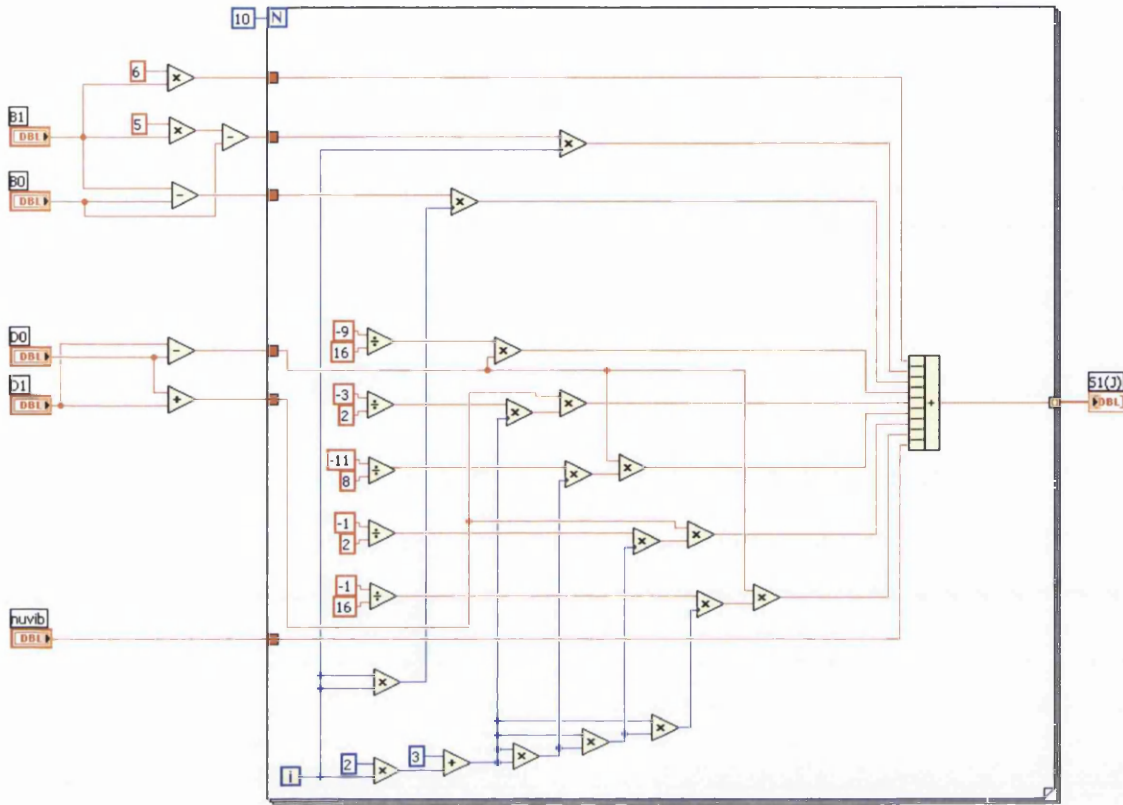
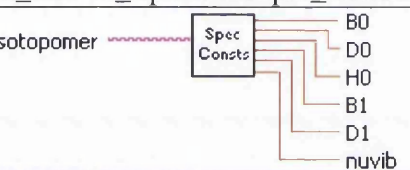
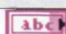







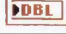
Figure A1.8 Block diagram for SpecGen\_SubVI\_S1(J)

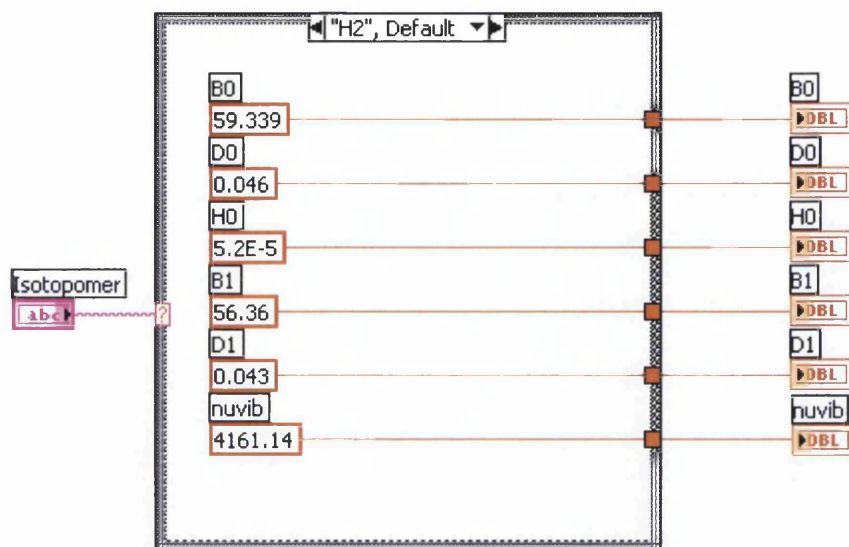
### A1.4.5 SpecGen\_SubVI\_Spectroscopic\_Constants.vi

This subVI outputs the values of the spectroscopic constants  $B_0$ ,  $D_0$ ,  $H_0$ ,  $B_1$ ,  $D_1$ , and  $\tilde{\nu}_{vib}$  for the isotopomer specified by the input string “Isotopomer” in reciprocal centimetres. Valid inputs for this string are “H2” (default), “HD”, “HT”, “D2”, “DT”, and “T2”. Note that the value of the spectroscopic constant  $H_1$  is not available (no values could be found in the published literature).

VI filename	SpecGen_SubVI_Spectroscopic_Constants.vi
Icon and connector pane	
Dependencies	SpecGen_Interface.vi
Dependents	SpecGen_SubVI_S0(J).vi SpecGen_SubVI_O1(J).vi SpecGen_SubVI_Q1(J).vi SpecGen_SubVI_S1(J).vi

Input	Source
 “Isotopomer”	SpecGen_Interface.vi

Output	Sink
 “B0”	SpecGen_SubVI_S0(J),O1(J),Q1(J),S1(J).vi
 “D0”	SpecGen_SubVI_S0(J),O1(J),Q1(J),S1(J).vi
 “H0”	SpecGen_SubVI_S0(J),O1(J),Q1(J),S1(J).vi
 “B1”	SpecGen_SubVI_S0(J),O1(J),Q1(J),S1(J).vi
 “D1”	SpecGen_SubVI_S0(J),O1(J),Q1(J),S1(J).vi
 nuvib	SpecGen_SubVI_S0(J),O1(J),Q1(J),S1(J).vi



**Figure A1.9** Block diagram for `SpecGen_SubVI_Spectroscopic_Constants.vi` (H<sub>2</sub> case shown). The case structure outputs values for the spectroscopic constants associated with HD, HT, D<sub>2</sub>, DT, or T<sub>2</sub> if specified by the string “Isotopomer”.

### ***A1.5 Tier 3b: Calculation of Raman Line Relative Intensities***

The tier 3b subVIs are handled by `SpecGen_SubVI_High_Raman_Spectrum.vi` in the same manner as for the tier 3a subVIs. The quantities to be calculated are the relative intensities,  $I_{rel}(\theta; p^s, p^i)$ , of the Raman lines corresponding to the line positions calculated by the tier 3a subVIs, i.e.

$$I_{rel}(\theta; p^s, p^i) = (\tilde{\nu}_s)^4 g_i N_i \Phi(a^2, \gamma^2, \theta)$$

Only the factor  $(\tilde{\nu})^4$  (calculated by `SpecGen_SubVI_vs^4.vi`) has any explicit dependence on the line positions, and the correspondence is handled by `SpecGen_SubVI_High_Raman_Spectrum.vi`. For this reason `SpecGen_SubVI_vs^4.vi` lists `SpecGen_SubVI_High_Raman_Spectrum.vi` as a dependency, but not the tier 3a subVI that calculated the line position.

#### ***A1.5.1 SpecGen\_SubVI\_vs^4.vi***

For each member of the input array “Raman shift / cm<sup>-1</sup>”, `SpecGen_SubVI_vs^4.vi` generates the fourth power of the absolute wavenumber of a specified Raman shift,  $\tilde{\nu}_s^4$ . As is standard practice in spectroscopy, *SpecGen* calculates the Raman shifts in reciprocal centimetres and the wavelength of the exciting radiation is a user specified parameter in units of nanometres. `SpecGen_SubVI_vs^4.vi` performs all the necessary unit conversions.

VI filename	SpecGen_SubVI_vs^4.vi
Icon and connector pane	
Dependencies	SpecGen_Interface.vi SpecGen_SubVI_High_Raman_Spectrum.vi
Dependents	SpecGen_SubVI_High_Raman_Spectrum.vi

Input	Source
"Lambda / nm"	SpecGen_Interface.vi
"Raman shift / cm^-1" (1D array)	SpecGen_SubVI_High_Raman_Spectrum.vi

Output	Sink
"vs^4 / m^-4" (1D array)	SpecGen_SubVI_High_Raman_Spectrum.vi

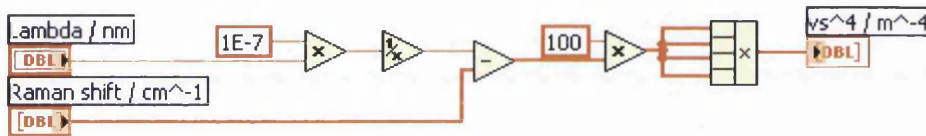


Figure A1.10 Block diagram for SpecGen\_SubVI\_vs^4.vi

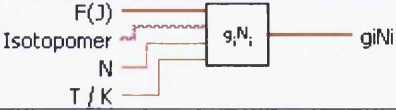
### A1.5.2 SpecGen\_SubVI\_giNi.vi





This subVI generates the population factor  $g_i N_i$  for the first ten rotational levels ( $J = J'' = 0, 1, \dots, 9$ ) of the ground vibrational state ( $v = 0$ ) of a diatomic molecule in the form of a ten-element 1D array. The population factor is given by


$$N_i(J) = \frac{N g_{N_j} (2J + 1) \exp\{-\tilde{F}(J)/\eta T\}}{\sum_J g_{N_j} (2J + 1) \exp\{-\tilde{F}(J)/\eta T\}},$$

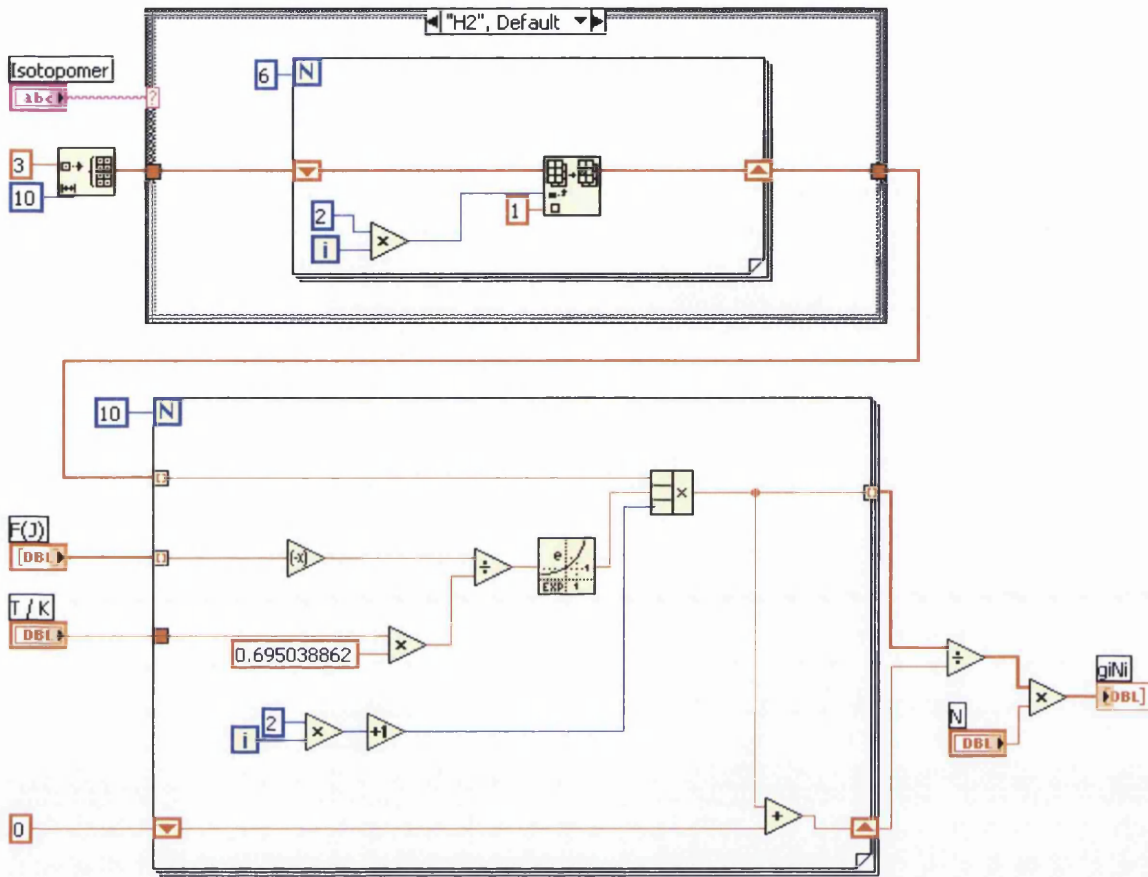
where  $N$  is the total number of molecules,  $g_{N_j} (2J + 1)$  is the statistical weight of rotational level  $J$ ,  $g_N$  is the statistical weight due to the effects of nuclear spin statistics on the relative populations of even and odd rotational levels in the case of homonuclear molecules (for heteronuclear molecules  $g_N = 1$  for all levels),  $\tilde{F}(J)$  is the rotational energy term,  $T$  is the temperature, and  $\eta = 0.695\,038\,862$ . The index of the array matches the  $J''$  value.

The appropriate statistical weighting between even and odd levels is applied by a case structure whose form is specified by the input string “Isotopomer”. Valid inputs for this string are “H2” (default), “HD”, “HT”, “D2”, “DT”, and “T2”.

VI filename	SpecGen_SubVI_giNi.vi
Icon and connector pane	
Dependencies	SpecGen_Interface.vi SpecGen_SubVI_F(J).vi
Dependents	SpecGen_SubVI_High_Raman_Spectrum.vi

Input	Source
 “F(J)” (1D array)	SpecGen_SubVI_F(J).vi
 “T / K”	SpecGen_Interface.vi
 “N”	SpecGen_Interface.vi
 “Isotopomer”	SpecGen_Interface.vi

Output	Sink
 “giNi” (1D array)	SpecGen_SubVI_High_Raman_Spectrum.vi



**Figure A1.11** Block diagram for SpecGen\_SubVI\_giNi.vi (H<sub>2</sub> case shown). The case structure applies the statistical weight due to the effects of nuclear spin statistics on the relative populations of even and odd rotational levels in the case of homonuclear molecules, i.e. 1/3 (even/odd *J*) for H<sub>2</sub> and T<sub>2</sub>, 6/3 (even/odd *J*) for D<sub>2</sub>. For heteronuclear molecules the statistical weight is 1/1 (even/odd *J*).

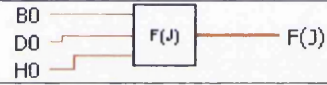


### A1.5.3 SpecGen\_SubVI\_F(J).vi

This subVI generates the rotational term  $F(J)$  for the first ten rotational levels ( $J = J'' = 0, 1, \dots, 9$ ) of the ground vibrational state ( $v = 0$ ) of a diatomic molecule in the form of a ten-element 1D array. The rotational term is given by the expression:

$$\tilde{F}(J) = B_0 J(J+1) - D_0 J^2(J+1)^2 + H_0 J^3(J+1)^3 - \dots,$$

where  $B_0$ ,  $D_0$ , and  $H_0$  are the vibrational ground state rotational constants supplied by SpecGen\_SubVI\_Spectroscopic\_Constants.vi for the relevant isotopomer (coordinated by SpecGen\_SubVI\_High\_Raman\_Spectrum.vi). The index of the array matches the  $J''$  value.

VI filename	SpecGen_SubVI_F(J).vi
Icon and connector pane	
Dependencies	SpecGen_SubVI_Spectroscopic_Constants.vi
Dependents	SpecGen_SubVI_giNi.vi

Input	Source
DBL "B0"	SpecGen_SubVI_Spectroscopic_Constants.vi
DBL "D0"	SpecGen_SubVI_Spectroscopic_Constants.vi
DBL "H0"	SpecGen_SubVI_Spectroscopic_Constants.vi

Output	Sink
DBL "F(J)" (1D array)	SpecGen_SubVI_giNi.vi

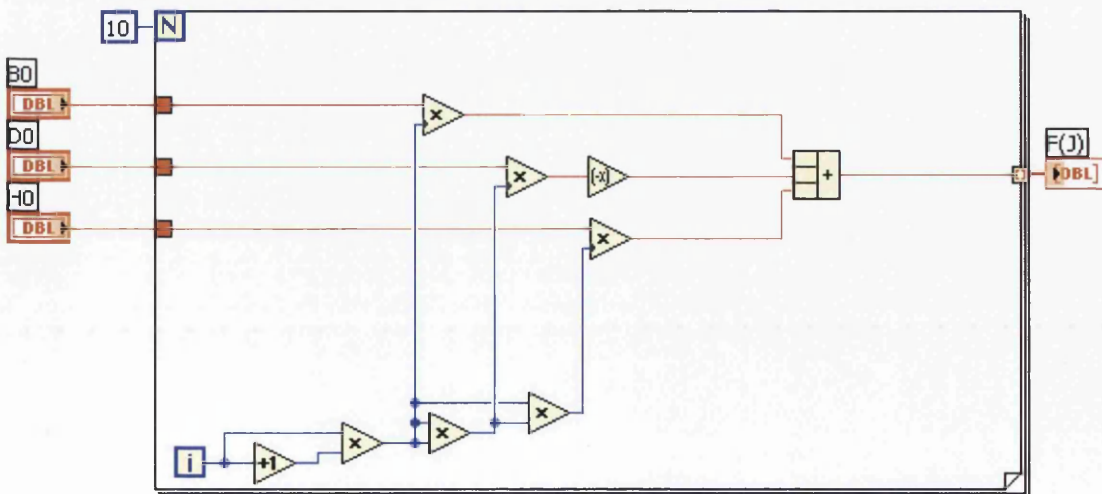
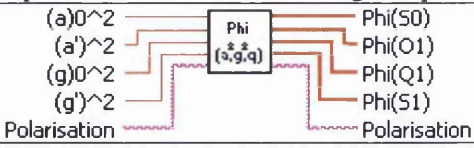


Figure A1.12 Block diagram for SpecGen\_SubVI\_F(J).vi

#### A1.5.4 *SpecGen\_SubVI\_Phi(a^2\_g^2\_q) .vi*

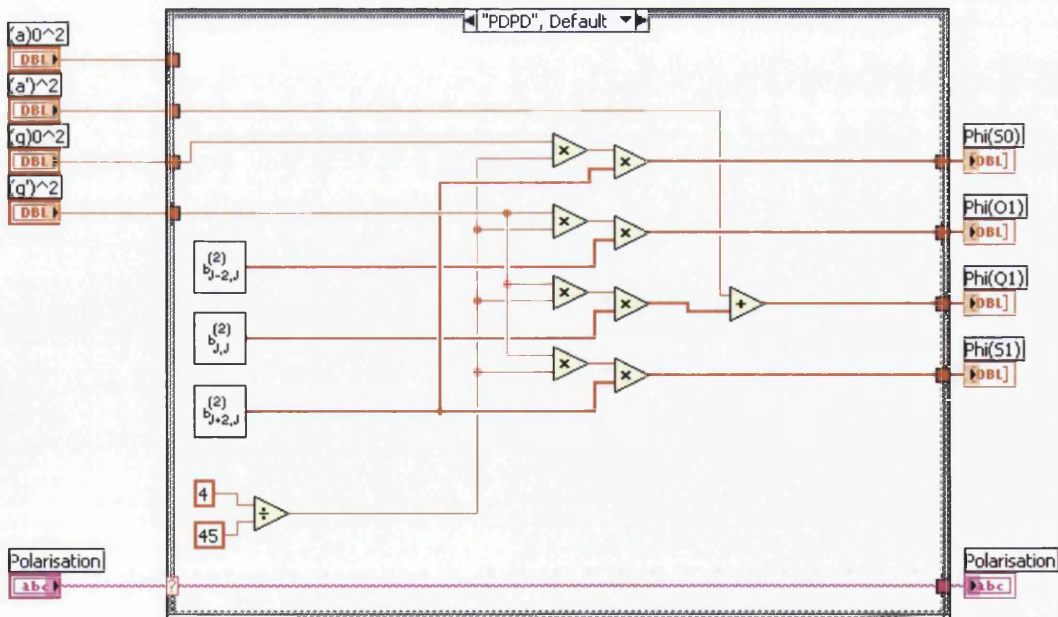
This subVI generates the line strength function  $\Phi(a^2, \gamma^2, \theta)$  for the inputted values of the tensor invariants  $(a')^2$ ,  $(\gamma)_0^2$ , and  $(\gamma')^2$  for the  $S_0$ -,  $O_1$ -,  $Q_1$ -, and  $S_1$ -branches. The value of the tensor invariant  $(a)_0^2$  is also an input, but it is not used in the current version of *SpecGen* – the  $Q_0$ -branch (Rayleigh scattering) is not currently included in the simulations. The polarisation regime is specified by the input string “Polarisation”. Valid inputs for this string are “PDPD”, “PAPD”, “RIRI”, and “LERI”, corresponding to the polarisation regimes  $I(\pi/2; \perp^s, \perp^i)$ ,  $I(\pi/2; \parallel^s, \perp^i)$ ,  $I(0; R^s, R^i)$ , and  $I(0; L^s, R^i)$ , respectively. The value of the string “Polarisation” is passed as an output but currently this is not required by any dependent VI.

The subVI has three embedded subVIs for generating the Placzek-Teller  $b$ -factors  $b_{J-2, J}^{(2)}$ ,  $b_{J, J}^{(2)}$ , and  $b_{J+2, J}^{(2)}$ , which are *SpecGen\_SubVI\_b(2)J-2,J*, *SpecGen\_SubVI\_b(2)J,J*, and *SpecGen\_SubVI\_b(2)J+2,J*, respectively. The number of elements in the arrays outputted by these routines determines the number of elements in the outputs “Phi(S0)”, “Phi(O1)”, “Phi(Q1)”, and “Phi(S1)”. This number is set to ten elements by default (corresponding to the first ten  $S_0$ -,  $Q_1$ -, and  $S_1$ -branch lines. Note that although all three  $b$ -factors are calculated using the range  $J = J'' = 0, 1, \dots, 9$ , the value of  $b_{J-2, J}^{(2)}$  is only non-zero for  $J = J'' > 1$  since  $b_{J-2, J}^{(2)}$  is the  $b$ -factor for the  $O_1$ -branch lines. Therefore, although “Phi(S1)” is a ten-element array, only the last eight elements will be non zero; having equal numbers of elements for each array simplifies programming considerations. If the first ten lines of the  $O_1$ -branch were required then it would be a simple matter of increasing the number of elements of all the  $b$ -factor arrays to twelve, which would incur no noticeable performance penalty. The index of the array matches the  $J''$  value.

VI filename	SpecGen_SubVI_Phi(a^2_g^2_q).vi
Icon and connector pane	
Dependencies	SpecGen_SubVI_Tensor_Invariants.vi SpecGen_SubVI_b(2)J-2,J.vi (embedded) SpecGen_SubVI_b(2)J,J.vi (embedded) SpecGen_SubVI_b(2)J+2,J.vi (embedded)
Dependents	SpecGen_SubVI_High_Raman_Spectrum.vi

Input	Source
"(a)0^2"	SpecGen_SubVI_Tensor_Invariants.vi
"(a')^2"	SpecGen_SubVI_Tensor_Invariants.vi
"(g)0^2"	SpecGen_SubVI_Tensor_Invariants.vi
"(g')^2"	SpecGen_SubVI_Tensor_Invariants.vi
"Polarisation"	SpecGen_Interface.vi

Output	Sink
"Phi(S0)" (1D array)	SpecGen_SubVI_High_Raman_Spectrum.vi
"Phi(O1)" (1D array)	SpecGen_SubVI_High_Raman_Spectrum.vi
"Phi(Q1)" (1D array)	SpecGen_SubVI_High_Raman_Spectrum.vi
"Phi(S1)" (1D array)	SpecGen_SubVI_High_Raman_Spectrum.vi
"Polarisation"	N/A



**Figure A1.13** Block diagram for SpecGen\_SubVI\_Phi(a^2\_g^2\_q).vi ( $I(\pi/2; \perp^s, \perp^i)$  case shown). The case structure handles the generation of the line strength function any one of the four currently modelled polarisation regimes:  $I(\pi/2; \perp^s, \perp^i)$ ,  $I(\pi/2; \parallel^s, \perp^i)$ ,  $I(0; R^s, R^i)$ , and  $I(0; L^s, R^i)$ .

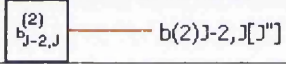
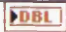
A1.5.5 SpecGen\_SubVI\_b(2)J-2,J.vi

This subVI generates a ten-element 1D array of the values of the Placzek-Teller *b*-factor

$b_{J-2,J}^{(2)}$ :

$$b_{J-2,J}^{(2)} = \frac{3J(J-1)}{2(2J-1)(2J+1)},$$

where  $J = J'' = 2, 3, \dots, 11$ . The index of the array equals  $J'' - 2$ .

VI filename	SpecGen_SubVI_b(2)J-2,J.vi
Icon and connector pane	
Dependencies	N/A
Dependents	SpecGen_SubVI_Phi(a^2_g^2_q).vi
Output	Sink
 "b(2)J-2,J[J']" (1D array)	SpecGen_SubVI_Phi(a^2_g^2_q).vi

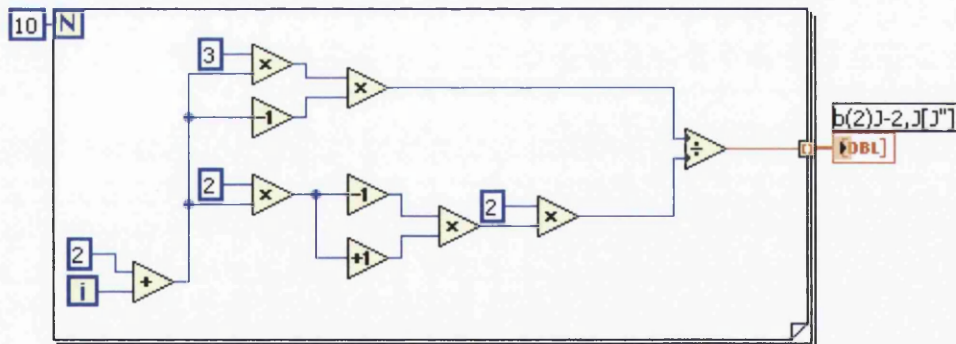


Figure A1.14 Block diagram for SpecGen\_SubVI\_b(2)J-2,J.vi



## A1.5.6 SpecGen\_SubVI\_b(2)J,J.vi

This subVI generates a ten-element 1D array of the values of the Placzek-Teller  $b$ -factor

$b_{J,J}^{(2)}$ :

$$b_{J,J}^{(2)} = \frac{J(J+1)}{(2J-1)(2J+3)},$$

where  $J = J'' = 0, 1, \dots, 9$ , and the first element of the array is zero since  $b_{J,J}^{(2)}$  is only non-zero for  $J = J'' > 0$ . The index of the array matches the  $J''$  value. Although the first element is always non-zero, the  $J'' = 0$  Q<sub>1</sub>-branch line intensity is non-zero for the polarisation regimes  $I(\pi/2; \perp^s, \perp^i)$  and  $I(0; R^s, R^i)$  since there is a non-zero contribution from the tensor invariant  $(a')^2$  to  $\Phi(a^2, \gamma^2, \theta)$  in these regimes.

VI filename	SpecGen_SubVI_b(2)J,J.vi
Icon and connector pane	
Dependencies	N/A
Dependents	SpecGen_SubVI_Phi(a^2_g^2_q).vi
Output	Sink
 "b(2)J,J[J'']" (1D array)	SpecGen_SubVI_Phi(a^2_g^2_q).vi

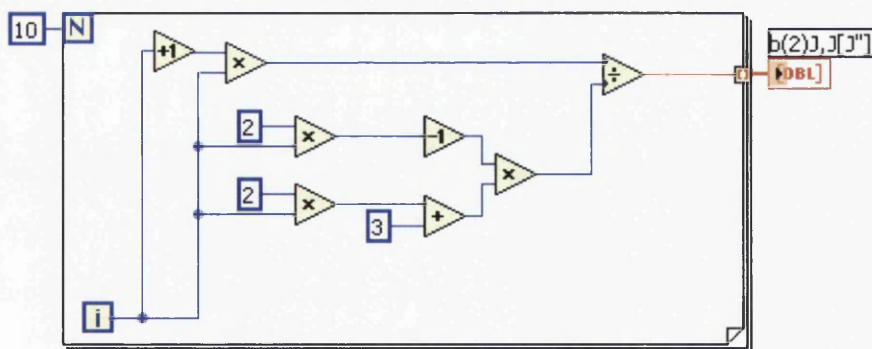


Figure A1.15 Block diagram for SpecGen\_SubVI\_b(2)J,J.vi

A1.5.7 SpecGen\_SubVI\_b(2)J+2,J.vi

This subVI generates a ten-element 1D array of the values of the Placzek-Teller *b*-factor

$b_{J+2,J}^{(2)}$ :

$$b_{J+2,J}^{(2)} = \frac{3(J+1)(J+2)}{2(2J+1)(2J+3)},$$

where  $J = J'' = 0, 1, \dots, 9$ , and  $b_{J+2,J}^{(2)}$  is always non-zero. The index of the array matches the  $J''$  value.

VI filename	SpecGen_SubVI_b(2)J+2,J.vi
Icon and connector pane	
Dependencies	N/A
Dependents	SpecGen_SubVI_Phi(a^2_g^2_q).vi

Output	Sink
"b(2)J+2,J[J'']" (1D array)	SpecGen_SubVI_Phi(a^2_g^2_q).vi

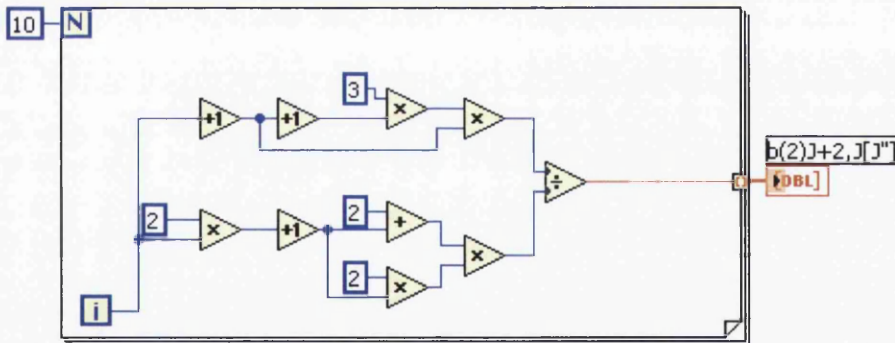
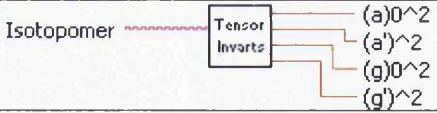



Figure A1.16 Block diagram for SpecGen\_SubVI\_b(2)J+2,J.vi





### A1.5.8 SpecGen\_SubVI\_Tensor\_Invariants.vi

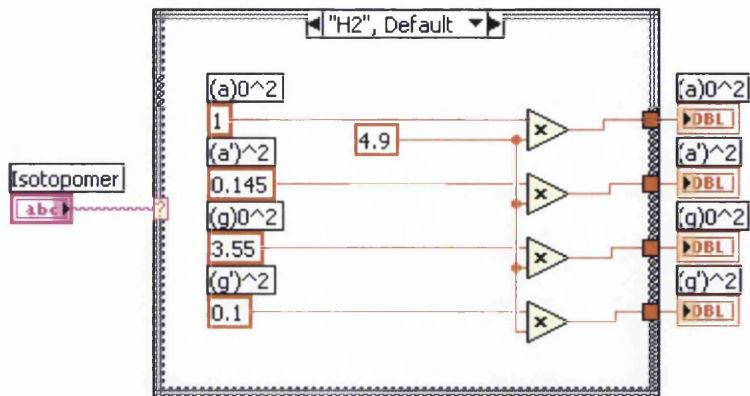
This subVI outputs the estimated relative values of the tensor invariants  $(a)_0^2$ ,  $(a')^2$ ,  $(\gamma)_0^2$ , and  $(\gamma')^2$ . These are outputted for the isotopomer specified by the input string “Isotopomer”. Valid inputs for this string are “H2” (default), “HD”, “HT”, “D2”, “DT”, and “T2”. The units of these invariants are  $\text{C}^2\text{V}^{-2}\text{m}^4\text{sr}^{-1}$ , but this is irrelevant in a relative intensity calculation (the current application).

Since the intensities calculated in the current version of *SpecGen* are relative and not absolute, so the tensor invariant values stored in this subVI are estimates of relative values. These have been fixed between the  $S_0$ -,  $O_1$ -,  $Q_1$ -, and  $S_1$ -branches for each isotopomer (i.e. the relative values of the invariants  $(a')^2$ ,  $(\gamma)_0^2$ , and  $(\gamma')^2$ ) and between isotopomers. The latter is accomplished with an overall coefficient applied to the estimated values for the invariants  $(a')^2$ ,  $(\gamma)_0^2$ , and  $(\gamma')^2$ . Note that the HD isotopomer’s tensor invariant values are unshifted (i.e. coefficient = 1), but this is an arbitrary choice.

VI filename	SpecGen_SubVI_Tensor_Invariants.vi
Icon and connector pane	
Dependencies	SpecGen_Interface.vi
Dependents	SpecGen_SubVI_Phi(a^2_g^2_q).vi

Input	Source
 “Isotopomer”	SpecGen_Interface.vi

Output	Sink
 “(a)0^2”	SpecGen_SubVI_Phi(a^2_g^2_q).vi
 “(a')^2”	SpecGen_SubVI_Phi(a^2_g^2_q).vi
 “(g)0^2”	SpecGen_SubVI_Phi(a^2_g^2_q).vi
 “(g')^2”	SpecGen_SubVI_Phi(a^2_g^2_q).vi



**Figure A1.17** Block diagram for SpecGen\_SubVI\_Tensor\_Invariants.vi ( $H_2$  case shown). The case structure outputs values for HD, HT,  $D_2$ , DT, or  $T_2$  if specified by the string "Isotopomer". The "4.9" in this case is an overall coefficient used to fix relative intensities between isotopomers. All  $H_2$  and  $D_2$  values are currently shifted in this way relative to the estimated values for the HD isotopomer.



### ***A1.6 Tier 3c: Spectral Lineshape Convolution***

At the time of writing, the only lineshape simulated by *SpecGen* is the Gaussian distribution; therefore Tier 3c currently only contains one subVI. As can be seen from the simple nature of the block diagram, writing a similar routine for Lorentzian or Voigt lineshapes would be straightforward.

#### ***A1.6.1 SpecGen\_SubVI\_Convolute\_Gaussian.vi***

This subVI calculates the value,  $\text{Gauss}(x, \mu, \sigma, n)$ , of the normalised Gaussian distribution

$$\text{Gauss}(x, \mu, \sigma, n) = \frac{n}{\sigma\sqrt{2\pi}} \exp\left[\frac{-(x-\mu)^2}{2\sigma^2}\right],$$

where  $x$  is the position variable (i.e. the wavenumber shift),  $\mu$  is the position of the line centre,  $\sigma$  is the standard deviation of the distribution, and  $n$  is the relative intensity of the Raman line being convoluted.

The standard deviation,  $\sigma$ , is related to the full width at half maximum (FWHM) by the expression:

$$\text{FWHM} = 2\sigma\sqrt{2\ln(2)}.$$

Note that increasing the  $\sigma$  value will correspondingly reduce the peak intensity, since the Gaussian distribution is normalised:

$$\int \text{Gauss}(x) dx = 1.$$

VI filename	SpecGen_SubVI_Convolute_Gaussian.vi
Icon and connector pane	
Dependencies	SpecGen_Interface.vi SpecGen_SubVI_High_Raman_Spectrum.vi
Dependents	SpecGen_Interface.vi

Input	Source
DBL "x"	SpecGen_Interface.vi
DBL "mu"	SpecGen_SubVI_High_Raman_Spectrum.vi
DBL "sigma"	SpecGen_Interface.vi
DBL "n"	SpecGen_SubVI_High_Raman_Spectrum.vi

Output	Sink
DBL "Gauss(x,mu,sigma,n)"	SpecGen_Interface.vi

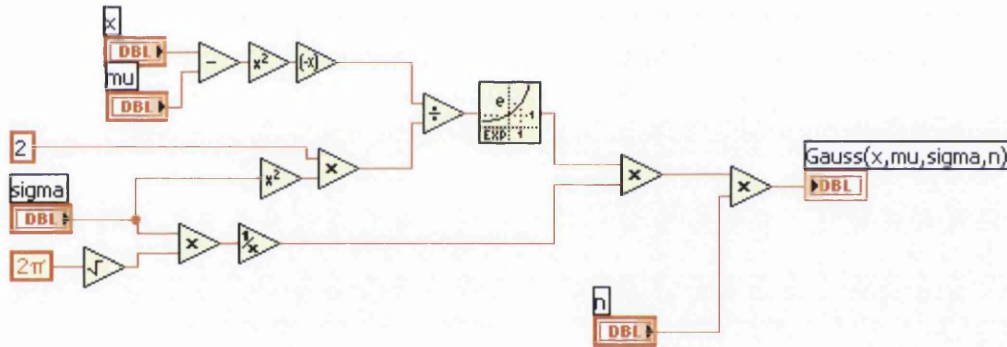


Figure A1.18 Block diagram for SpecGen\_SubVI\_Convolute\_Gaussian.vi

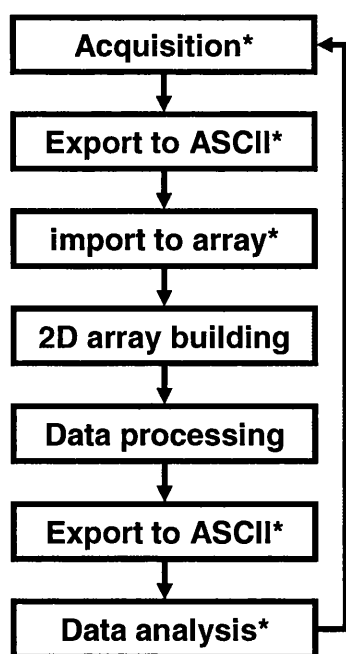
## APPENDIX A2

### POST-ACQUISITION PROCESSING AND CORRECTION OF RAMAN SPECTRA

#### (LABVIEW CODE)

This appendix provides details regarding the *LabVIEW* code used to process raw spectroscopic data exported from *WinSpec/32* and examples of control (high-level) VIs used to handle the various subVIs written for each corrective technique.

The dataflow of a typical acquisition / processing / analysis cycle is given in Figure A2.1. Note that many of the steps are manual – this matter is being addressed by the development of an integrated control program that will handle all the steps programmatically. The native .SPE file format of *WinSpec/32* is not intelligible to *LabVIEW* without the use of software such as RCubed Software Consultants' *SITK for LabVIEW*. Since such software has not yet been implemented in the current set of VIs, an export step is necessary to convert from .SPE to ASCII, which can then be imported the *LabVIEW* programs.



**Acquisition:** the user must set the acquisition parameters in *WinSpec/32* and manually start an acquisition.

**Export to ASCII:** the user must manually use the “Covert to ASCII” tool in *WinSpec/32* in order to produce ASCII files intelligible to *LabVIEW*.

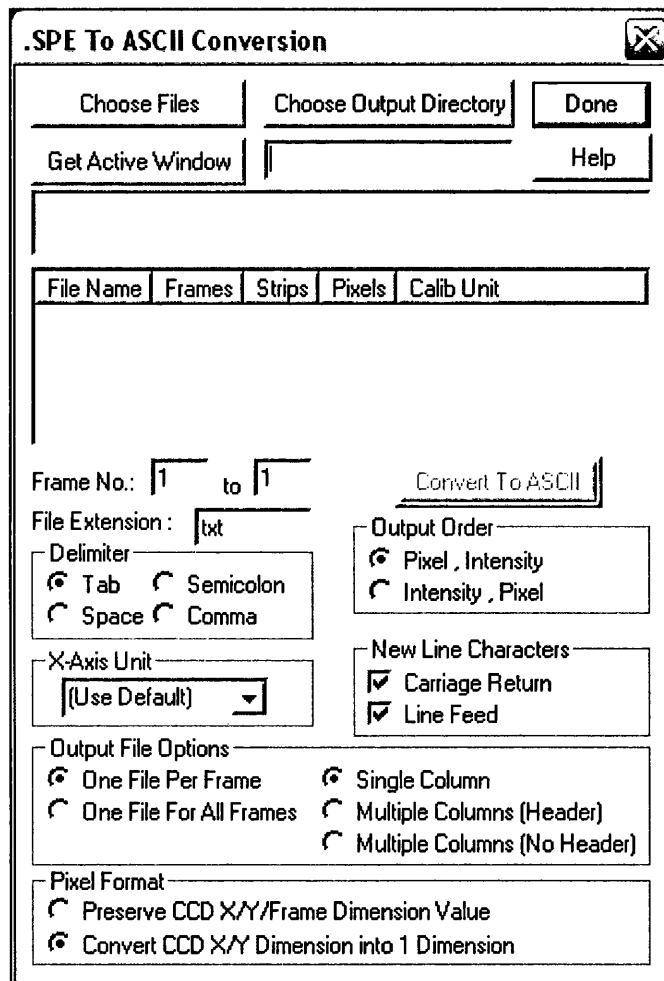
**Import to array:** the path to the file(s) to be processed must be specified to the relevant *LabVIEW* program.

**Export to ASCII:** the user must specify the path to the output file.

**Data analysis:** the data analysis package *Origin* is currently used to interpret data.

**Figure A2.1** Typical dataflow for correction of 2D spectra. The steps flagged with an asterisk (\*) currently require input from the user per cycle.

A note should be made here of the format of the exported ASCII files, since at the present time the VIs included here are not polymorphic with regard to the format of the ASCII files. Figure A2.2 shows the export format options in the “Convert to ASCII” tool window of *WinSpec/32* that is appropriate to the VIs in this appendix. The window shown is from version 2.5.19.7 of *WinSpec/32*, and may well be different in later versions.



**Figure A2.2** Export options used to specify the correct ASCII format required by the (currently) non-polymorphic VIs detailed in this appendix.

The output options may be summarised as follows:

Parameter	Value / Setting
Delimiter	Tab
Output Order	Pixel, Intensity
X-Axis Unit	(Use Default) – this is ignored in any case –
New Line Characters	Carriage Return and Line Feed
Output Files Options	One File Per Frame, Single Column
Pixel Format	Convert CCD X/Y Dimension into 1 Dimension

A file exported in this manner will be a two-column ASCII file with the calibration (“X-Axis Unit”) in the first column. This internal calibration is ignored in favour of a (more accurate) calibration performed externally using *Origin* to find the pixel positions of known peaks (using calibration lamps) and thus perform a calibration with a large number of points (*WinSpec/32* is limited to ten points). When imported without transposition, the first (calibration) column (column 0) is ignored and the second (intensity) column (column 1) is generally built into a 512×2048 (row x column) 2D array that corresponds to the dimensionality of the CCD chip. Once in 2D array form, the data can easily be visualised and the code becomes conceptually simpler\*.

In this thesis, the majority of files were single frames, i.e. binnings of multiple acquisitions. Note that this is binning in the sense of summation of entire 2D arrays and not in the sense of binning rows or columns ‘within a file’ to produce a 1D array. For example, the .SPE file containing the data of a 5×1000s acquisition would be a single 2D array of values (we can discount *WinSpec/32*’s internal calibration data for now). This is because each 1000s acquisition is summed with those already in memory. Single frames share the same format when exported to ASCII regardless of the number of acquisitions. The VIs that subsequently import the data can therefore be non-polymorphic, and hence simpler. A further advantage is that each correction (astigmatism, cosmic ray events, etc.) need only be applied once per file, and so the correction procedure is quicker. The binning also averages out the variations in background noise as the square root of the number of acquisitions.

---

\* TrigCRR.vi and RCRR\_SubVI.vi are exceptions since they do not include this array building step during import, passing the corrected data out in the same form as it was imported.

The disadvantages of such a single-frame approach are that cosmic ray events will tend to dominate for large numbers of long acquisitions, and the beneficial effects of a background subtraction are diminished. From the point of view of data quality, it would be preferred to treat each frame individually. It can be specified in *WinSpec/32*'s "Experimental Setup" options to not bin each frame, in which case a 5×1000s export would either be five separate files of the same dimensionality (2D) as a binned 'single-frame' file, or a longer single file, depending on the export options chosen. In the former case, a control program has to be specifically written to handle multiple files (see Section A2.3 for an example). In the latter case, a degree of polymorphic capability has to be written into the importing VI to handle the varying file size. This latter option may well become feasible when direct *LabVIEW* handling of .SPE files is realised, since the export / import step would be removed from the dataflow.

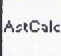
## ***A2.1 Astigmatism Correction***


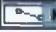
The principles behind the astigmatism correction routine *AstCorr.vi* have been detailed in Section 4.8, and will not be repeated here. *AstCalc.vi* and *AstCorr.vi* are standalone programs that are easily adaptable to subVIs, although they do not appear as discrete nodes in currently used high-level handling programs (see Section A2.3) since the core code of the astigmatism correction routine *AstCorr.vi* forms (directly) the basis of *DCRR\_SubVI.vi* (see Sections A2.2.3 and A2.3 further below). *AstCalc.vi* and *AstCorr.vi* require the form of ASCII file detailed above for spectrum files.




### ***A2.1.1 AstCalc.vi***

The application *AstCalc.vi* was written to automate the process of calculating the astigmatism curve. Although effective, *AstCalc.vi* requires that the spectrum be free of cosmic ray events and that there be only one very strong line on the trace. It is therefore advisable to use a short (<1s) acquisition of a laser line (the 632.816nm HeNe emission is perfectly adequate for the region of interest covered in this thesis) with as narrow an entrance slit as possible. The 25.4µm minimum slit width of the Spec-10, for example, corresponds to a FWHM for the HeNe line of about 2 pixels.

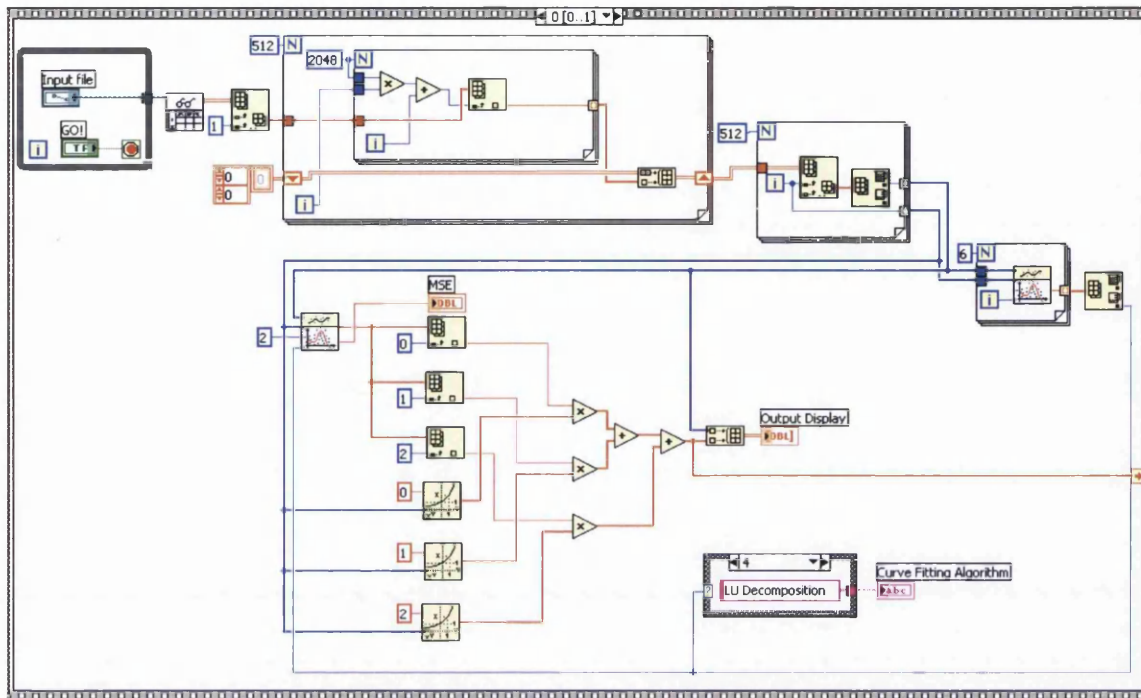
The user specifies the location of the spectrum file with the front panel control “Input file”. The remainder of the process is automatic. The program imports the ASCII file specified and builds column 1 (the concatenated y-values of each of the 512 rows) into a 512×2048 2D array. Each of the 512 rows is then scanned and the index (corresponding to the pixel#) of the maximum value is noted and stored in a 512-element 1D array. A second-order polynomial curve fit is then performed for six different curve fitting algorithms, namely SVD, Givens, Givens2, Householder, LU Decomposition, and Cholesky fits. The fit that minimises the mean square error of the fit is repeated and the value of the curve at row indices 0 to 511 is passed as a 1D array of double-precision numbers. Each of these values is then subtracted from the value of the central row (row#256, i.e. array index 255) and the results exported to an ASCII file. This file provides the required (fractional) row shifts that can then be used by AstCorr.vi.

VI filename	AstCalc.vi
Icon	
Dependencies	N/A (Stand-alone application)
Dependents	N/A

User-defined input (front panel control)	Purpose
 “GO!” (governs WHILE loop)	Executes main section of program
 “Input file”	Specifies path of spectrum ASCII file

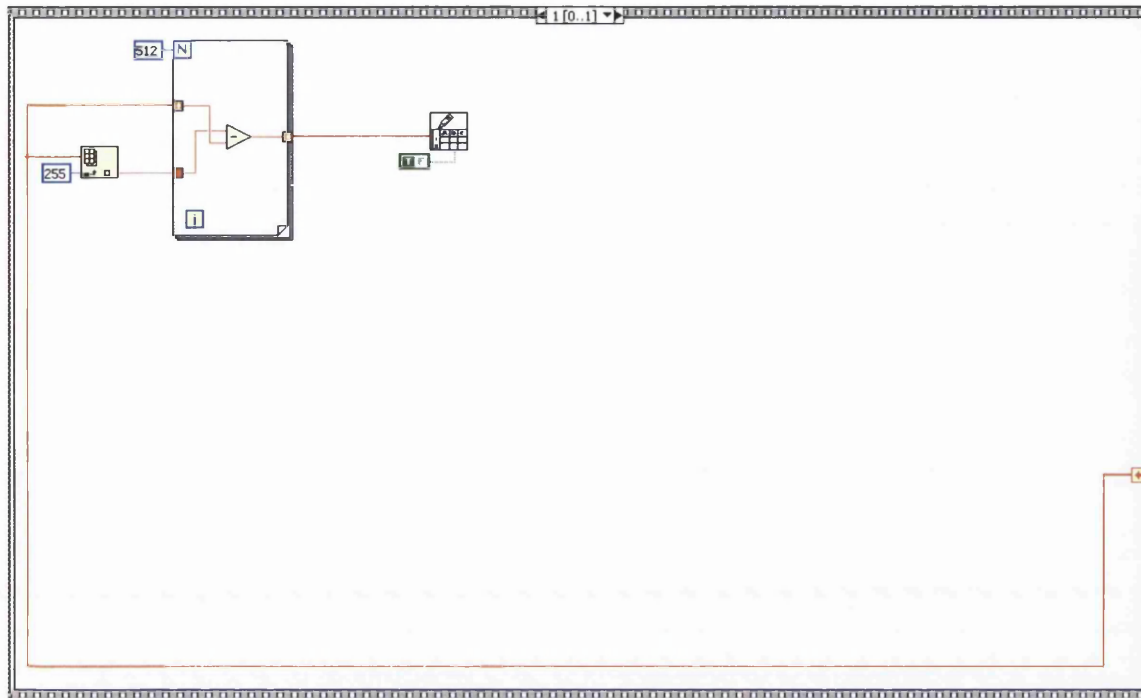
Front panel indicator	Purpose
 “Output display” (2D array)	Displays the position of the maximum values (white) of the imported spectrum and the best curve fit (red) to be exported
 “MSE”	Displays the mean square error of the best fit
 “Curve Fitting Algorithm”	Displays the curve fitting algorithm that minimised the mean square error (MSE)

The exporting of the astigmatism file is handled by the system VI “Write To Spreadsheet File.vi”. Note that a TRUE Boolean constant has been wired to the “transpose?” terminal (this is FALSE by default) in order to ensure the correct form of the ASCII file required by AstCorr.vi – i.e. a single column of double-precision numbers.



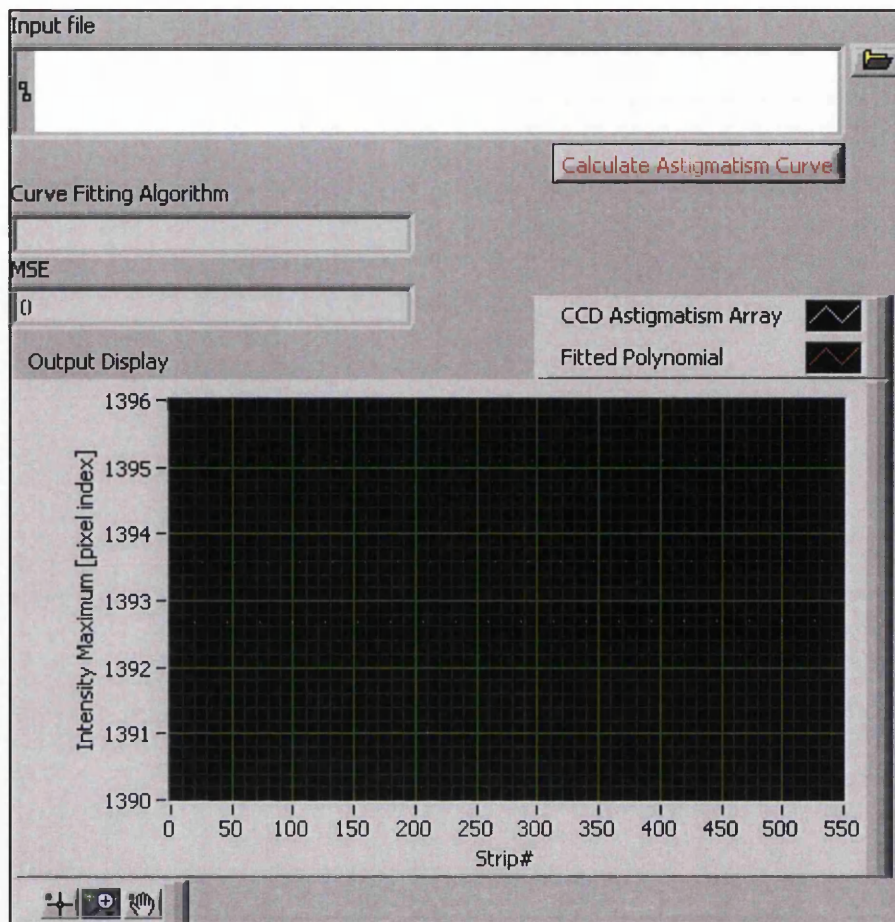
**Figure A2.3** Block diagram for AstCalc.vi (sequence structure frame 1 of 2 shown). Note the first set of nested FOR loops that build column 1 of the imported ASCII file into a conceptually simpler 512×2048 array. The second FOR loop determines the position (index) of the maximum value of each of the 512 rows, and the third performs the six fits and reports the MSE. The best fit is then repeated, the result reported to the front panel indicator “Output Display” and the fit passed to the second sequence structure frame.





**Figure A2.4** Block diagram for AstCalc.vi. (sequence structure frame 2 of 2 shown). In this last FOR loop, the fitted values for the maximum position are subtracted from the value at the central row (row#256, i.e. array index 255) and passed to “Write To Spreadsheet File.vi” for export to ASCII format. Note the TRUE Boolean constant wired to the “transpose?” terminal (FALSE by default) to ensure correct dimensionality of the exported ASCII file.

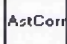
On execution the user should use the browse button on the “Input file” path control to specify the location of the spectrum file before pressing the “GO!” Boolean (labelled as “Calculate Astigmatism Curve” on the front panel). If a path is not specified, then the user will be prompted after pressing “GO!” to specify a path by the “Read From Spreadsheet File.vi” node. The export dialog comes up automatically at the end of an execution cycle since the “path” terminal on the “Write To Spreadsheet File.vi” node has been left unwired.










**Figure A2.5** Front panel of AstCalc.vi. Note that the range of the y-axis (“Intensity Maximum [pixel index]”) has been limited to the relevant interval for the extent of the astigmatism (this is done automatically by *LabVIEW*).

A2.1.2 *AstCorr.vi*

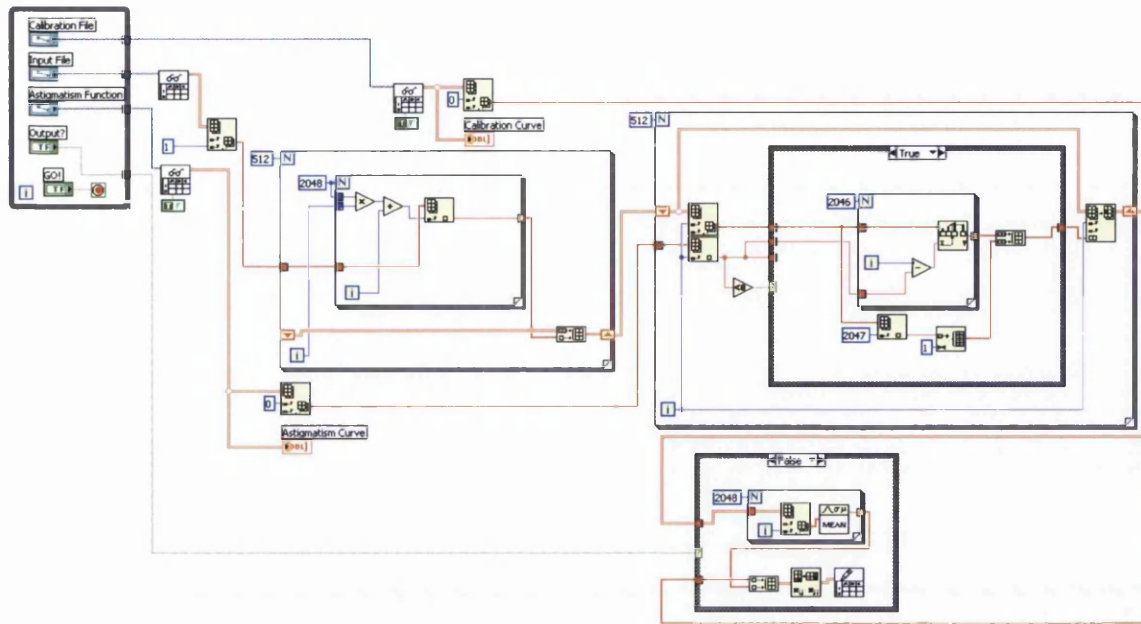
This VI corrects the astigmatism in the input spectrum ASCII file referenced by “Input File” by using fractional value interpolation on a per-row basis. The required shifts are specified by the ASCII file referenced by “Astigmatism Function”. Calibration values are specified by the “Calibration File” path control, and the user has the option of exporting the corrected spectrum in binned ( $2 \times 2048$  array) or matrix ( $513 \times 2048$  array)<sup>†</sup> form. As in the case of *AstCalc.vi*, the 1D column of spectrum intensity values is built into a  $512 \times 2048$  2D array before processing for easier handling.

VI filename	AstCorr.vi
Icon	
Dependencies	N/A (Stand-alone application)
Dependents	N/A

User-defined input (front panel control)	Purpose
 “Output?”	Selects form of exported ASCII file. Governs final case structure. If TRUE the data is exported in matrix form, if FALSE the data is binned across rows and exported in (x,y) form.
 “GO!” (governs WHILE loop)	Executes main section of program
 “Calibration File”	Specifies path of calibration ASCII file
 “Input File”	Specifies path of spectrum ASCII file
 “Astigmatism Function”	Specifies path of astigmatism function ASCII file (e.g. <i>AstCalc.vi</i> output)

Front panel indicator	Purpose
 “Calibration Curve”	Displays the pixel to nanometre calibration curve obtained from the ASCII file specified by the path control “Calibration Curve”.
 “Astigmatism Curve”	Displays the astigmatism function (required shifts) obtained from the ASCII file specified by the path control “Astigmatism Function”.

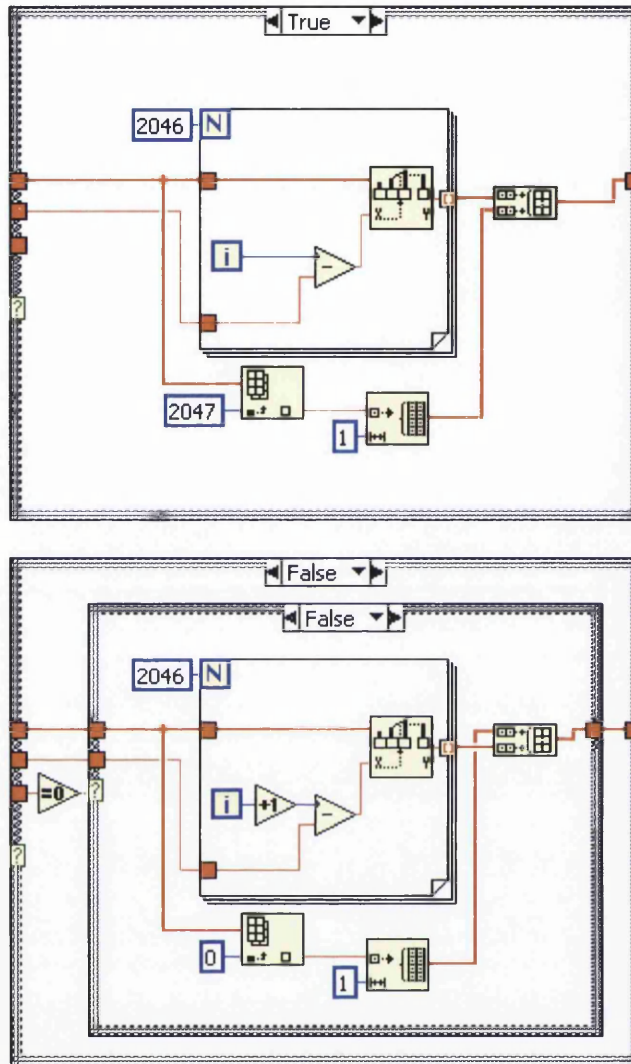
<sup>†</sup> The ‘additional’ row (row#513) contains the calibration values.



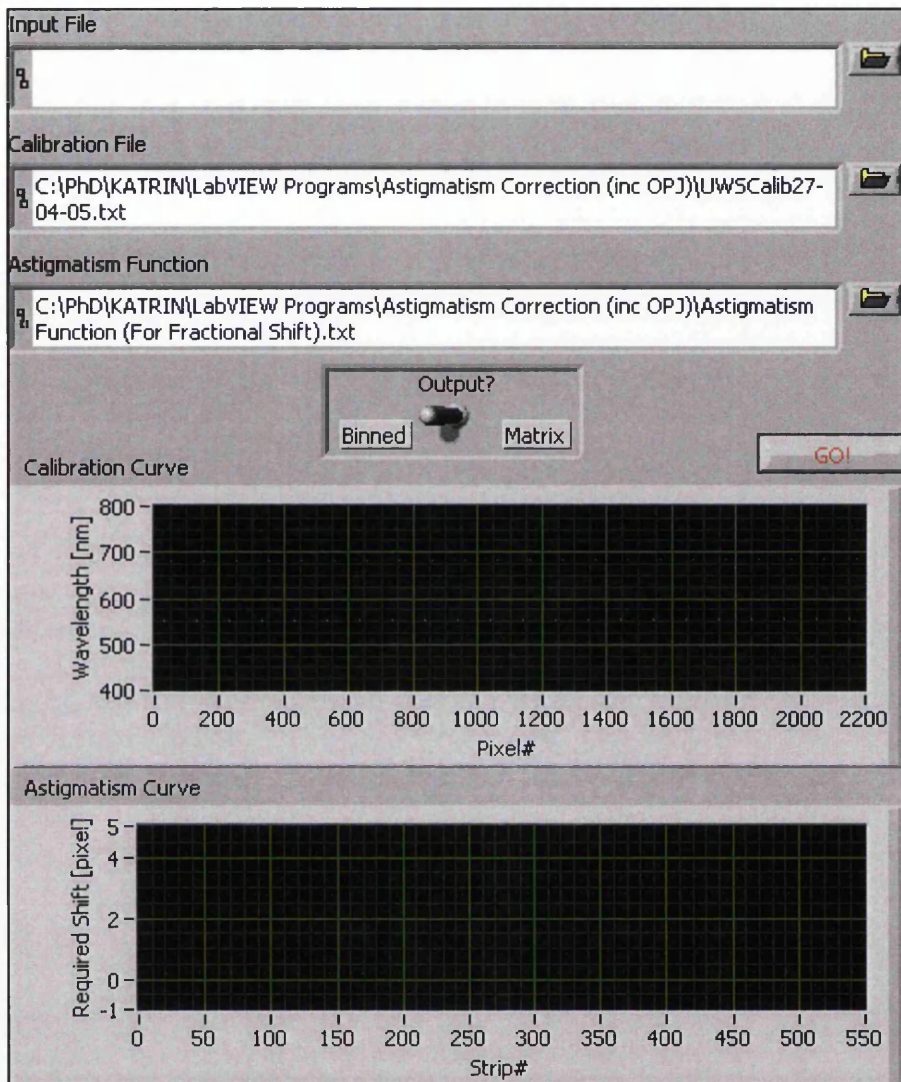
**Figure A2.6** Block diagram for AstCorr.vi. Note the nested FOR loops (left) that build the intensity values into a 512×2048 array. The FOR loop to the right contains the “Interpolate 1D Array.vi” node that provides the fractional shift of each row. The nested case structure provides handling for the three shift regimes, namely shift < 0, shift = 0, and shift > 0 (see Figure A2.7). The case structure at the end of the data flow handles the export of either binned (“Output?” Boolean = FALSE) or matrix (“Output?” Boolean = TRUE) form. Note the use of TRUE Boolean constants on the “Read From Spreadsheet File.vi” nodes for the “Astigmatism Function” and “Calibration File” paths.

The case structures containing the interpolation code can handle shifts of either sign as well as the trivial zero shift value at row#256 as shown in Figure A2.7.

On execution the user should use the browse buttons on the path controls to specify the location of the required ASCII files before pressing the “GO!” Boolean. If any of the paths are not specified, then the user will be prompted after pressing “GO!” to specify the missing paths by the relevant “Read From Spreadsheet File.vi” nodes. The export dialog comes up automatically at the end of an execution cycle since the “path” terminal on the “Write To Spreadsheet File.vi” node has been left unwired.



**Figure A2.7** Forms of the interpolation case structure for non-zero shift regimes. Top: shift  $< 0$ , Bottom: shift  $\geq 0$ . If correctly aligned, the central row (row#256, index 255) should be zero shift and shifts for the rows either side should be of the same sign. This case structure allows for slight misalignments of the system. If the daughter case structure in the lower diagram was TRUE (corresponding to zero shift), then the 1D array (thick orange wire entering the case structure at top left tunnel) is passed unshifted.



**Figure A2.8** Front panel of AstCorr.vi. The “Binned” option (“Output?” Boolean = FALSE) is usually the most appropriate and is a  $2 \times 2048$  2D array with the calibration in column 0 – the 512 rows are binned. The “Matrix” option (“Output?” Boolean = TRUE) outputs a  $513 \times 2048$  2D array with the calibration in column 0, and is the option to select if further per-row processing is required or if the surface map of the data is required (in the case of an *Origin* matrix, for example). The calibration can be subsequently ignored if required.

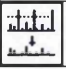
## *A2.2 Cosmic Ray Event Removal*

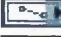




The principles behind the three cosmic ray removal techniques, viz. (i) substitution of a mean value for those above a threshold value, (ii) passing the lower value in a sequential row comparison, and (iii) double differential methods with respect to the direction orthogonal to the extent of spectral lines, have been covered in Section 4.8 and will not be repeated here. The threshold technique was applied in TrigCRR.vi, which is a standalone application. The more advanced techniques have been written as subVIs that can be integrated in higher-level programs such as demonstrated in Section A2.3.

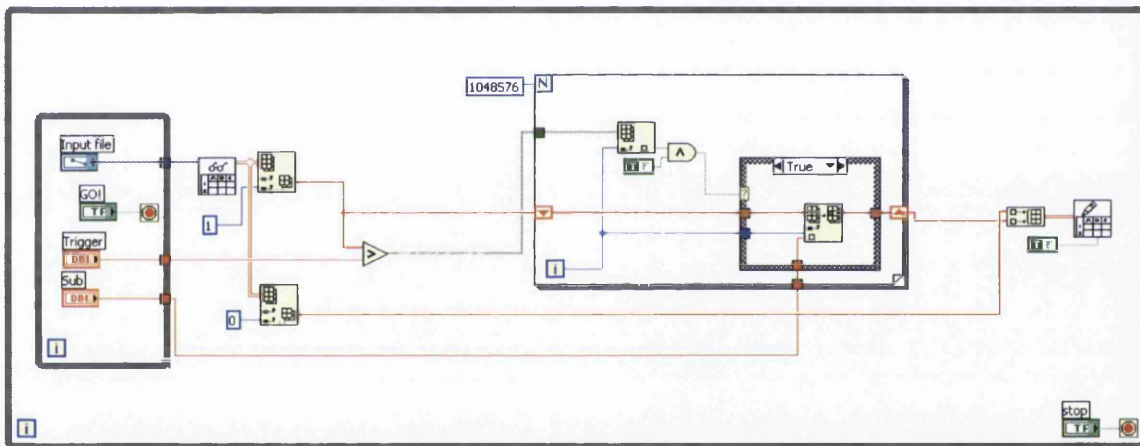
It should be noted that while TrigCRR.vi and RCRR\_SubVI.vi only apply cosmic ray correction to an input ASCII file, DCRR\_SubVI is an integrated cosmic ray removal and astigmatism correction routine. As in the case of the astigmatism correction routines, the cosmic ray event removal VIs require the spectrum ASCII file to be in the form specified in the preamble to this appendix.

### *A2.2.1 TrigCRR.vi*

TrigCRR.vi imports the ASCII file specified by “Input file” as a 2D array. The value of each element in column 1 (intensity) is compared to the value specified by “Trigger”. If the value of the element is greater than that of “Trigger”, it is replaced by the value specified by “Sub”. Column 0 (calibration values) is passed without alteration; its data are rebuilt into the 2D array which is then exported by the “Write To Spreadsheet File.vi” node. The TRUE Boolean constant is wired to the “transpose?” terminal of the “Write To Spreadsheet File.vi” node (FALSE by default) in order to preserve the orientation of the data. The exported ASCII file is then in the correct format to be treated by AstCalc.vi and / or AstCorr.vi.

VI filename	TrigCRR.vi
Icon	
Dependencies	N/A (Stand-alone application)
Dependents	N/A

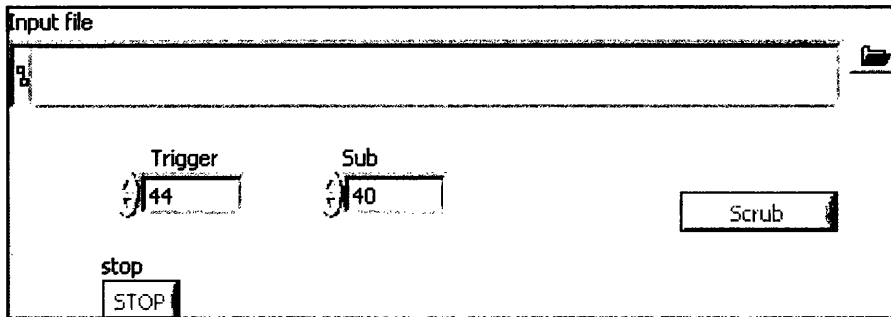
User-defined input (front panel control)	Purpose
 "Input file"	Specifies path of spectrum ASCII file
 "GO!" (Governs daughter WHILE loop)	Executes main section of program
 "Stop" (Governs mother WHILE loop)	Ends program when read by mother WHILE loop
 "Trigger"	Sets trigger value for comparison
 "Sub"	Sets value to be substituted in all elements of value greater than that specified by "Trigger"



**Figure A2.9** Block diagram for TrigCRR.vi. Note that the calibration column is rebuild into the 2D array before export. The TRUE Boolean constant wired to the "transpose?" terminal of the "Write To Spreadsheet File.vi" node (FALSE by default) preserves the format of the original data.

The front panel of TrigCRR is very simple. The user specifies the threshold ("Trigger") and substitution ("Sub") values to apply to a spectrum, and should use the browse button on the "Input file" path control to specify the location of the spectrum file before pressing the "GO!" Boolean (labelled as "Scrub" on the front panel). If a path is not specified, then the user will be prompted after pressing "GO!" to specify a path by the "Read From Spreadsheet File.vi" node. The export dialog comes up automatically at the end of an execution cycle since the "path" terminal on the "Write To Spreadsheet File.vi" node has been left unwired. The user should then specify the location of the next file to be cleaned (if applicable). The "stop" Boolean ends the program.





**Figure A2.10** Front panel for TrigCRR.vi. Showing the threshold (“Trigger”) and substitution (“Sub”) controls set at typical values for low-intensity signal spectrum cosmic ray event correction.

### A2.2.2 RCRR\_SubVI.vi

RCRR\_SubVI.vi performs row-comparison cosmic ray event correction on an  $N \times 2048$  array, where  $N$  is any integer greater than one. For each of the 2048 columns, the value of each row (i.e. element in the 1D subarray) is compared with the value of the next row and the lower of the two values is passed. The last row is compared with the first row in order to maintain the dimensionality of the input array. The value of an element of the passed array,  $P_{ij}$ , can be expressed in terms of the values of elements of the input array,  $A_{ij}$ , as

$$P_{ij} = \begin{cases} A_{ij} & \text{if } A_{ij} < A_{i+1,j} \\ A_{i+1,j} & \text{if } A_{i+1,j} < A_{ij} \end{cases},$$

where  $i$  is the row index and  $j$  is the column index.

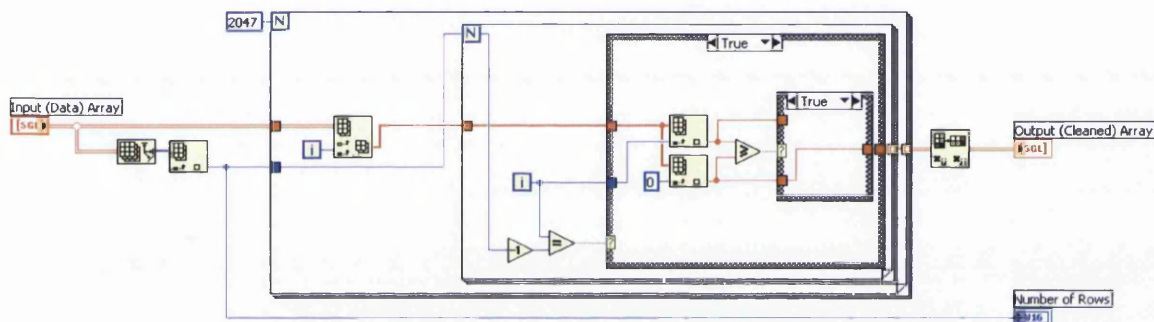
Unlike TrigCRR.vi, RCRR\_SubVI.vi is designed to be used in a high-level program as a discrete subVI node. It should be noted, however, that since this subVI does not build a 2D array from an imported ASCII file as with the astigmatism correction routines, this (necessary) step should be performed in the high-level program or a preceding node in the dataflow.

RCRR\_SubVI.vi passes the corrected data out in the same form as it was inputted (2D array), and additionally outputs the number of rows ( $N$ ) to (optionally) indicate the dimensionality of the output array.

VI filename	RCRR_SubVI.vi
Icon and connector pane	<div style="display: flex; align-items: center; gap: 10px;"> <span>Input (Data) Array</span> <span>Output (Cleaned) Array</span>  <span>Number of Rows</span> </div>
Dependencies	Control / higher-tier VI (provides 2D input array)
Dependents	Control / higher-tier VI (obtains output array)

Input	Source
“Input (Data) Array” (2D array)	Control / higher-tier VI

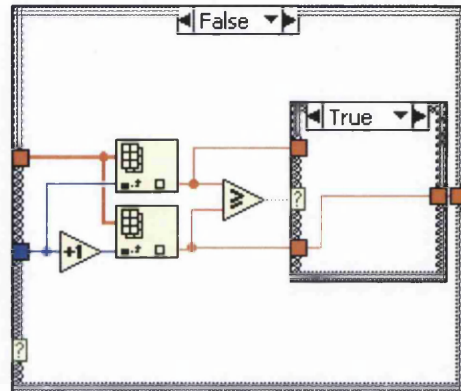
Output	Sink
“Output (Cleaned) Array” (2D array)	Control / higher-tier VI
“Number of rows”	Control / higher-tier VI



**Figure A2.11** Block diagram for RCRR\_v1.1\_SubVI.vi. The mother case structure handles the case of whether or not the last row is being compared (see Figure A2.12), while the daughter case structures pass the lower of the two values presented to the “Greater Or Equal Than” node. The case shown here is that of the last row being interrogated – the case structure compares this value with that of the first row so that it has a value to be compared with and thus preserve the dimensionality of the input subarray.

It is recommended that the astigmatism correction be performed before sending the data through RCRR\_SubVI.vi as the astigmatism correction routines contain the 2D array building code and will align the first and last rows correctly so that they can be meaningfully compared. For example, if one wanted to include RCRR\_SubVI.vi in the AstCorr.vi code, the 2D data array output tunnel in the FOR loop containing the interpolation code should be wired to RCRR\_SubVI.vi’s “Input (Data) Array” terminal, and the array from RCRR\_SubVI.vi’s “Output (Cleaned) Array” terminal could then be reintroduced into the dataflow as in AstCorr.vi.

Figure A2.12 shows the form of the daughter case structure that compares element  $A_{ij}$  with element  $A_{i+1,j}$ .




**Figure A2.12** Case structure form for the first 2047 rows. The interrogated array element is compared with the value of the next element in the subarray.

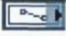

### A2.2.3 DCRR\_SubVI.vi

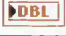
DCRR\_SubVI.vi is the most sophisticated of all the cosmic ray event removal routines, and the most effective. In its current implementation, a single-frame ASCII file can be cleaned almost entirely of cosmic rays, even for very long exposure times, uneven backgrounds, and ultra-low signal levels. DCRR\_SubVI.vi differs from TrigCRR.vi and RCRR\_SubVI.vi in that it includes the astigmatism correction step in its code.

The following is a brief overview of the subVI operation. DCRR\_SubVI.vi imports the ASCII file specified by “input file path”, discards the *WinSpec/32* calibration, builds a 512×2048 2D array from column 1 and applies the astigmatism correction specified by the array wired to the “astigmatism array” input terminal. This section of the code is identical to AstCorr.vi. The VI then performs a double differentiation of the array in the direction of the axis parallel to the direction of constant pixel# (column index), in other words orthogonal to the axis parallel to the calibration axis. See section 4.8 for a more detailed summary. The values of the elements of the doubly differentiated array are compared with a threshold value, and those above the threshold value are indexed in a 512×2048 Boolean array. This array is then used to specify which elements should be replaced from the data

array<sup>‡</sup>, which are replaced by a specified type of average over the column to which the element belongs. The array is then passed in the same 512×2048 form to the output terminal “cleaned array”. The dataflow is dealt in more detail below.

VI filename	DCRR_SubVI.vi
Icon	
Dependencies	Control / higher-tier VI (provides path to ASCII file and astigmatism array)
Dependents	Control / higher-tier VI (obtains output array)

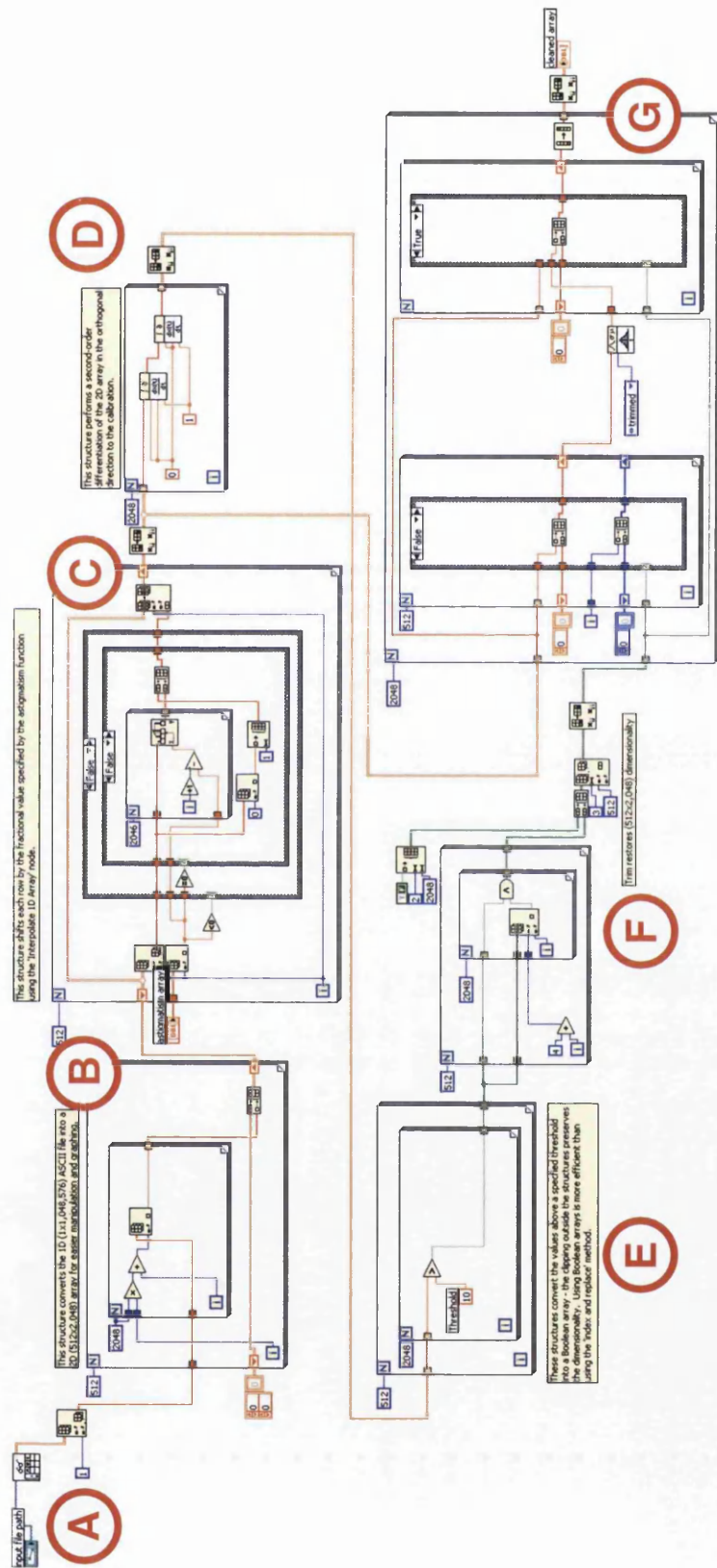
Input	Source
 “input file path”	Control / higher-tier VI
 “astigmatism array” (1D array)	Control / higher-tier VI (1×512 format)

Output	Sink
 “cleaned array” (2D array)	Control / higher-tier VI (512×2048 format)

The block diagram of DCRR\_SubVI.vi is quite complicated as can be seen in Figure A2.13. To ease interpretation of the code, labels have been placed on the diagram to remind the user of the purpose of each code segment. The labels A,B,C,... represent the direction of dataflow.

The elements of DCRR\_SubVI.vi are now treated in more detail, following the alphabetical labelling given in Figure A2.13.

<sup>‡</sup> The double differentiation produces a distinct pattern around pixels containing cosmic ray events, but is essentially blind to the variation in intensity of spectral lines in the direction parallel to the row index.



**Figure A2.13** Block diagram for DCRR\_SubVI.vi. The alphabetic labels A,B,C,... represent the direction of dataflow through major code segments.

**Segment A:** file import handling.

**Segment B:** 512x2048 2D array building.

**Segment C:** astigmatism correction routine.

**Segment D:** double differentiation of the data array in the direction of constant column index.

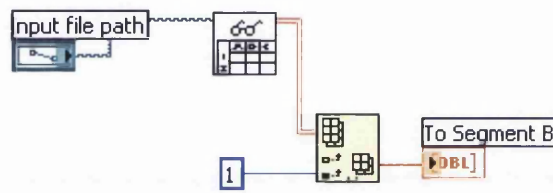
**Segment E:** comparison of elements of doubly differentiated array passed by segment D with threshold value, passing of Boolean array with TRUE elements in the position of values greater than "Threshold".

**Segment F:** pattern recognition to specify location of cosmic events.

**Segment G:** replacement of cosmic ray event containing elements with specified type of column average.

#### A2.2.4 DCRR\_SubVI.vi (Segment A)

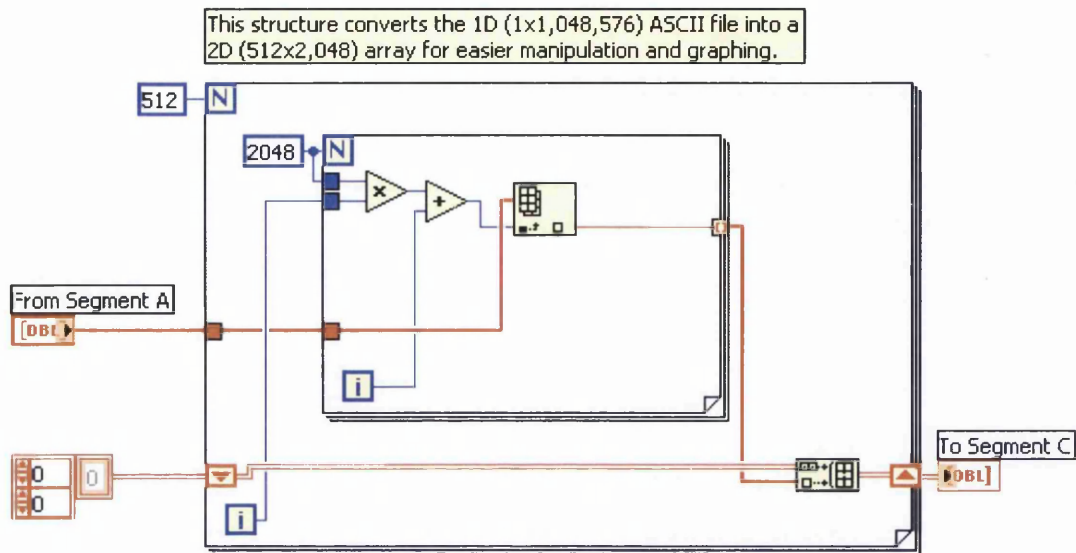
Segment A handles the import of the ASCII file. Since the export from *WinSpec/32* was chosen to coincide with the defaults of the “Read From Spreadsheet File.vi” node, the only terminal that is wired is that of “input file path”, which corresponds to DCRR\_SubVI.vi’s input terminal. The “1” wired to the column index selects column 1 (the intensity column) from the ASCII file and passes it as a 1D array to segment B.



**Figure A2.14** Block diagram for DCRR\_SubVI.vi (Segment A). This segment handles the import of the ASCII file specified by “input file path”.

#### A2.2.5 DCRR\_SubVI.vi (Segment B)

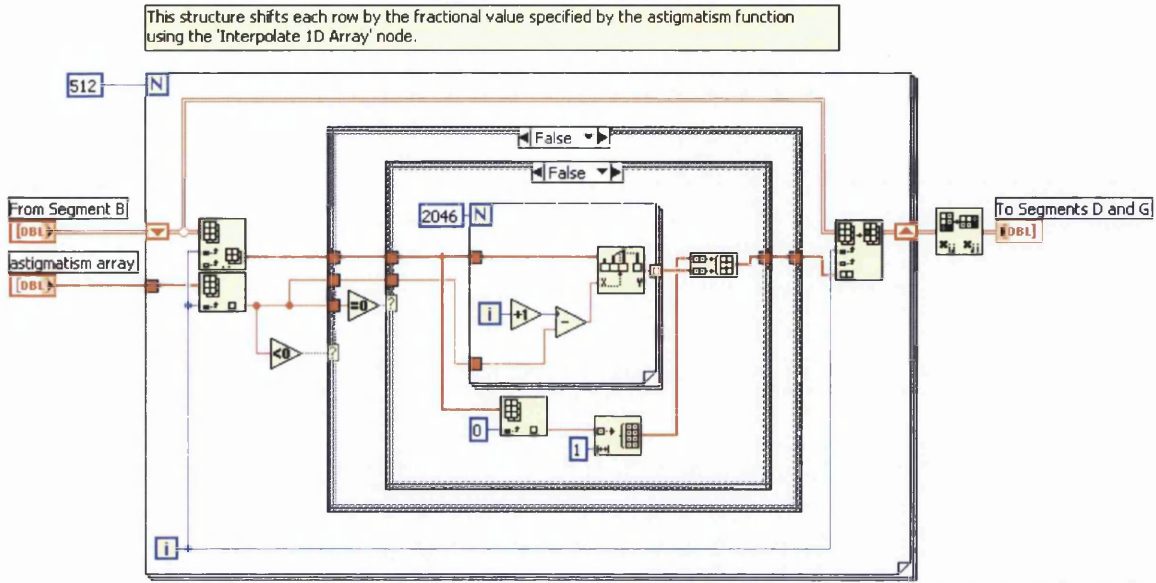
Segment B uses the same nested FOR loop structure as *AstCalc.vi* and *AstCorr.vi* to convert the  $1 \times 1,048,576$  1D array passed by Segment A into the conceptually simpler  $512 \times 2048$  2D array, which is then passed to Segment C. Note the use of a void array constant at the input terminal of the shift register. This prevents retention of the data array in the case of multiple calls of DCRR\_SubVI.vi in higher-level programs – if the void array constant was not wired, the previous data segment (still retained in memory) would be added to the new array, resulting in a  $512N \times 2048$  2D array containing the current data and the  $N-1$  sets of older  $512 \times 2048$  data, where  $N$  is the number of times DCRR\_SubVI.vi had been called in the current session. This would clearly be disastrous for the program.



**Figure A2.15** Block diagram for DCRR\_SubVI.vi (Segment B). This segment handles the building of a 512x2048 array from the 1x1,048,576 1D array passed from segment A.

#### A2.2.6 DCRR\_SubVI.vi (Segment C)

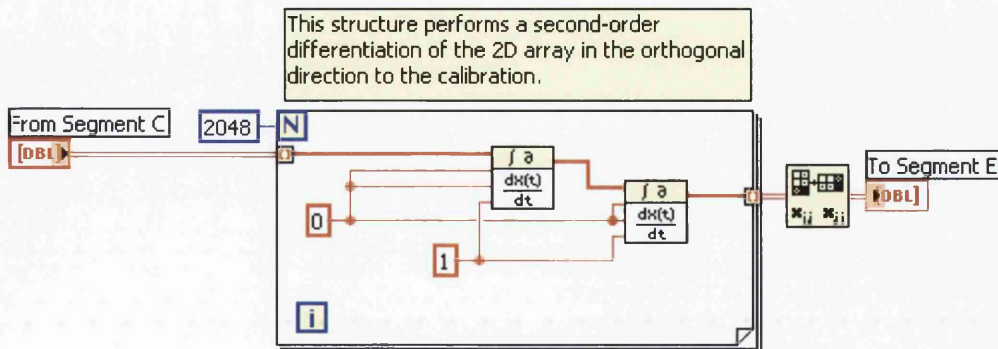
Segment C's code is mostly identical with the interpolation routine used in AstCorr.vi. It shifts each row fractionally by the amounts specified in "astigmatism array" (1x512 1D array). See Section A2.1.2 for details regarding the structure of this segment. The only real difference between Segment C and the corresponding section of code in AstCorr.vi is the addition of a "Transpose Array" node at the exit terminal of the shift register. This is in order to flip the axis referenced by the auto-indexing terminal in Segment D from rows to columns (see section A2.2.7). The output 2048x512 array (note transposition) is passed to both segment D and G.



**Figure A2.16** Block diagram for DCCR\_SubVI.vi (Segment C). This segment applies the astigmatism correction in the same manner as AstCorr.vi, and then passes the corrected array in transposed form.

*A2.2.7 DCCR\_SubVI.vi (Segment D)*

Segment D performs a double differentiation on the values of each columnar subarray, i.e. the column index is held constant and is doubly differentiated along its 512 elements. The 2048x512 2D array passed from the FOR loop is transposed and passed to Segment E as a 512x2048 2D array.

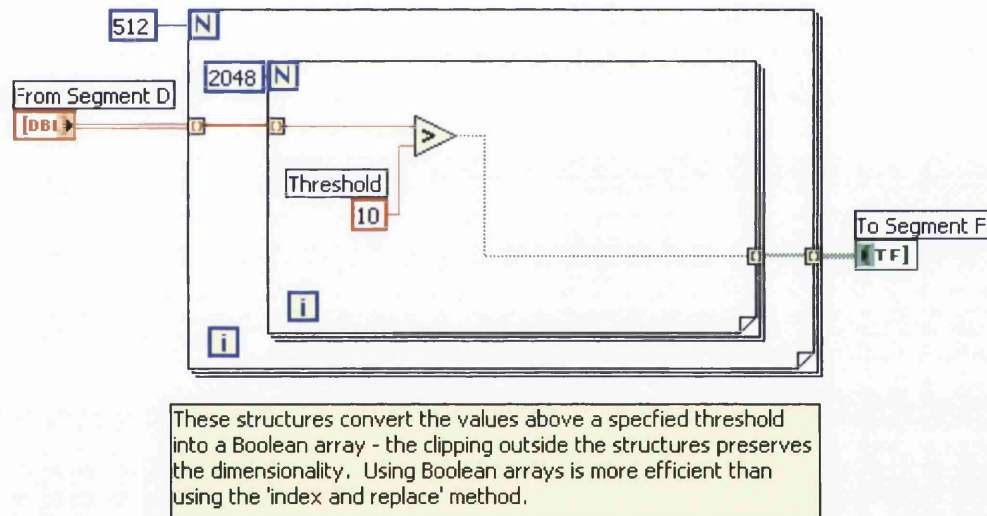


**Figure A2.17** Block diagram for DCCR\_SubVI.vi (Segment D). This segment applies a double differentiation to the transposed astigmatism-corrected 2048x512 array passed from Segment C, transposes the array back to 512x2048 form and passes the result to Segment E.



### A2.2.8 DCRR\_SubVI.vi (Segment E)

Segment E is rather similar to TrigCRR.vi in that every element of the  $512 \times 2048$  array passed from Segment D is compared with a threshold value. Unlike TrigCRR.vi, however, the result of the comparison is passed as a  $512 \times 2048$  Boolean array. This is more efficient than indexing and replacing each element of the array, since the cosmic rays are not in the same position as the TRUE elements of this Boolean array. It is much quicker to perform pattern recognition on an array of Boolean elements than that of double-precision numbers. Section 4.8.2 discusses the distinct pattern formed by cosmic ray events and will not be repeated here. Segment E passes the Boolean array to Segment F for pattern recognition.



**Figure A2.18** Block diagram for DCRR\_SubVI.vi (Segment E). This segment generates a  $512 \times 2048$  2D Boolean array referencing each element whose value is greater than that specified by the constant “Threshold” and passes the result to Segment F for pattern recognition.

At the present time, the value of the threshold is arbitrarily chosen to be constantly equal to 10. This value was found by trial and error to detect the majority of cosmic ray events without significant adverse effects on “good” pixels. It is planned to replace this method with a more statistically rigorous approach in future versions of DCRR\_SubVI.vi.

### A2.2.9 DCRR\_SubVI.vi (Segment F)

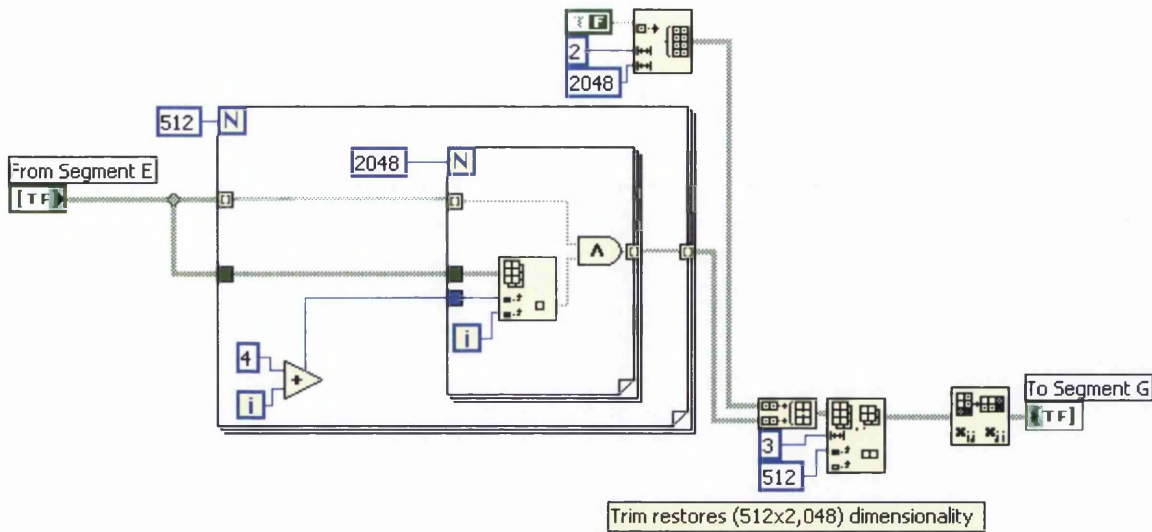
Segment F works on the 512×2048 Boolean array passed by Segment E in order to detect the distinct pattern (TRUE, FALSE, FALSE, FALSE, TRUE) produced by a cosmic ray event along each row. The pixel containing the cosmic ray event itself is in the central pixel between the two true values. Therefore, if the pattern

<b>TRUE</b>	<b>FALSE</b>	<b>FALSE</b>	<b>FALSE</b>	<b>TRUE</b>
-------------	--------------	--------------	--------------	-------------

is detected (by using an AND logical statement), then the program infers the position of the cosmic ray event in the central pixel and flags it as TRUE in the output array, therefore specifying the position of the event. The effective command to the output array is then

<b>NO CHANGE</b>	<b>NO CHANGE</b>	<b>FLAG TRUE</b>	<b>NO CHANGE</b>	<b>NO CHANGE</b>
------------------	------------------	------------------	------------------	------------------

This procedure is repeated along each row and the positions of the cosmic ray events are therefore built up. Due to the order in which the input Boolean array is built up and the fact that pixels are being referenced four indices apart, the position of the TRUE element of the output array passed from the FOR loop structure are shifted with respect to the actual positions of the cosmic ray events. Two rows (1×2048 1D subarray) of FALSE elements are concatenated to the 512×2048 Boolean array passed from the FOR loop. Rows beyond row index 511 (i.e. row#512) are trimmed using the “Delete From Array” node. The 512×2048 dimensionality is restored, but at the cost of two rows (no events can be removed from them). This is generally perfectly acceptable. In order that the TRUE elements of the output array correctly correspond to the positions of cosmic ray events in the data array passed from Segment C, the 512×2048 Boolean array must be transposed before being passed to Segment G (i.e. a 2048×512 array is passed).



**Figure A2.19** Block diagram for DCCR\_SubVI.vi (Segment F). This segment performs the pattern recognition in order to flag the location of cosmic ray events. The segment shifts, trims, and transposes the output array to the correct dimensionality before passing it to Segment G for use in replacing cosmic ray event elements in the data array passed from Segment C.

#### A2.2.10 DCCR\_SubVI.vi (Segment G)

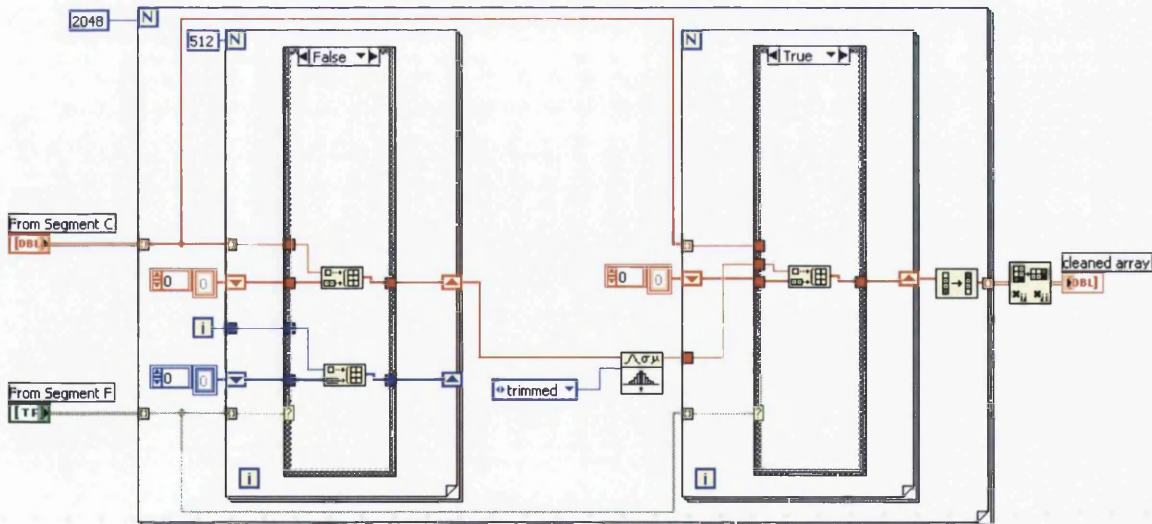
Segment G uses the Boolean array from Segment F to index only the elements of the data array passed from Segment C (undifferentiated but astigmatism corrected data) for replacement with a specified type of column average.

This segment auto-indexes with respect to column index via the mother FOR loop. There are two daughter FOR loops, one (to the left) whose count terminal is wired to a constant value of 512, the other (to the right) whose count terminal is unwired.

The left FOR loop uses the Boolean array from Segment G to pass a 1D subarray containing the values of the elements of the subarray that are not flagged as cosmic ray events. These values are used by the “Measures Of Mean” node to generate the average value that will be substituted in the cosmic ray event-affected elements in the subarray in the second FOR loop. The array of indices (blue wires) were used in debugging and are not used by the second loop (the output shift register acts as the sink for this array).

The second FOR loop uses the Boolean sub array to specify which elements need replacing with the average value calculated by the “Measures Of Mean” node. The case structure passes either the value of the element of the original array or the average value. The case structure is governed by the auto-indexed element of the Boolean subarray and so, if the element is TRUE, the element of the data array is flagged as requiring replacement and the average value is passed to the shift register. If FALSE the original data element is passed. The use of auto-indexing builds up a 2048×512 2D array (note the use of the “Reverse 1D Array” node before the output tunnel of the mother FOR loop), which is then transposed to the original 2048×512 format before being passed to DCRR\_SubVI.vi’s output terminal (“cleaned array”).

Column averages correspond to constant spectral position (wavelength), and so are the appropriate choice for averaging and substitution. The “Measures Of Mean” node is wired to calculate the trimmed mean in the block diagrams shown, but the arithmetic, geometric, harmonic, or median measures of mean can be used instead if desired. This could easily be made user-selectable by making a front panel control to wire to the “type” terminal of the “Measures of Mean” node.




**Figure A2.20** Block diagram for DCRR\_SubVI.vi (Segment G). This segment makes use of the transposed data array from Segment C and the transposed Boolean array from Segment F to replace the elements of the data array effected by cosmic ray events with column averages. The cleaned array is then passed out of DCRR\_SubVI.vi. Note the use throughout of void array constants on the input terminals of shift registers.





### A2.3 High-Level Handling of Spectrum Correction SubVIs

In this section we present an example of how DCRR\_SubVI.vi can be used in a high-level program, although DCRR\_SubVI.vi is obviously not limited to the specific application demonstrated here.

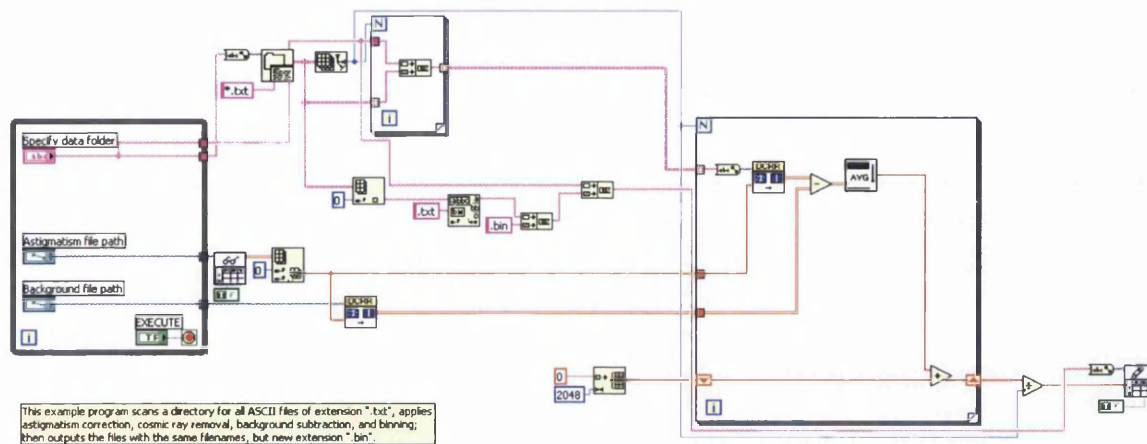
The following example program DCRR\_High\_Example.vi shows DCRR\_SubVI.vi being called multiple times in order to process a large number of ASCII files automatically in one session.

#### A2.3.1 DCRR\_High\_Example.vi

VI filename	DCRR_High_Example.vi
Icon	
Dependencies	N/A (Stand-alone application)
Dependents	Average_2D_Array_SubVI.vi

Front panel control	Purpose
 "EXECUTE"	Executes main section of program
 "Specify data folder"	Specifies location of spectrum ASCII files to be processed (.txt extension)
 "Astigmatism file path"	Specifies path of astigmatism function ASCII file (e.g. AstCalc.vi output)
 "Background file path"	Specifies path of ASCII file of the same format as the spectrum files to be used for background subtraction (.txt extension)

File export is handled by a "Write To Spreadsheet File.vi" node (note use of TRUE Boolean constant wired to "transpose?" terminal).

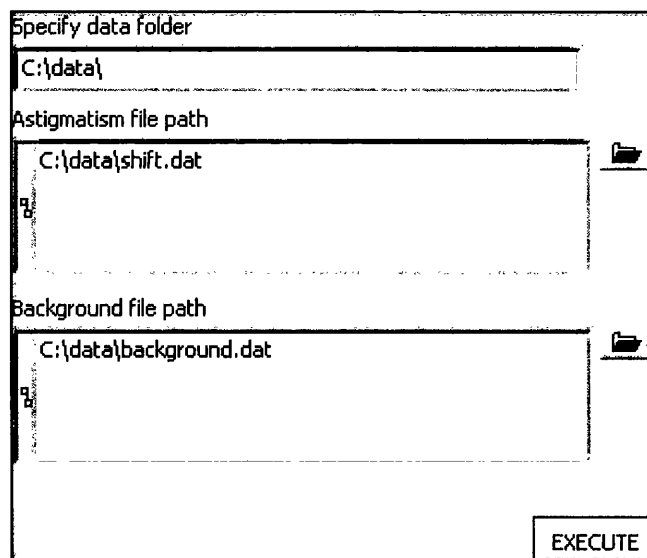


**Figure A2.21** Block diagram for DCRR\_High\_Example.vi, showing how DCRR\_SubVI.vi can be used in high-level programming. This example program scans a specified directory for all ASCII files of extension “.txt”, and uses DCRR\_SubVI.vi to apply astigmatism correction, cosmic ray removal, and background subtraction, and then Average\_2D\_Array\_SubVI.vi to apply row binning. The 1D arrays produced are summed and then divided by the number of files to produce a single array which is the mean of the corrected and binned arrays. This file is then exported with a new extension “.bin” and is the mean of the all the files in the working directory (“data folder”), post-correction.

This example shows DCRR\_SubVI.vi being called  $N+1$  times, where  $N$  is the number of files to be processed in the directory specified by “Specify data folder”. This string is then used to construct an array of the file names of the specified extension “.txt” (an arbitrary choice) so that the files can be processed by DCRR\_SubVI.vi in the FOR loop. The FOR loop’s count terminal is set equal to the number of files to be processed ( $N$ ). DCRR\_SubVI.vi is called  $N$  times in the FOR loop to process each of the files specified by the elements of the array of paths.

DCRR\_SubVI.vi is also called once outside the FOR loop to process the background file. This 2D array is then subtracted from each of the 2D arrays outputted by the DCRR\_SubVI.vi node inside the FOR loop. The subVI “Average\_2D\_Array\_SubVI.vi” is then used to bin the 512 rows of the cleaned array and is added to the ‘running total’ kept by the shift registers, i.e. the 1D binned arrays are summed together. Once all the files in the specified directory have been processed, the elements of the 1D array outputted from the shift register are divided by the number of files processed to obtain the mean value for each element. The resulting 1D array then exported and given the filename of the first file in the working directory (“data folder”), but with the new extension “.bin”.

This program is currently used to process multi-frame spectra exported using the “One File Per Frame” option in the “Convert to ASCII” tool in *WinSpec/32*. The front panel of DCRR\_High\_Example.vi is shown in Figure A2.22. The data folder has to be carefully typed manually by the user in this example since the control is of the string (not path) type. As for previous examples, the user should use the browse buttons on the path controls to specify the location of the required files before pressing the “EXECUTE” Boolean. If a path is not specified, then the user will be prompted after pressing “EXECUTE” to specify a path by the relevant “Read From Spreadsheet File.vi” node. The export dialog comes up automatically at the end of an execution cycle since the “path” terminal on the “Write To Spreadsheet File.vi” node has been left unwired.





**Figure A2.22** Front panel of DCRR\_High\_Example.vi.

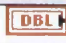
The subVI “Average\_2D\_Array\_SubVI.vi” is embedded in this example and is briefly covered below.

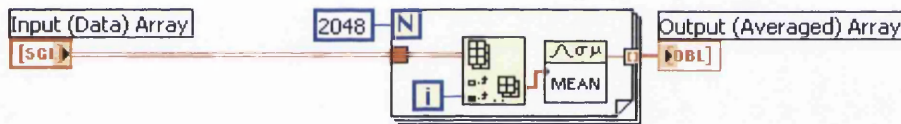
A2.3.2 Average\_2D\_Array\_SubVI.vi

This subVI is used to tidy up the block diagram of DCRR\_High\_Example.vi. It is essentially the code used in AstCorr.vi to bin the corrected 2D array in the final case structure (the Boolean = FALSE case).

VI filename	Average_2D_Array_SubVI.vi
Icon	
Dependencies	DCRR_High_Example.vi
Dependents	DCRR_High_Example.vi

Input	Source
 "Input (Data) Array" (2D array)	DCRR_High_Example.vi

Output	Sink
 "Output (Averaged) Array" (1D array)	DCRR_High_Example.vi



**Figure A2.23** Block diagram for Average\_2D\_Array\_SubVI.vi. The code is similar to that used in AstCorr.vi for the “binned” front panel option.



## ***A2.4 Outlook***

It is planned to use RCubed Software Consultants' *SITK for LabVIEW* in order to handle .SPE files directly, without the need to export the data to ASCII format first. The *SITK* package will also allow programmatic control of the Spec-10 in the *LabVIEW* environment envisioned for the overall control of the KATRIN experiment. The removal of the export / import / 2D construction step from the current data processing technique should provide a significant improvement in the speed of data correction and processing; it currently takes about 10s to export a 2D spectrum, and manual opening of the correction programs and subsequent file handling and analysis are performed manually.

The VIs detailed in this appendix represent the development of processing techniques during the course of this thesis as the nature of the spectral data itself changed. DCRR\_SubVI.vi is currently the post-acquisition correction routine of choice for this work, and provides a solid foundation for the processing stage of the planned master control program that will handle acquisition, processing, analysis, and reporting programmatically.